[redacted]

NACA

RESEARCH MEMORANDUM

for the

U. S. Air Force

INVESTIGATION OF A 1/22-SCALE MODEL OF THE REPUBLIC F-105 AIRPLANE IN THE LANGLEY 8-FOOT TRANSONIC TUNNEL

LATERAL, DIRECTIONAL, AND ADDITIONAL LONGITUDINAL STATIC STABILITY AND CONTROL

By Arvo A. Luoma

Langley Aeronautical Laboratory
Langley Field, Va.

[redacted]

NATIONAL ADVISORY COMMITTEE FOR AERONAUTICS

WASHINGTON

AUG 23 1957

[redacted]

NACA RM SL57H05

NATIONAL ADVISORY COMMITTEE FOR AERONAUTICS

RESEARCH MEMORANDUM

for the

U. S. Air Force

INVESTIGATION OF A 1/22-SCALE MODEL OF THE REPUBLIC F-105 AIRPLANE IN THE LANGLEY 8-FOOT TRANSONIC TUNNEL

LATERAL, DIRECTIONAL, AND ADDITIONAL LONGITUDINAL STATIC STABILITY AND CONTROL

By Arvo A. Luoma

SUMMARY

An investigation of the aerodynamic characteristics of various configurations of a 1/22-scale model of the Republic F-105 airplane has been made in the Langley 8-foot transonic tunnel at Mach numbers from 0.60 to 1.13. Most of the configurations tested included internal flow in the model. The results of the initial phase of the investigation have been published. The results of the second phase of the investigation are presented herein. These results contain information primarily on the static lateral and directional stability and control characteristics of the model. Results on the static longitudinal characteristics of some additional configuration modifications which were not included in the initial phase of the investigation are also presented.

The directional-stability derivative (the rate of change of yawing-moment coefficient with angle of sideslip) was positive (stable) throughout the angle-of-attack and Mach number ranges, but decreased substantially with an increase in angle of attack. A ventral fin and a larger vertical tail increased the directional stability generally by 15 to 20 percent. The rate of change of rolling-moment coefficient with angle of sideslip became zero or positive (negative dihedral effect) at high angles of attack at several subsonic Mach numbers. The spoiler effectiveness decreased markedly with an increase in angle of attack at the higher angles of attack, and became zero or reversed in several instances. The configuration modifications tested had minor effect on longitudinal stability.

INTRODUCTION

An extensive wind-tunnel investigation of the aerodynamic characteristics of the Republic F-105 airplane at subsonic, transonic, and supersonic speeds has been made by the National Advisory Committee for Aeronautics at the request of the U. S. Air Force. The results of the initial phase of a transonic-speed investigation of a 1/22-scale model of the Republic F-105 airplane in the Langley 8-foot transonic tunnel are presented in reference 1. This report presents information on the static longitudinal aerodynamic characteristics of the model, including the effect of various modifications made to the wing and body in an attempt to improve the transonic drag and lift-drag characteristics.

The results of the second phase of the investigation of the 1/22-scale model of the Republic F-105 airplane in the Langley 8-foot transonic tunnel are presented herein. These results contain information primarily on the static lateral and directional stability and control characteristics of the model. Results on the static longitudinal characteristics of some additional configuration modifications not included in reference 1 are also presented.

SYMBOLS

The aerodynamic force and moment data are referred to the stability axes, with the origin at the center-of-gravity location shown in figure 1. This location coincided with the 25-percent point of the mean aerodynamic chord of the wing.

The term "complete model" as used herein refers to the combination of wing (including air inlets), body (including canopy), basic vertical tail, and horizontal tail. The symbols are defined as follows:

A	aspect ratio of wing, b^2/S
b	span (projected) of wing
C_D	external drag coefficient, ($C_D = -C_X$ when $\beta = 0^\circ$), $\frac{\text{External drag}}{qS}$
C_{D_o}	zero-lift external-drag coefficient
C_L	lift coefficient, $\frac{\text{Lift}}{qS}$

[redacted]

C_X external longitudinal-force coefficient, $\frac{\text{External longitudinal force}}{qS}$

C_Y lateral-force coefficient, $\frac{\text{Lateral force}}{qS}$

C_l rolling-moment coefficient, $\frac{\text{Rolling moment}}{qSb}$

C_m pitching-moment coefficient, $\frac{\text{Pitching moment}}{qS\bar{c}}$

C_n yawing-moment coefficient, $\frac{\text{Yawing moment}}{qSb}$

ΔC_D, ΔC_l, ΔC_L, ΔC_m, ΔC_Y, ΔC_n incremental coefficients due to spoiler, speed brakes, or shark fin

c section chord of wing (in region of inlets, wing defined by extending straight portions of leading and trailing edges of wing to plane of symmetry of model), measured parallel to model plane of symmetry

$\bar{c}$ mean aerodynamic chord of wing, $\frac{2}{3} c_r \frac{1 + \lambda + \lambda^2}{1 + \lambda}$

c_e nominal tip chord of wing, obtained by extending leading and trailing edges of wing to plane which is tangent to tip of wing, parallel to root chord of wing, and perpendicular to chord plane of wing

c_r root chord of wing, obtained by extending straight portions of leading and trailing edges of wing to plane of symmetry of model

i_t incidence of horizontal tail, determined by angle between plane of horizontal tail and reference line of body; positive direction when trailing edge is down

$(L/D)_{max}$ maximum value of lift-drag ratio

M Mach number of undisturbed stream

[redacted]

m/m_o	inlet mass-flow ratio, measured by ratio of mass flow in model duct to mass flow through free-stream tube with area equal to inlet throat area (see table I for inlet throat area)
q	dynamic pressure of undisturbed stream
R	Reynolds number of tests, based on $\bar{c}$
S	area (projected) of wing, $(b/2)(c_r + c_e)$
α	angle of attack of model, based on reference line of body
β	angle of sideslip of model
δ_n	deflection of leading-edge flaps, measured in plane perpendicular to hinge line, positive direction when leading edge is up
δ_r	deflection of rudder, measured in plane perpendicular to hinge line, positive direction when trailing edge is to the left
δ_s	deflection of spoiler, measured in plane perpendicular to hinge line
δ_{tr}	deflection of wing trim tab, measured in plane perpendicular to hinge line, positive direction when trailing edge is down
λ	taper ratio of wing, c_e/c_r

$C_{L_\alpha} = \frac{dC_L}{d\alpha}$ per degree

$C_{m_{C_L}} = \frac{dC_m}{dC_L}$

$C_{m_{i_t}} = \frac{dC_m}{di_t}$ per degree

$C_{n_\beta} = \frac{dC_n}{d\beta}$ per degree

$C_{l_\beta} = \frac{dC_l}{d\beta}$ per degree

$C_{Y_\beta} = \frac{dC_Y}{d\beta}$ per degree

$C_{n_{\delta_r}} = \frac{dC_n}{d\delta_r}$ per degree

$C_{l_{\delta_r}} = \frac{dC_l}{d\delta_r}$ per degree

$C_{Y_{\delta_r}} = \frac{dC_Y}{d\delta_r}$ per degree

$C_{n_{\delta_{tr}}} = \frac{dC_n}{d\delta_{tr}}$ per degree

$C_{l_{\delta_{tr}}} = \frac{dC_l}{d\delta_{tr}}$ per degree

$C_{Y_{\delta_{tr}}} = \frac{dC_Y}{d\delta_{tr}}$ per degree

APPARATUS

Tunnel

The tests were made in the Langley 8-foot transonic tunnel. This tunnel operates at a stagnation pressure approximately equal to atmospheric pressure.

Model

Complete model.- The model used in the present investigation was a sting-supported, 1/22-scale model of the Republic F-105 airplane. This airplane is of the fighter-bomber type and is designed for supersonic flight. The airplane is turbojet powered, and has wing-root air inlets. The wing, horizontal tail, and basic vertical tail have 45° of sweepback. The airfoil sections (parallel to the body reference line) of the wing are NACA 65A005.5 at the 0.38b/2 station and NACA 65A003.7 at the tip. The model wing was built of steel. A three-view drawing

[redacted]

of the model is given in figure 1, and the geometric characteristics are given in table I.

The configurations of the present investigation included a flat windshield on the canopy; the configurations of reference 1 had a vee windshield on the canopy. Except for the difference in windshield, the body (without afterbody bump) of the configurations of the present investigation was the same as the body (basic nose and without afterbody bump) of the configurations of reference 1.

An afterbody bump designed for installation on the F-105 airplane was included on the model for about one-half the runs. The longitudinal distribution of the normal cross-sectional area of the complete model with and without the afterbody bump is given in figure 2(a). An area of 1.40 square inches, which corresponded to 90 percent of the inlet area of the supersonic inlet (cruise condition), was subtracted from the area plots to compensate for the internal flow in the model. Photographs of the model with the afterbody bump are shown as figures 2(b) to (d). The afterbody bump was somewhat different in longitudinal and cross-sectional area distributions from those investigated in reference 1.

The model was designed for internal flow. Ducting from the wing-root inlets led into a single duct which had an exit at the body base. A supersonic inlet with a boundary-layer diverter was tested both drooped and undrooped (fig. 3). The drooped inlet tested in the present invesgation was of different design than that tested in the investigation of reference 1. The area of the inlet throat of the model in the present tests corresponded to the cruise condition, and is given in table I. The duct exit area used with this inlet is given in figure 1.

Controls.- The dimensions and location on the wing of leading-edge flaps, a spoiler aileron (mounted on upper surface of left semispan), and a wing trim tab (located on left semispan) are shown in figure 4. (See also table I.) The chord of the trim tab was 0.075c and the span of the trim tab extended from the 0.38b/2 station to the 0.67b/2 station. Individual spoilers were screwed to the wing to obtain the various spoiler deflections and to simulate a flap-type spoiler with the hinge line at approximately the 0.70c line. The spoiler chord was 0.12c and the spoiler span extended from the 0.19b/2 station to the 0.71b/2 station.

The horizontal tail was of the all-movable type and was mounted below the root chord (extended) of the wing. The rudder was of the trailing-edge flap type. The dimensions of the horizontal tail and of the rudder are given in figure 1 and table I. The horizontal tail and rudder were the same as those in reference 1.

Speed brakes consisting of four panels were attached to the rear end of the fuselage as indicated in figure 1. The speed brakes were

[redacted]

tested with each panel deflected 50° (relative to the body reference line).

A "shark" fin was located on the top of the body as shown in figure 5. The deflection tested was 10°; the 0° deflection was not tested.

Additional modifications.- The wing was modified for one run by the addition of a trailing-edge fairing in the region of the inlets as indicated in figure 4. The trailing-edge fairing increased the exposed area of the wing by 0.056 square foot. The leading-edge radius on the leading-edge flaps was modified into a blunt leading-edge radius for one run and into a sharp leading-edge radius for another run. The blunt leading-edge radius was approximately twice the normal leading-edge radius. A fence was added to the wing for one run. Details and location of the fence on the wing are given in figure 4.

Gun blisters (2) were installed on the model for one run as indicated in figure 1. The longitudinal distribution of normal cross-sectional area of the blisters is shown in figure 2(a).

A modified vertical tail and a ventral fin were installed on the model as shown in figure 5, and several runs in sideslip were made of this configuration. The geometric characteristics of the modified vertical tail are included in table I. The modification to the vertical tail increased the area of the vertical tail (to body reference line) by 18 percent.

One run was made with no internal flow in the model. Balsa plugs were placed in the duct as indicated in figure 3 for stopping the internal flow.

Instrumentation

A six-component strain-gage balance housed within the fuselage was used for determining the overall forces and moments on the model. Two static-pressure orifices were located within the chamber surrounding the strain-gage balance and two others on the sides of the sting adjacent to the base of the body.

A strain-gage, pendulum-type attitude transmitter was used for getting the no-load angle of attack of the model. The attitude transmitter was housed in the extension of the model sting and was located approximately 61 inches downstream of the model center-of-gravity location. Flexibility under aerodynamic load of the balance, model sting, and sting extension between the model and the attitude transmitter required a correction to the reading of the attitude transmitter to obtain the model angle of attack.

[redacted]

TEST CONFIGURATIONS AND PROCEDURE

The identification number and description of the configurations tested and a listing of the control deflections are given in table II. All the tests were made with the model in the smooth condition. All the configurations were investigated through an angle-of-attack range at generally eight or nine Mach numbers from 0.60 to 1.13. The angle of attack varied from approximately -2° to 16° at the lowest Mach number to -2° to 9° at the highest Mach number. The angle of sideslip was 0° for all but four runs. In these four runs, the angle of sideslip was either approximately -2.2° or -5.4°. The average Reynolds number of the investigation is shown plotted against Mach number in figure 6.

All the configurations except configuration 31 were investigated with internal flow in the model. The static pressure in the chamber surrounding the strain-gage balance and at the sides of the sting at the body base was measured for all configurations. The internal mass flow and internal drag of the model were not measured in the present investigation since these results were determined in the investigation of reference 1.

CORRECTIONS AND ACCURACY

Pressure and Internal Flow Corrections

No internal flow in model.- The drag coefficient C_D of the configuration with the blocked inlet (configuration 31) has been adjusted for the difference between the actual measured static pressure at the base of the body and that in the undisturbed stream, so that the drag coefficient C_D corresponds to a static pressure at the base of the body equal to that of the undisturbed stream.

Internal flow in model.- The external drag coefficient C_D and external longitudinal-force coefficient C_X of the configurations with internal flow in the model includes corrections for the internal drag coefficient and for the deviation from the free-stream value of the static pressure in the balance chamber and at the rim of the body base. The correction for the internal drag coefficient of the model was determined in the investigation of reference 1.

No corrections were included herein for the effects of internal flow on lift, pitching-moment, rolling-moment, yawing-moment, and

[redacted]

lateral-force coefficients. The maximum effect of internal flow on lift coefficient occurred at the highest angles of attack and amounted to only 0.005.

Tunnel-Boundary Interference

At subsonic Mach numbers, the interference effect of a tunnel boundary on the flow over a model in the test region near the center line of a tunnel have been made negligible by means of a slotted test section (ref. 2).

Data are presented herein at supersonic Mach numbers of 1.03 and 1.13. At a Mach number of 1.03, the interference effects on the data of compression and expansion disturbances reflected from the tunnel boundary were probably small and are believed to have affected primarily the drag data. At a Mach number of 1.13, the data are believed to be insignificantly affected by tunnel-boundary interference.

No corrections have been made to the data for tunnel-boundary interference except to the extent of the partial correction for tunnel-boundary interference inherent in the base-pressure correction, which was made by using the actual measured value of base static pressure.

Sting-Interference Corrections

No sting-interference corrections have been made to the data except to the extent of the partial correction for sting interference inherent in the base-pressure correction, which was made by using the actual measured value of base static pressure.

Angles of Attack and Sideslip

The angle of attack of the model includes an adjustment for the flexibility of the balance and sting under aerodynamic load as discussed in the section entitled "Instrumentation."

In the yaw runs, the angle of sideslip varied slightly with angle of attack and Mach number due to variations in aerodynamic loading. The average value of the angle of sideslip over the angle-of-attack and Mach number ranges is listed in table II. The actual value of the angle of sideslip at a test point was generally within 0.1° of the average value. The figures presenting the derivatives C_{n_β}, C_{l_β}, and C_{Y_β} were computed by using the actual value of the angle of sideslip.

[redacted]

Precision of Data

The estimated accuracy of the data based primarily on the repeatability of the data was as follows:

C_L	±0.01
C_D (at small angles of attack)	±0.0015
C_m	±0.003
C_l	±0.0003
C_n	±0.0004
C_Y	±0.002
α, deg	±0.1
M	±0.003

RESULTS AND DISCUSSION

Presentation of Results

Basic force and moment results.- The basic force and moment results for the various configurations are presented in figures 7 to 37. An index of these figures is given in table II. Values of the control deflections and angle of sideslip are included in the titles of the basic figures only when the values were different from 0°. All configurations except one were tested at a horizontal-tail incidence of -3°. The exception was configuration 14, which included a horizontal-tail incidence of -8°.

The inlet mass-flow ratio m/m_o, based on the results of the investigation of reference 1, was approximately 0.90 at most of the test conditions. The results of reference 1 showed that the inlet mass-flow ratio at a given Mach number decreased at the highest angles of attack; the decrease amounted to approximately 5 percent at an angle of attack of 9° and approximately 20 percent at an angle of attack of 17°. The inlet mass-flow ratio at a given angle of attack generally varied only slightly with change in Mach number.

Summary force and moment results.- Summary plots derived from the basic force and moment data are shown in figures 38 to 56. An index of these plots is given in table III. Control deflections are included in the titles of the summary figures only when the deflections were different from 0°. The longitudinal characteristics of several additional configuration modifications not included in reference 1 are presented herein. Many of the configuration modifications for which comparisons are shown in the figures had slight effect on the aerodynamic characteristics, and such cases are generally not discussed.

[redacted]

Longitudinal Characteristics

Lift and maximum lift-drag ratio.- The lift-curve slope C_{L_α} is presented herein at lift coefficients of 0 and 0.4, and is the average value from 0.1 below to 0.1 above the specified lift coefficient. The maximum effect of configuration modifications on lift-curve slope for which comparisons are shown was about 10 percent (for the afterbody bump, fig. 43).

The effect of configuration modifications on maximum lift-drag ratio showed no significant changes not already shown by the results of reference 1.

Drag.- Addition of the afterbody bump reduced the zero-lift drag coefficient by approximately 0.005 at Mach numbers near 1 and by 0.002 to 0.003 (depending on δ_n setting) at a Mach number of 1.13 (fig. 43). The bump also generally reduced the drag coefficient throughout the lift-coefficient range (figs. 16 and 21, 17 and 22). The gun blisters had negligible effect on the drag coefficient at zero lift (fig. 44) and at lifting conditions (figs. 16 and 18). The ventral fin and the modified vertical tail had small effect on the zero-lift drag coefficient (fig. 46).

The 50°-deflected speed brakes increased the drag coefficient by approximately 0.07 at small angles of attack at the low Mach numbers (fig. 45(b)). The incremental drag coefficient decreased with increase in angle of attack at a Mach number of 0.60.

Pitching moment.- The static longitudinal stability derivative $C_{m_{C_L}}$ is shown herein at the trim condition $C_m = 0$; the lift coefficient corresponding to the trim condition is also shown. The derivative presented is the average value for 0.1 below to 0.1 above the trim lift coefficient.

Configuration modifications generally had small effect on the derivative $C_{m_{C_L}}$ at trim conditions; the greatest effect corresponded to a shift in the aerodynamic center of the complete model of approximately 5 percent of the mean aerodynamic chord (fig. 43). The effect of configuration modifications on trim lift coefficient was also generally small, amounting at most to 0.09 (fig. 43(b)). The effect of a change in Mach number on the derivative $C_{m_{C_L}}$ of the complete model corresponded to a rearward shift of the aerodynamic center of approximately 16 percent of the mean aerodynamic chord between the lowest and highest Mach numbers (fig. 38).

[redacted]

The variation of pitching-moment coefficient with lift coefficient was generally nonlinear. Some decreases in stability, tending toward pitch-up characteristics, were evident at the higher lift coefficients at several Mach numbers. The wing trailing-edge fairing aggravated somewhat the decreases in stability occurring at the higher lift coefficients (figs. 14 and 15). The wing fences had small effect on the stability of the model (figs. 22 and 23).

The effect of the 50°-deflected speed brakes on the horizontal-tail effectiveness $C_{m_{i_t}}$ is indicated in figure 45(c). The effectiveness shown is the average value for horizontal-tail incidences from -3° to -8°. Excessive axial force balance loads limited the speed-brake investigation to the lowest Mach numbers. The speed brakes resulted in a decrease of horizontal-tail effectiveness of approximately 40 percent. The speed brakes caused a change of approximately -0.01 in pitching-moment coefficient over much of the angle-of-attack range at a horizontal-tail incidence of -3° (fig. 45(b)).

The spoilers increased the pitching-moment coefficient by a maximum of approximately 0.04 (nose-up moment) at an angle of attack of 0° (fig. 50). The effect of the spoilers on pitching moment generally decreased with an increase in angle of attack (fig. 50), generally decreased with an increase in spoiler deflection at the higher spoiler deflections (fig. 51), and increased between the lowest and highest test Mach numbers (figs. 52(a) and (b)).

Lateral and Directional Characteristics

Stability.- The static stability derivatives C_{n_β}, C_{l_β}, and C_{Y_β} are shown in figure 47 for the configuration with the basic tail and in figure 48 for the configuration with the ventral fin and the modified vertical tail, and are average values for angles of sideslip from 0° to -2.2° (unflagged symbols) and 0° to -5.4° (flagged symbols). The derivatives are plotted against angle of attack in figures 47(a) and 48(a) and against Mach number in figures 47(b) and 48(b). An indication of the linearity of the variation of C_n, C_l, and C_Y with angle of sideslip is shown by the degree of agreement of the unflagged and flagged points. The results of figures 47(b) and 48(b) for the β range from 0° to -2.2° are replotted in figure 49 to show more directly the effect of the ventral fin and the modified vertical tail on the stability derivatives.

The directional-stability derivative C_{n_β} was positive (stable) throughout the angle-of-attack and Mach number ranges of the investigation (figs. 47(a) and 48(a)). The derivative C_{n_β} decreased substantially with an increase in angle of attack, the decrease amounting to

[redacted]

40 or more percent of the value at an angle of attack of 0°. At subsonic speeds there was generally an increase in the derivative C_{n_β} between angles of sideslip of -2.2° and -5.4° over the angle-of-attack range (figs. 47(a) and 48(a)). The ventral fin and the larger vertical tail increased the directional stability generally by 15 to 20 percent (fig. 49). A substantial increase in C_{n_β} occurred between the lowest and highest Mach numbers at an angle of attack of 0° (figs. 47(b) and 48(b)). A lesser increase also occurred at an angle of attack of 9°.

The stability derivative C_{l_β} was negative (positive dihedral effect) at low and moderate angles of attack, but became zero or positive at high angles of attack at Mach numbers of 0.60, 0.80, and 0.90 (figs. 47(a) and 48(a)). The angle of attack at which the derivative became zero varied from approximately 11.5° at a Mach number of 0.60 to approximately 10° at a Mach number of 0.90 for both the basic configuration (fig. 47(a)) and the configuration with the ventral fin and the larger vertical tail (fig. 48(a)). The ventral fin and larger vertical tail reduced the magnitude of C_{l_β} at Mach numbers above 0.90 at angles of attack greater than approximately 4°. The derivative C_{l_β} was essentially invariant with Mach number at an angle of attack of 0° (figs. 47(b) and 48(b)). At angles of attack of 9° and 13°, however, large negative changes in C_{l_β} occurred with an increase of Mach number at the higher subsonic Mach numbers.

The derivative C_{Y_β} did not vary significantly with change in angle of attack (figs. 47(a) and 48(a)). The ventral fin and the larger vertical tail generally increased the magnitude of the derivative by about 15 percent at all angles of attack and Mach numbers. At angles of attack of 0° and 9°, the magnitude of the derivative increased somewhat with an increase in Mach number at the higher Mach numbers (figs. 47(b) and 48(b)).

Lateral control and trim.- The spoiler effectiveness ΔC_l at the higher deflections became a maximum at an angle of attack of approximately 6° (fig. 50). Similar results have been shown by other spoiler configurations on sweptback wings (ref. 4). The spoiler effectiveness decreased markedly with an increase in angle of attack at the higher angles of attack. This decrease generally began at angles of attack greater than 6°, but at the higher Mach numbers and for the smaller spoiler deflections the decrease began at lower angles of attack. In several instances, the spoiler effectiveness decreased to zero or became reversed at high angles of attack.

[redacted]

The variation of spoiler effectiveness ΔC_l with spoiler deflection is shown for two angles of attack in figure 51. Ineffectiveness of the lowest spoiler deflection at an angle of attack of 9° at Mach numbers up to 0.97 is evident in figure 51(b). At higher angles of attack, this ineffectiveness extended to higher spoiler deflections (fig. 50).

The variation of spoiler effectiveness ΔC_l with Mach number is shown for several angles of attack in figure 52. At angles of attack of 0° and 9°, the spoiler effectiveness at supersonic speeds was greater than that at a Mach number of 0.60 (figs. 52(a) and (b)).

The spoilers changed the yawing-moment coefficient by a maximum of approximately -0.008 (favorable) at an angle of attack of 0° (figs. 50 or 51(a)). The effect of the spoilers on yawing moment decreased with an increase in angle of attack (fig. 50), generally decreased with an increase in spoiler deflection at the higher spoiler deflections (fig. 51), and did not change greatly with a change in Mach number (fig. 52).

The derivatives $C_{n_{\delta_{tr}}}$, $C_{l_{\delta_{tr}}}$, and $C_{Y_{\delta_{tr}}}$ of the wing trim tab are shown in figure 53(c), and are average values for trim tab deflections from 0° to -12.2°. The variation of these derivatives with angle of attack and Mach number was generally small. A theoretical trim-tab effectiveness $C_{l_{\delta_{tr}}}$ of 0.0003 at a Mach number of 0.60 was obtained by the methods of reference 3. The corresponding experimental value was 0.0004 (fig. 53(c)).

Directional control.- The derivatives $C_{n_{\delta_r}}$, $C_{l_{\delta_r}}$, and $C_{Y_{\delta_r}}$ due to rudder deflection are shown in figure 54(b), and are average values for rudder deflections from 0° to 6° (unflagged symbols) and 0° to 12° (flagged symbols). An indication of the linearity of the variation of C_n, C_l, and C_Y with rudder deflection is shown by the degree of agreement of the unflagged and flagged points. On the whole, the divergence from linearity was quite small.

The derivatives $C_{n_{\delta_r}}$ and $C_{Y_{\delta_r}}$ varied only slightly with angle of attack (fig. 54(b)). The rudder effectiveness $C_{n_{\delta_r}}$ was about -0.002 per degree. An increase in angle of attack reduced $C_{l_{\delta_r}}$, making the derivative negative at high angles of attack. The variation of the rudder-deflection derivatives with Mach number is shown at two angles of attack in figure 54(c). Results on the rudder characteristics obtained in the investigation of reference 1 are included on this figure for comparison.

[redacted]

The changes in the derivatives with change in Mach number were generally small. The rudder effectiveness was somewhat less for the present configuration.

The effect on C_n, C_l, and C_Y of the addition of the 10°-deflected shark fin to the model is given in figure 55(b). The yawing-moment coefficient was changed by approximately -0.001 (5 percent as effective as rudder deflection) at subsonic speeds, and by a larger amount at supersonic speeds (fig. 55(b)). The effect of the shark fin on rolling moment at an angle of attack of 0° was about one-third that of rudder deflection.

CONCLUSIONS

An investigation was made in the Langley 8-foot transonic tunnel of the lateral, directional, and additional longitudinal static stability and control characteristics of various configurations of a 1/22-scale model of the Republic F-105 airplane. The Mach number range of the tests was generally from 0.60 to 1.13, and the Reynolds number based on the mean aerodynamic chord of the wing was approximately 2×10^6. All the configurations except one were investigated with internal flow in the model. The following conclusions are indicated:

1. The directional-stability derivative (the rate of change of yawing-moment coefficient with angle of sideslip) was positive (stable) throughout the angle-of-attack and Mach number ranges, but decreased substantially with an increase in angle of attack. A ventral fin and a larger vertical tail increased the directional stability generally by 15 to 20 percent.

2. The rate of change of rolling-moment coefficient with angle of sideslip became zero or positive (negative dihedral effect) at high angles of attack at several subsonic Mach numbers.

3. The spoiler effectiveness decreased markedly with an increase in angle of attack at the higher angles of attack, and became zero or reversed in several instances. The smaller spoiler deflections were relatively ineffective at high angles of attack at subsonic speeds.

4. The rudder effectiveness (the rate of change of yawing-moment coefficient with rudder deflection) was approximately -0.002 per degree throughout the angle-of-attack and Mach number ranges.

[redacted]

5. The configuration modifications tested had minor effect on longitudinal stability.

Langley Aeronautical Laboratory,
National Advisory Committee for Aeronautics,
Langley Field, Va., July 19, 1957.

Arvo A. Luoma
Aeronautical Research Engineer

Approved: Eugene C. Draley
Eugene C. Draley
Chief of Full-Scale Research Division

bcc

REFERENCES

1. Luoma, Arvo A.: Investigation of a 1/22-Scale Model of the Republic F-105 Airplane in the Langley 8-Foot Transonic Tunnel - Static Longitudinal Stability and Control and Performance Characteristics at Transonic Speeds. NACA RM SL56D12, U. S. Air Force, 1956.

2. Ritchie, Virgil S., and Pearson, Albin O.: Calibration of the Slotted Test Section of the Langley 8-Foot Transonic Tunnel and Preliminary Experimental Investigation of Boundary-Reflected Disturbances. NACA RM L51K14, 1952.

3. DeYoung, John: Theoretical Antisymmetric Span Loading for Wings of Arbitrary Plan Form at Subsonic Speeds. NACA Rep. 1056, 1951. (Supersedes NACA TN 2140.)

4. West, F. E., Jr., Solomon, William, and Brummal, Edward M.: Investigation of Spoiler Ailerons With and Without a Gap Behind the Spoiler on a 45° Sweptback Wing-Fuselage Combination at Mach Numbers From 0.60 to 1.03. NACA RM L53G07a, 1953.

[redacted]

TABLE I.- GEOMETRIC CHARACTERISTICS OF 1/22-SCALE MODEL

OF REPUBLIC F-105 AIRPLANE

Body (without afterbody bump):	
Length, in.	32.830
Maximum width, in.	2.387
Maximum depth (excluding canopy), in.	3.546
Frontal area (including canopy), sq ft	0.0510
Side area (including canopy), sq ft	0.698
Volume (including canopy), cu ft	0.106
$\frac{\text{Frontal area}}{\text{Wing area}}$	0.0643
$\frac{\text{Total base area}}{\text{Wing area}}$	0.0307
Wing:	
Airfoil section (parallel to body reference line):	
At 0.38b/2 station	NACA 65A005.5
Tip	NACA 65A003.7
Root chord c_r:	
Length, in.	8.181
Incidence with respect to body reference line, deg	0
Location above body reference line, in.	0.614
Location (parallel to body reference line) of leading edge of root chord from nose of body, in.	11.758
Tip chord c_e, in.	3.818
Span b, in.	19.054
Area S, sq ft	0.794
Aspect ratio A	3.18
Taper ratio λ	0.467
Mean aerodynamic chord:	
Length, in.	6.264
Location above body reference line, in.	0.358
Location (parallel to body reference line) of leading edge of mean aerodynamic chord from leading edge of root chord, in.	4.666
Sweepback of projected 25-percent-chord line, deg	45
Dihedral, deg	-3.5
Twist, deg	0
Leading-edge flaps:	
Type	Drooped-plain flap
Area (two flaps), sq ft	0.0472
Span (one flap), in.	5.336
Sweepback at hinge line	49° 07' 26"
Chord (average), in.	0.638
Spoiler aileron:	
Type	Flap
Location of spoiler on wing	Left semispan, upper surface
Location (chordwise) of hinge line	Approximately 0.70c
Area, sq ft	0.0256
Span, in.	4.944
Chord	0.12c
Trim tab:	
Type	Plain
Location of trim tab on wing	Left semispan
Location (chordwise) of hinge line	0.925c
Sweepback of hinge line	35° 30'
Area, sq ft	0.00837
Span, in.	2.727
Chord	0.075c
Horizontal tail:	
Type	All movable
Airfoil section (parallel to model plane of symmetry):	
Root	NACA 65A006
Tip	NACA 65A004
Root chord, in.	4.091
Tip chord, in.	1.864
Span, in.	9.090
Area (total), sq ft	0.188
Aspect ratio	3.06
Taper ratio	0.456

TABLE I.- GEOMETRIC CHARACTERISTICS OF 1/22-SCALE MODEL OF REPUBLIC F-105 AIRPLANE - Concluded

Mean aerodynamic chord:	
Length, in.	3.114
Location of leading edge of mean aerodynamic chord from leading edge of root chord, in.	2.231
Sweepback of 25-percent-chord line, deg	45
Dihedral, deg	0
Twist, deg	0
Vertical tail (basic):	
Airfoil section (parallel to body reference line):	
Exposed root (1.591 in. above body reference line)	NACA 65A006
Tip	NACA 65A004
Root chord (at body reference line), in.	5.473
Tip chord, in.	2.000
Span (to body reference line), in.	5.955
Area (to body reference line), sq ft	0.155
Aspect ratio $\left(\frac{(\text{Span})^2}{\text{Area}}\right)$	1.60
Taper ratio	0.365
Mean aerodynamic chord:	
Length, in.	4.003
Location (parallel to the body reference line) of leading edge of mean aerodynamic chord from leading edge of root chord, in.	2.887
Location (spanwise) of mean aerodynamic chord from root chord, in.	2.514
Sweepback of 25-percent-chord line, deg	45
Rudder:	
Type	Trailing-edge flap
Chord, in.	0.902
Span, in.	3.726
Area, sq ft	0.0235
Aspect ratio	4.10
Sweepback of hinge line	29° 21.5'
Vertical tail (modified):	
Root chord (at body reference line), in.	6.888
Tip chord, in.	1.956
Span (to body reference line), in.	5.955
Area (to body reference line), sq ft	0.183
Aspect ratio $\left(\frac{(\text{Span})^2}{\text{Area}}\right)$	1.35
Taper ratio	0.284
Mean aerodynamic chord:	
Length, in.	4.882
Location (parallel to body reference line) of leading edge of mean aerodynamic chord from leading edge of root chord, in.	3.371
Location (spanwise) of mean aerodynamic chord from root chord, in.	2.424
Sweepback of 25-percent-chord line	49° 48.6'
Rudder:	
Type	Trailing-edge flap
Chord, in.	0.902
Span, in.	3.726
Area, sq ft	0.0235
Aspect ratio	4.10
Sweepback of hinge line	29° 21.5'
Duct areas:	
Inlet throat (scaled down from full-scale value):	
Supersonic inlet (cruise condition), sq in.	1.550
Projected inlet (scaled down from full-scale value):	
Supersonic inlet (cruise condition), sq in.	1.746
Exit:	
Supersonic inlet (cruise condition), sq in.	2.024

[redacted]

TABLE II

CONFIGURATIONS AND INDEX OF BASIC FIGURES

Configuration										Figure
Number	Description	Control-surface deflection					Inlet	After-body bump	β, deg	
		i_t, deg	δ_n, deg	δ_s, deg	δ_{tr}, deg	δ_r, deg				
1	Complete model	-3	0	0	0	0	Drooped	Off	0	7
2	Complete model	-3	0	8.3	0	0	Drooped	Off	0	8
3	Complete model	-3	0	14.8	0	0	Drooped	Off	0	9
4	Complete model	-3	0	23.2	0	0	Drooped	Off	0	10
5	Complete model	-3	0	41.1	0	0	Drooped	Off	0	11
6	Complete model	-3	0	54.8	0	0	Drooped	Off	0	12
7	Complete model	-3	0	64.0	0	0	Drooped	Off	0	13
8	Complete model	-3	-7.5	0	0	0	Drooped	Off	0	14
9	Complete model plus wing trailing-edge fairing	-3	-7.5	0	0	0	Drooped	Off	0	15
10	Complete model	-3	0	0	0	0	Undrooped	Off	0	16
11	Complete model	-3	-7.5	0	0	0	Undrooped	Off	0	17
12	Complete model plus gun blisters	-3	0	0	0	0	Undrooped	Off	0	18
13	Complete model plus 50°-deflected speed brakes	-3	0	0	0	0	Undrooped	Off	0	19
14	Complete model plus 50°-deflected speed brakes	-8	0	0	0	0	Undrooped	Off	0	20
15	Complete model	-3	0	0	0	0	Undrooped	On	0	21
16	Complete model	-3	-7.5	0	0	0	Undrooped	On	0	22
17	Complete model plus wing fences	-3	-7.5	0	0	0	Undrooped	On	0	23
18	Complete model plus blunt L.E. radius on L.E. flap	-3	-7.5	0	0	0	Undrooped	On	0	24
19	Complete model plus sharp L.E. radius on L.E. flap	-3	-7.5	0	0	0	Undrooped	On	0	25
20	Complete model	-3	0	0	-12.2	0	Undrooped	On	0	26
21	Complete model	-3	0 Right -7.5 Left	0	-12.2	0	Undrooped	On	0	27
22	Complete model	-3	-7.5	0	-12.2	0	Undrooped	On	0	28
23	Complete model plus 10°-deflected shark fin	-3	0	0	0	0	Undrooped	On	0	29
24	Complete model	-3	0	0	0	6	Undrooped	On	0	30
25	Complete model	-3	0	0	0	12	Undrooped	On	0	31
26	Complete model	-3	0	0	0	0	Undrooped	On	-2.2	32
27	Complete model	-3	0	0	0	0	Undrooped	On	-5.4	33
28	Complete model plus ventral fin and plus modified vertical tail	-3	0	0	0	0	Undrooped	On	0	34
29	Complete model plus ventral fin and plus modified vertical tail	-3	0	0	0	0	Undrooped	On	-2.2	35
30	Complete model plus ventral fin and plus modified vertical tail	-3	0	0	0	0	Undrooped	On	-5.4	36
31	Complete model with blocked inlet	-3	0	0	0	0	Undrooped	On	0	37

[redacted]

TABLE III

INDEX OF SUMMARY PLOTS

Description	Figure
Effect of inlet droop	38
Effect of wing trailing-edge fairing	39
Effect of deflection of leading-edge flaps	40
Effect of leading-edge radius of leading-edge flaps	41
Effect of wing fences	42
Effect of afterbody bump	43
Effect of gun blisters	44
Effect of 50°-deflected speed brakes	45
Effect of ventral fin and modified vertical tail on longitudinal aerodynamic characteristics	46
Static lateral-stability derivatives; complete model	47
Static lateral-stability derivatives; complete model plus ventral fin and plus modified vertical tail	48
Effect of ventral fin and modified vertical tail on static lateral-stability derivatives	49
Spoiler characteristics against α	50
Spoiler characteristics against δ_s	51
Spoiler characteristics against M	52
Effect of deflection of wing trim tab	53
Effect of rudder deflection	54
Effect of 10°-deflected shark fin	55
Effect of blocked inlet	56

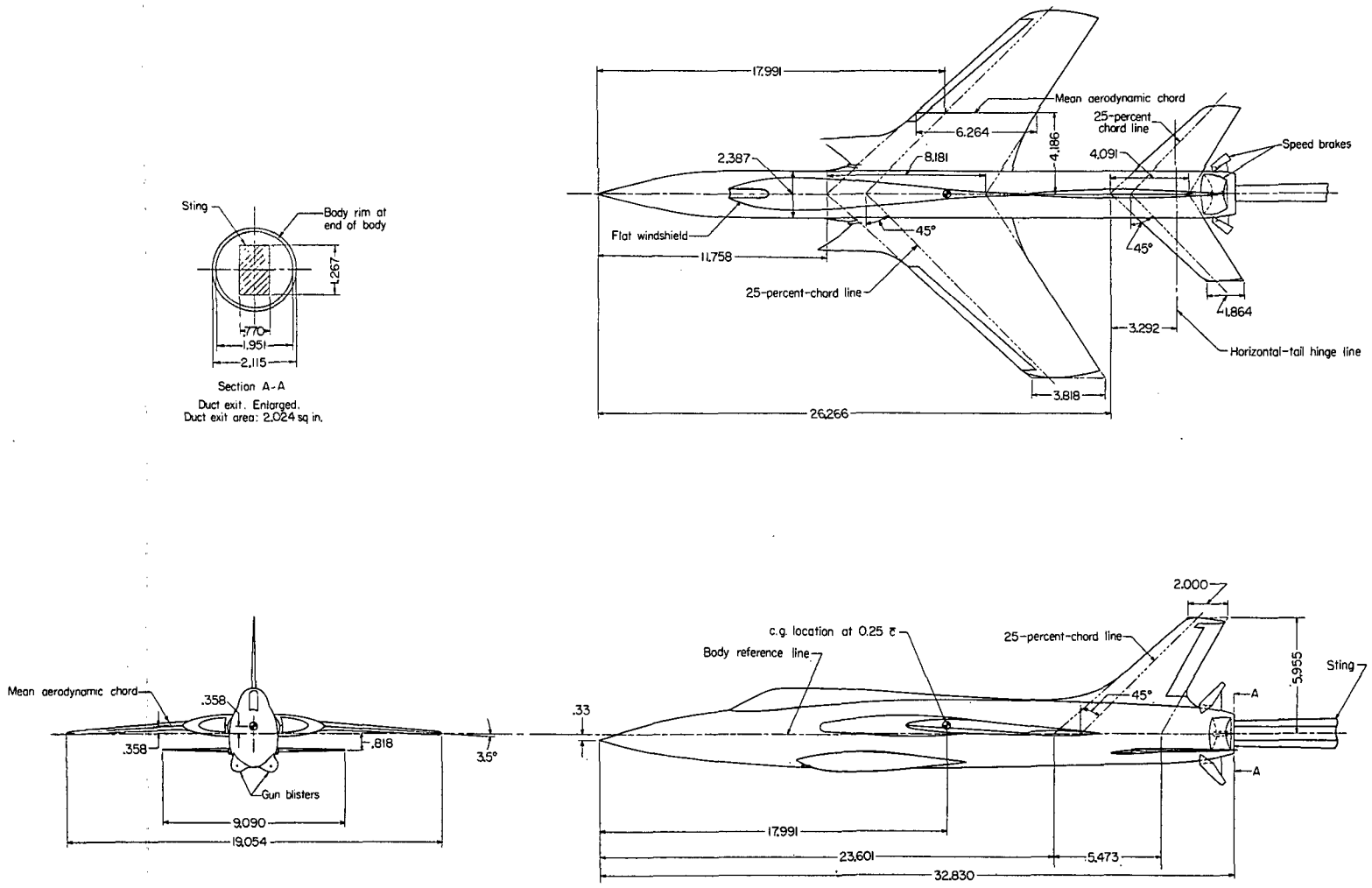

Figure 1.- General arrangement of 1/22-scale model of Republic F-105 airplane. Complete model with gun blisters and speed brakes; body without afterbody bump; A = 3.18; supersonic inlet (cruise condition). All dimensions are in inches except as noted.

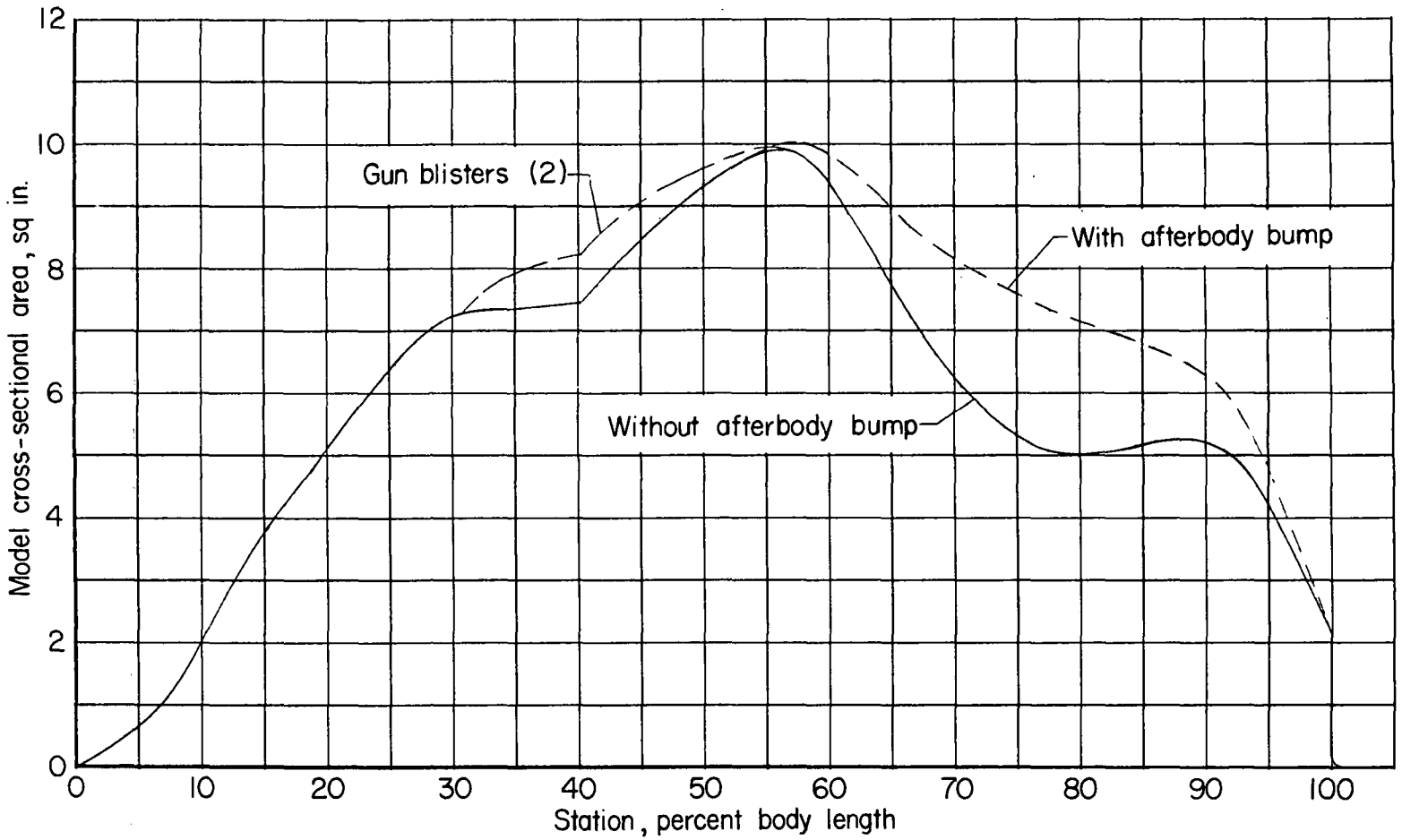

(a) Longitudinal distribution of normal cross-sectional area.

Figure 2.- Area-rule applications to 1/22-scale model of Republic F-105 airplane. Complete model with and without an afterbody bump and complete model plus gun blisters; A = 3.18; supersonic inlet (cruise condition).

L-87030

(b) Side view of configuration 15; body with afterbody bump.

Figure 2.- Continued.

L-87029

(c) Plan view of configuration 15; body with afterbody bump.

Figure 2.- Continued.

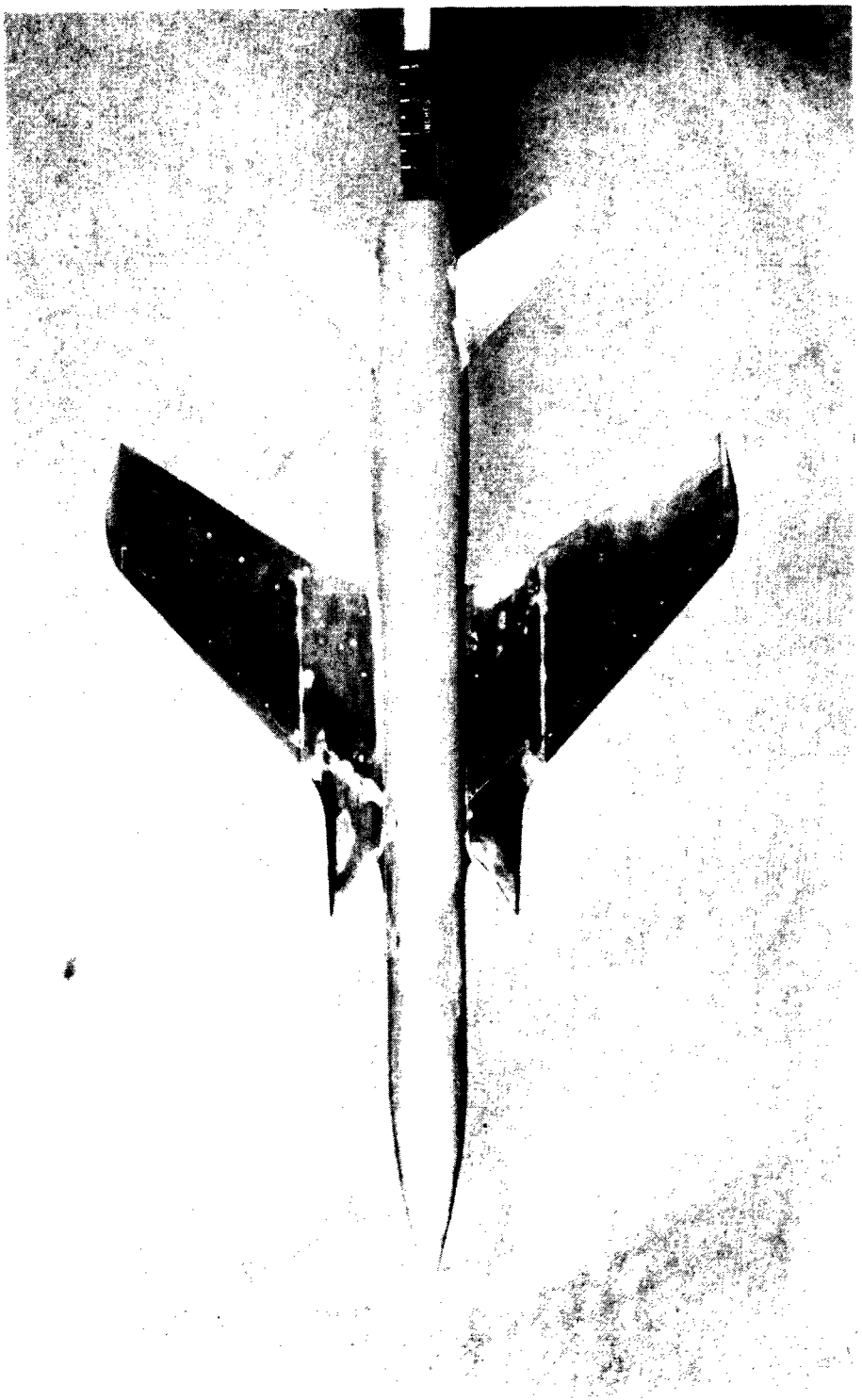

L-87031

(d) Bottom view of configuration 15; body with afterbody bump.

Figure 2.- Concluded.

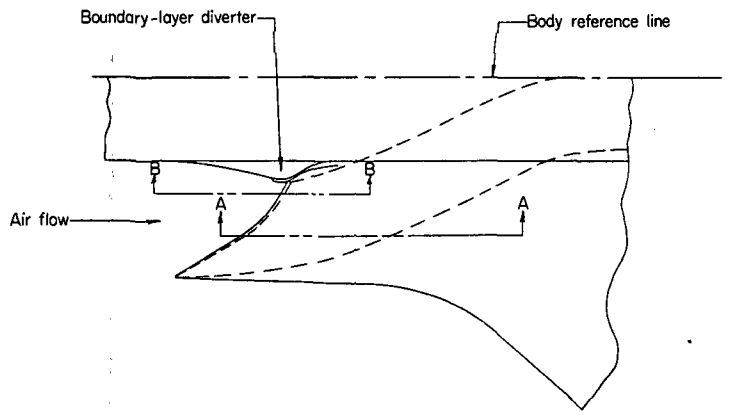

Drooped supersonic inlet (cruise condition)

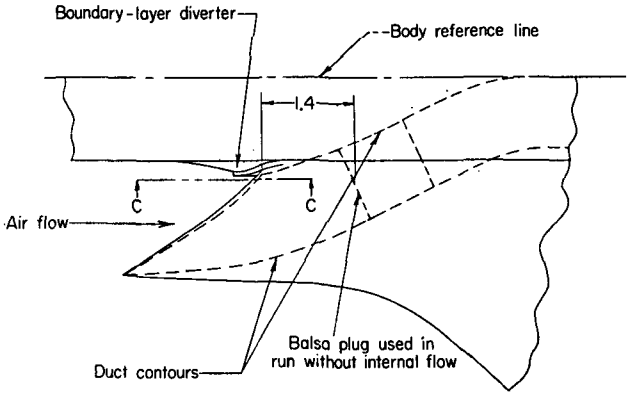

Undrooped supersonic inlet (cruise condition)

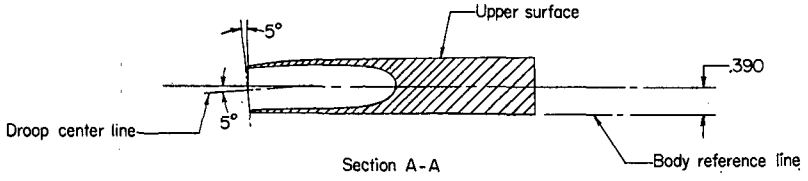

Section A-A

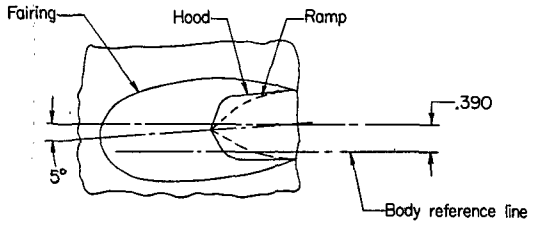

Section B-B

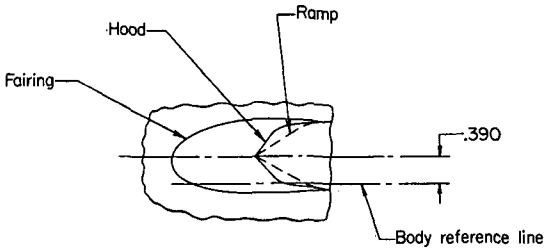

Section C-C

Figure 3.- Drooped and undrooped supersonic inlet (cruise condition) on 1/22-scale model of Republic F-105 airplane. All dimensions are in inches except as noted.

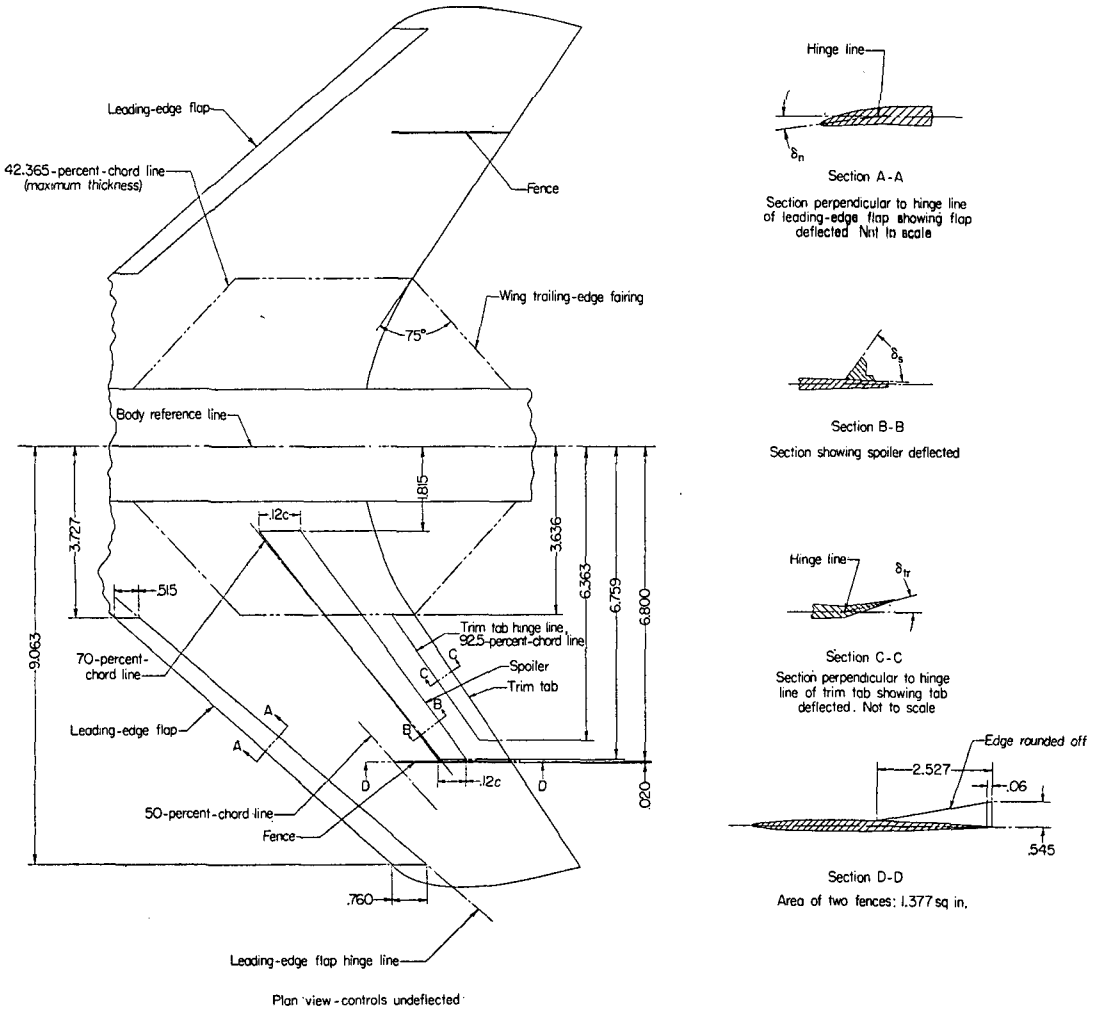

Figure 4.- Dimensions and location of leading-edge flaps, spoiler, trim tab, fence, and trailing-edge fairing on wing of 1/22-scale model of Republic F-105 airplane. All dimensions are in inches except as noted.

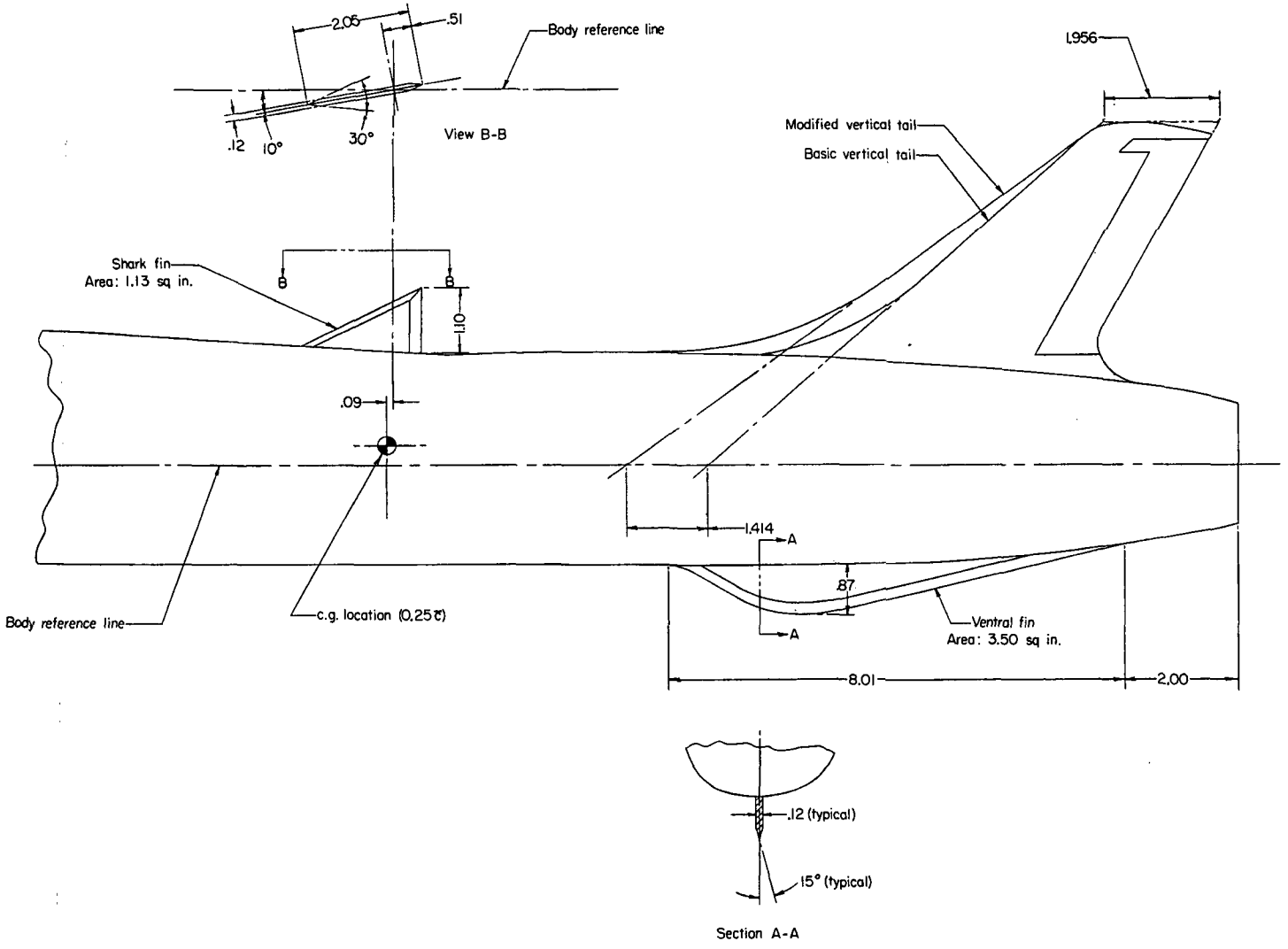

Figure 5.- Dimensions and location of shark fin, ventral fin, and modified vertical tail on 1/22-scale model of Republic F-105 airplane. All dimensions are in inches except as noted.

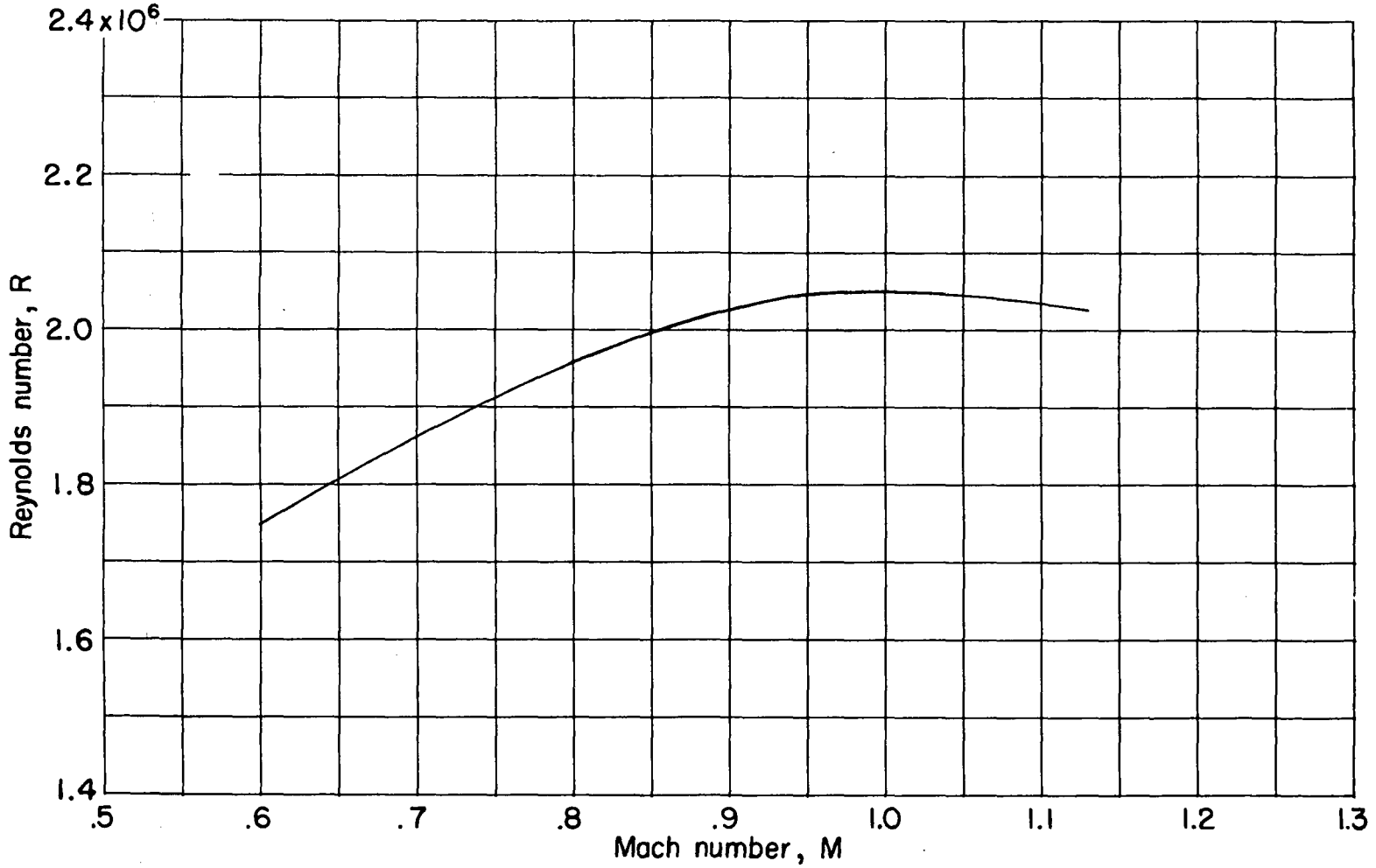

Figure 6.- Variation of Reynolds number (based on mean aerodynamic chord of 6.264 inches) with Mach number in tests of 1/22-scale model of Republic F-105 airplane in Langley 8-foot transonic tunnel.

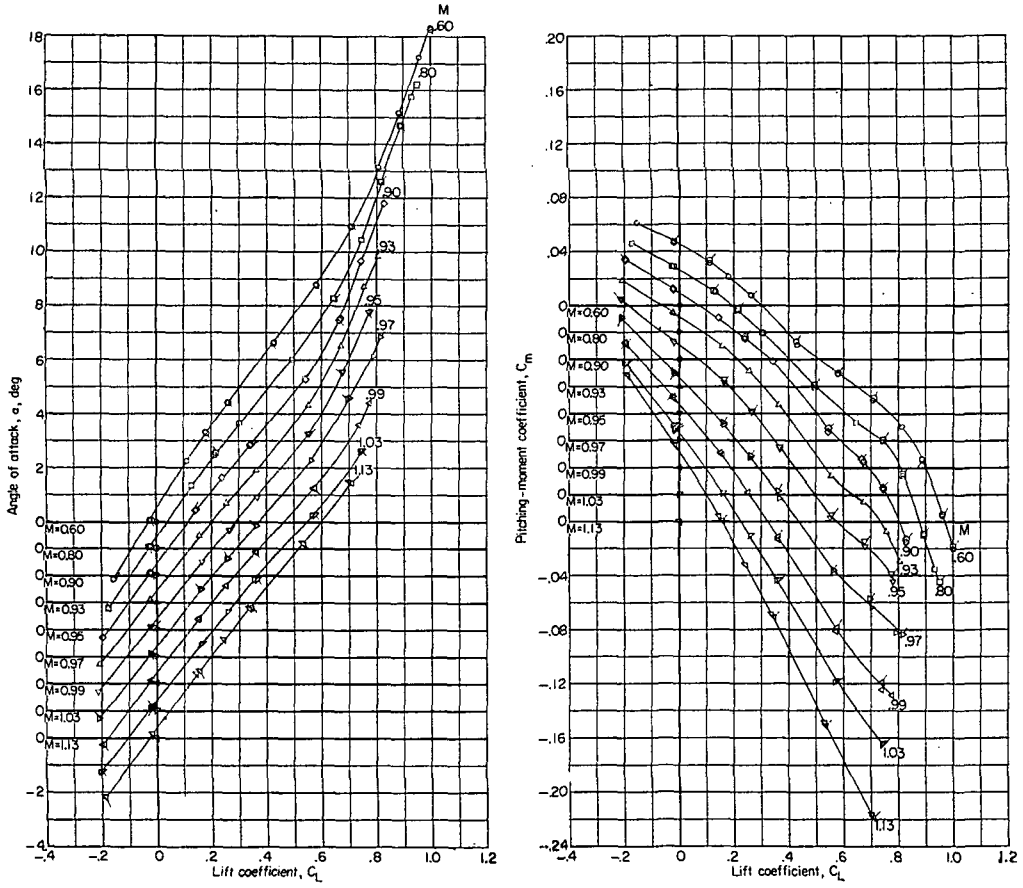

(a) Angle of attack and pitching-moment coefficient.

Figure 7.- Variation of aerodynamic characteristics with either lift coefficient or angle of attack. Configuration 1; complete model; $i_t = -3^\circ$; drooped supersonic inlet (cruise condition). (Flagged symbols indicate points from repeat run.)

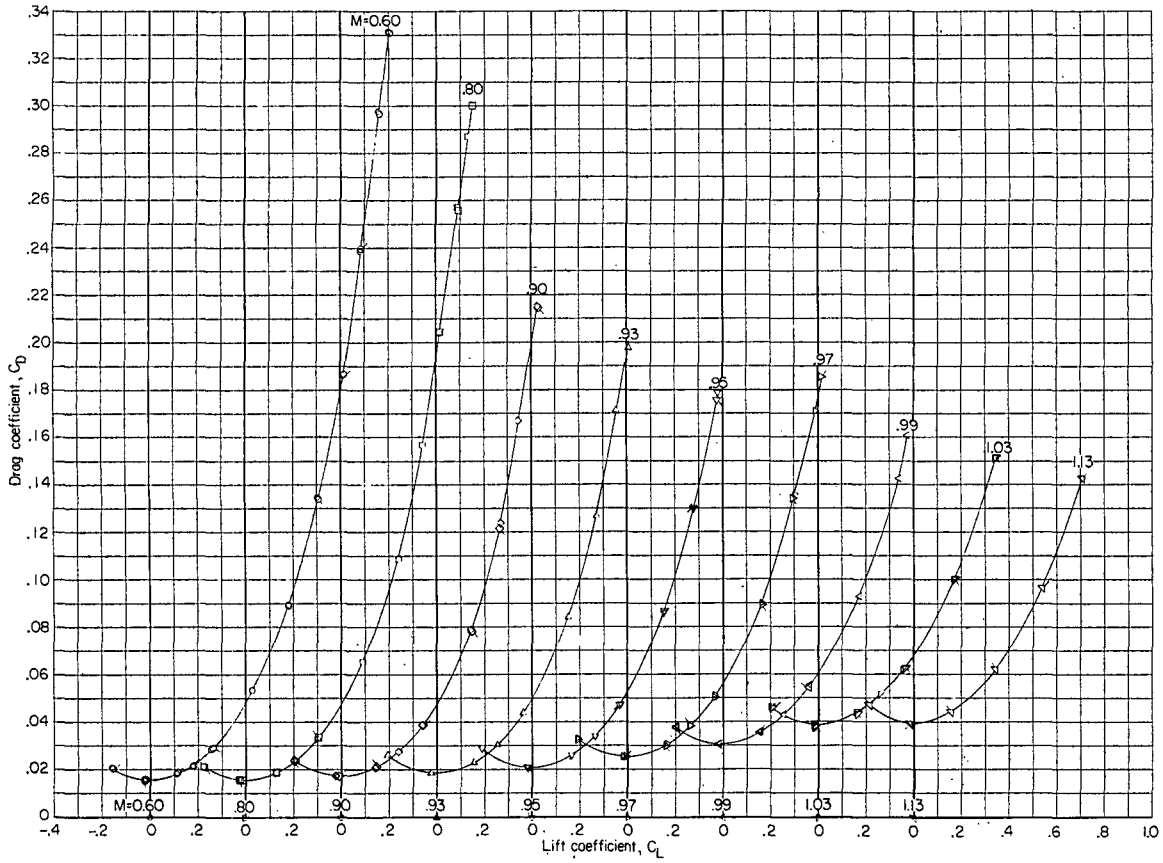

(b) Drag coefficient.

Figure 7.- Continued.

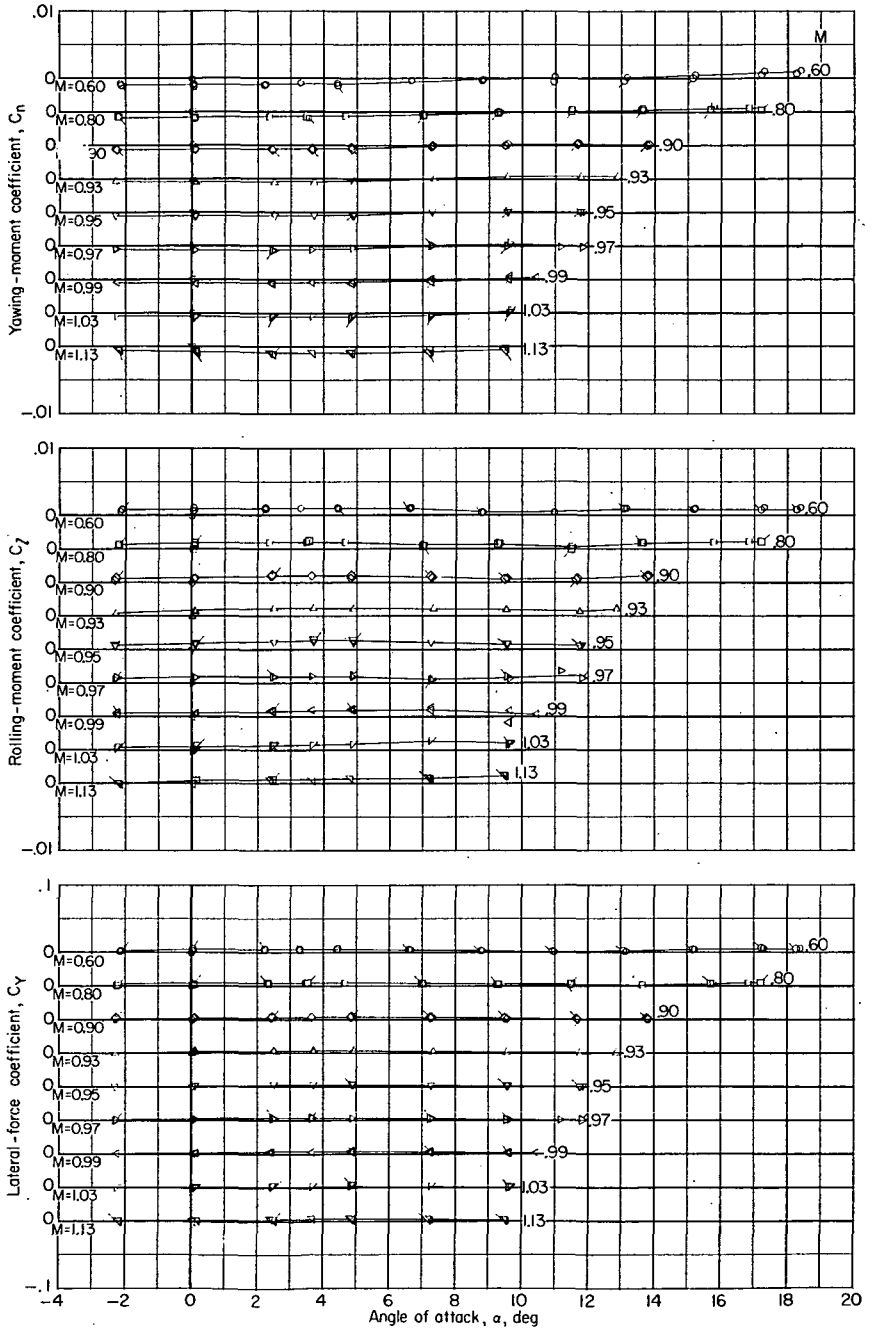

(c) Yawing-moment, rolling-moment, and lateral-force coefficients.

Figure 7.- Concluded.

[redacted]

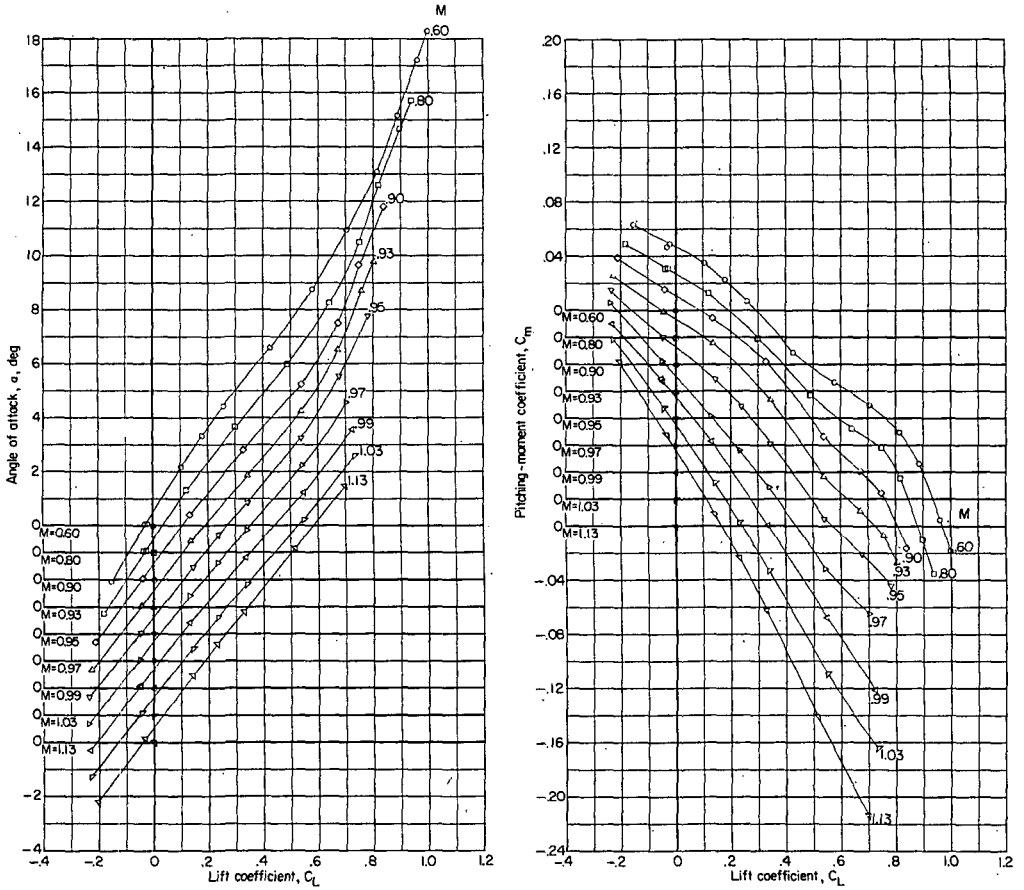

(a) Angle of attack and pitching-moment coefficient.

Figure 8.- Variation of aerodynamic characteristics with either lift coefficient or angle of attack. Configuration 2; complete model; $i_t = -3^\circ$; $\delta_s = 8.3^\circ$; drooped supersonic inlet (cruise condition).

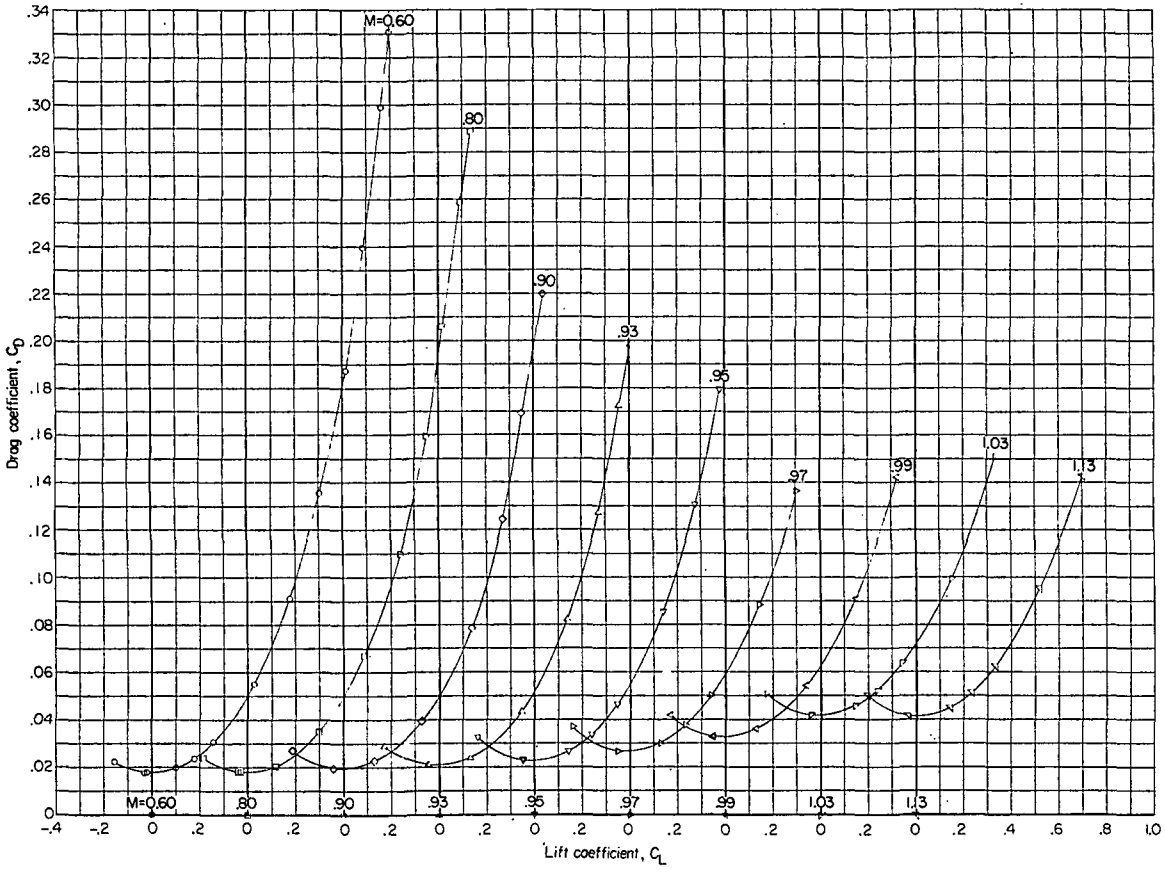

(b) Drag coefficient.

Figure 8.- Continued.

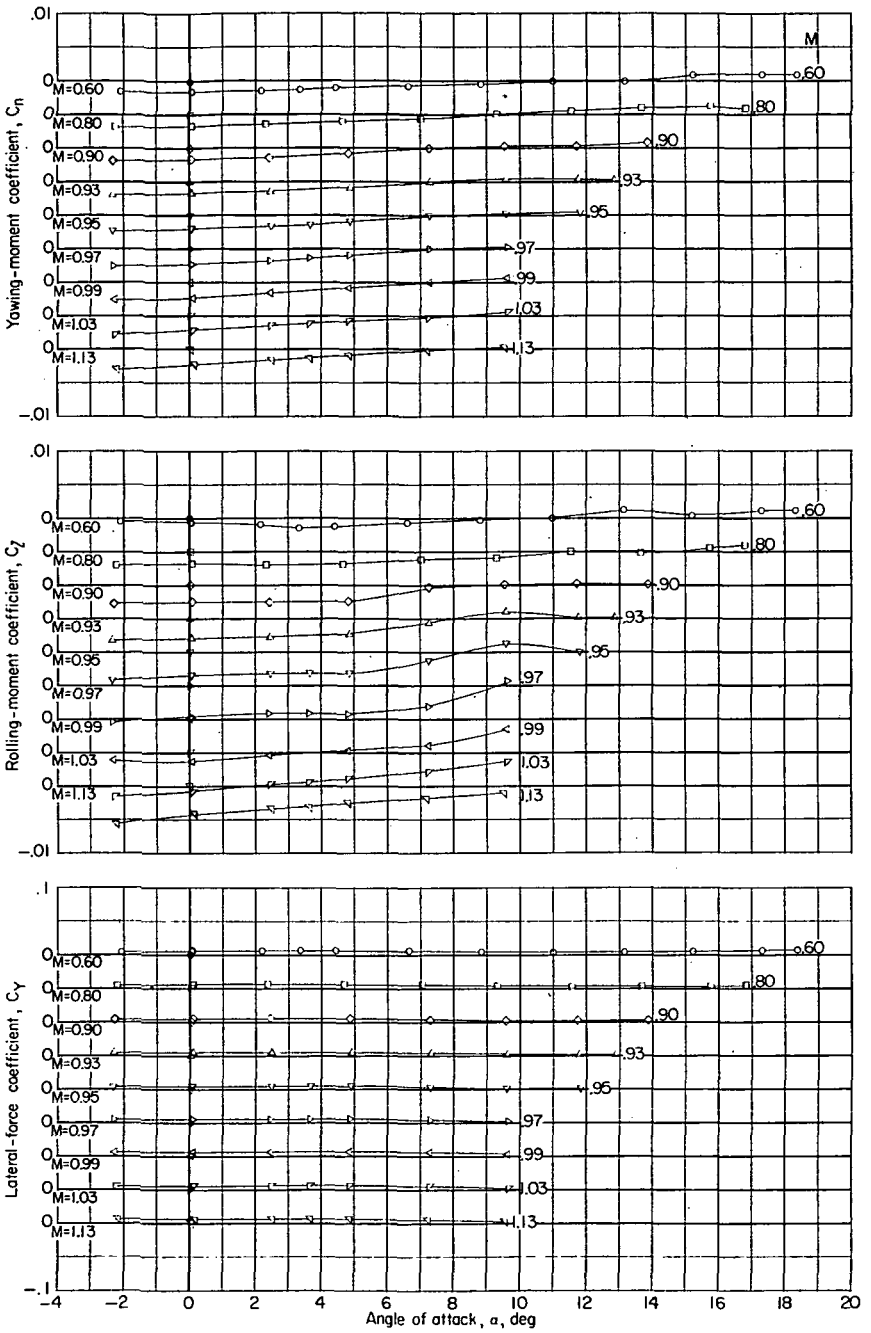

(c) Yawing-moment, rolling-moment, and lateral-force coefficients.

Figure 8.- Concluded.

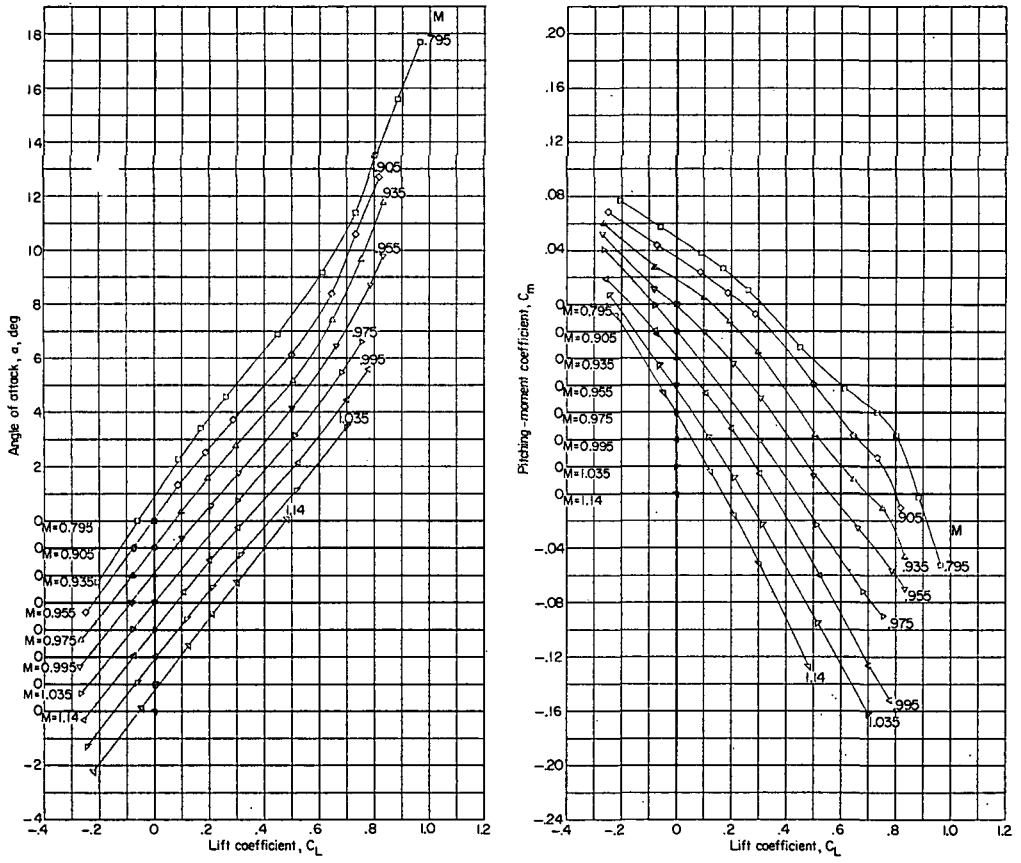

(a) Angle of attack and pitching-moment coefficient.

Figure 9.- Variation of aerodynamic characteristics with either lift coefficient or angle of attack. Configuration 3; complete model; $i_t = -3^\circ$; $\delta_s = 14.8^\circ$; drooped supersonic inlet (cruise condition).

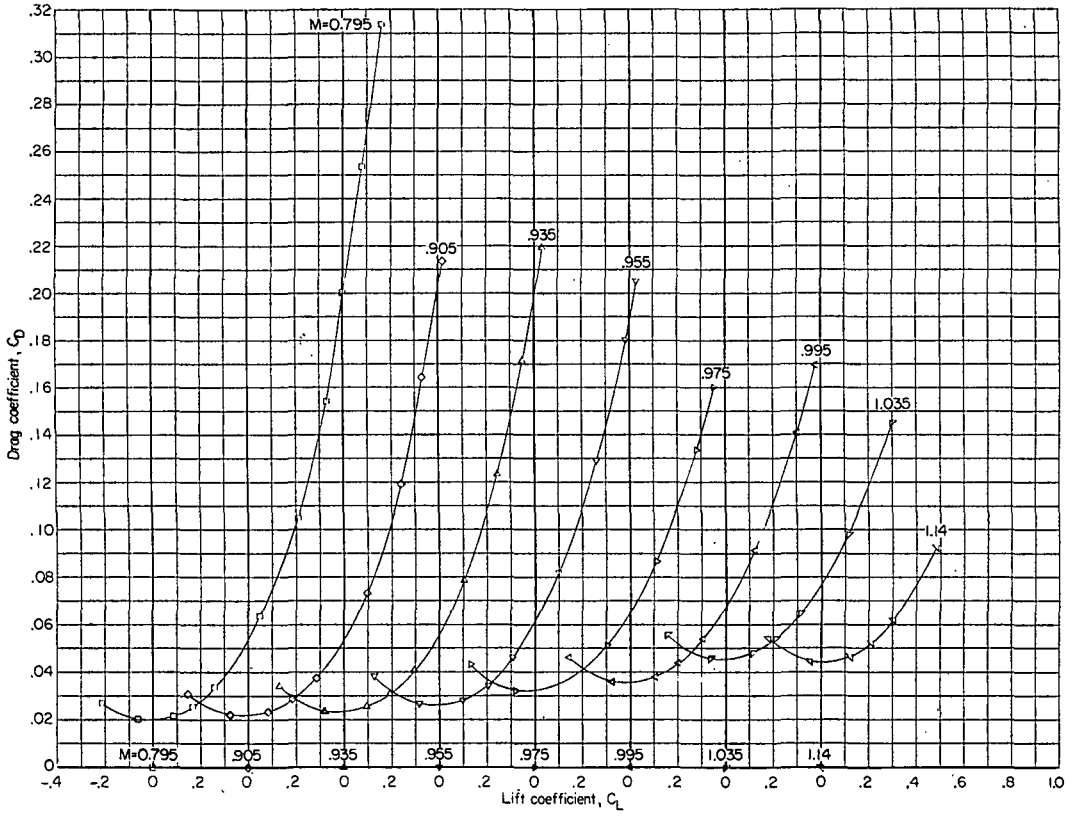

(b) Drag coefficient.

Figure 9.- Continued.

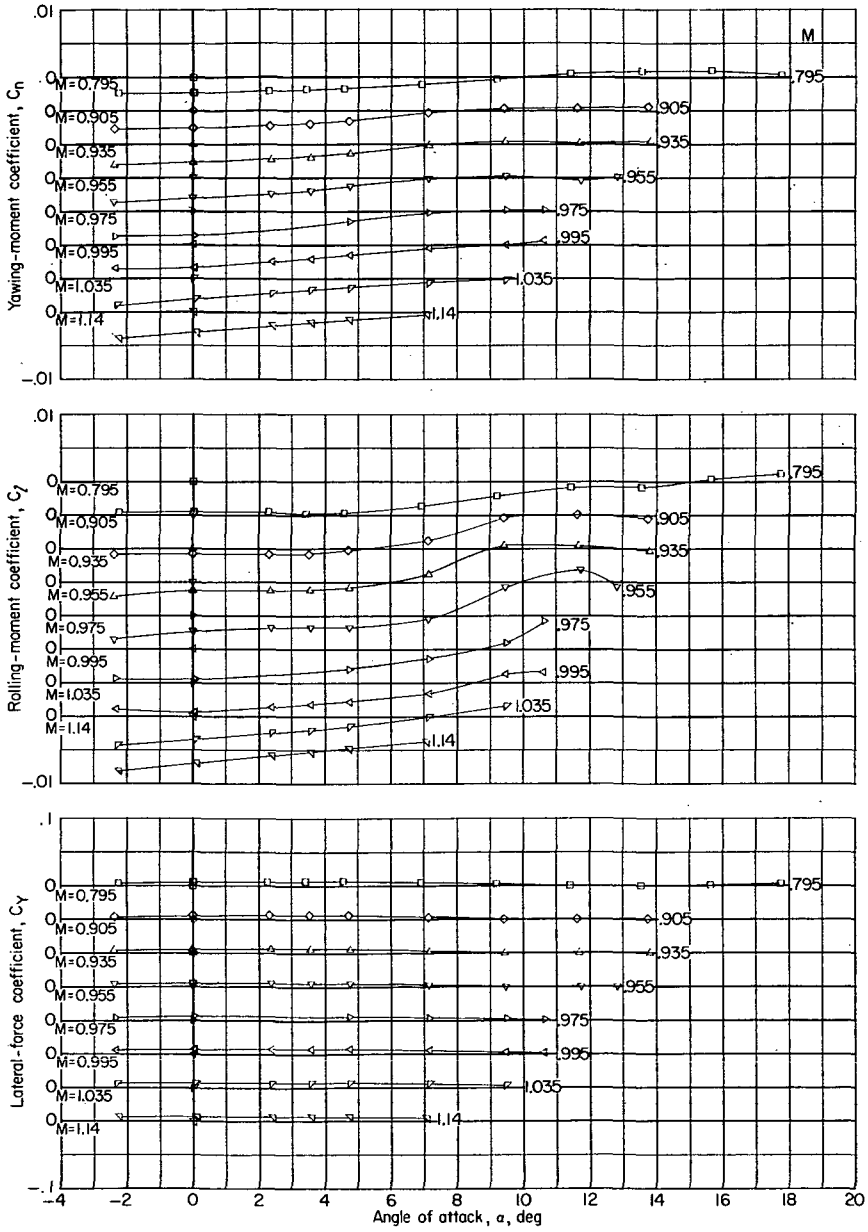

(c) Yawing-moment, rolling-moment, and lateral-force coefficients.

Figure 9.- Concluded.

[redacted]

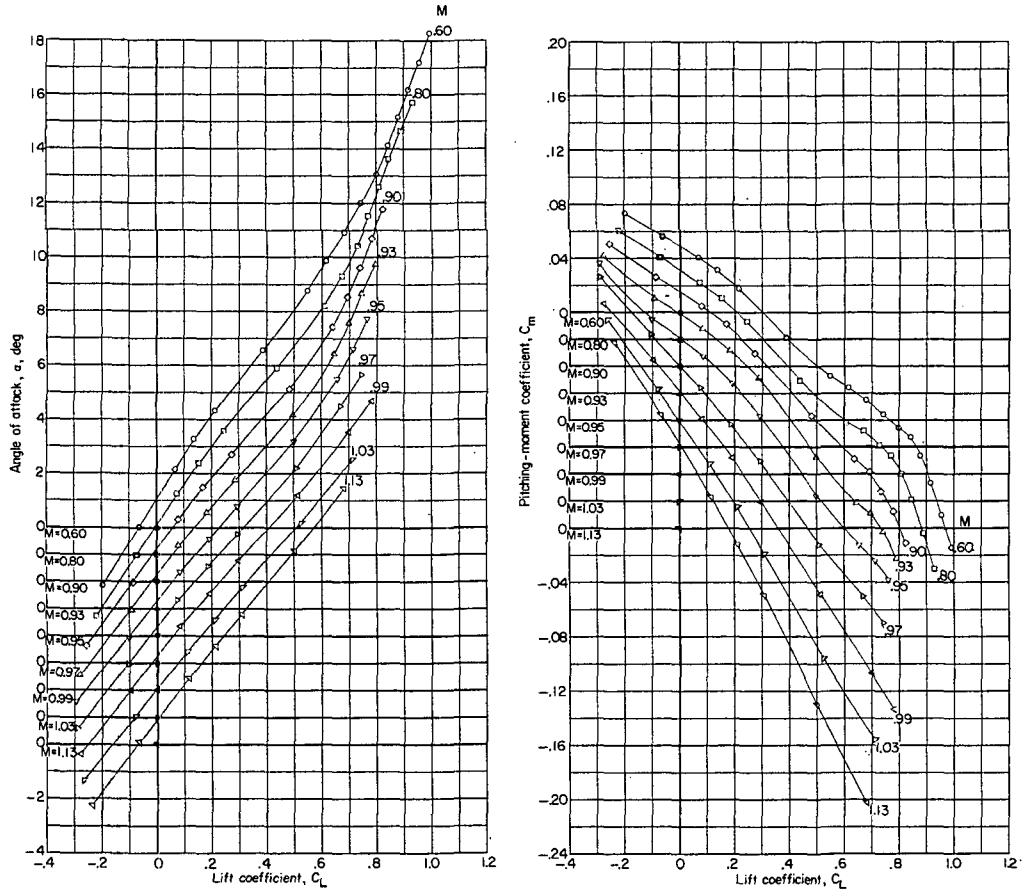

(a) Angle of attack and pitching-moment coefficient.

Figure 10.- Variation of aerodynamic characteristics with either lift coefficient or angle of attack. Configuration 4; complete model; $i_t = -3^o$; $\delta_s = 23.2^o$; drooped supersonic inlet (cruise condition).

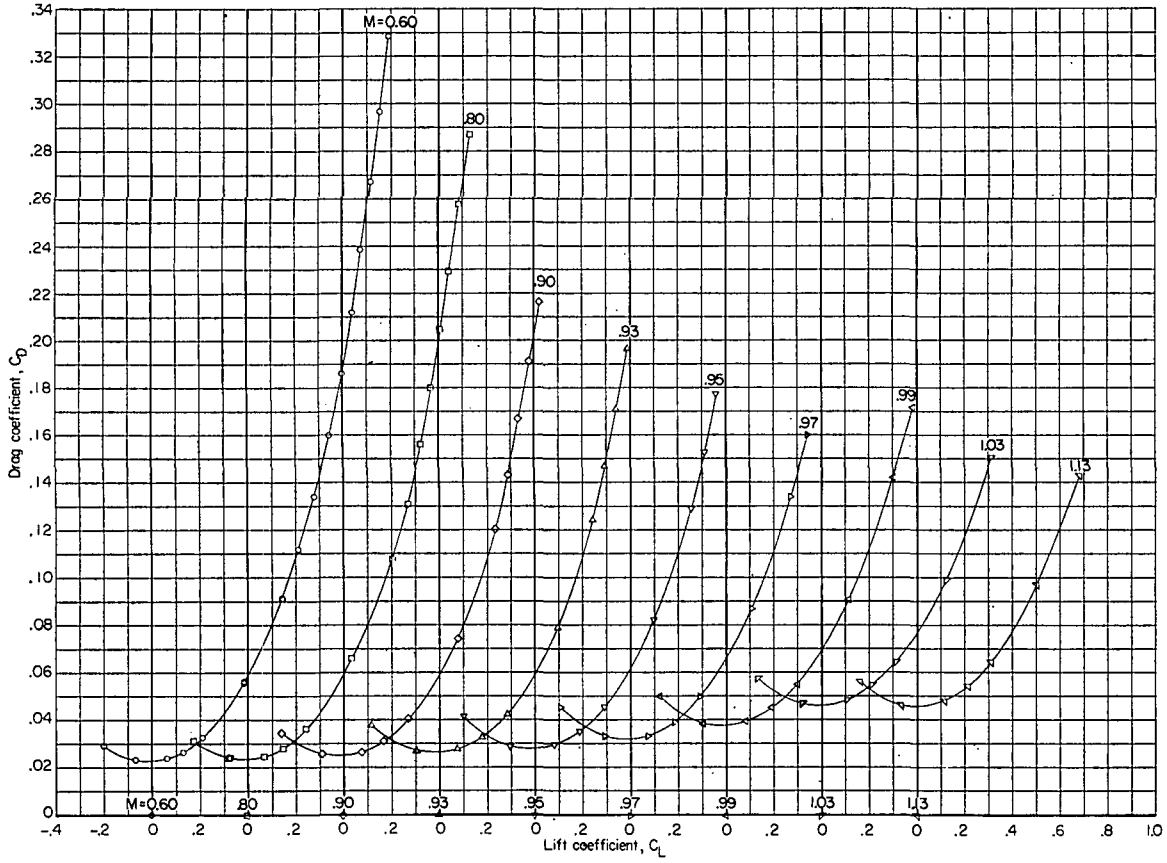

(b) Drag coefficient.

Figure 10.- Continued.

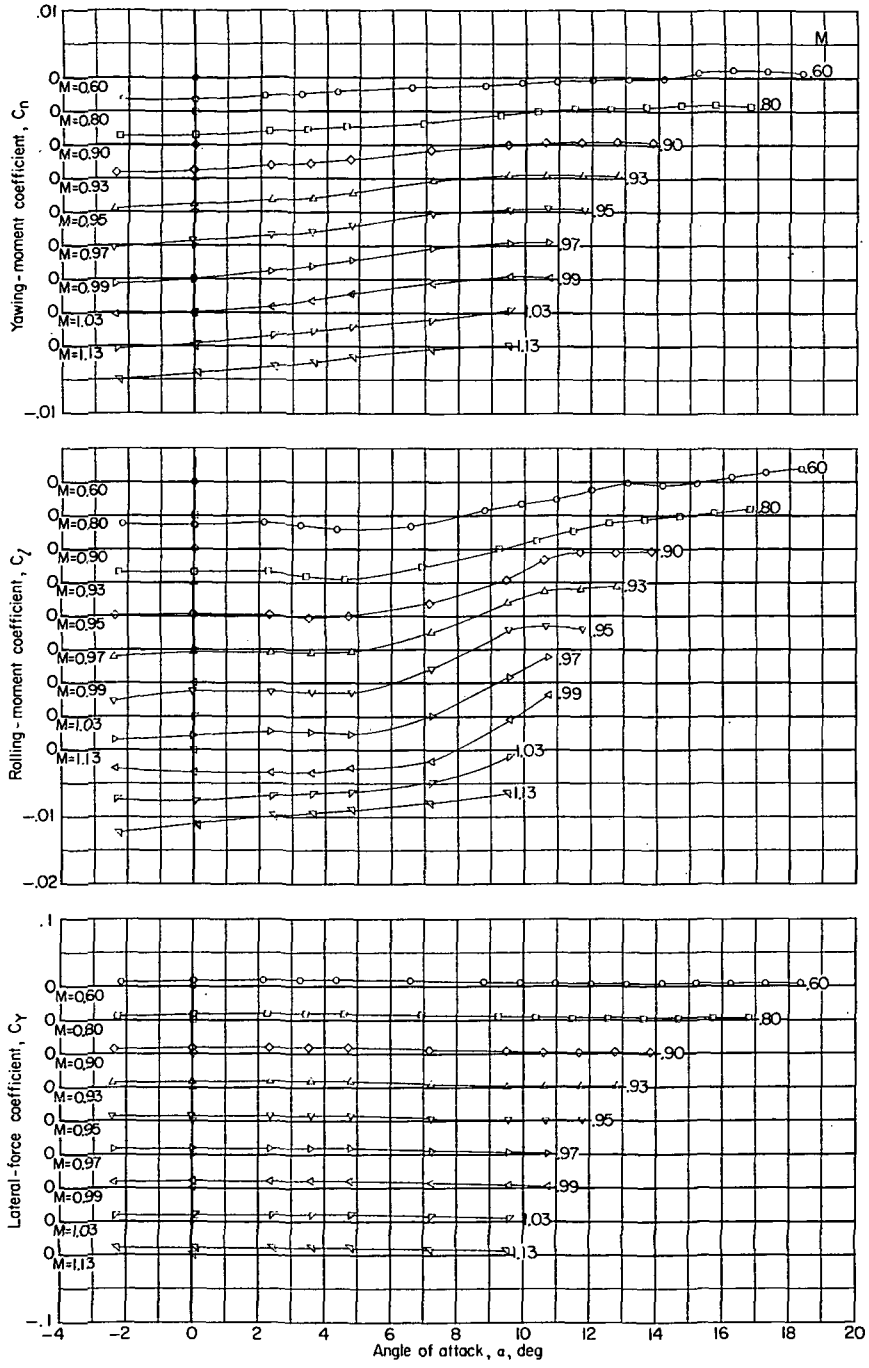

(c) Yawing-moment, rolling-moment, and lateral-force coefficients.

Figure 10.- Concluded.

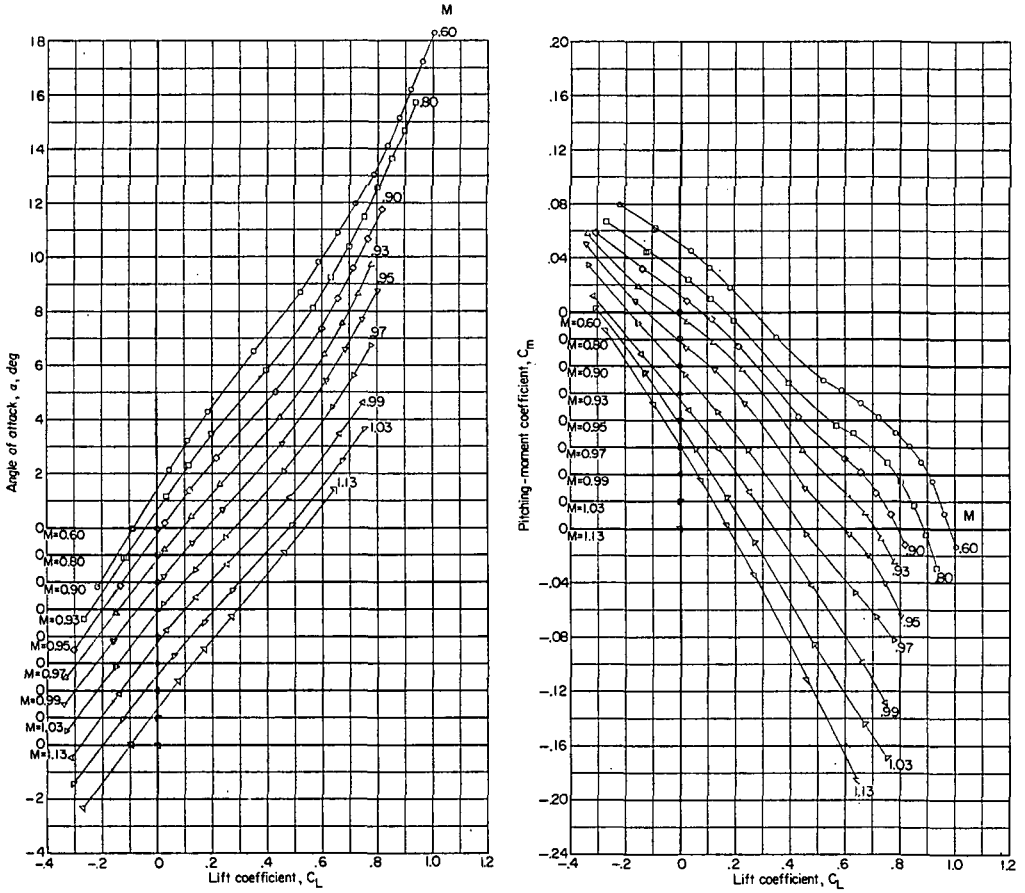

(a) Angle of attack and pitching-moment coefficient.

Figure 11.- Variation of aerodynamic characteristics with either lift coefficient or angle of attack. Configuration 5; complete model; $i_t = -3^\circ$; $\delta_s = 41.1^\circ$; drooped supersonic inlet (cruise condition).

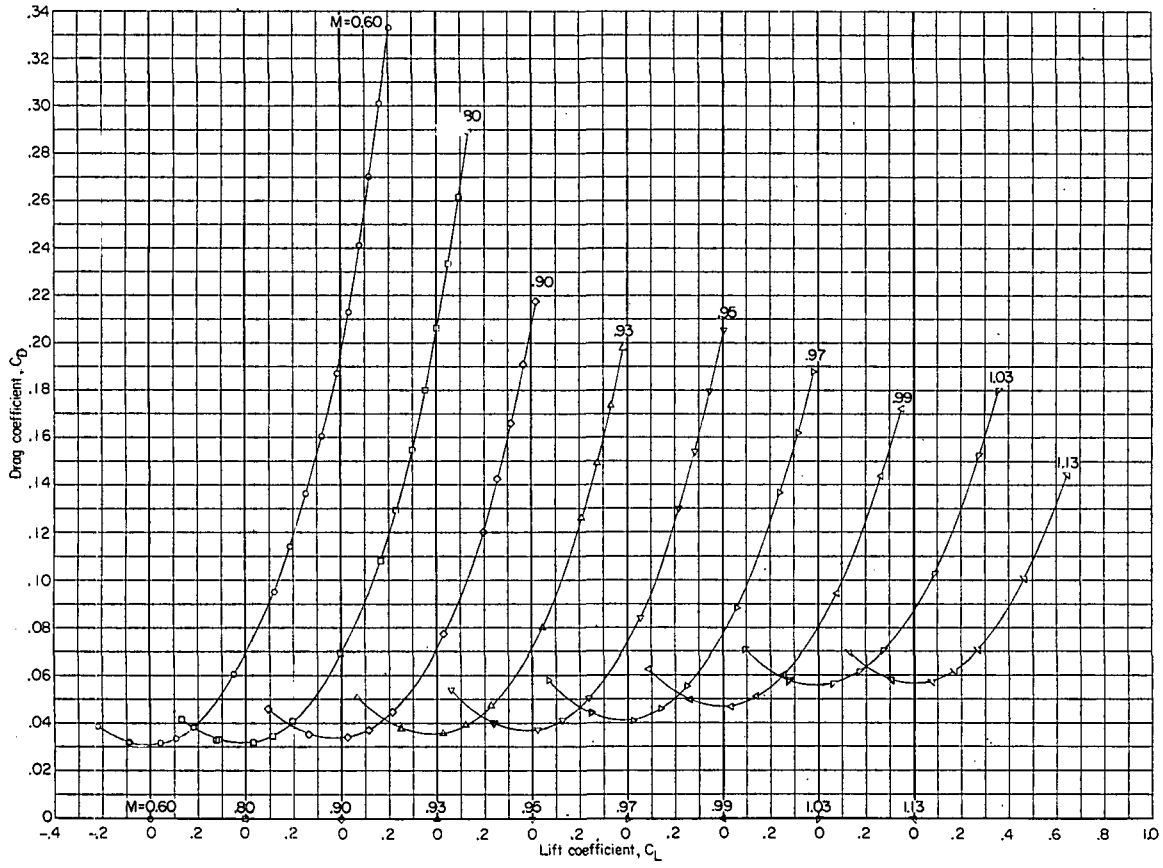

(b) Drag coefficient.

Figure 11.- Continued.

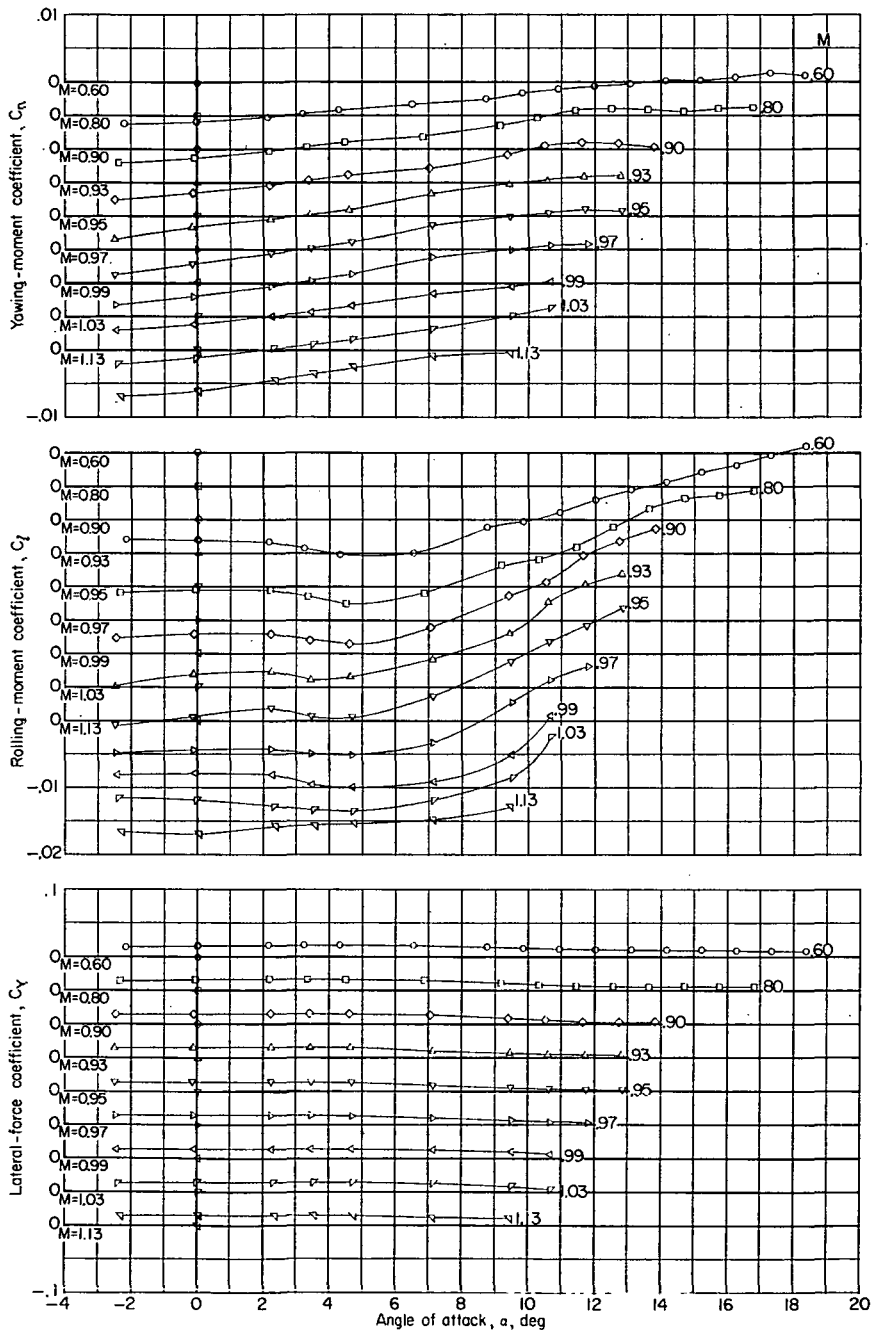

(c) Yawing-moment, rolling-moment, and lateral-force coefficients.

Figure 11.- Concluded.

[redacted]

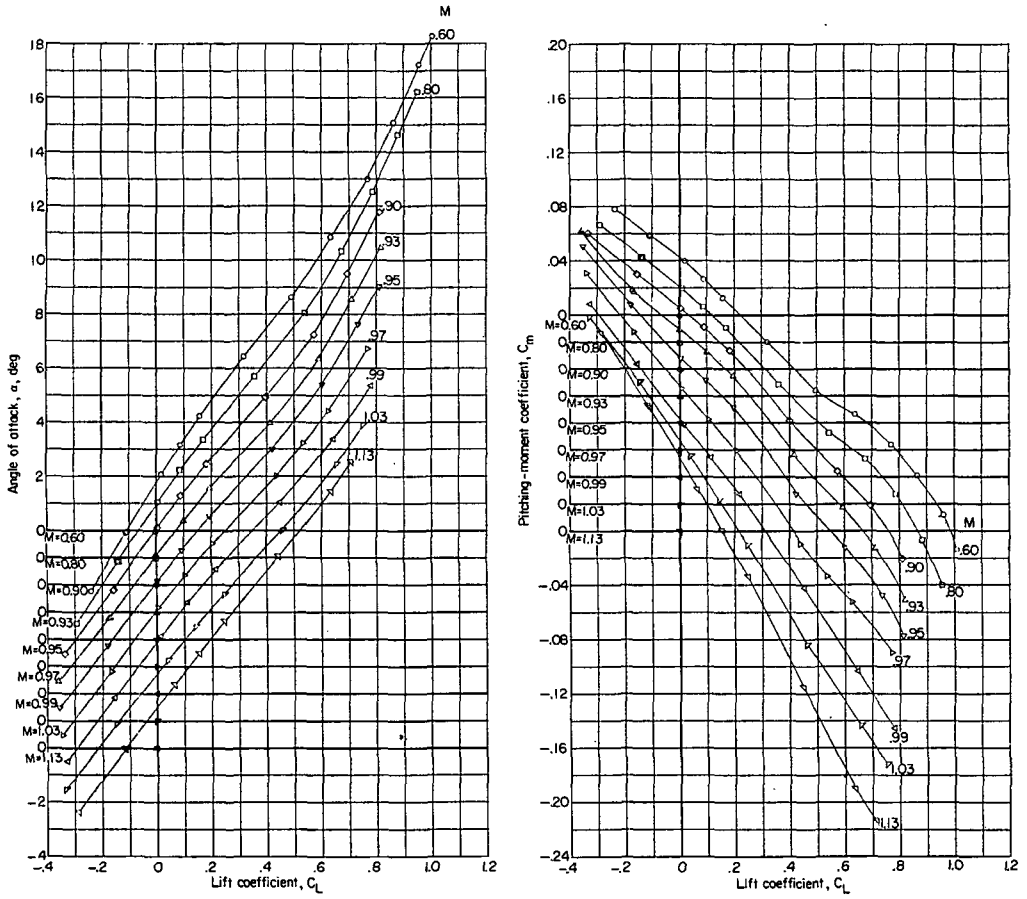

(a) Angle of attack and pitching-moment coefficient.

Figure 12.- Variation of aerodynamic characteristics with either lift coefficient or angle of attack. Configuration 6; complete model; $i_t = -3^\circ$; $\delta_s = 54.8^\circ$; drooped supersonic inlet (cruise condition).

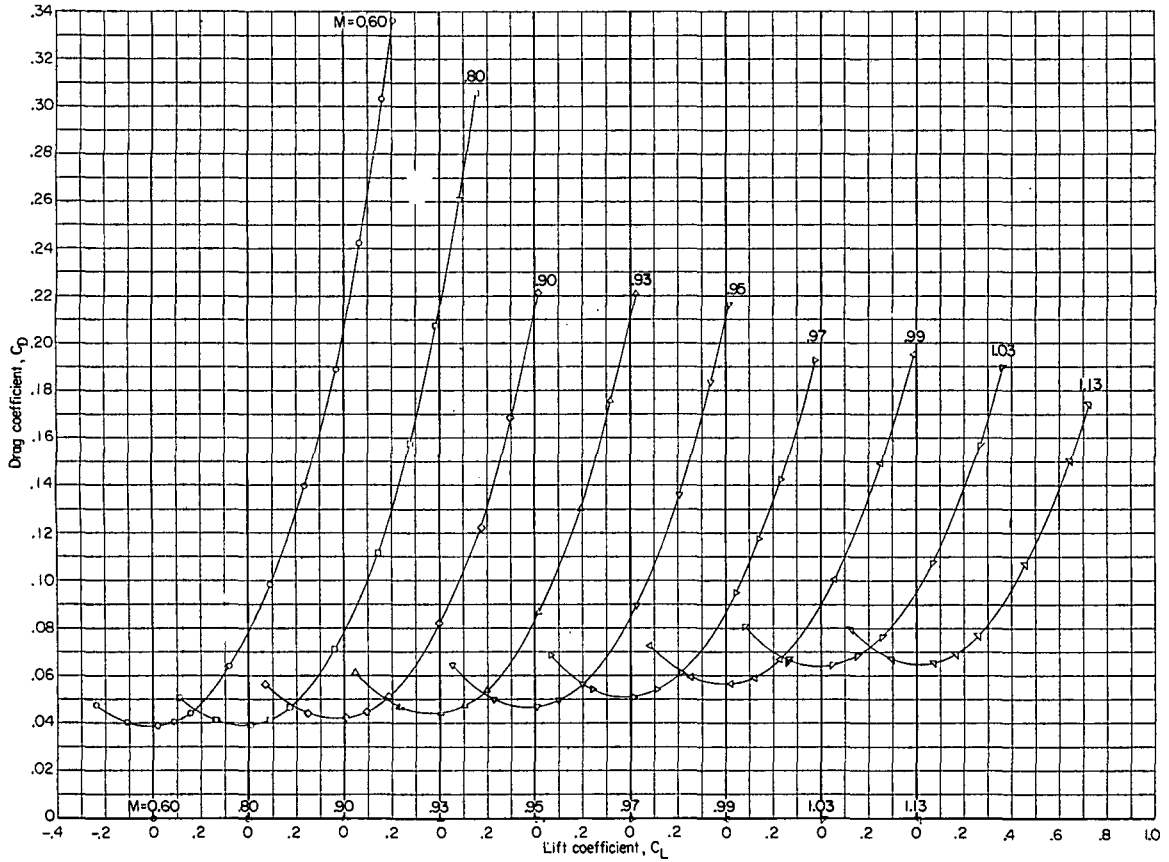

(b) Drag coefficient.

Figure 12.- Continued.

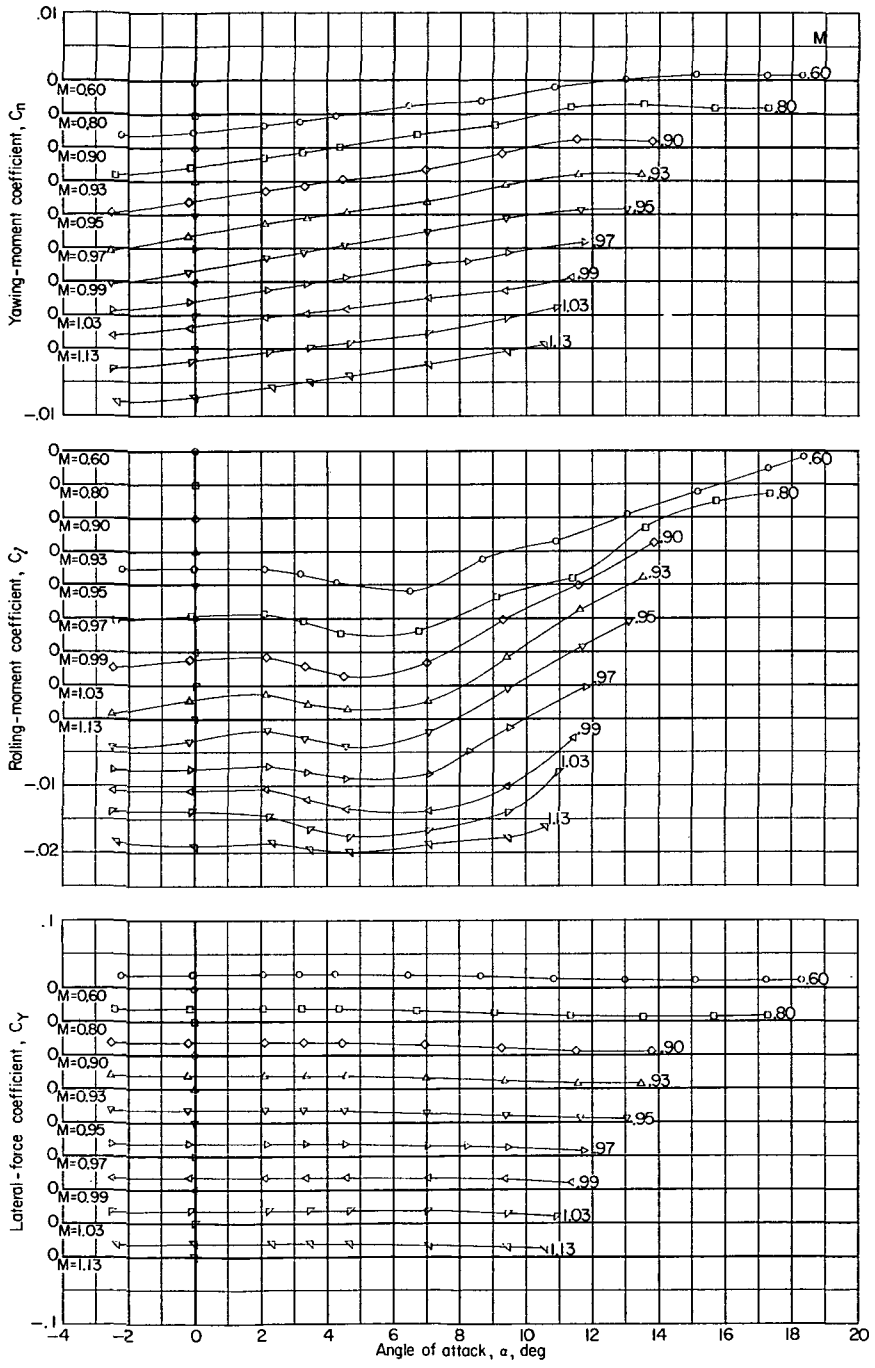

(c) Yawing-moment, rolling-moment, and lateral-force coefficients.

Figure 12.- Concluded.

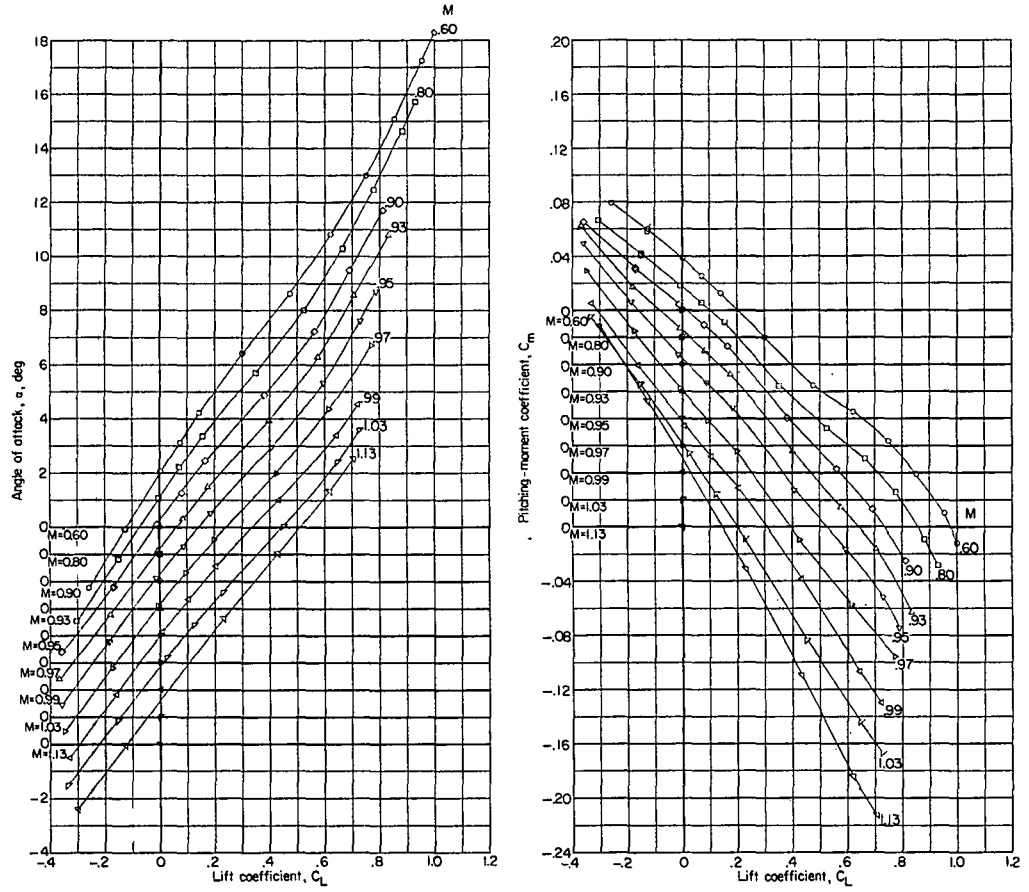

(a) Angle of attack and pitching-moment coefficient.

Figure 13.- Variation of aerodynamic characteristics with either lift coefficient or angle of attack. Configuration 7; complete model; $i_t = -3^\circ$; $\delta_s = 64.0^\circ$; drooped supersonic inlet (cruise condition).

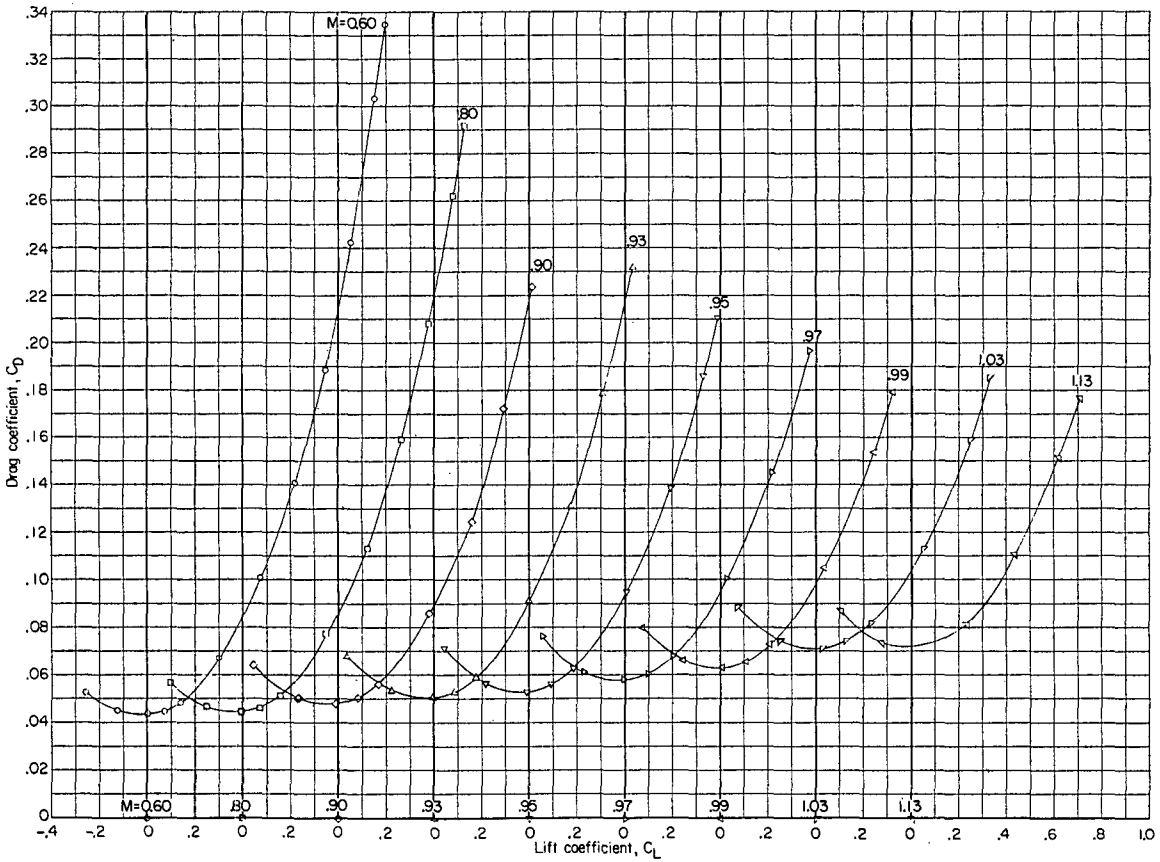

(b) Drag coefficient.

Figure 13.- Continued.

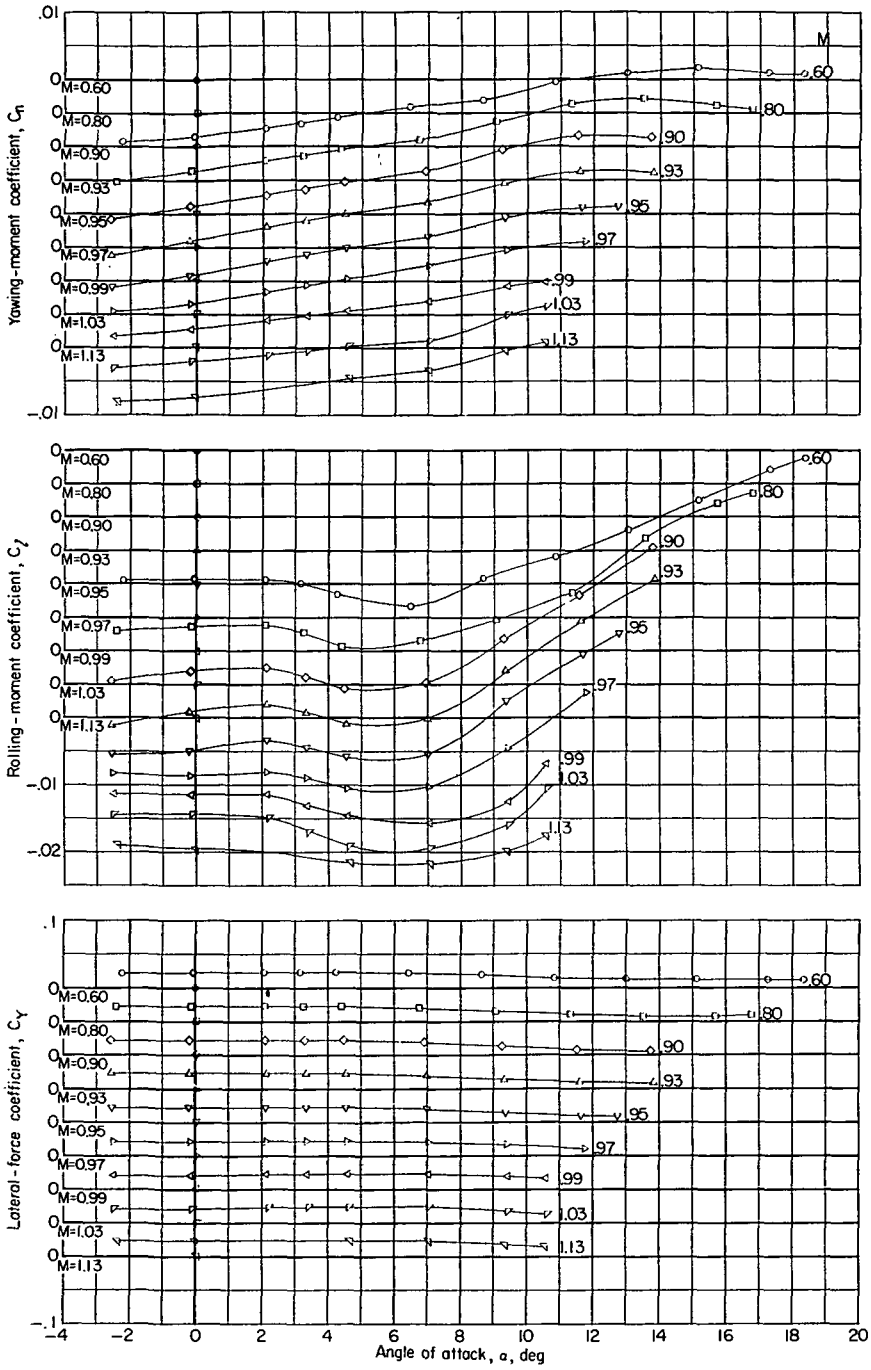

(c) Yawing-moment, rolling-moment, and lateral-force coefficients.

Figure 13.- Concluded.

[redacted]

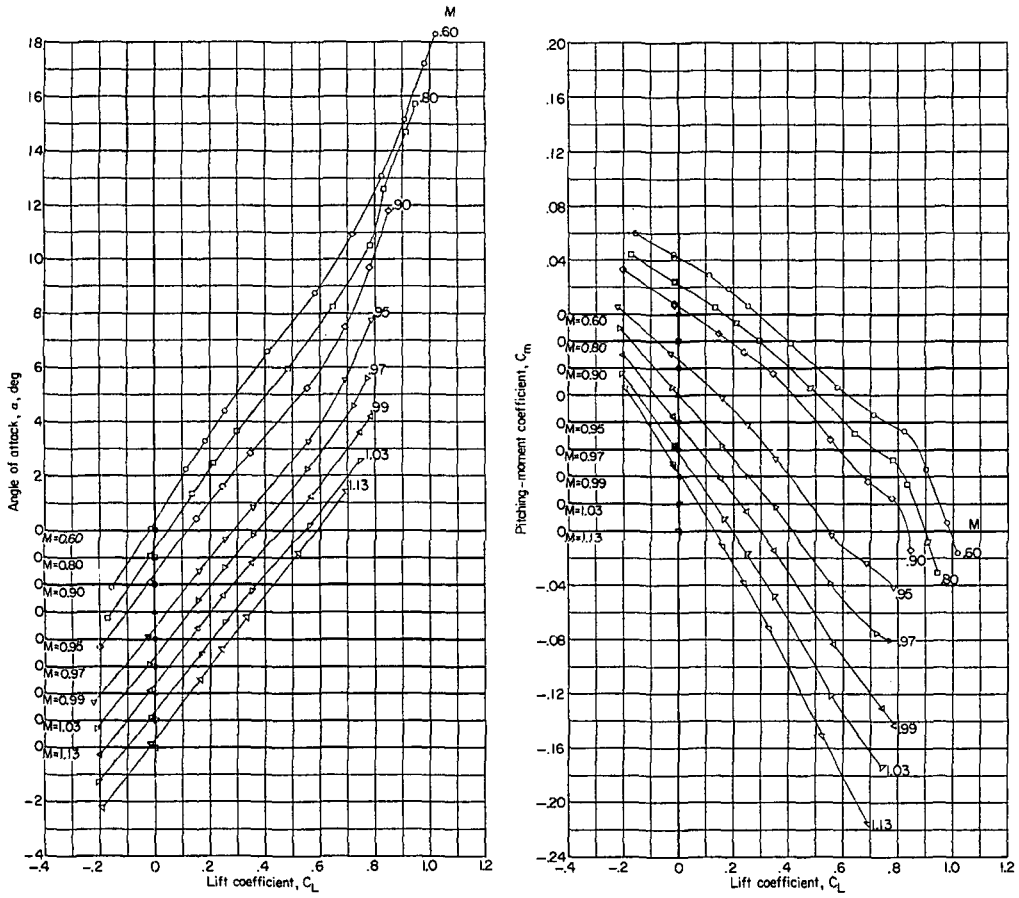

(a) Angle of attack and pitching-moment coefficient.

Figure 14.- Variation of aerodynamic characteristics with lift coefficient. Configuration 8; complete model; $i_t = -3^\circ$; $\delta_n = -7.5^\circ$; drooped supersonic inlet (cruise condition).

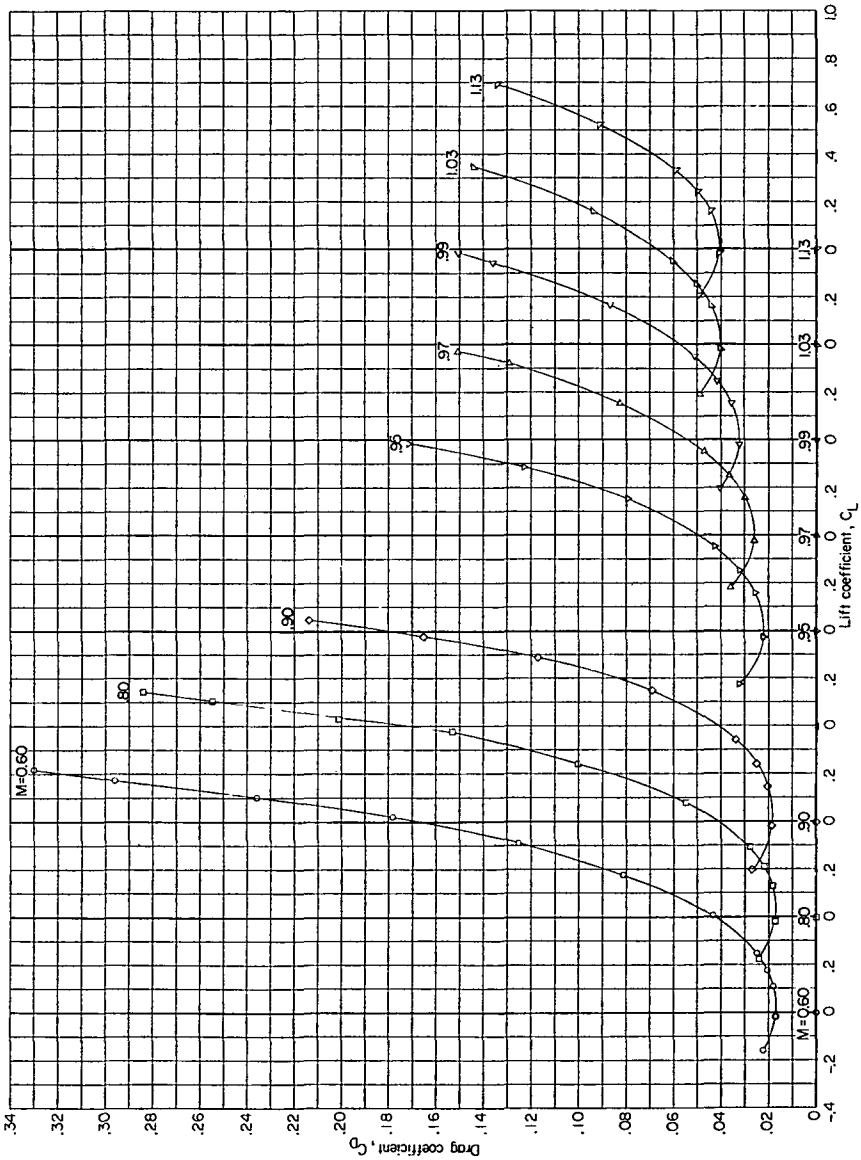

(b) Drag coefficient.

Figure 14.- Concluded.

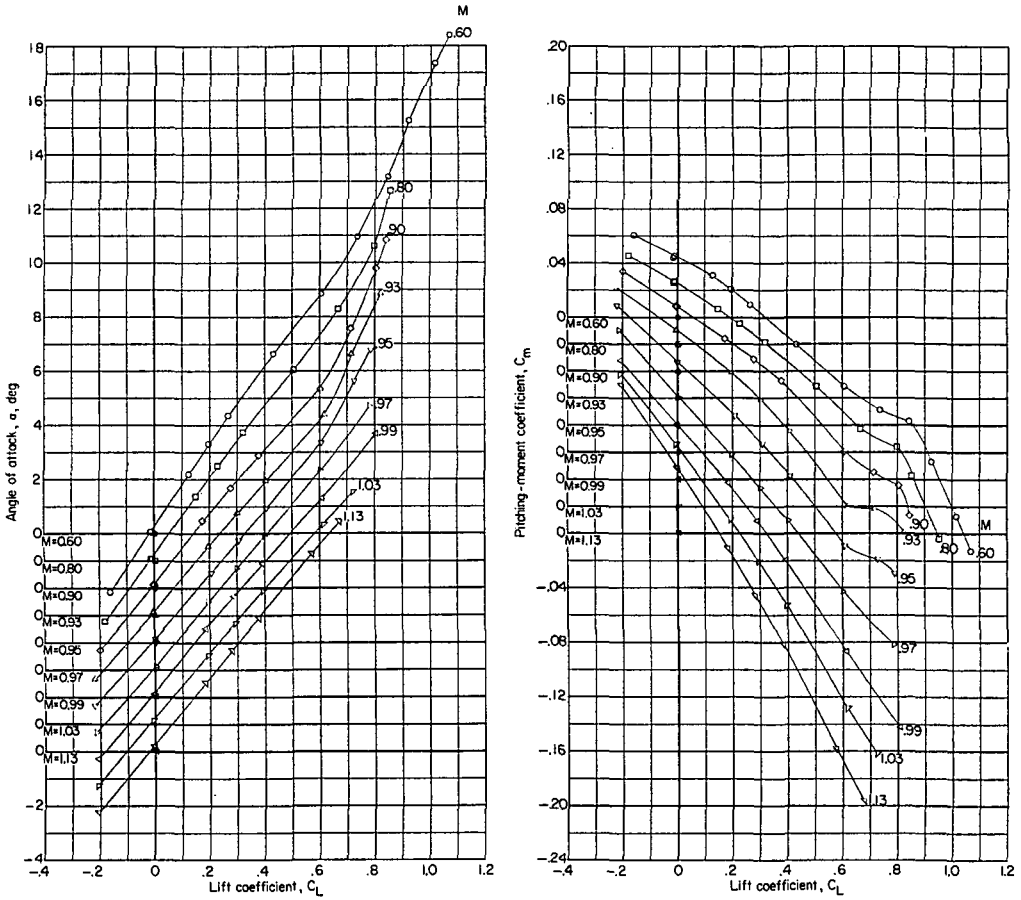

(a) Angle of attack and pitching-moment coefficient.

Figure 15.- Variation of aerodynamic characteristics with lift coefficient. Configuration 9; complete model plus wing trailing-edge fairing; $i_t = -3^\circ$; $\delta_n = -7.5^\circ$; drooped supersonic inlet (cruise condition).

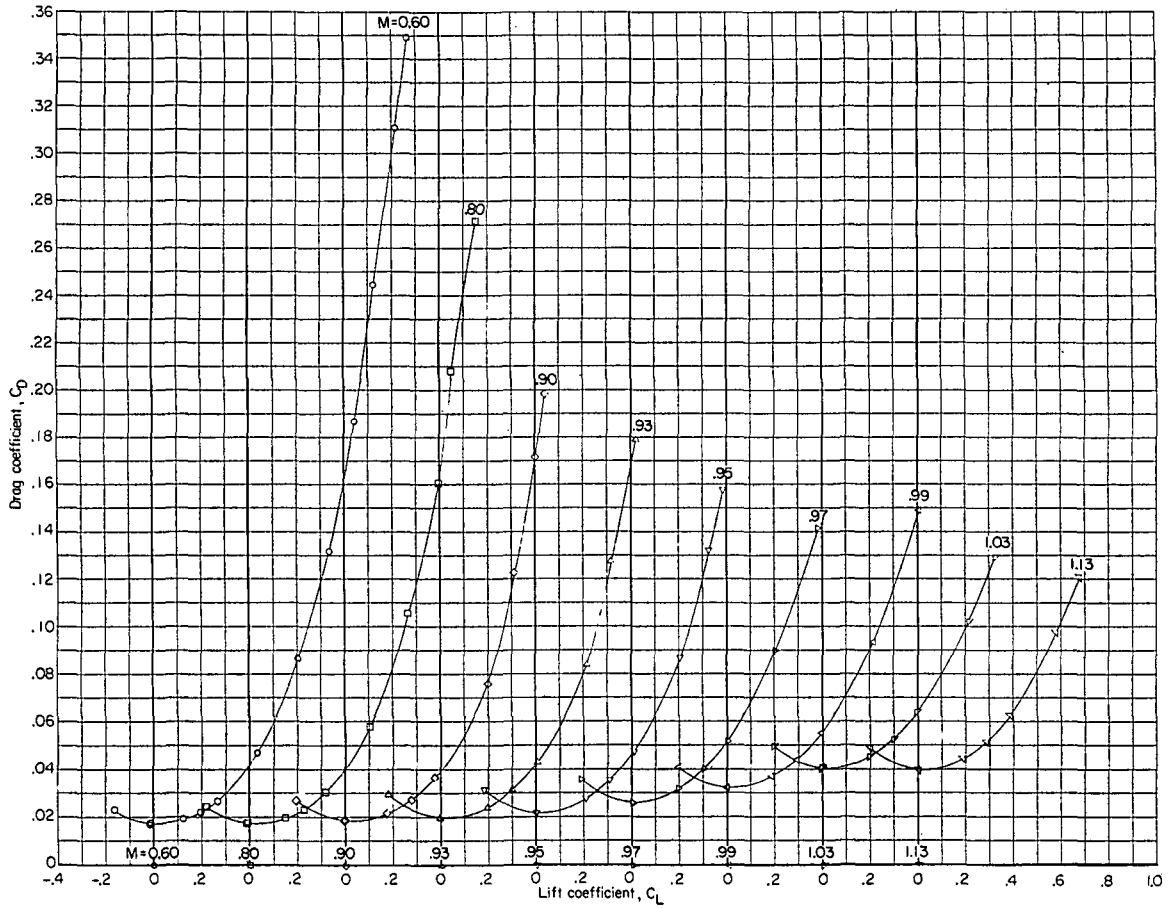

(b) Drag coefficient.

Figure 15.- Concluded.

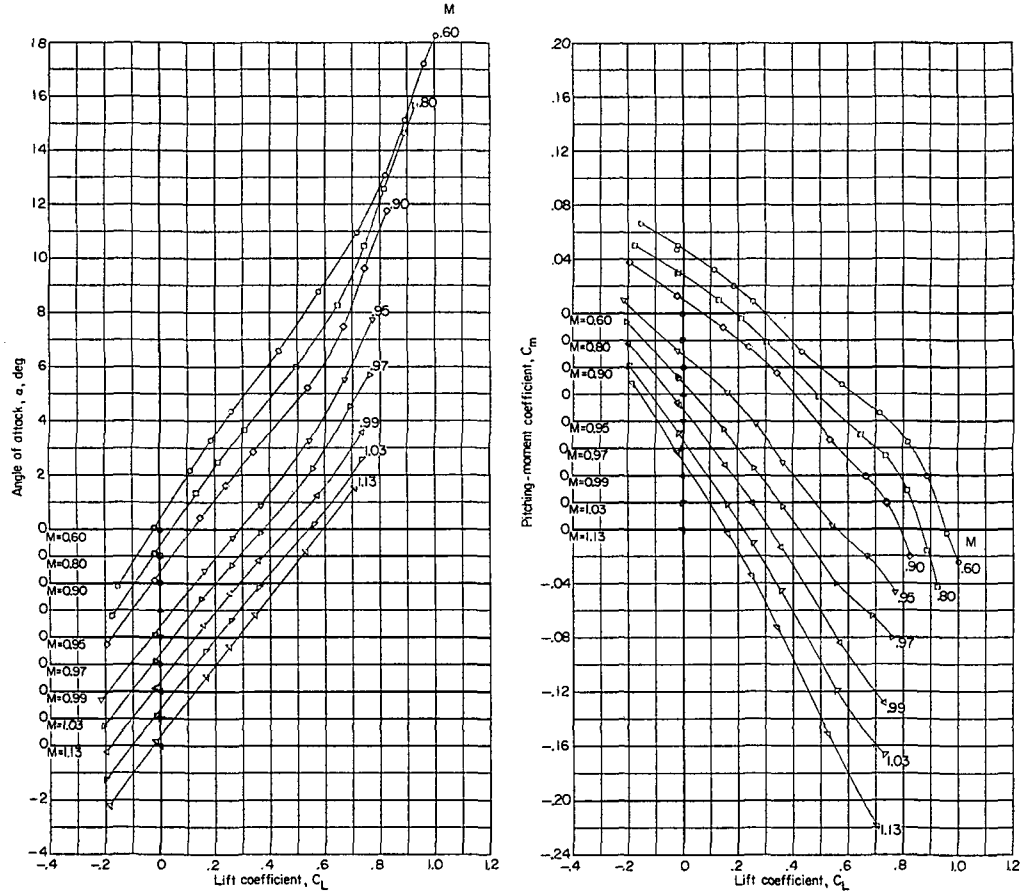

(a) Angle of attack and pitching-moment coefficient.

Figure 16.- Variation of aerodynamic characteristics with lift coefficient. Configuration 10; complete model; $i_t = -3^\circ$; undrooped supersonic inlet (cruise condition).

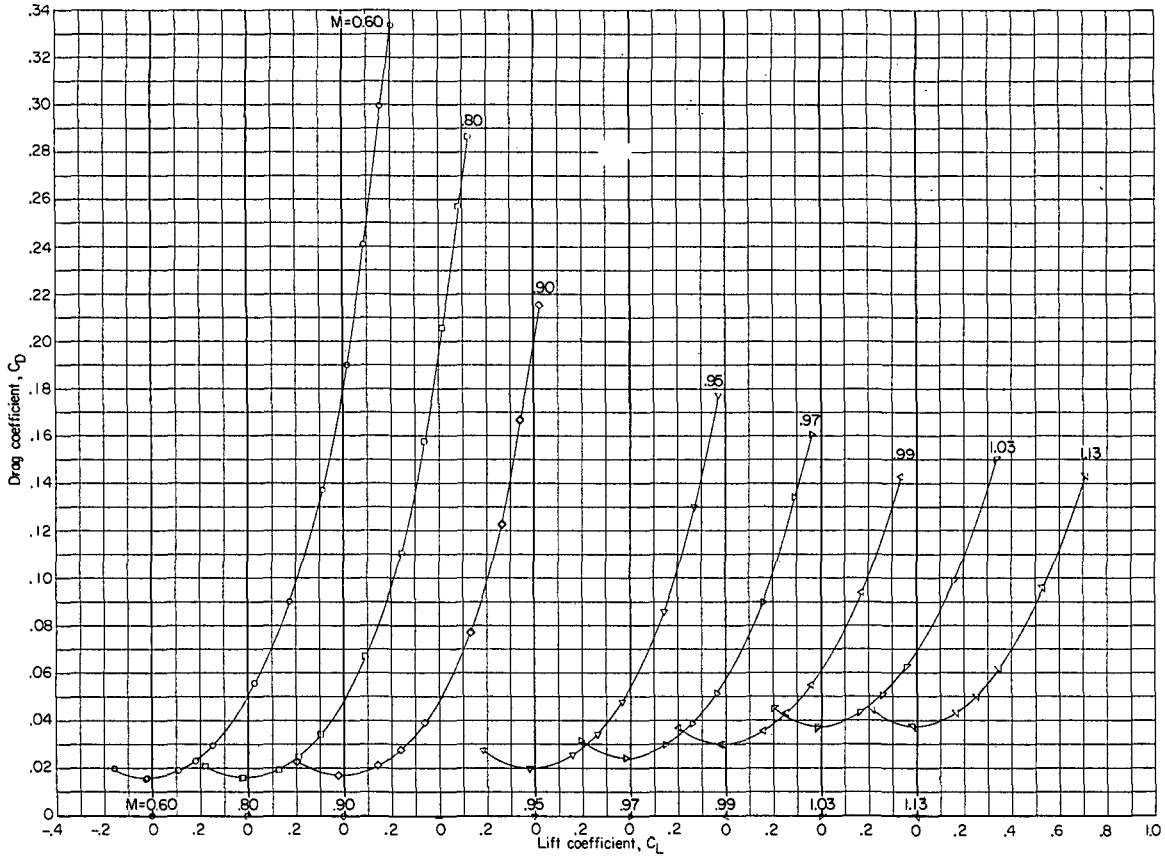

(b) Drag coefficient.

Figure 16.- Concluded.

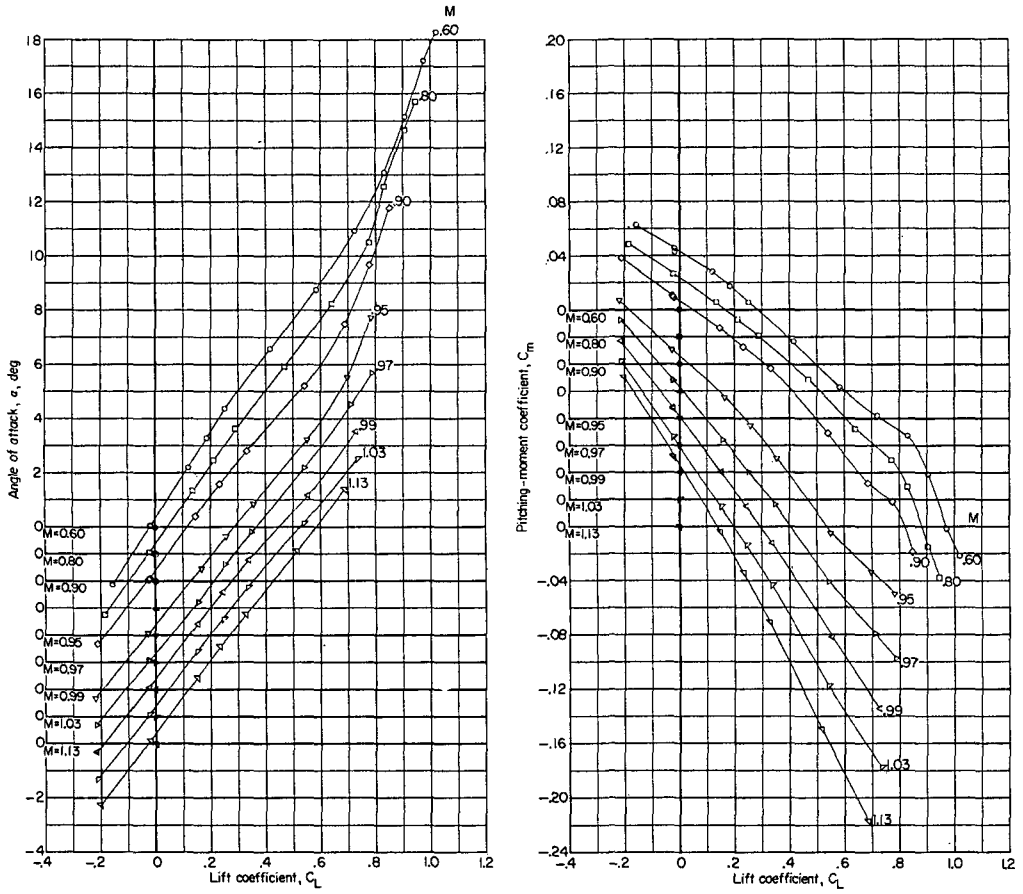

(a) Angle of attack and pitching-moment coefficient.

Figure 17.- Variation of aerodynamic characteristics with lift coefficient. Configuration 11; complete model; $i_t = -3^\circ$; $\delta_n = -7.5^\circ$; undrooped supersonic inlet (cruise condition).

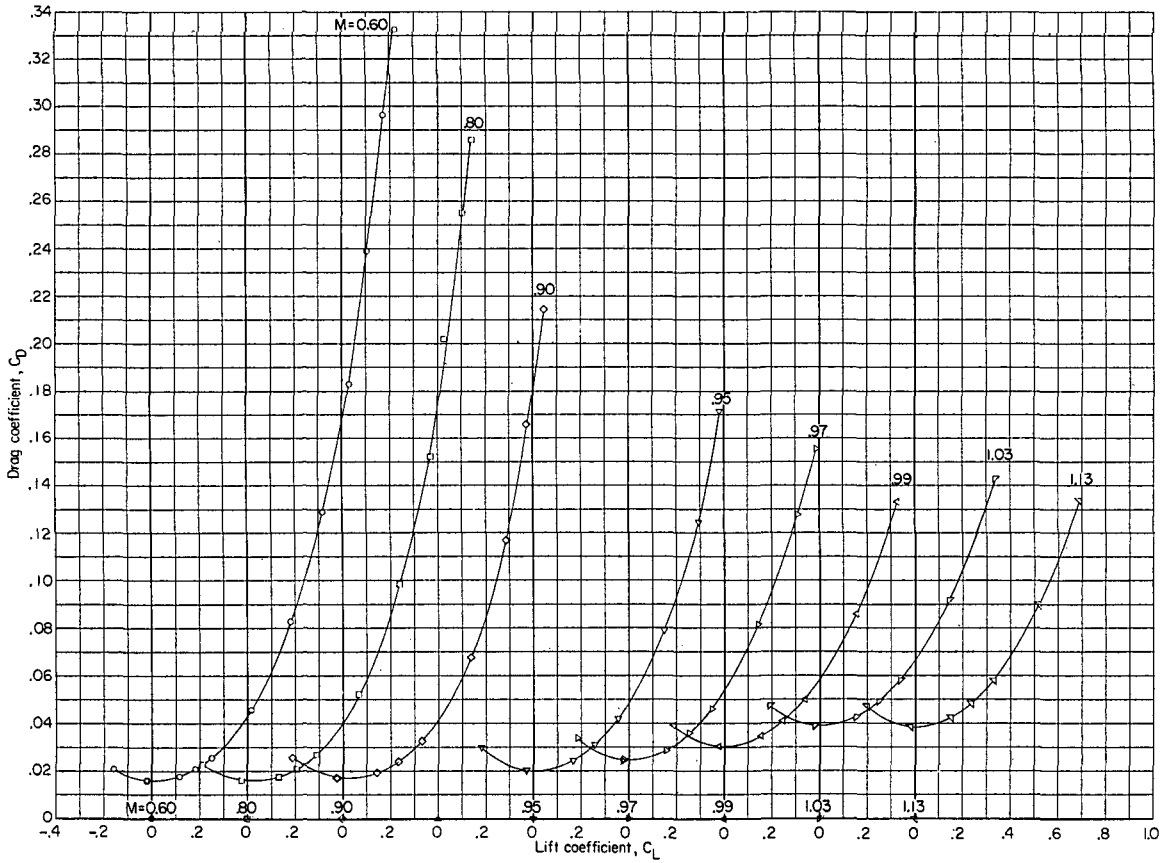

(b) Drag coefficient.

Figure 17.- Concluded.

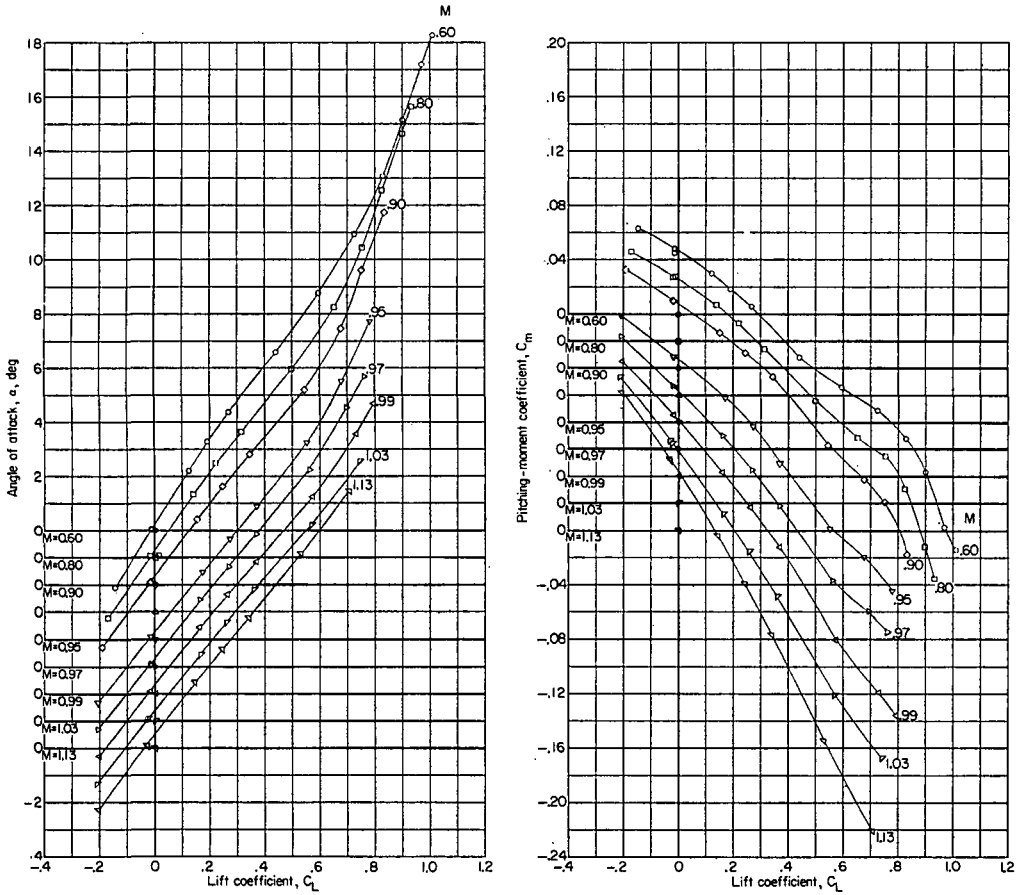

(a) Angle of attack and pitching-moment coefficient.

Figure 18.- Variation of aerodynamic characteristics with lift coefficient. Configuration 12; complete model plus gun blisters; $i_t = -3^\circ$; undrooped supersonic inlet (cruise condition).

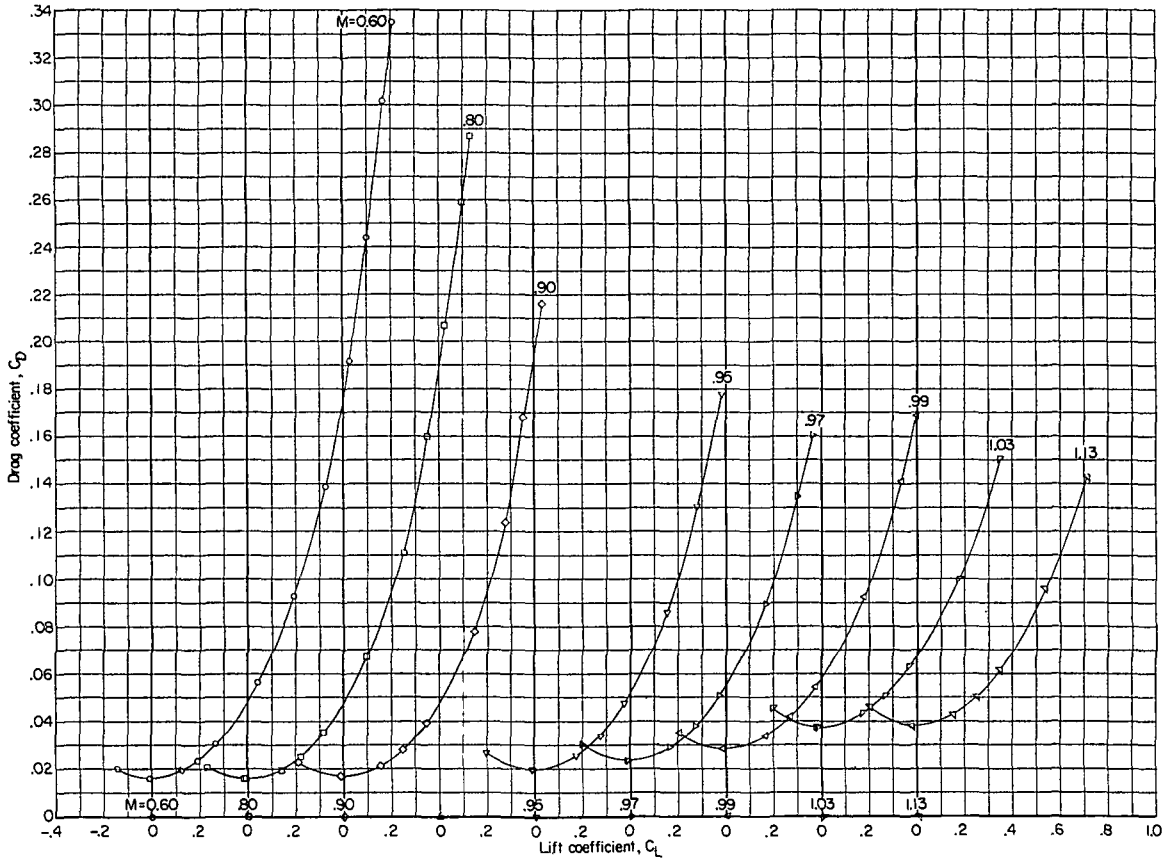

(b) Drag coefficient.

Figure 18.- Concluded.

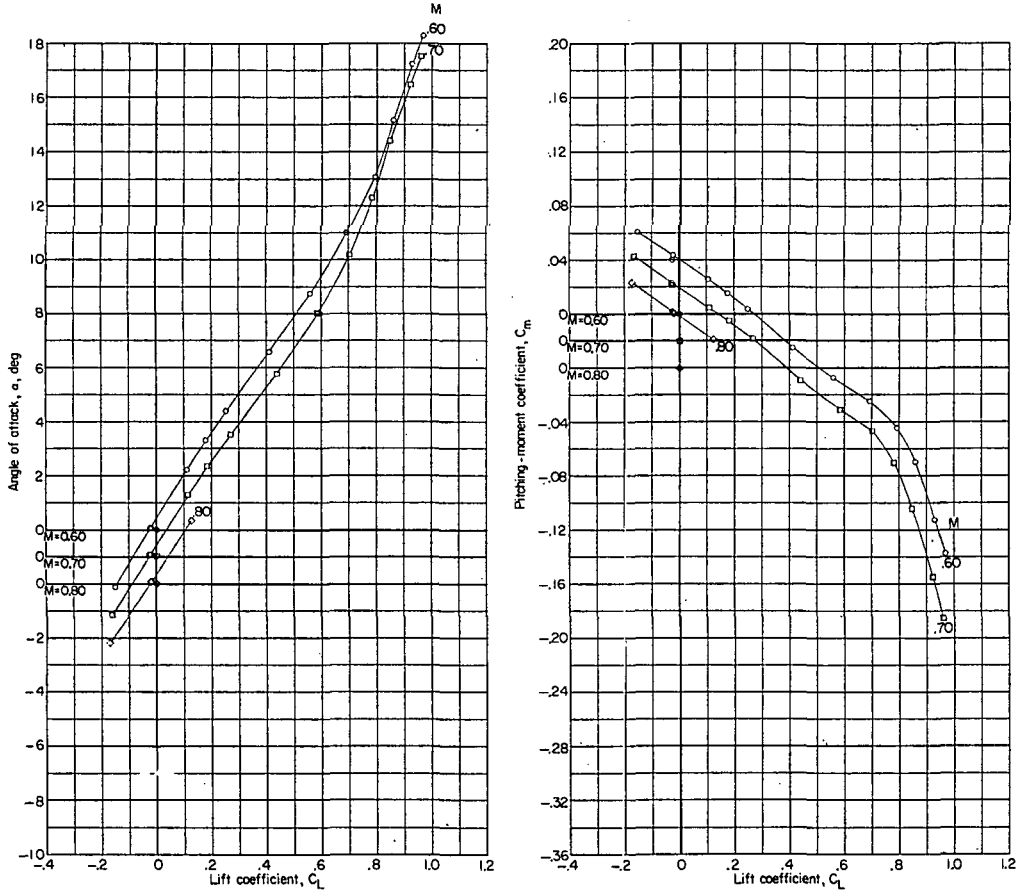

(a) Angle of attack and pitching-moment coefficient.

Figure 19.- Variation of aerodynamic characteristics with lift coefficient. Configuration 13; complete model plus 50°-deflected speed brakes; i_t = -3°; undrooped supersonic inlet (cruise condition).

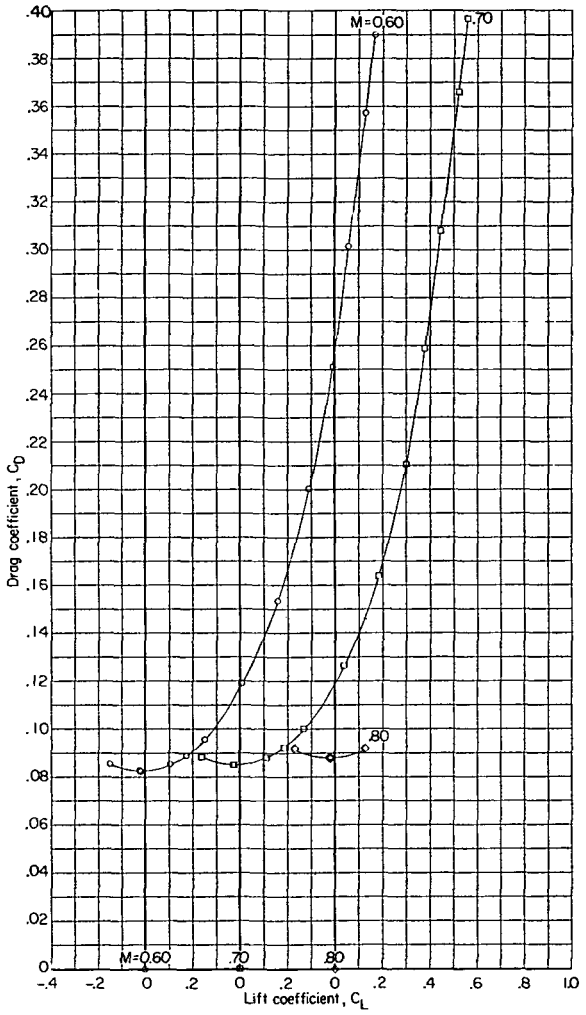

(b) Drag coefficient.

Figure 19.- Concluded.

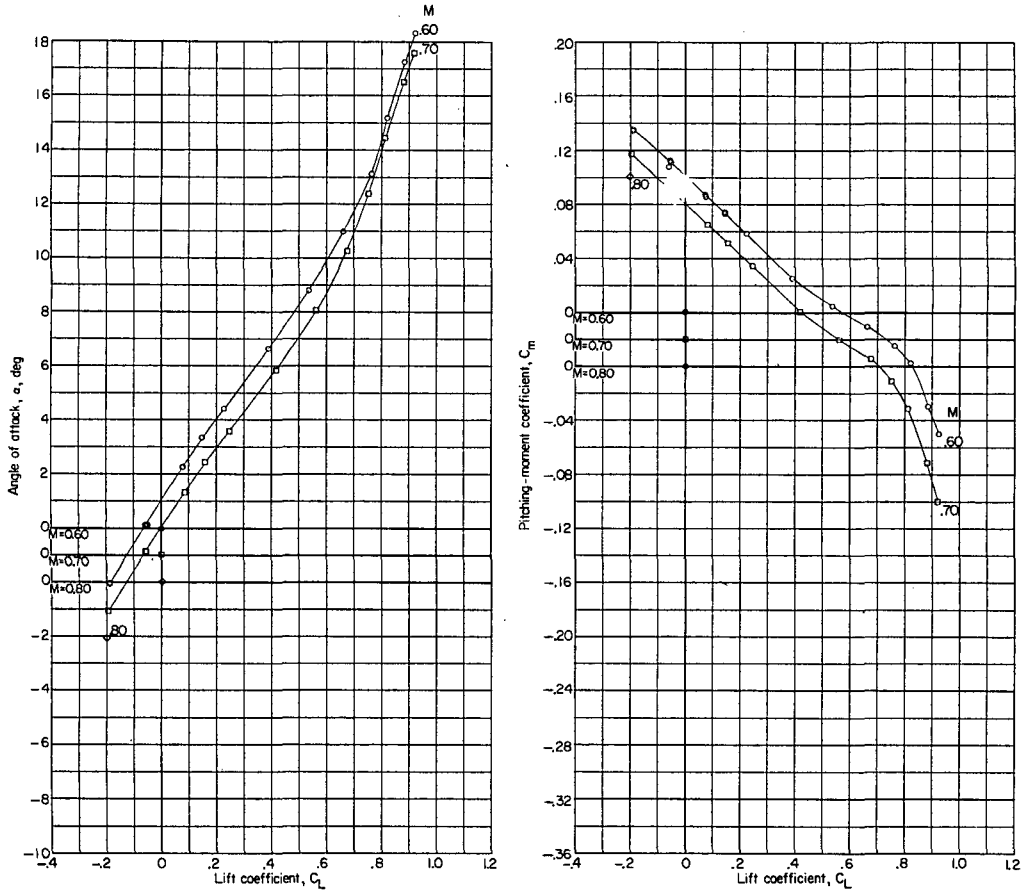

(a) Angle of attack and pitching-moment coefficient.

Figure 20.- Variation of aerodynamic characteristics with lift coefficient. Configuration 14; complete model plus 50°-deflected speed brakes; i_t = -8°; undrooped supersonic inlet (cruise condition).

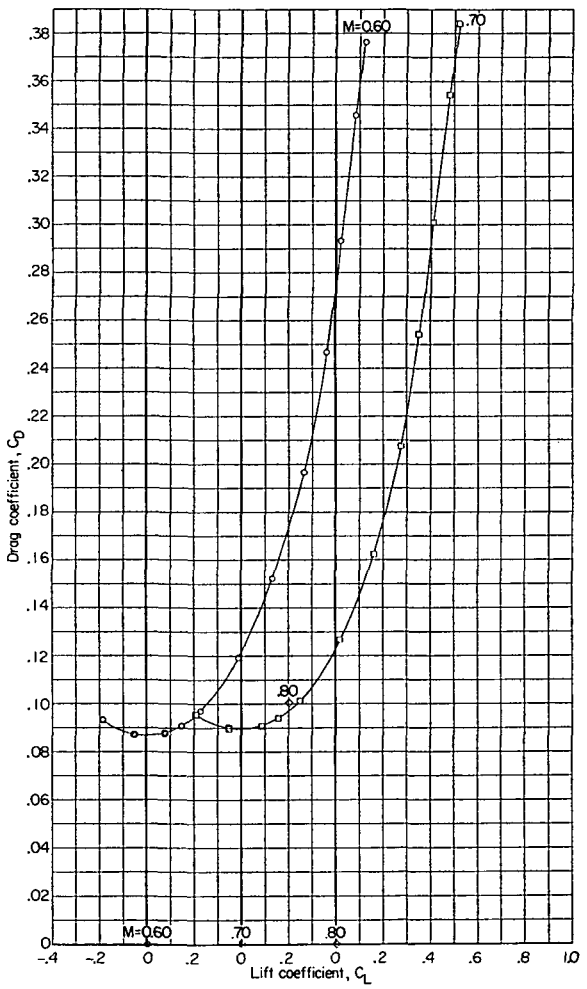

(b) Drag coefficient.

Figure 20.- Concluded.

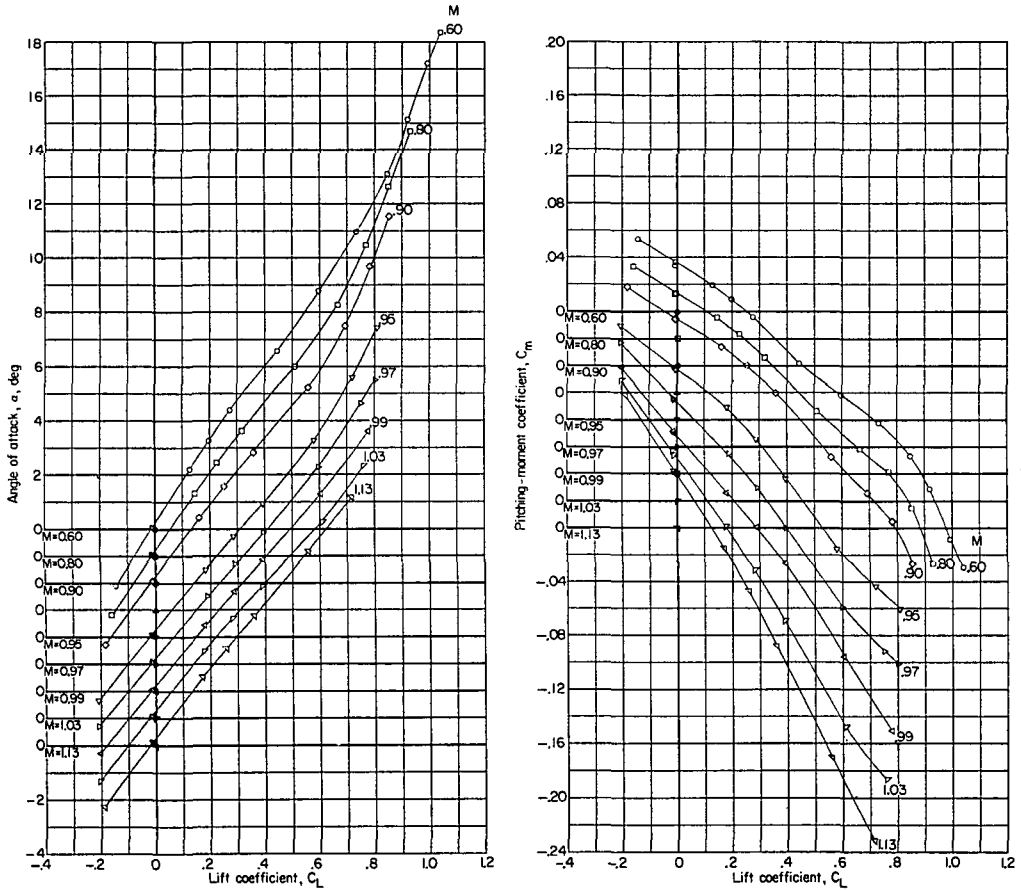

(a) Angle of attack and pitching-moment coefficient.

Figure 21.- Variation of aerodynamic characteristics with either lift coefficient or angle of attack. Configuration 15; complete model; $i_t = -3^\circ$; body with afterbody bump; undrooped supersonic inlet (cruise condition).

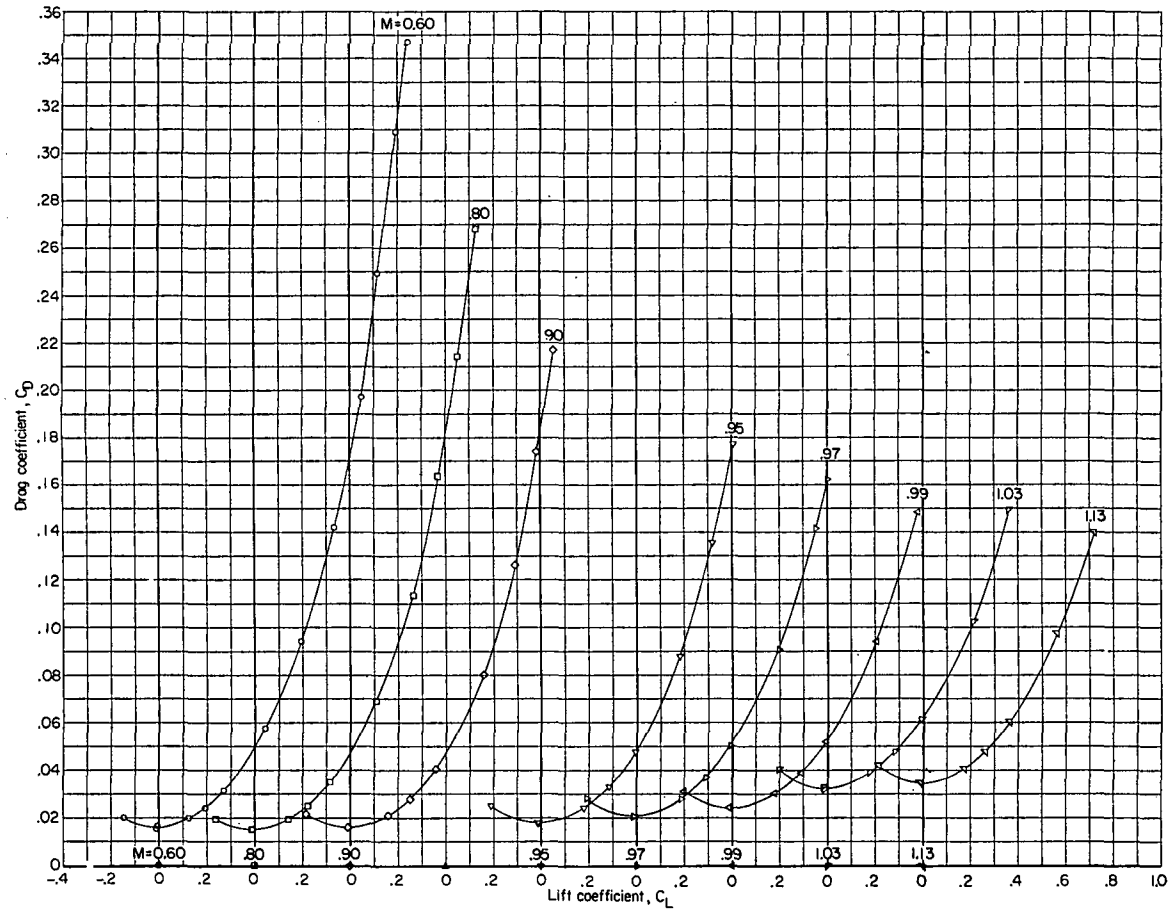

(b) Drag coefficient.

Figure 21.- Continued.

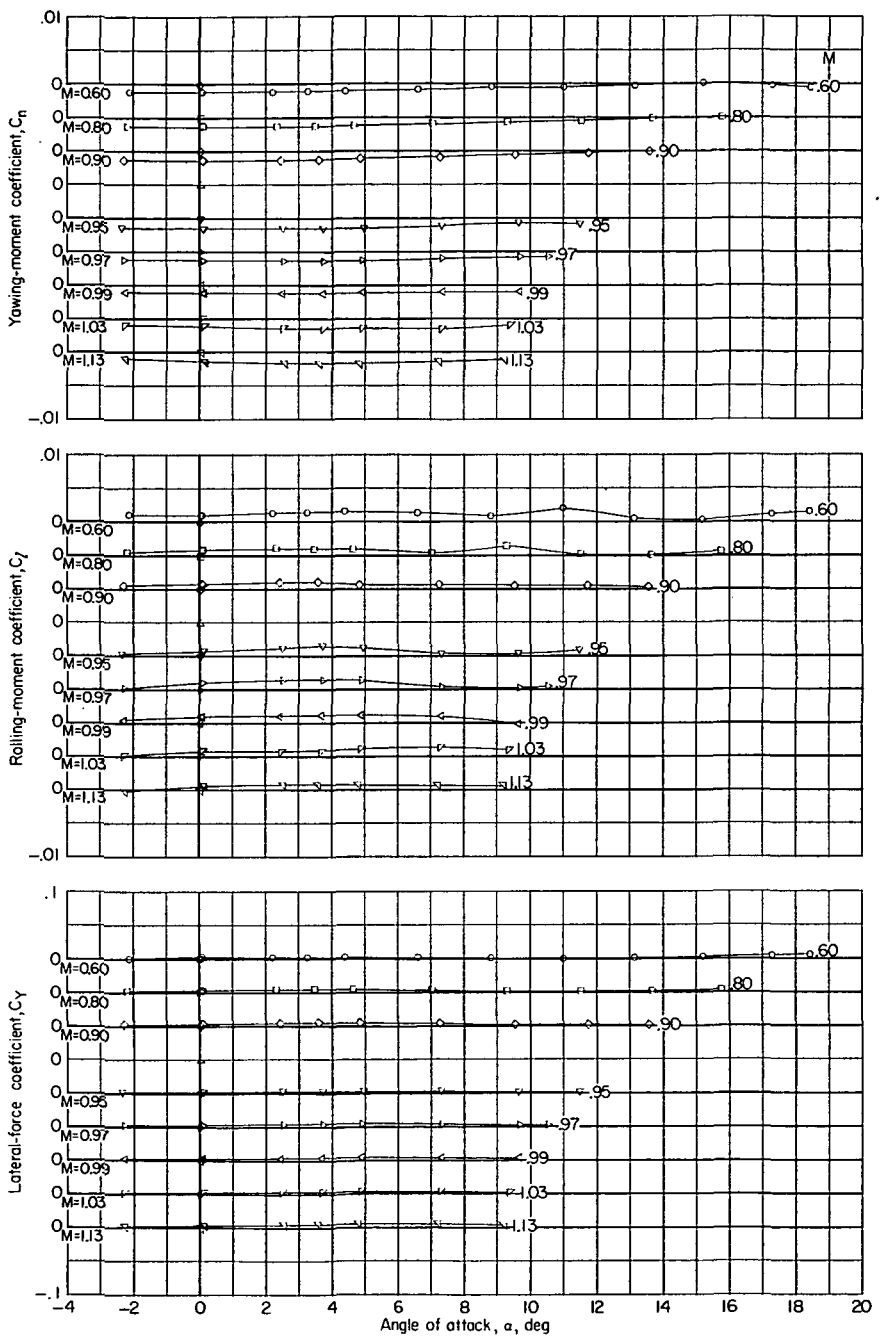

(c) Yawing-moment, rolling-moment, and lateral-force coefficients.

Figure 21.- Concluded.

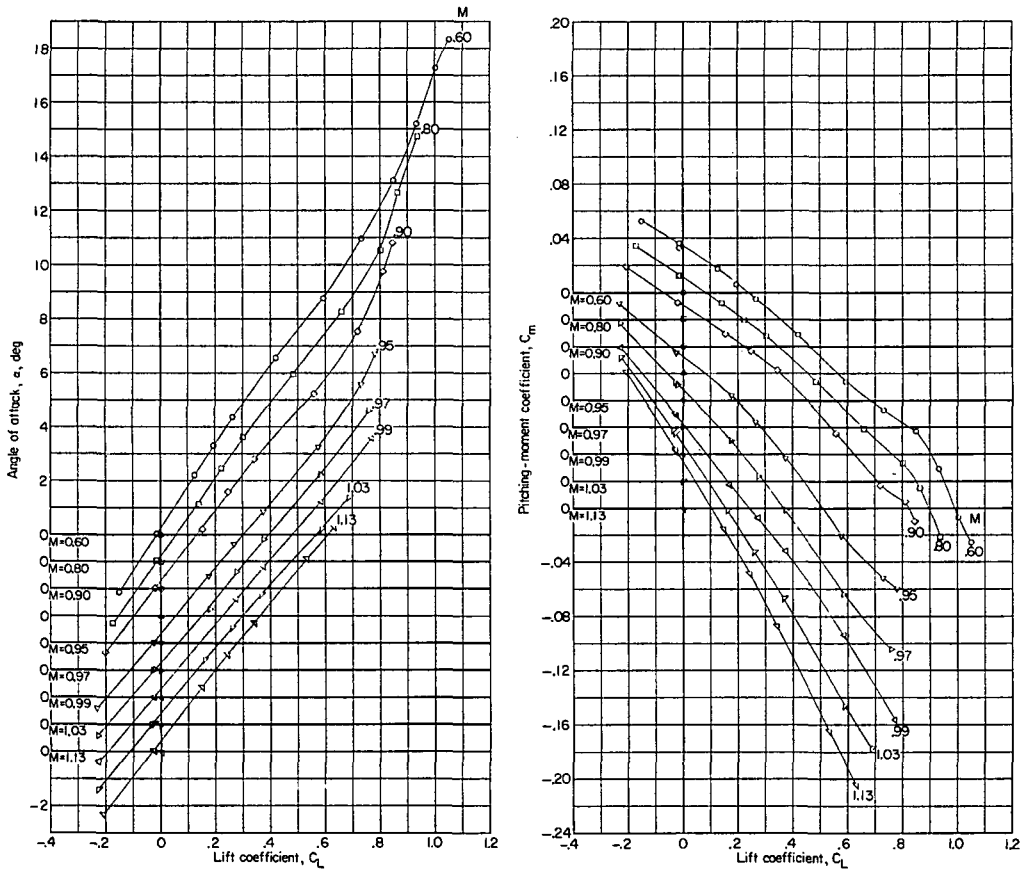

(a) Angle of attack and pitching-moment coefficient.

Figure 22.- Variation of aerodynamic characteristics with either lift coefficient or angle of attack. Configuration 16; complete model; $i_t = -3^\circ$; $\delta_n = -7.5^\circ$; body with afterbody bump; undrooped supersonic inlet (cruise condition).

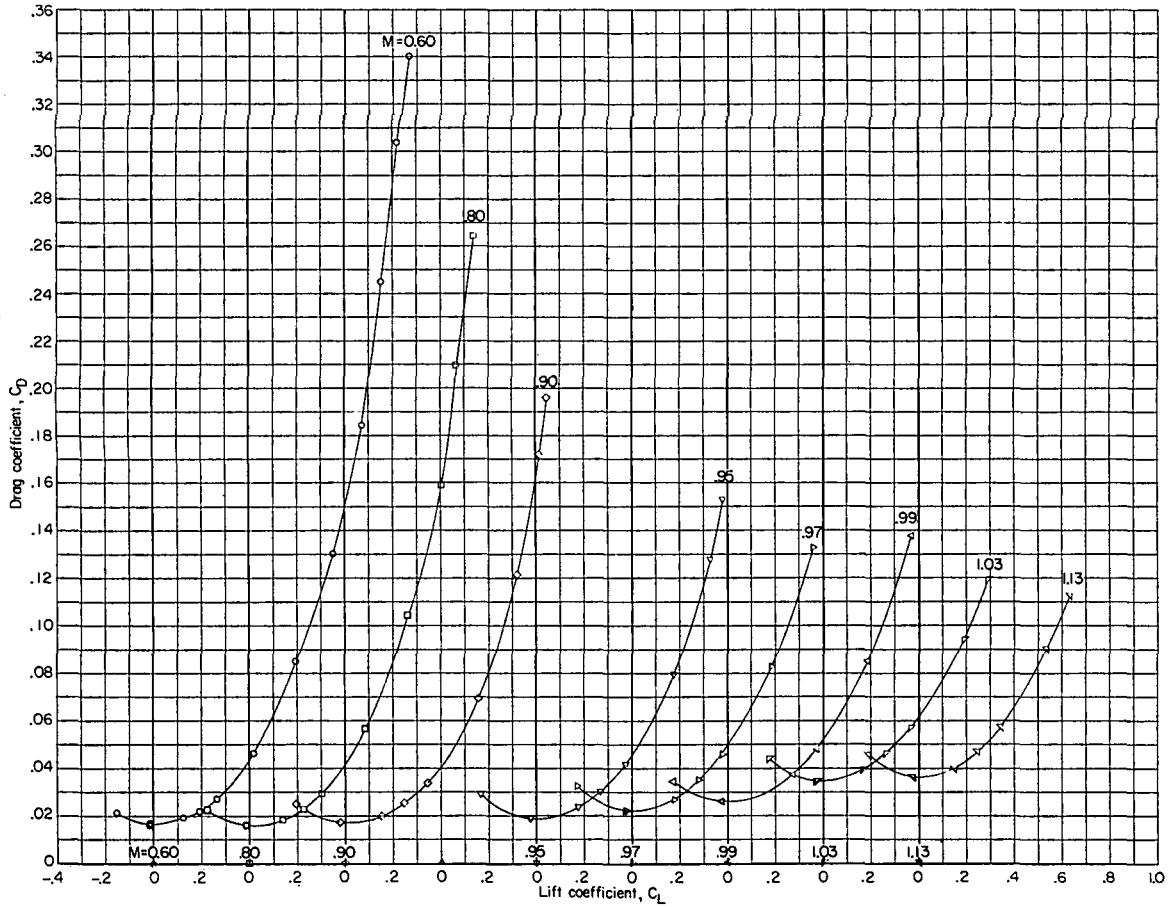

(b) Drag coefficient.

Figure 22.- Continued.

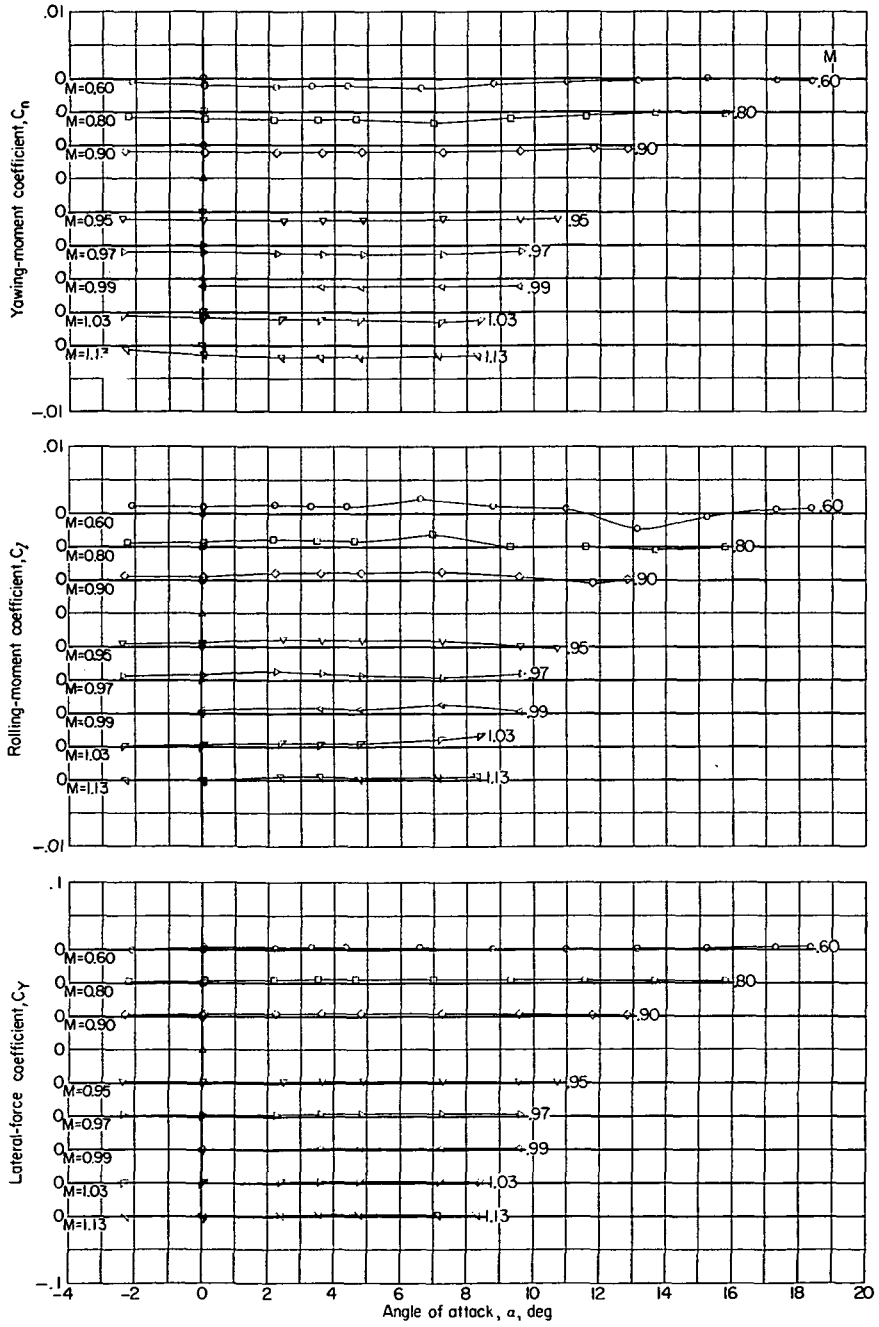

(c) Yawing-moment, rolling-moment, and lateral-force coefficients.

Figure 22.- Concluded.

[redacted]

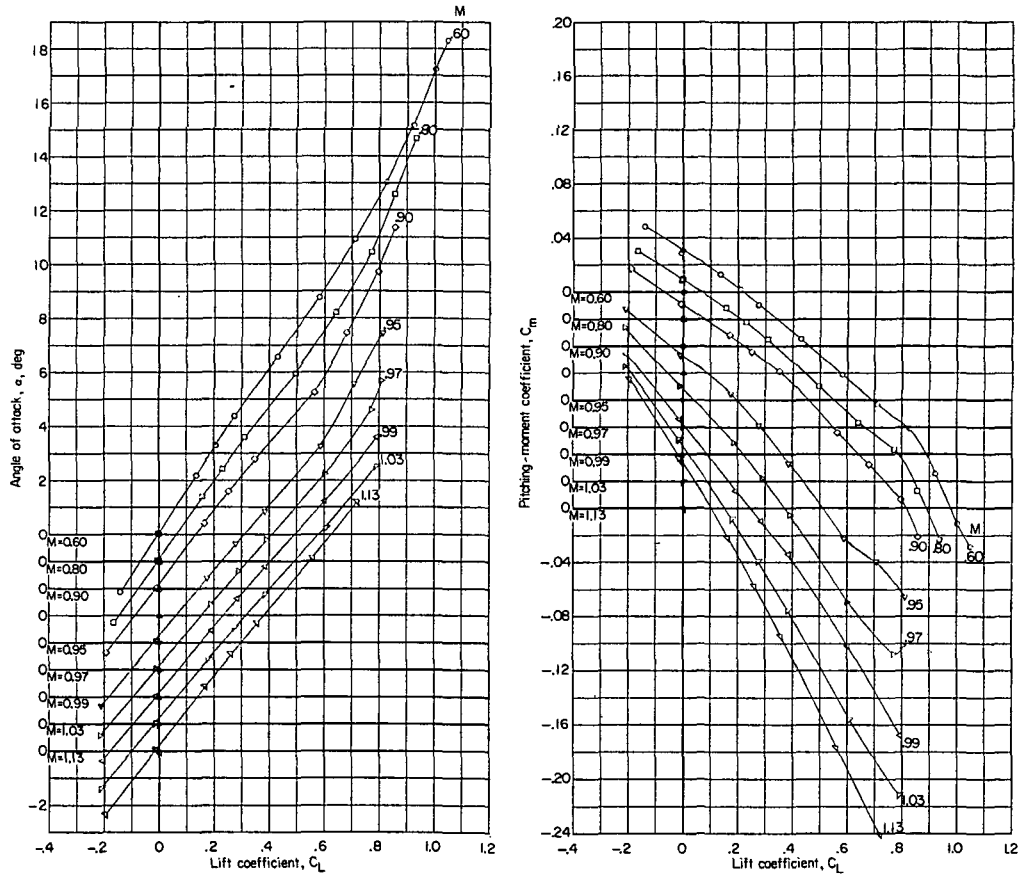

(a) Angle of attack and pitching-moment coefficient.

Figure 23.- Variation of aerodynamic characteristics with lift coefficient. Configuration 17; complete model plus wing fences; $i_t = -3^\circ$; $\delta_n = -7.5^\circ$; body with afterbody bump; undrooped supersonic inlet (cruise condition).

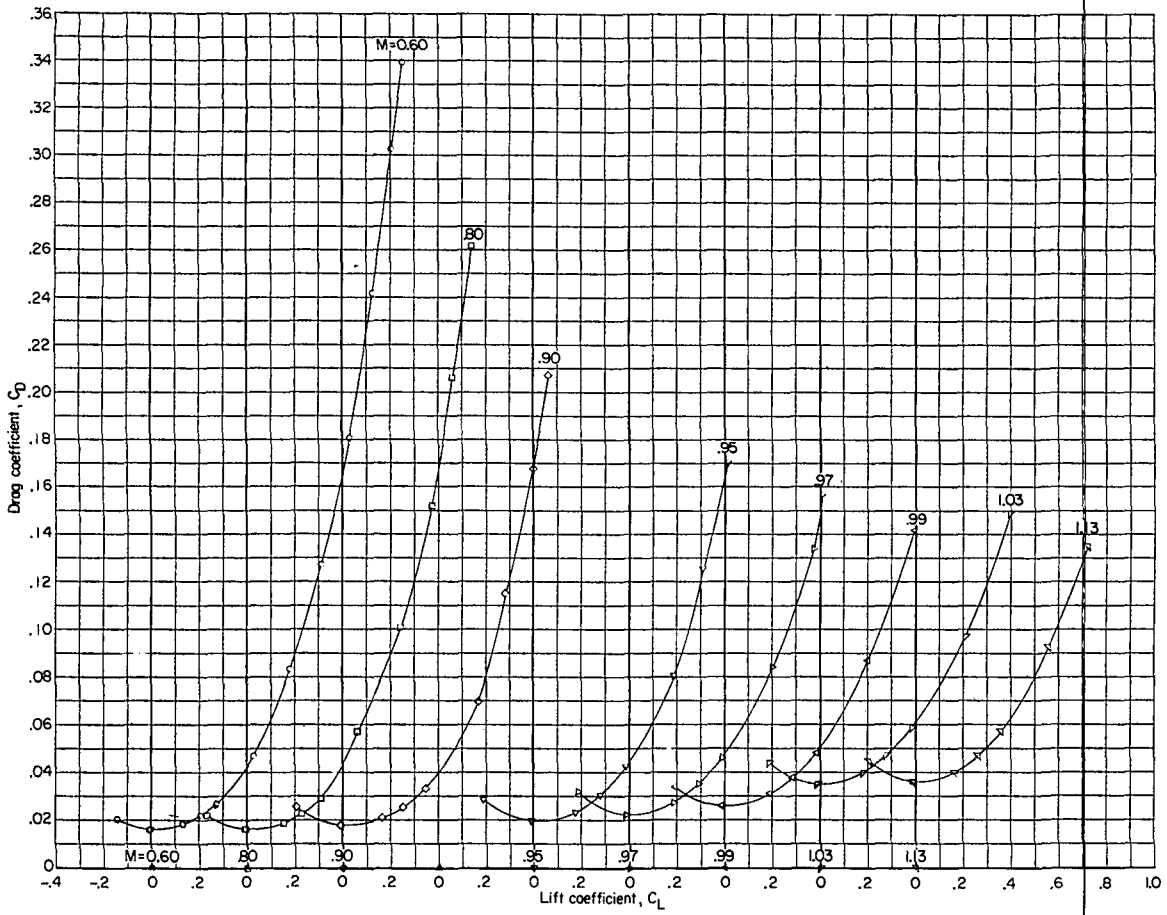

(b) Drag coefficient.

Figure 23.- Concluded.

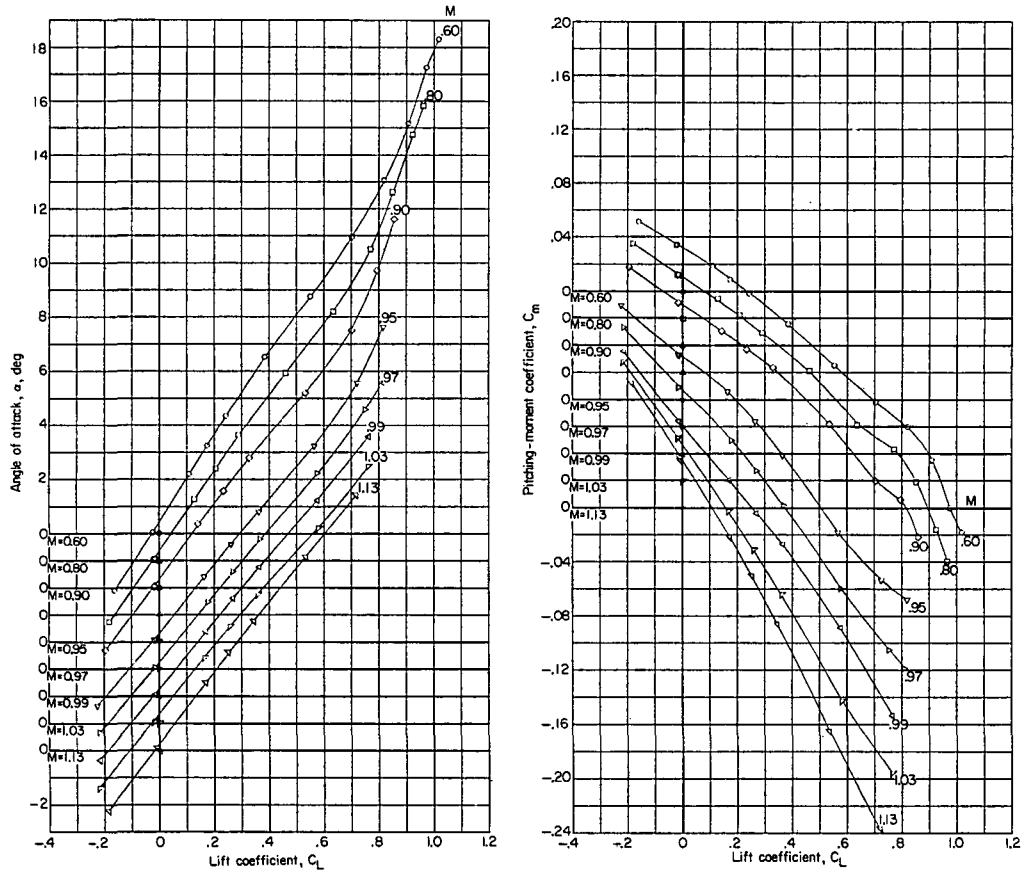

(a) Angle of attack and pitching-moment coefficient.

Figure 24.- Variation of aerodynamic characteristics with lift coefficient. Configuration 18; complete model plus blunt leading-edge radius on leading-edge flap; $i_t = -3^\circ$; $\delta_n = -7.5^\circ$; body with afterbody bump; undrooped supersonic inlet (cruise condition).

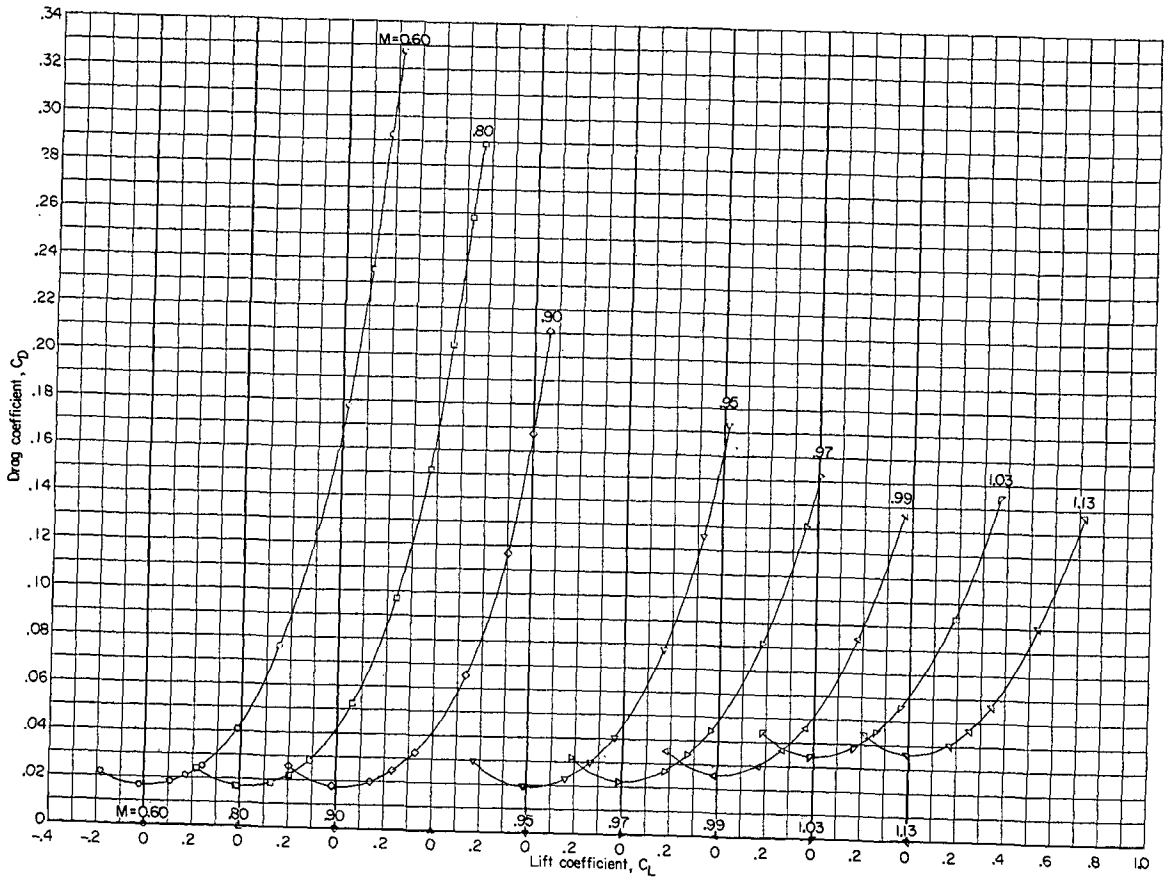

(b) Drag coefficient.

Figure 24.- Concluded.

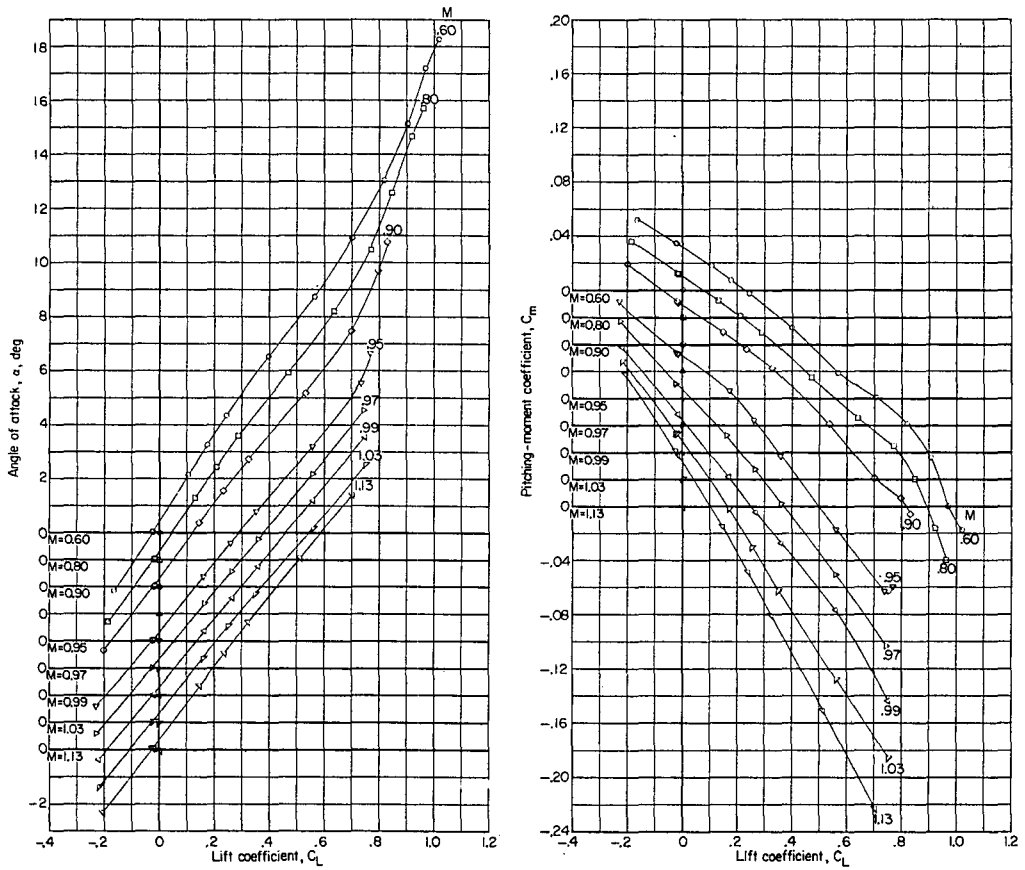

(a) Angle of attack and pitching-moment coefficient.

Figure 25.- Variation of aerodynamic characteristics with lift coefficient. Configuration 19; complete model plus sharp leading-edge radius on leading-edge flap; $i_t = -3^\circ$; $\delta_n = -7.5^\circ$; body with afterbody bump; undrooped supersonic inlet (cruise condition).

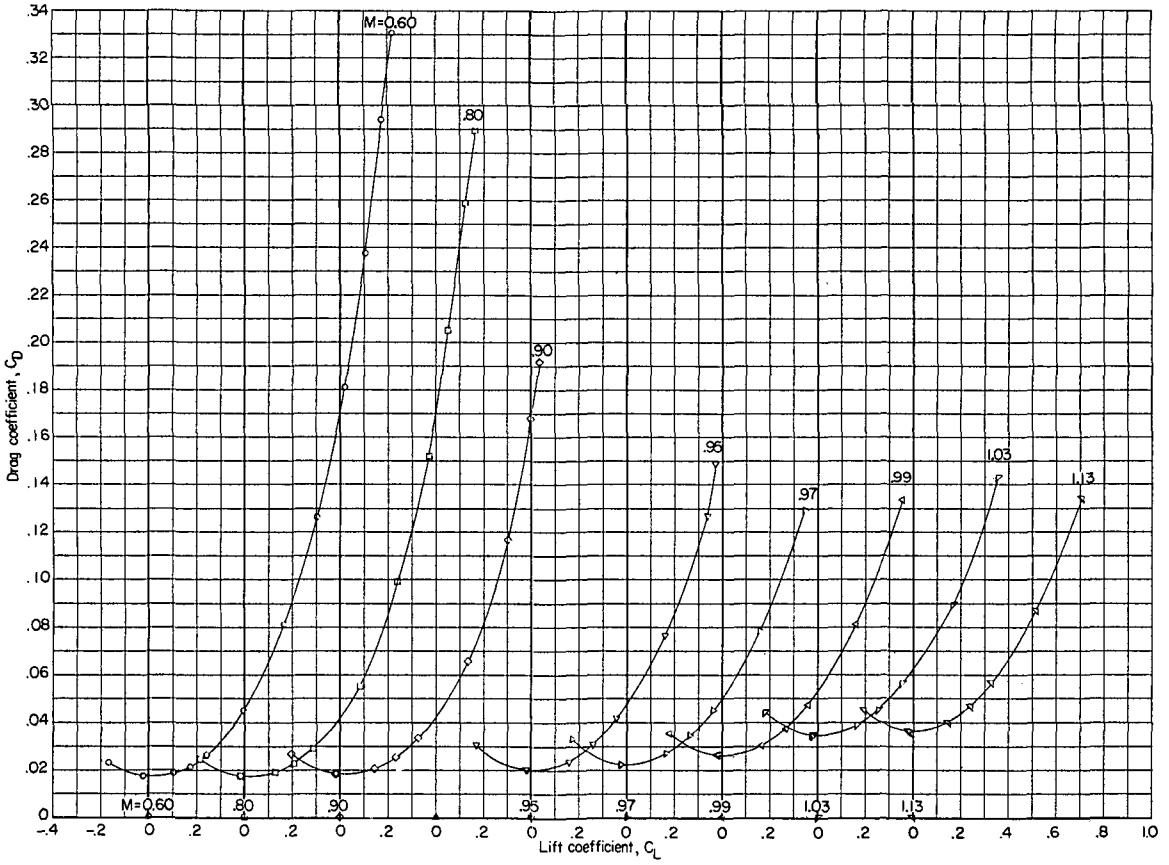

(b) Drag coefficient.

Figure 25.- Concluded.

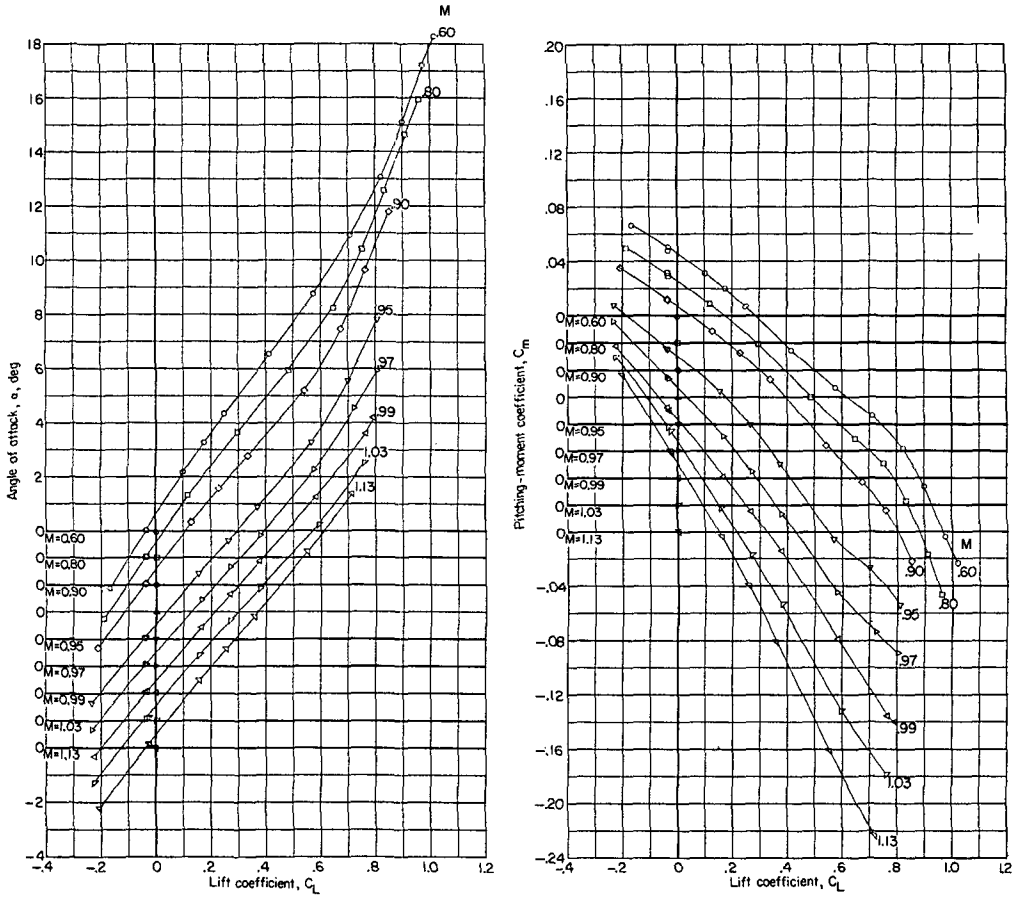

(a) Angle of attack and pitching-moment coefficient.

Figure 26.- Variation of aerodynamic characteristics with either lift coefficient or angle of attack. Configuration 20; complete model; $i_t = -3^\circ$; $\delta_{tr} = -12.2^\circ$; body with afterbody bump; undrooped supersonic inlet (cruise condition).

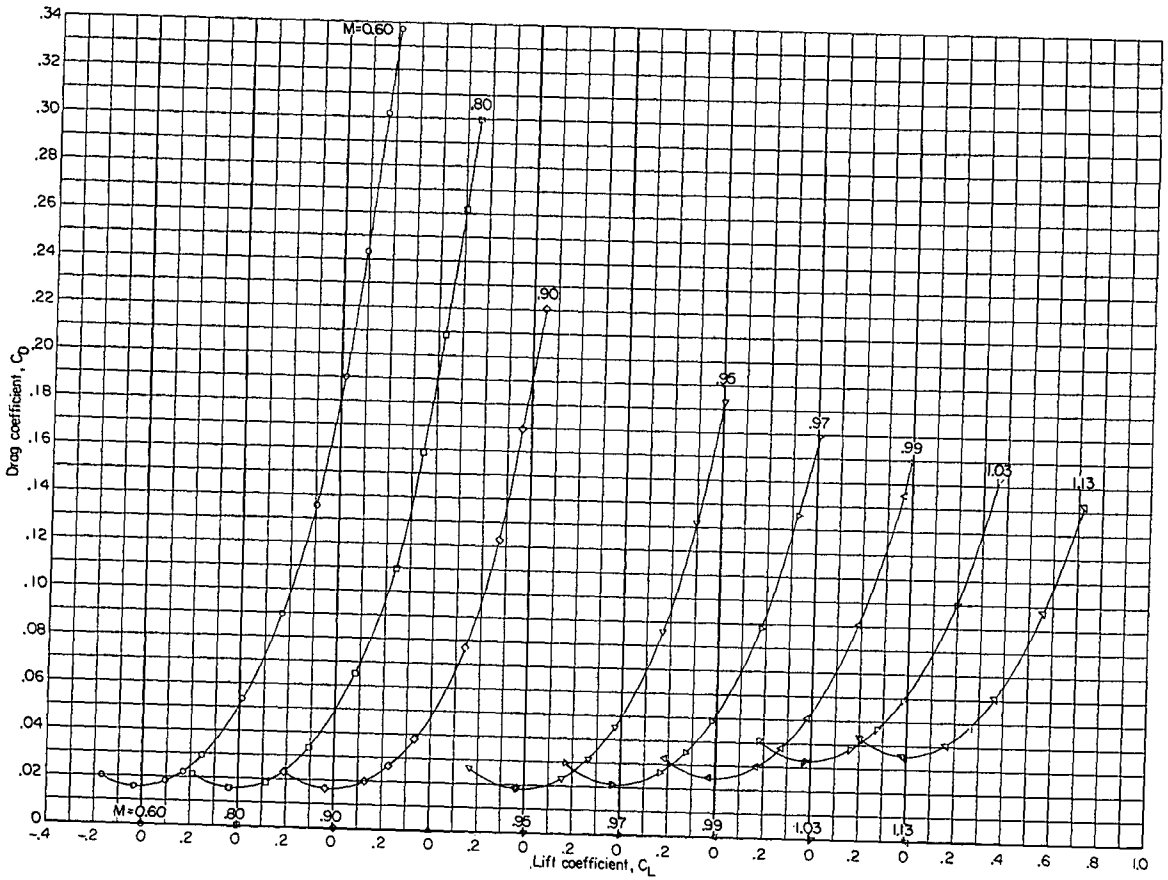

(b) Drag coefficient.

Figure 26.- Continued.

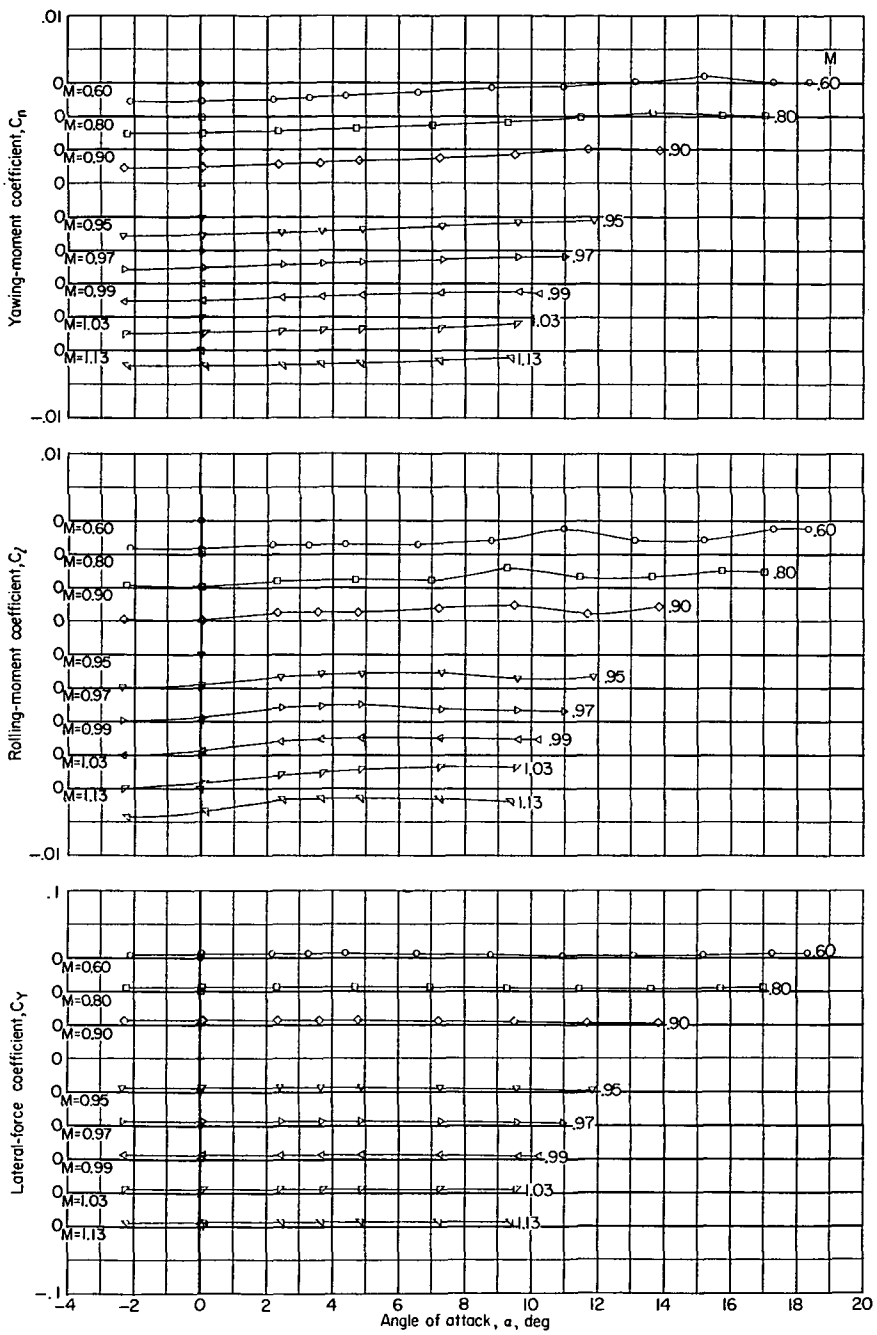

(c) Yawing-moment, rolling-moment, and lateral-force coefficients.

Figure 26.- Concluded.

[redacted]

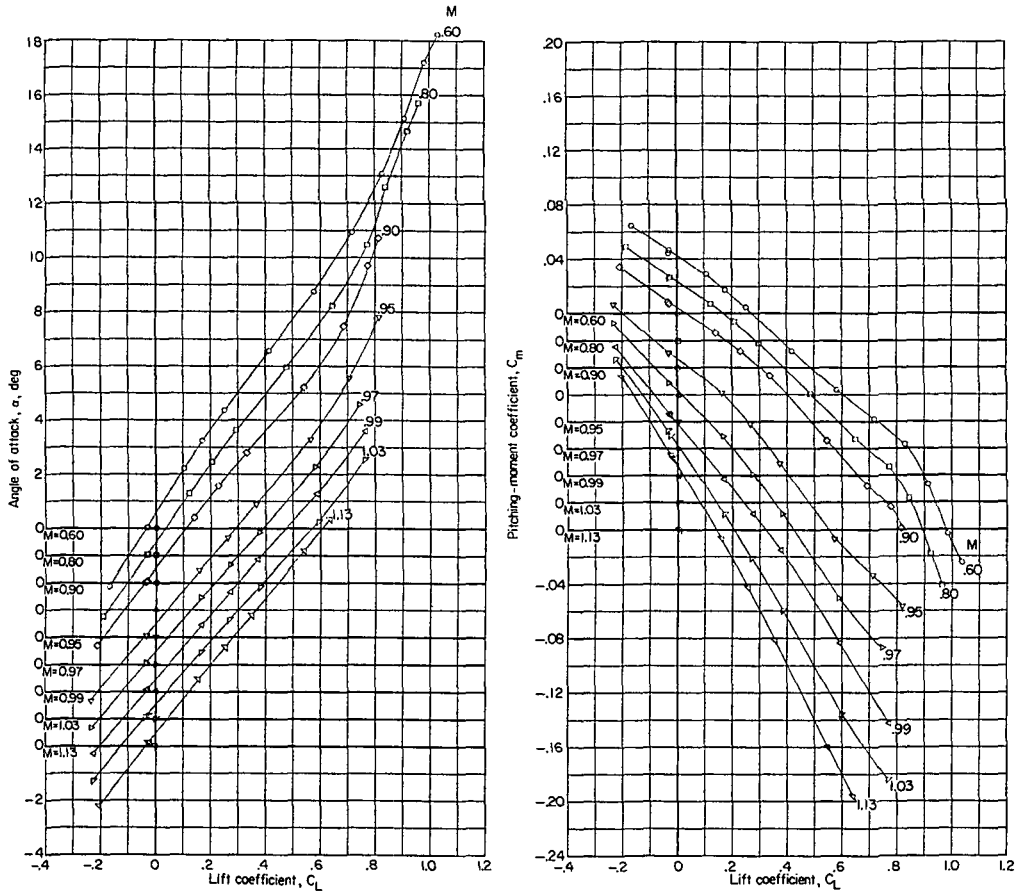

(a) Angle of attack and pitching-moment coefficient.

Figure 27.- Variation of aerodynamic characteristics with either lift coefficient or angle of attack. Configuration 21; complete model; $i_t = -3^\circ$; $\delta_n = 0^\circ$ on right wing and $\delta_n = -7.5^\circ$ on the left wing; $\delta_{tr} = -12.2^\circ$; body with afterbody bump; undrooped supersonic inlet (cruise condition).

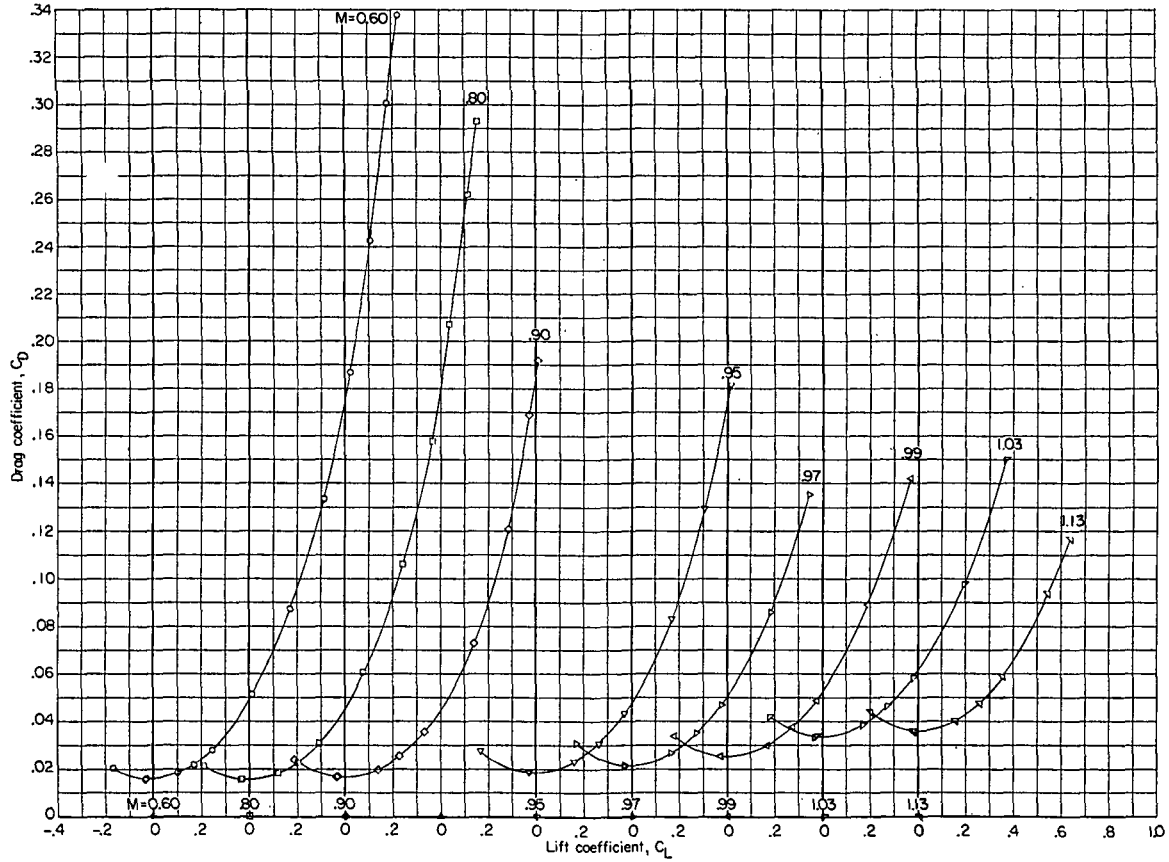

(b) Drag coefficient.

Figure 27.- Continued.

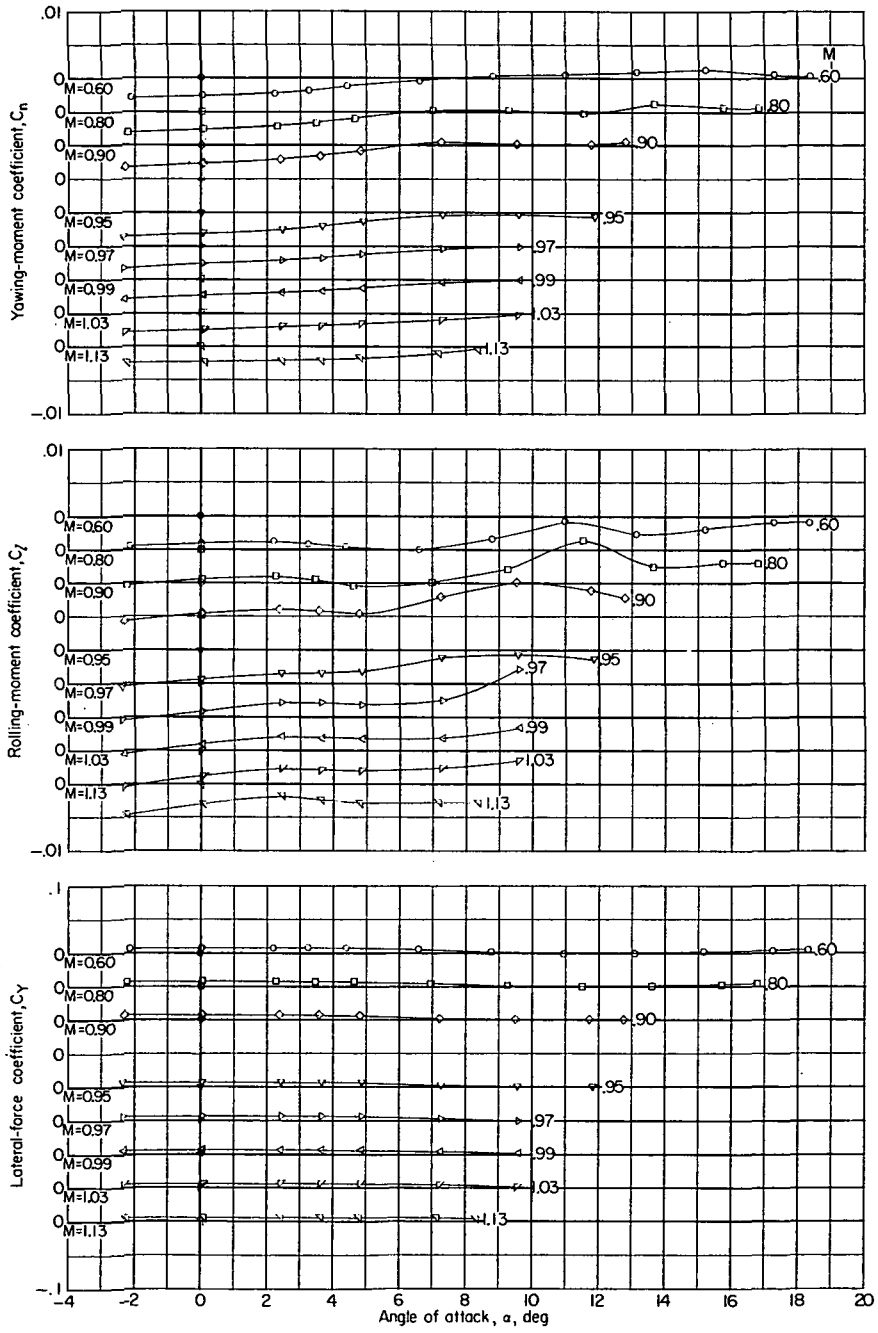

(c) Yawing-moment, rolling-moment, and lateral-force coefficients.

Figure 27.- Concluded.

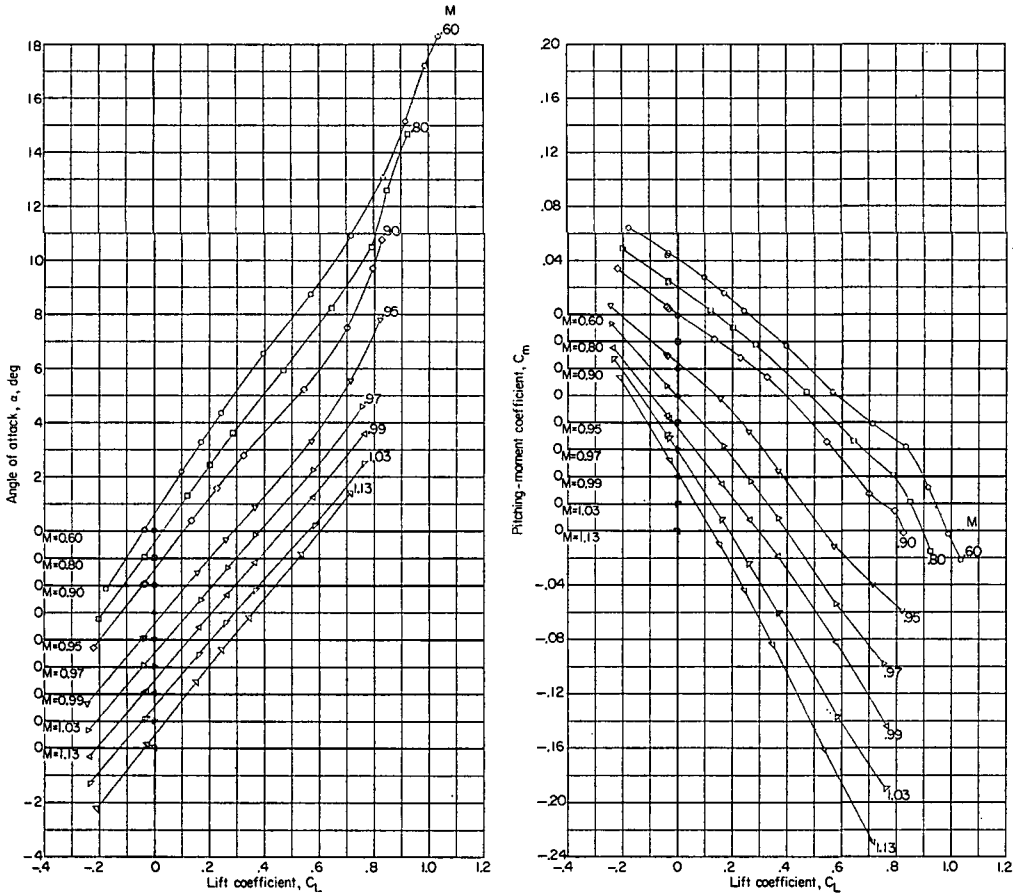

(a) Angle of attack and pitching-moment coefficient.

Figure 28.- Variation of aerodynamic characteristics with either lift coefficient or angle of attack. Configuration 22; complete model; $i_t = -3^\circ$; $\delta_n = -7.5^\circ$; $\delta_{tr} = -12.2^\circ$; body with afterbody bump; undrooped supersonic inlet (cruise condition).

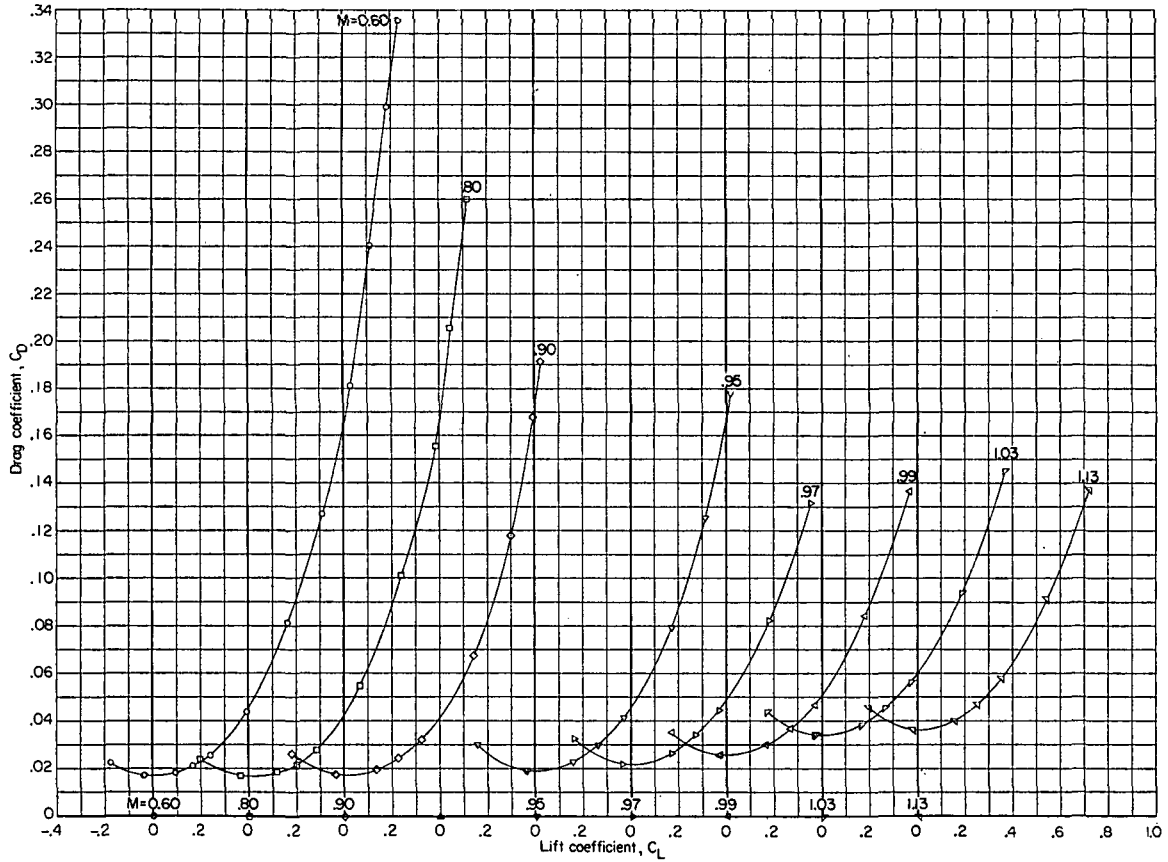

(b) Drag coefficient.

Figure 28.- Continued.

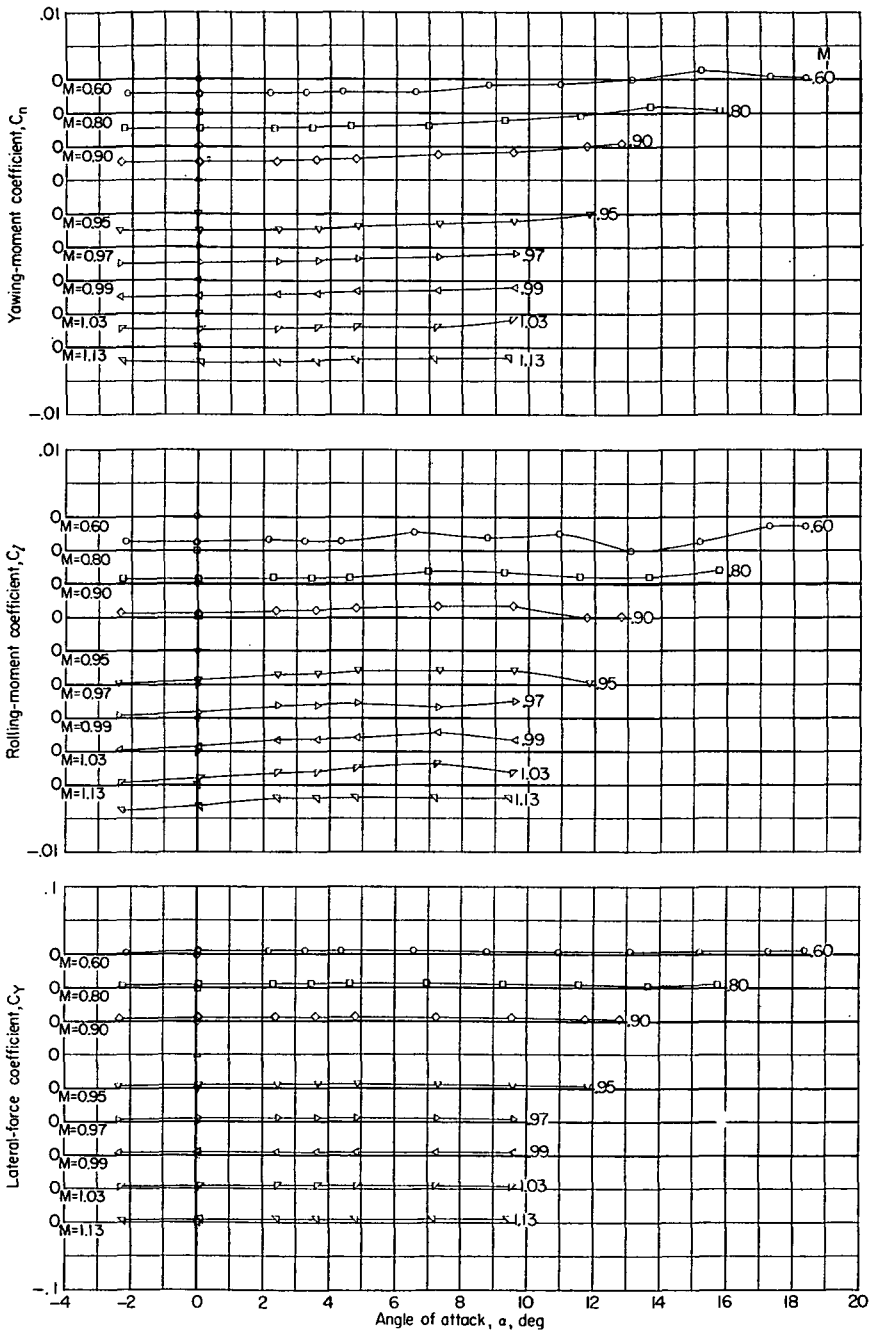

(c) Yawing-moment, rolling-moment, and lateral-force coefficients.

Figure 28.- Concluded.

[redacted]

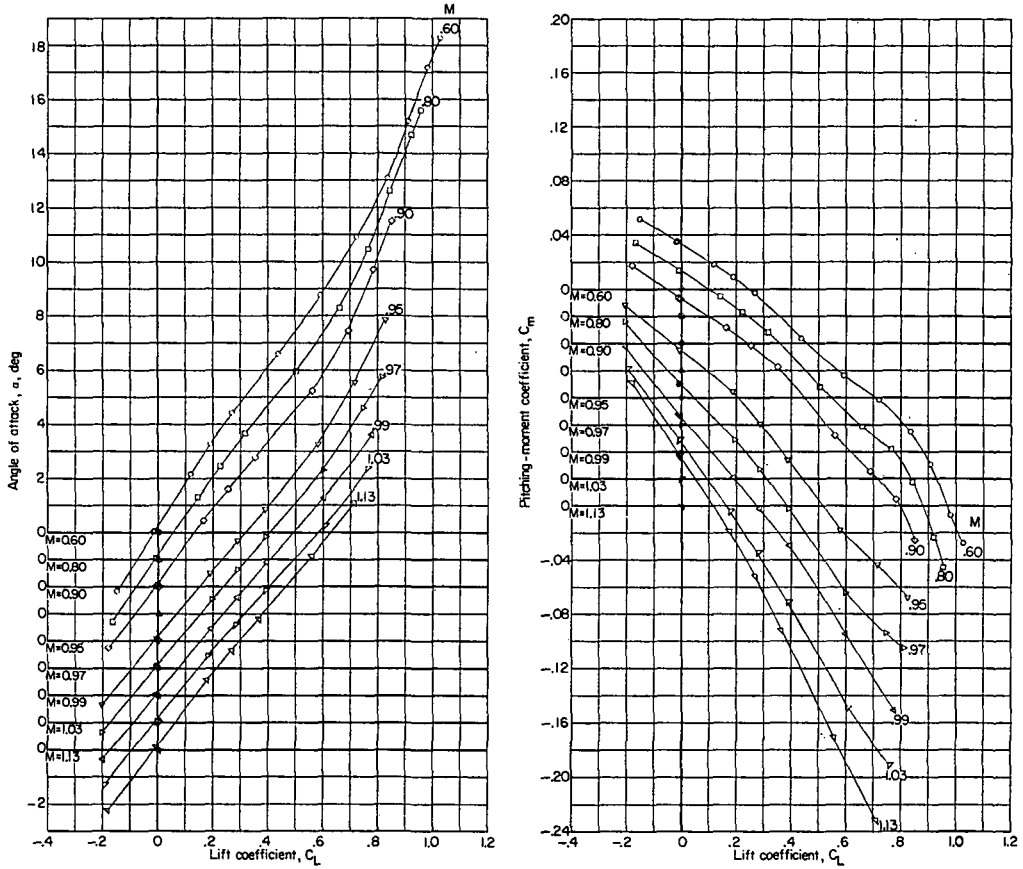

(a) Angle of attack and pitching-moment coefficient.

Figure 29.- Variation of aerodynamic characteristics with either lift coefficient or angle of attack. Configuration 23; complete model plus 10°-deflected shark fin; i_t = -3°; body with afterbody bump; undrooped supersonic inlet (cruise condition).

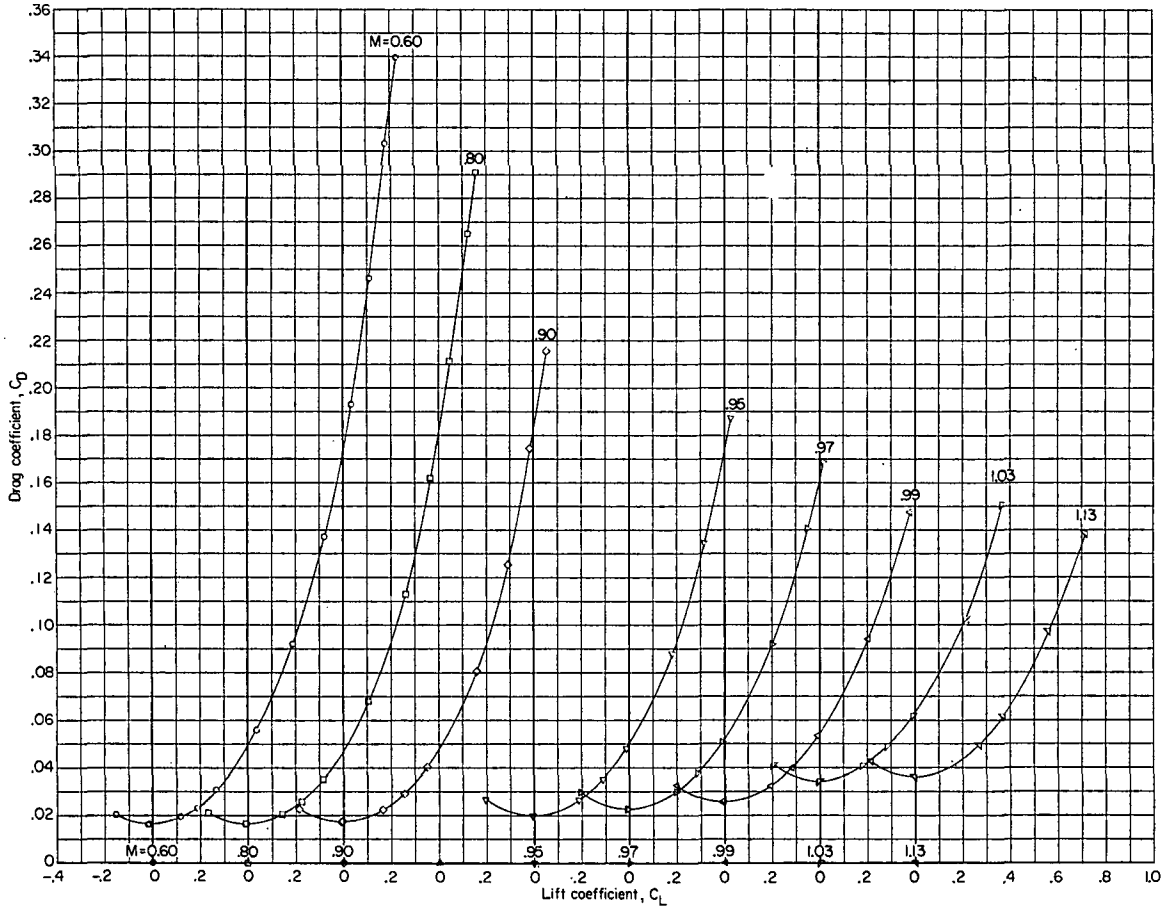

(b) Drag coefficient.

Figure 29.- Continued.

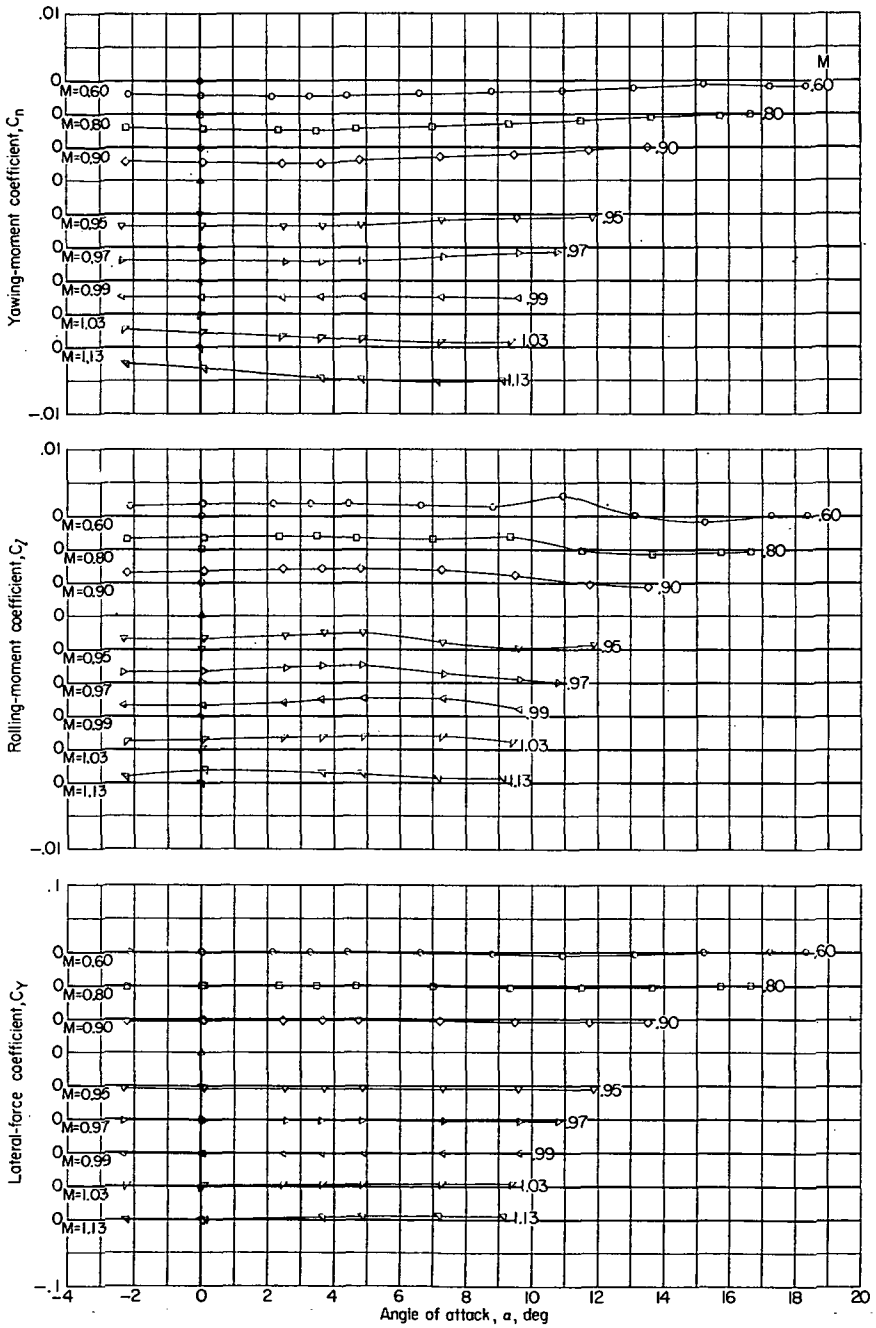

(c) Yawing-moment, rolling-moment, and lateral-force coefficients.

Figure 29.- Concluded.

[redacted]

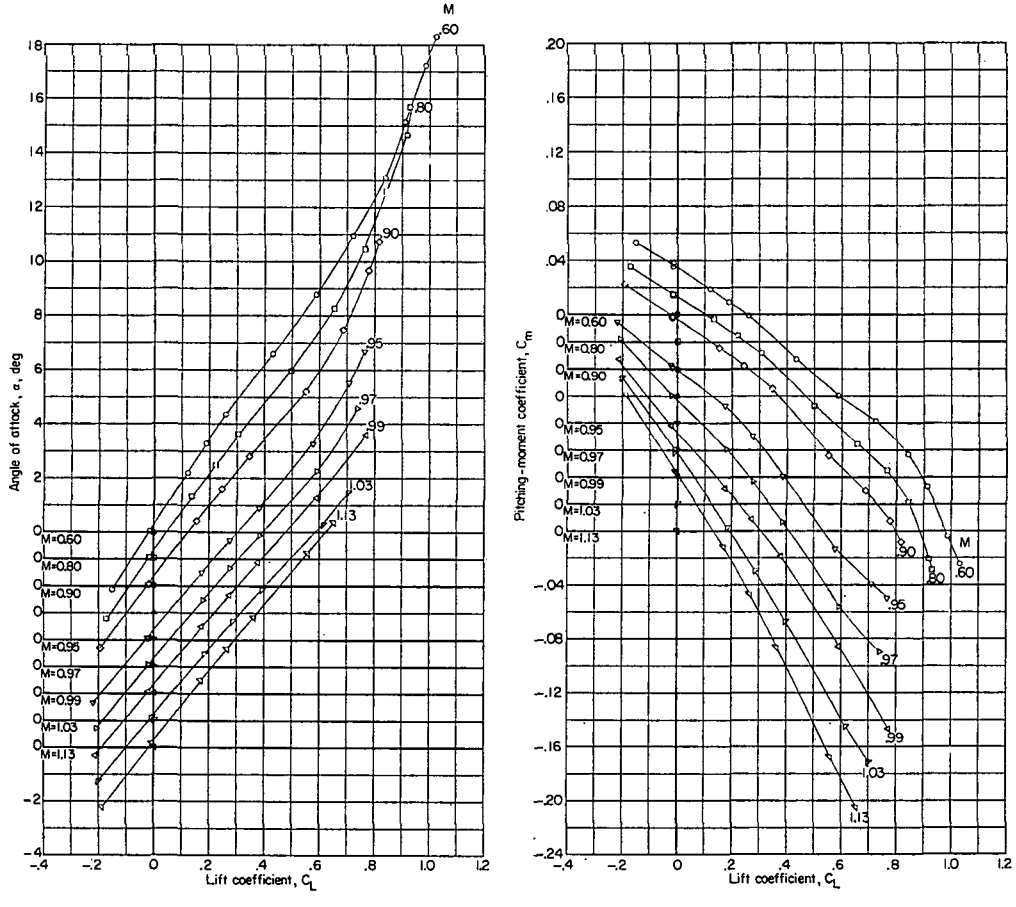

(a) Angle of attack and pitching-moment coefficient.

Figure 30.- Variation of aerodynamic characteristics with either lift coefficient or angle of attack. Configuration 24; complete model; $i_t = -3^\circ$; $\delta_r = 6^\circ$; body with afterbody bump; undrooped supersonic inlet (cruise condition).

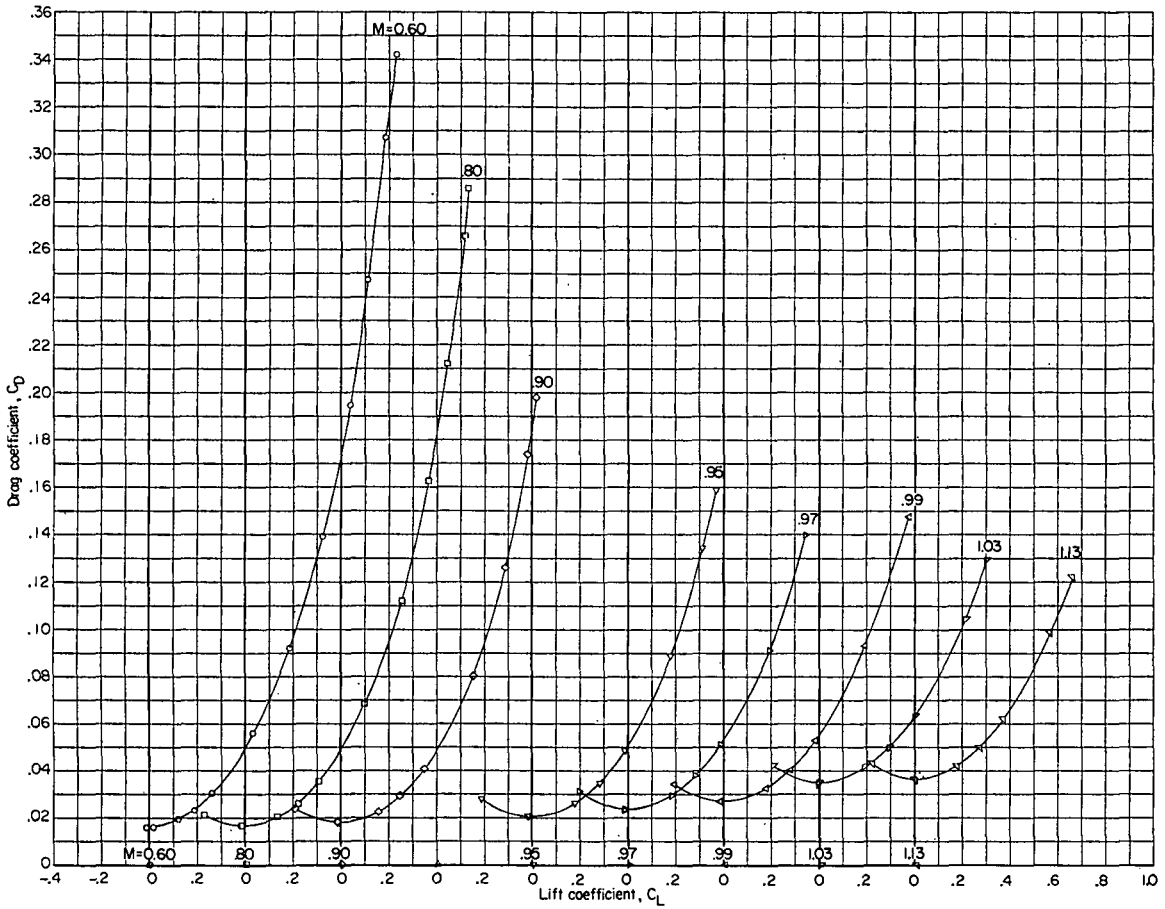

(b) Drag coefficient.

Figure 30.- Continued.

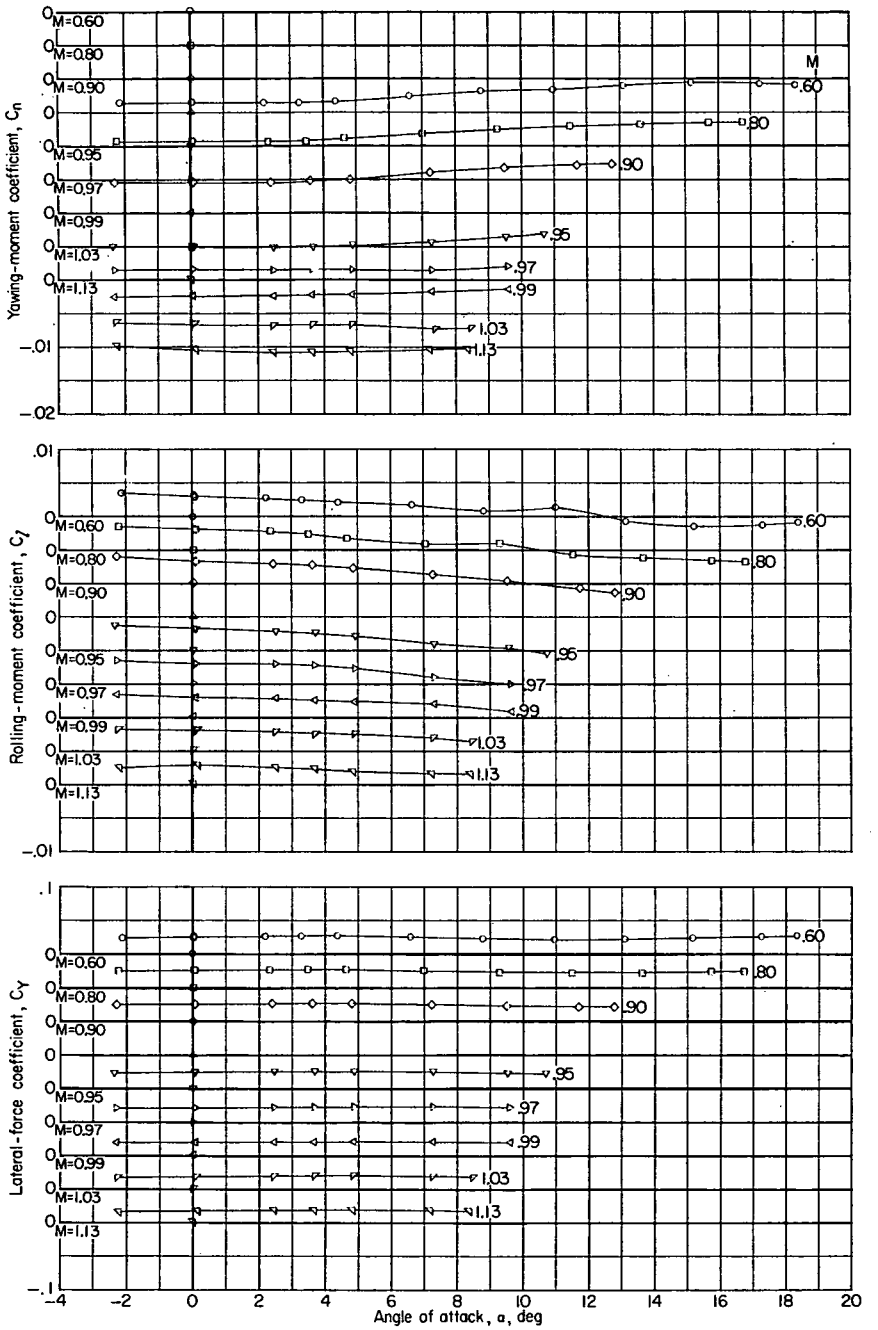

(c) Yawing-moment, rolling-moment, and lateral-force coefficients.

Figure 30.- Concluded.

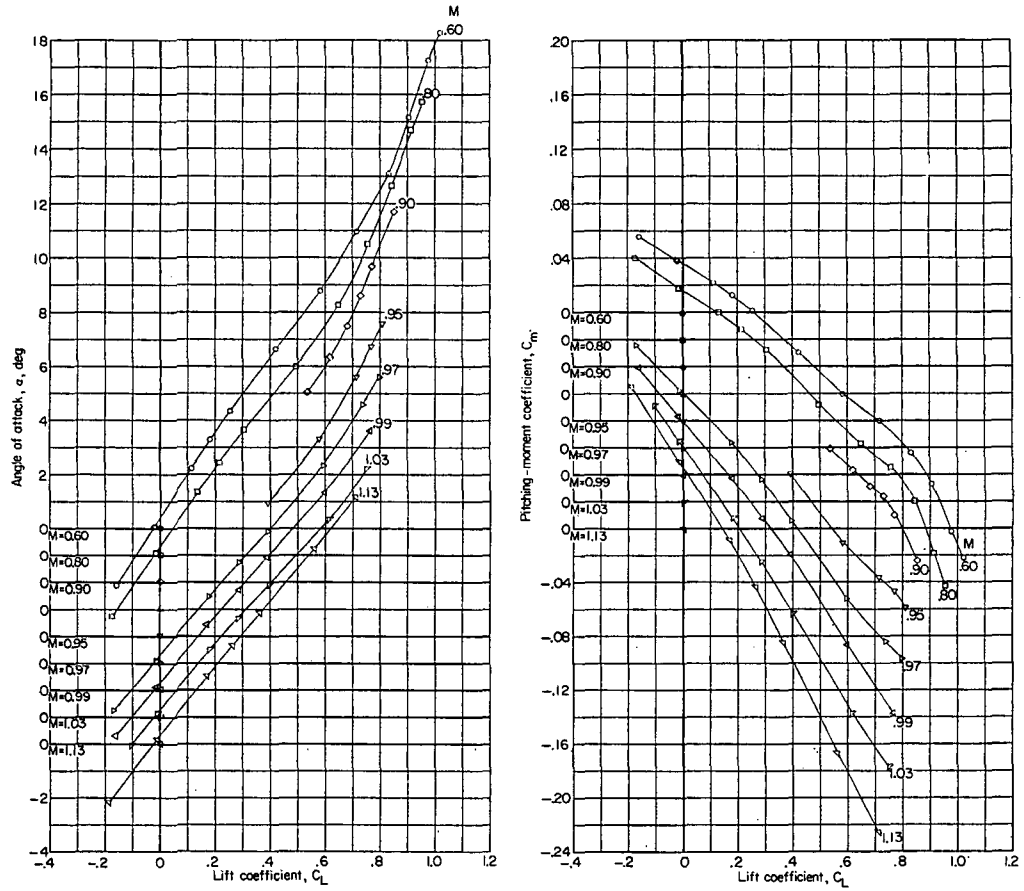

(a) Angle of attack and pitching-moment coefficient.

Figure 31.- Variation of aerodynamic characteristics with either lift coefficient of angle of attack. Configuration 25; complete model; $i_t = -3^\circ$; $\delta_r = 12^\circ$; body with afterbody bump; undrooped supersonic inlet (cruise condition).

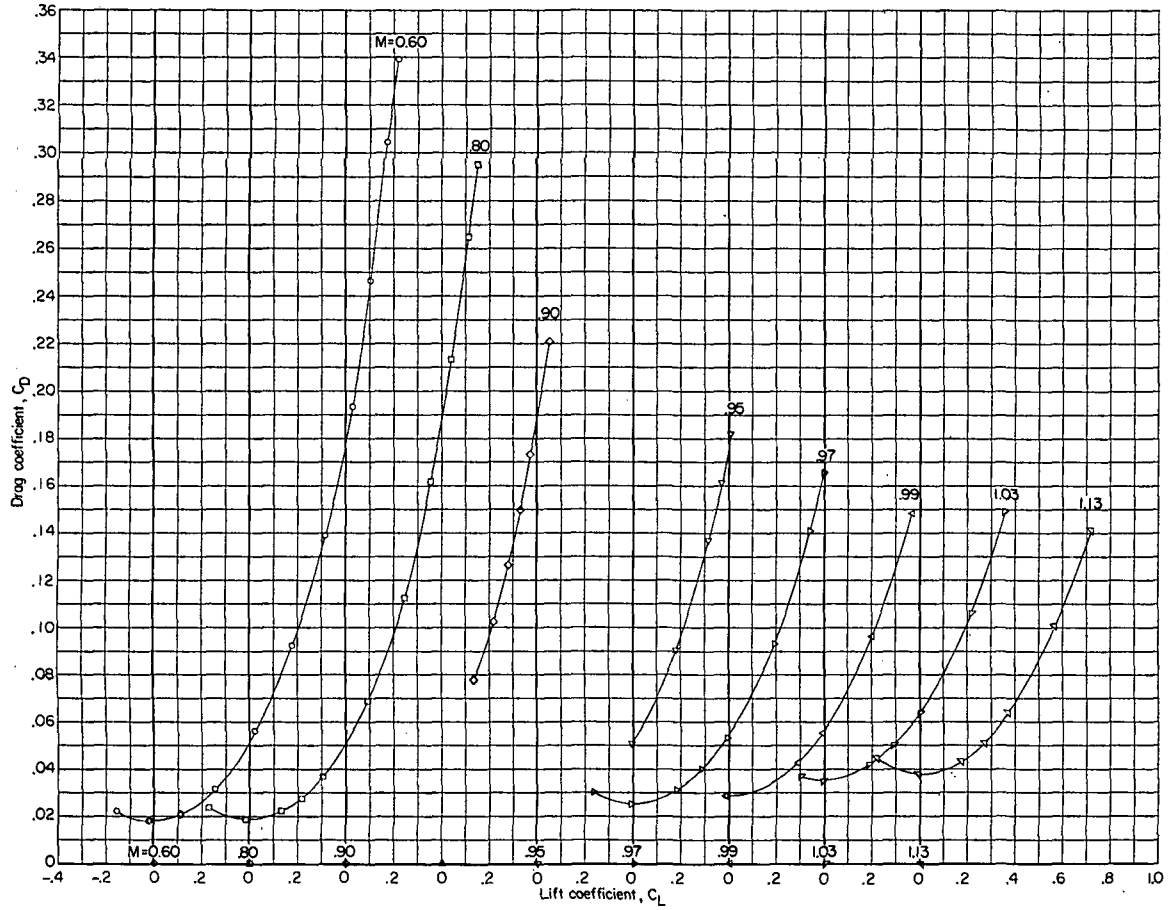

(b) Drag coefficient.

Figure 31.- Continued.

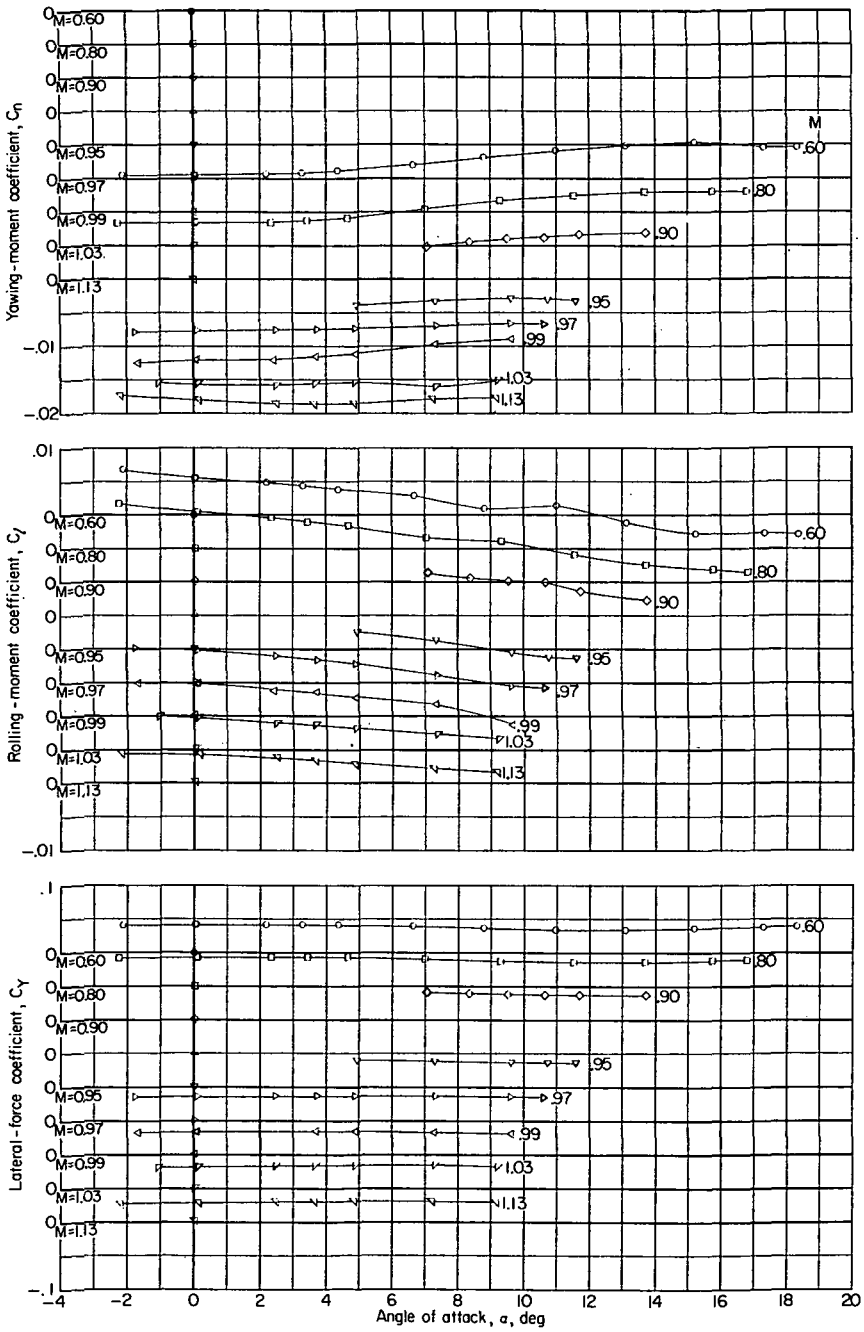

(c) Yawing-moment, rolling-moment, and lateral-force coefficients.

Figure 31.- Concluded.

[redacted]

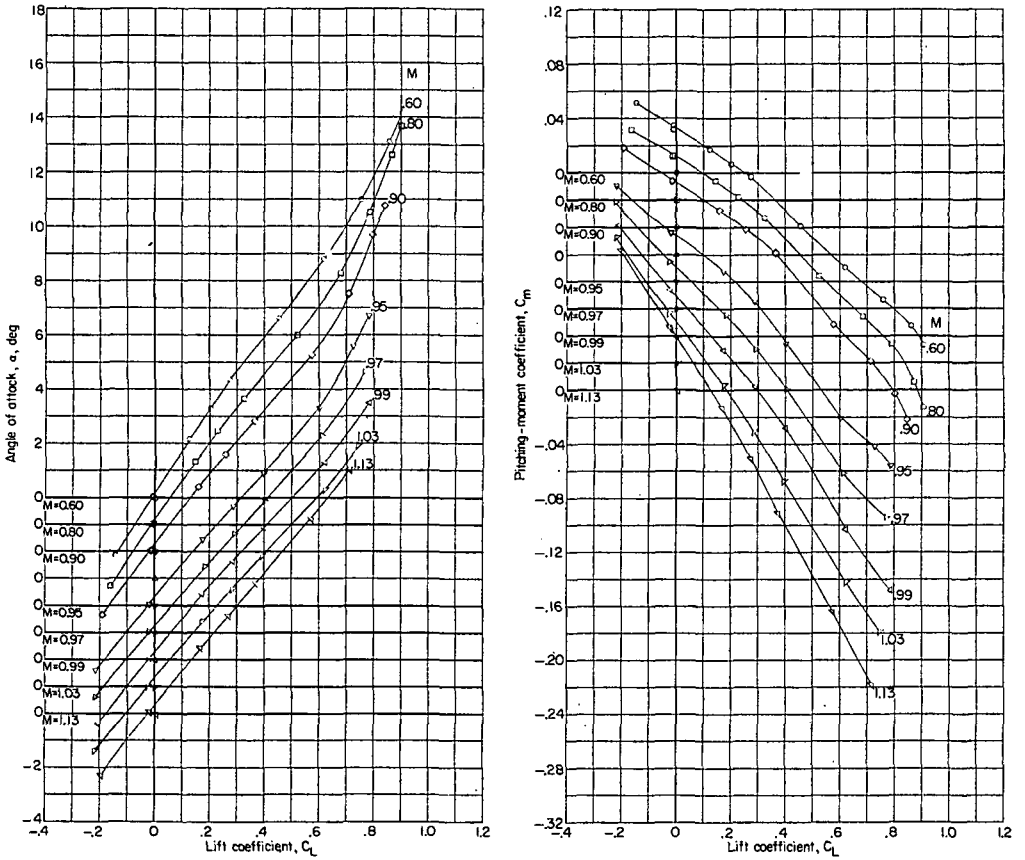

(a) Angle of attack and pitching-moment coefficient.

Figure 32.- Variation of aerodynamic characteristics with either lift coefficient or angle of attack. Configuration 26; complete model; $i_t = -3^\circ$; $\beta = -2.2^\circ$; body with afterbody bump; undrooped supersonic inlet (cruise condition).

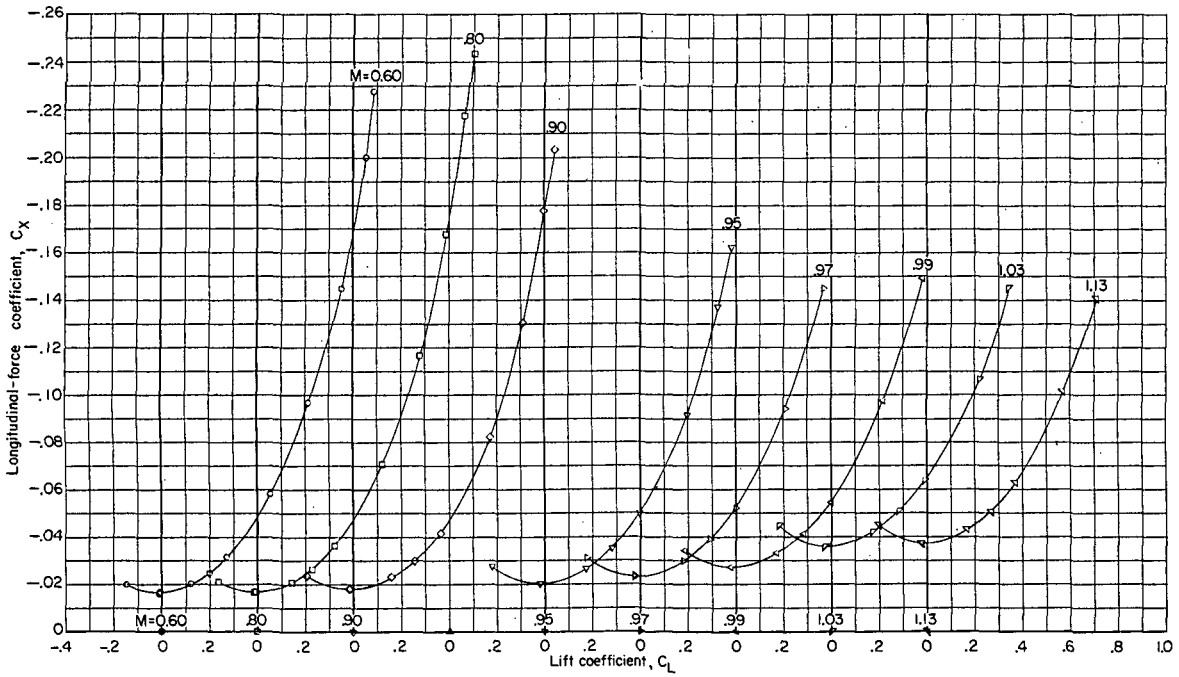

(b) Longitudinal-force coefficient.

Figure 32.- Continued.

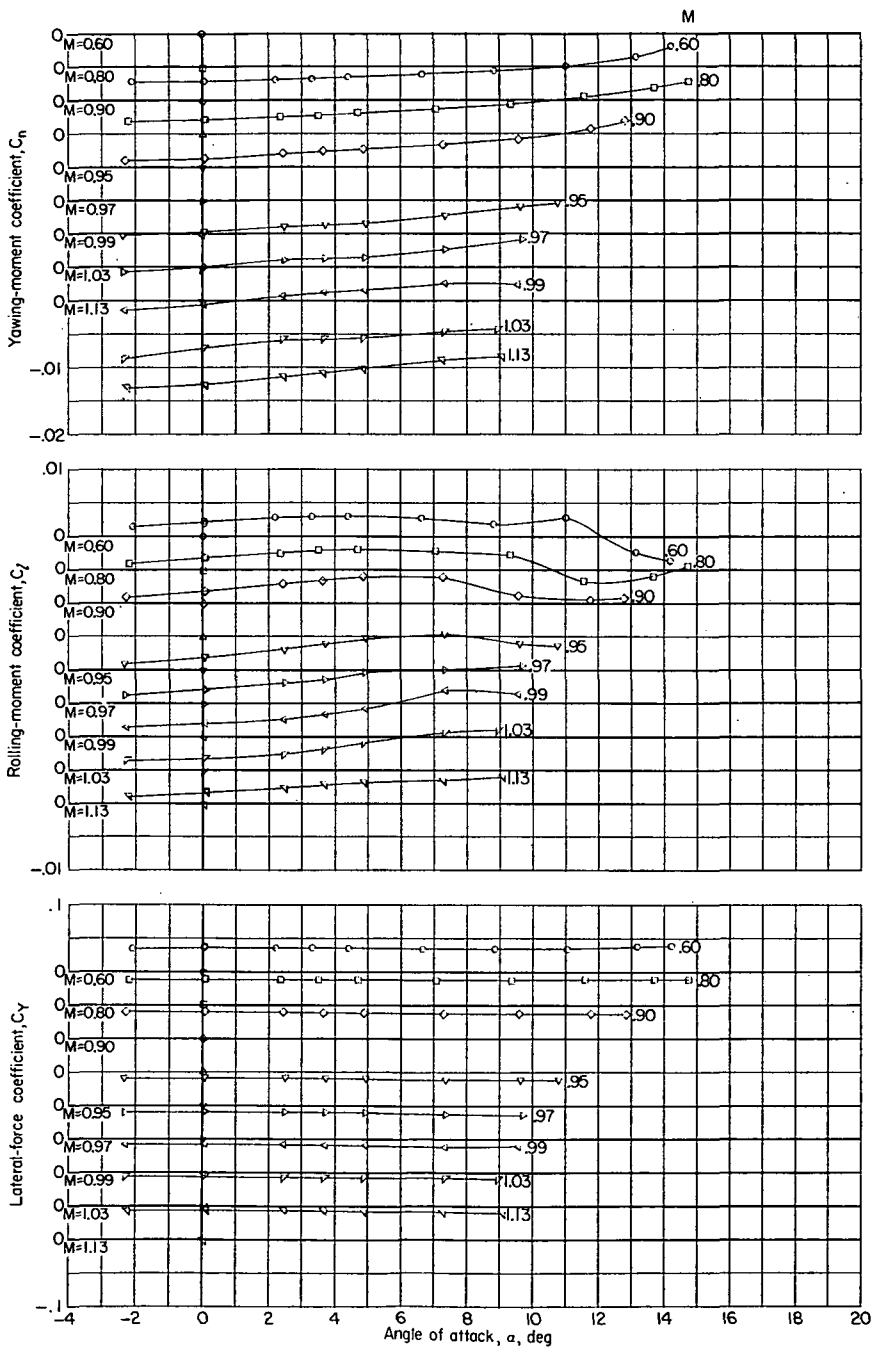

(c) Yawing-moment, rolling-moment, and lateral-force coefficients.

Figure 32.- Concluded.

[redacted]

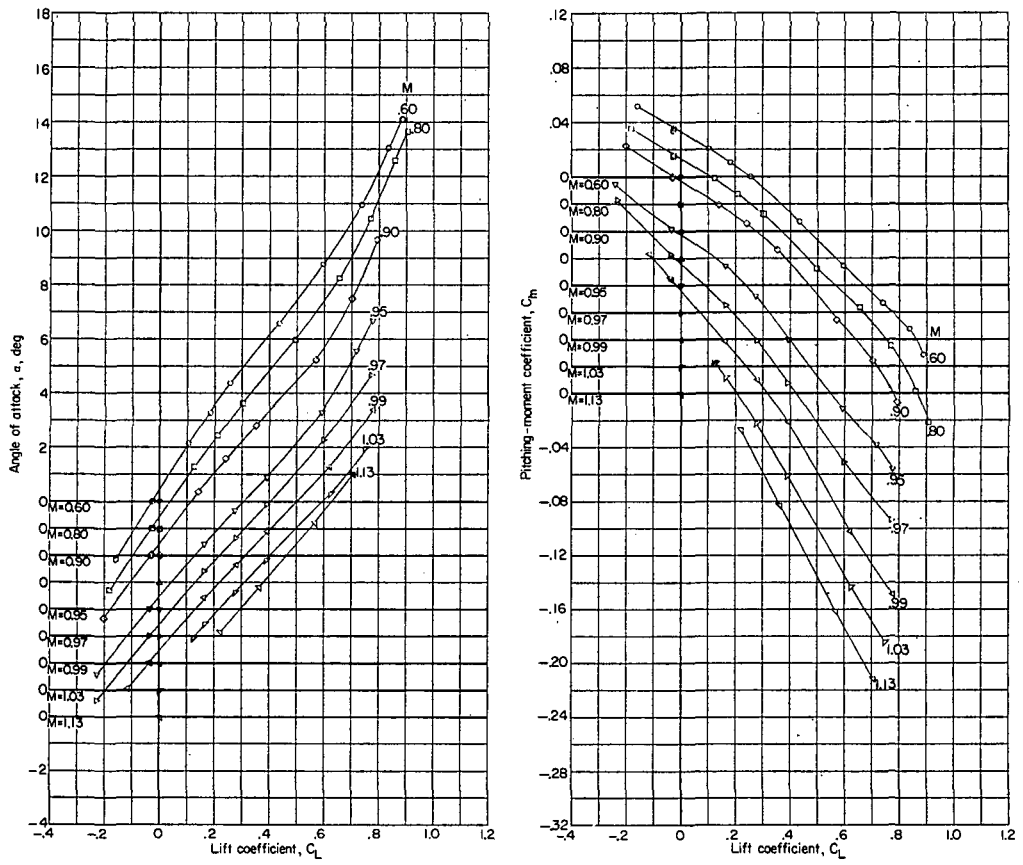

(a) Angle of attack and pitching-moment coefficient.

Figure 33.- Variation of aerodynamic characteristics with either lift coefficient or angle of attack. Configuration 27; complete model; $i_t = -3^\circ$; $\beta = -5.4^\circ$; body with afterbody bump; undrooped supersonic inlet (cruise condition).

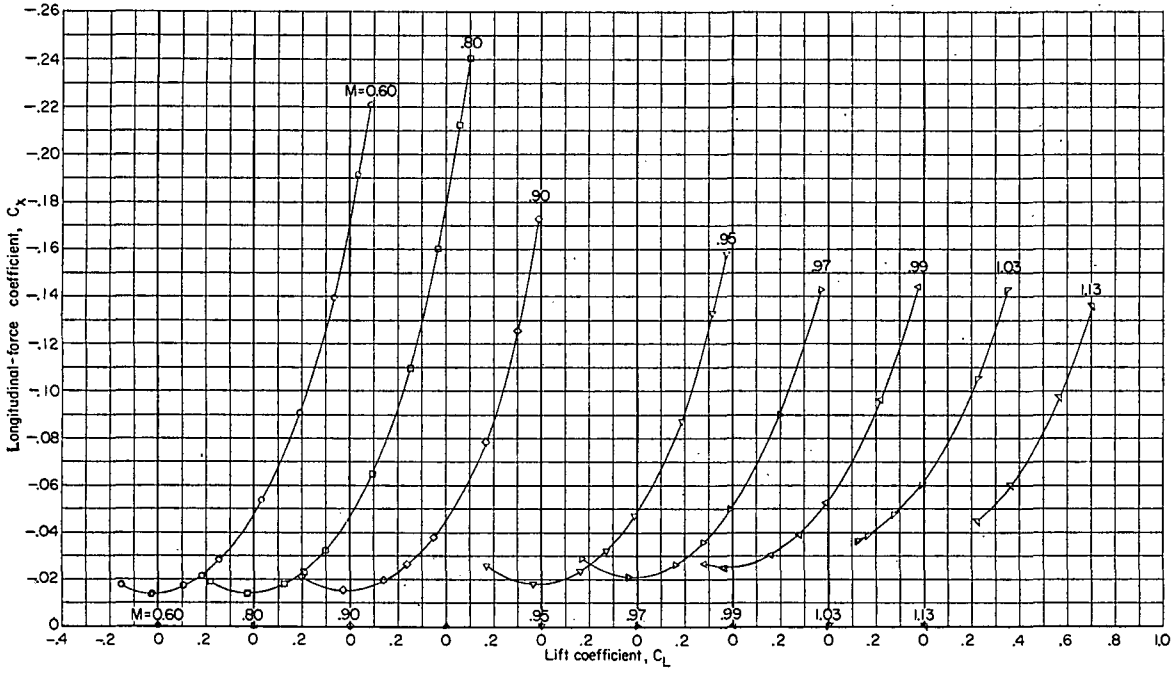

(b) Longitudinal-force coefficient.

Figure 33.- Continued.

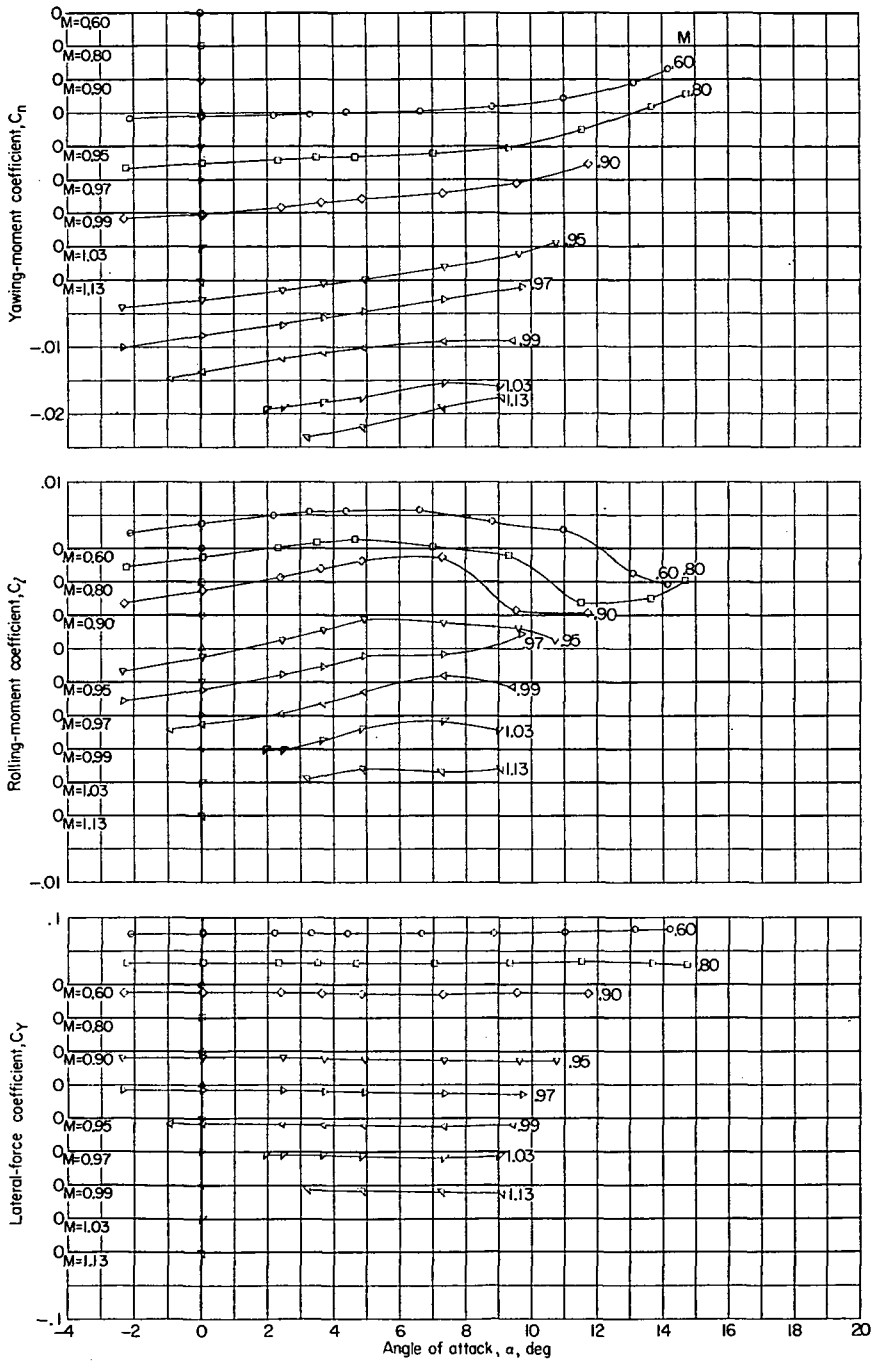

(c) Yawing-moment, rolling-moment, and lateral-force coefficients.

Figure 33.- Concluded.

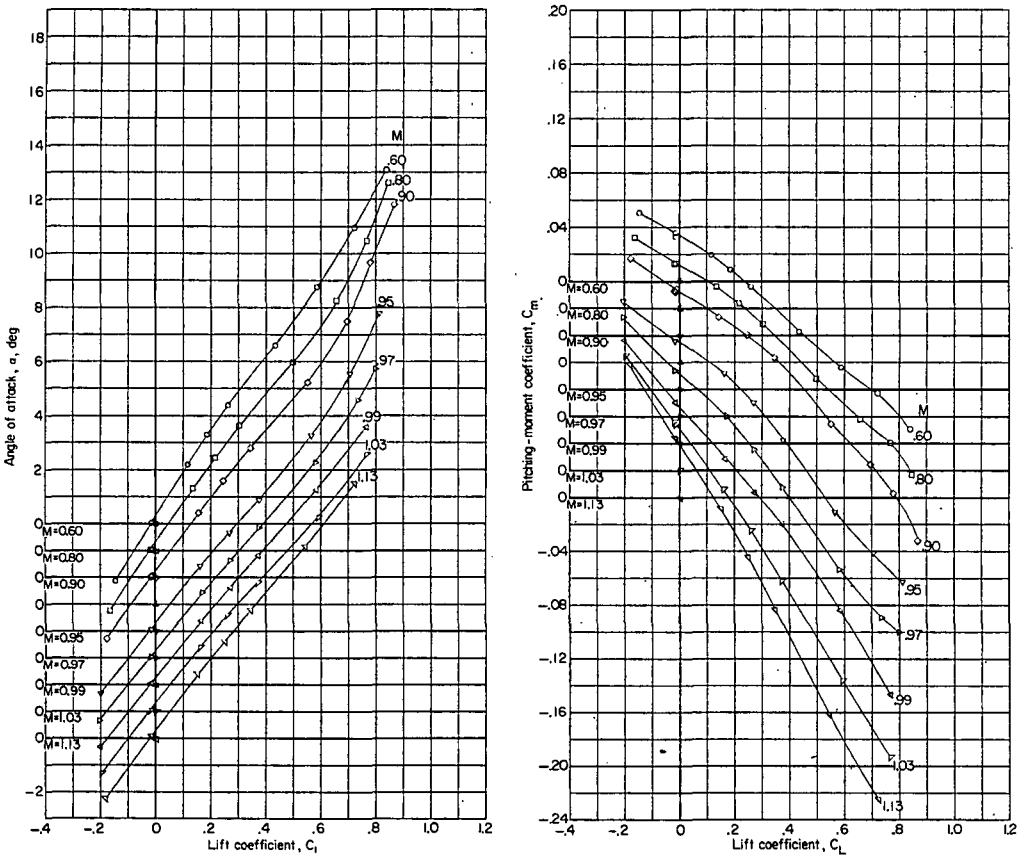

(a) Angle of attack and pitching-moment coefficient.

Figure 34.- Variation of aerodynamic characteristics with either lift coefficient or angle of attack. Configuration 28; complete model plus ventral fin and plus modified vertical tail; $i_t = -3^\circ$; body with afterbody bump; undrooped supersonic inlet (cruise condition).

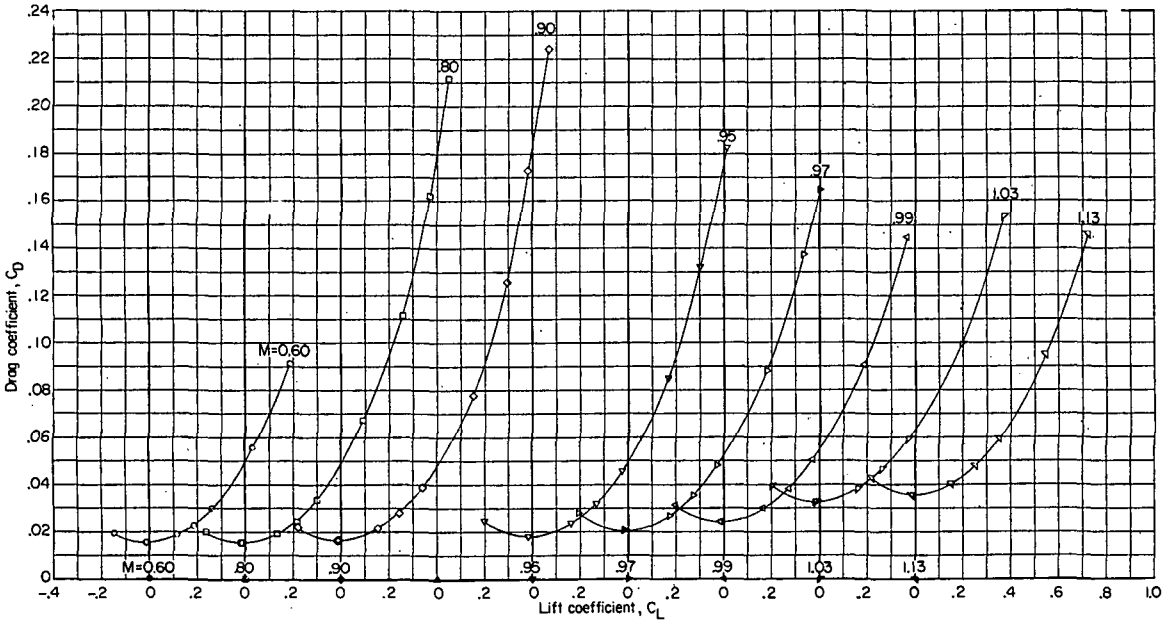

(b) Drag coefficient.

Figure 34.- Continued.

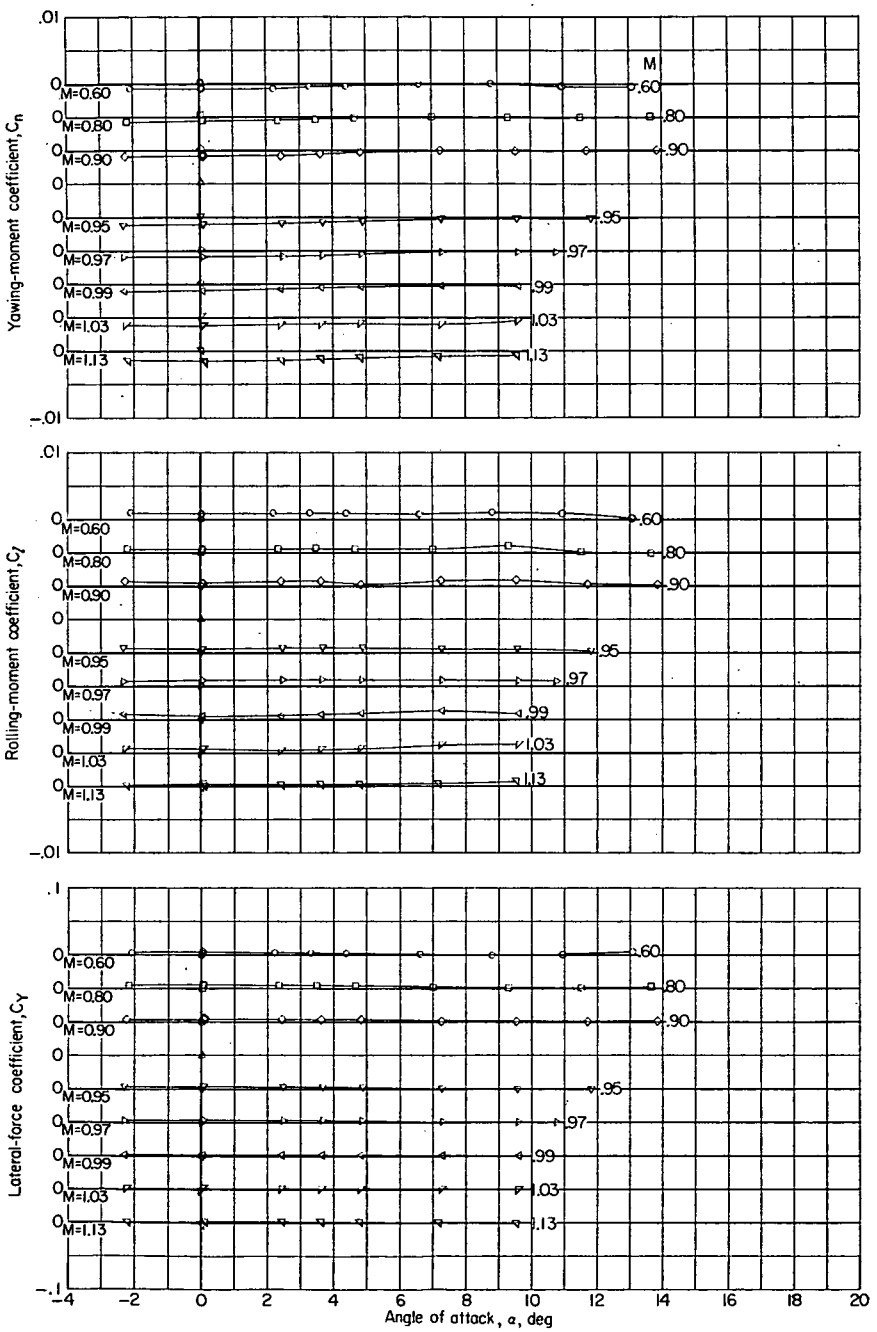

(c) Yawing-moment, rolling-moment, and lateral-force coefficients.

Figure 34.- Concluded.

[redacted]

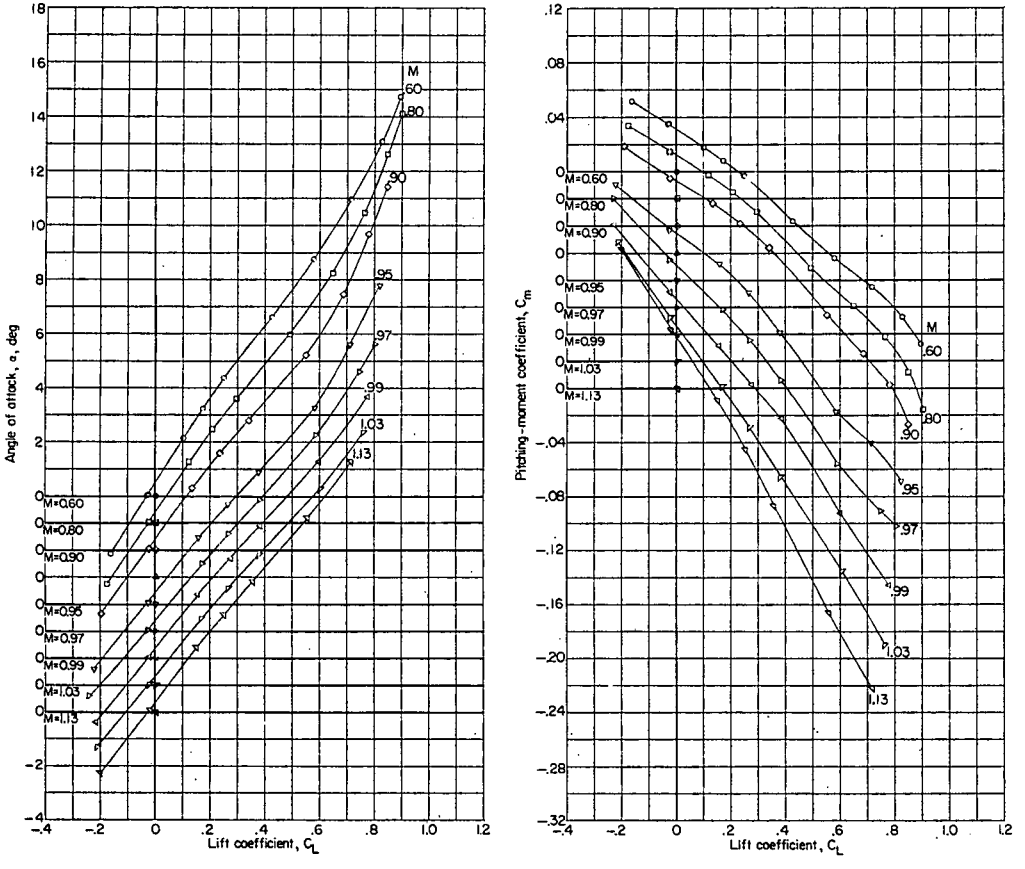

(a) Angle of attack and pitching-moment coefficient.

Figure 35.- Variation of aerodynamic characteristics with either lift coefficient or angle of attack. Configuration 29; complete model plus ventral fin and plus modified vertical tail; $i_t = -3^\circ$; $\beta = -2.2^\circ$; body with afterbody bump; undrooped supersonic inlet (cruise condition).

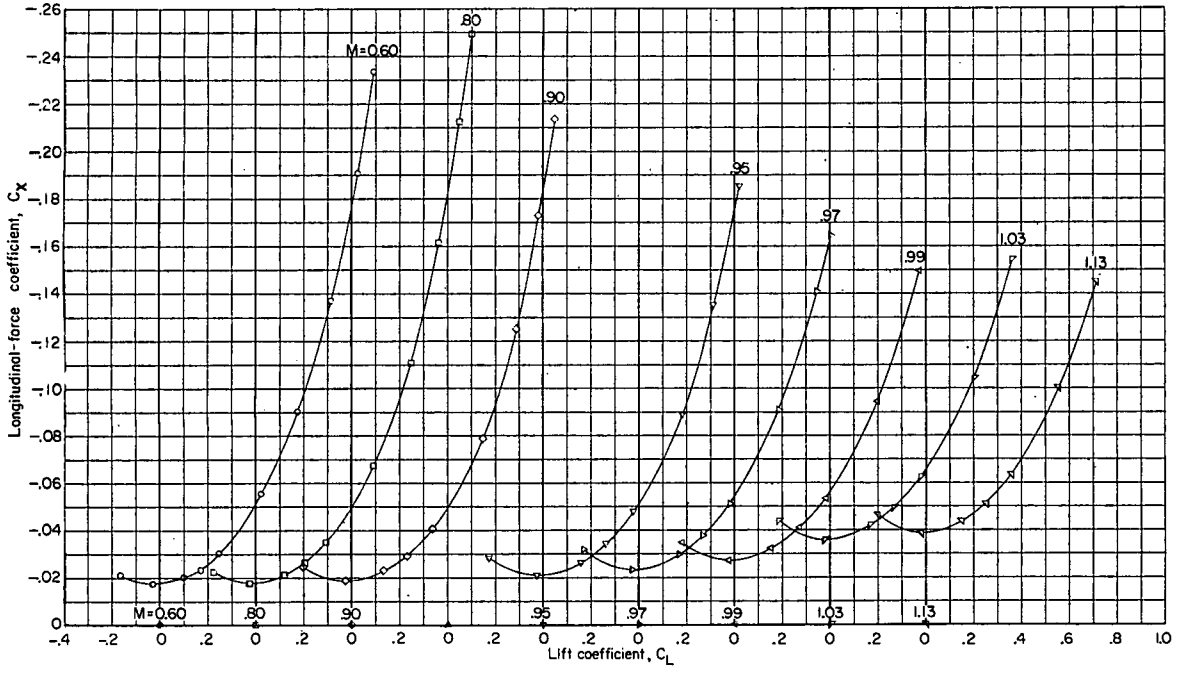

(b) Longitudinal-force coefficient.

Figure 35.- Continued.

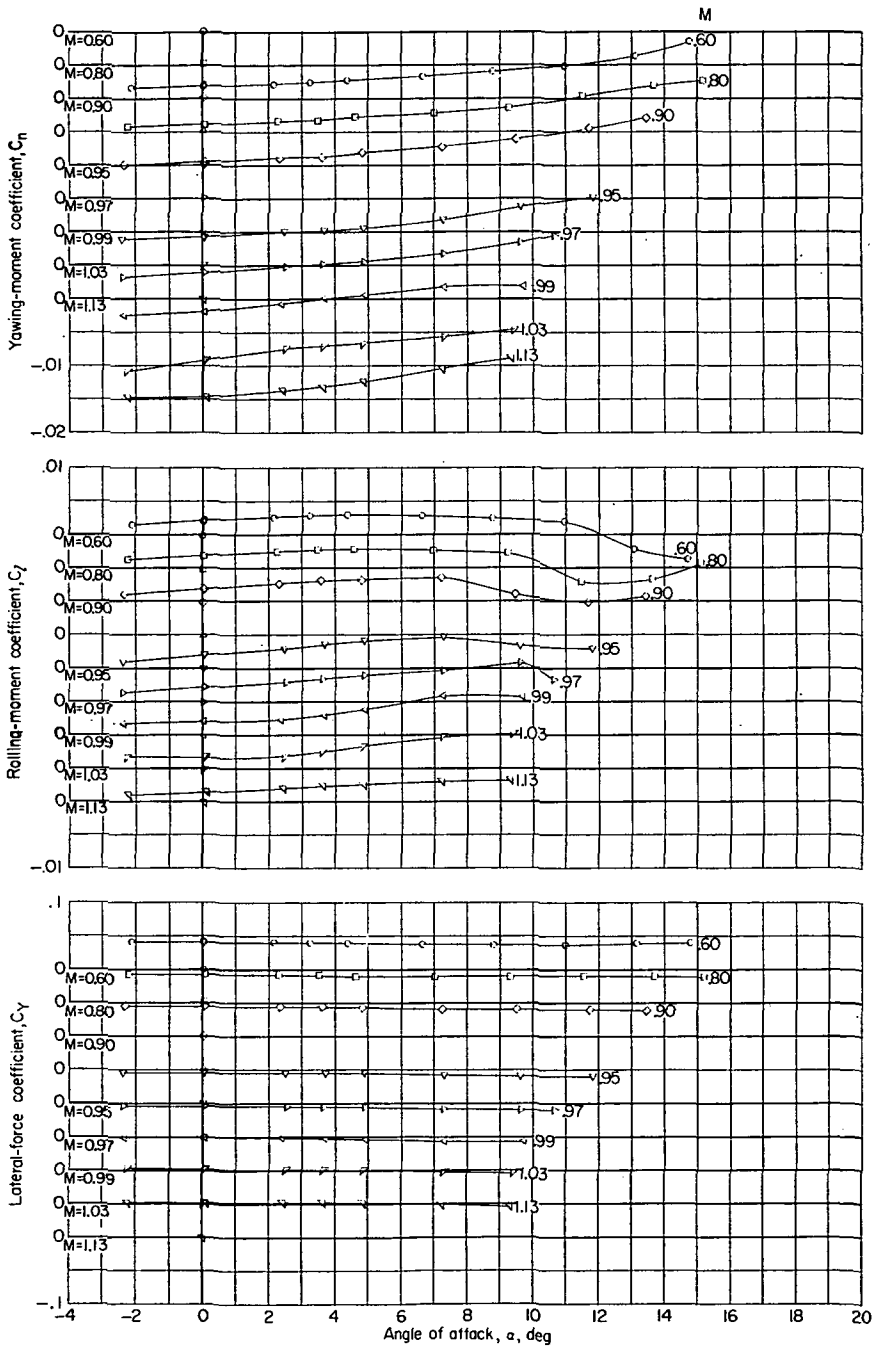

(c) Yawing-moment, rolling-moment, and lateral-force coefficients.

Figure 35.- Concluded.

[redacted]

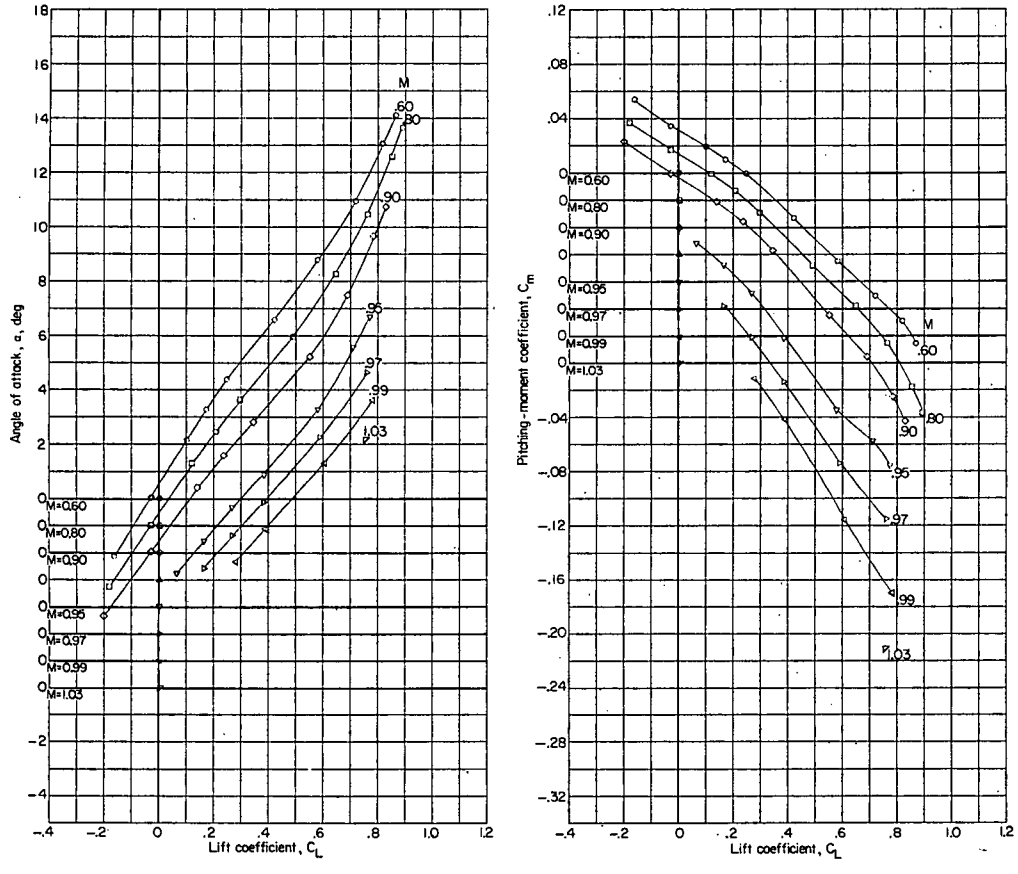

(a) Angle of attack and pitching-moment coefficient.

Figure 36.- Variation of aerodynamic characteristics with either lift coefficient or angle of attack. Configuration 30; complete model plus ventral fin and plus modified vertical tail; $i_t = -3^\circ$; $\beta = -5.4^\circ$; body with afterbody bump; undrooped supersonic inlet (cruise condition).

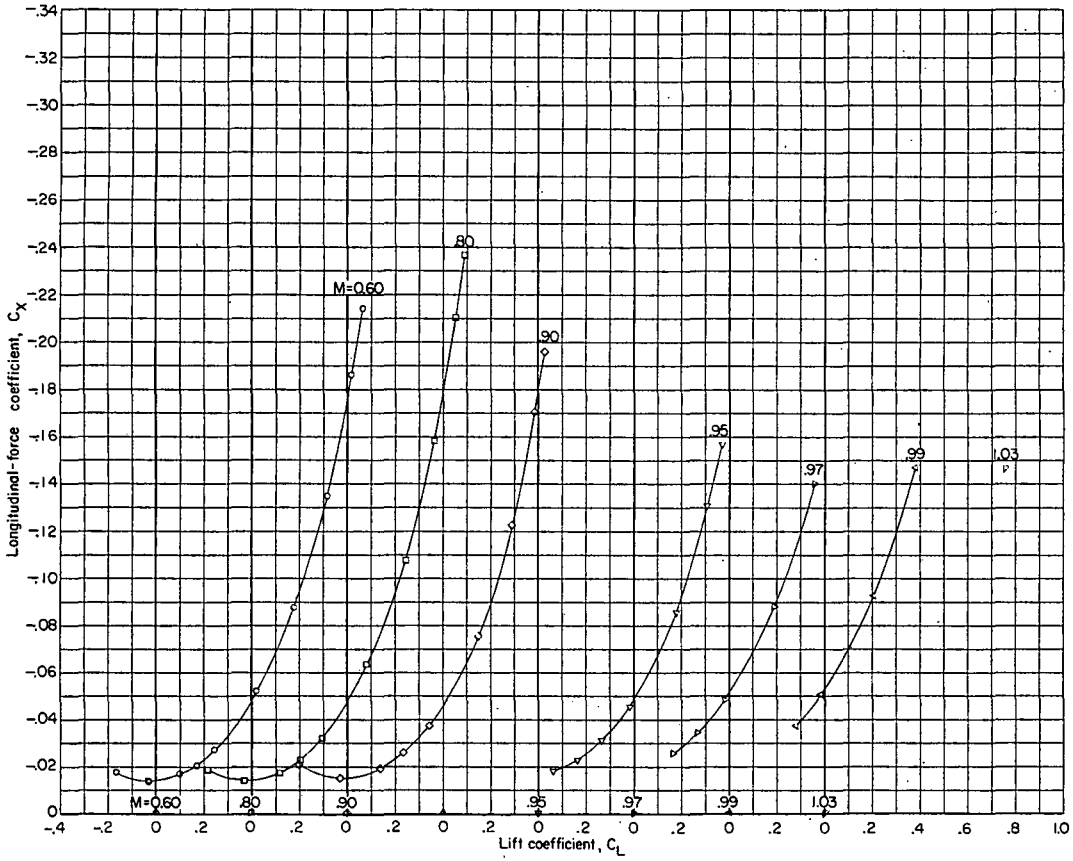

(b) Longitudinal-force coefficient.

Figure 36.- Continued.

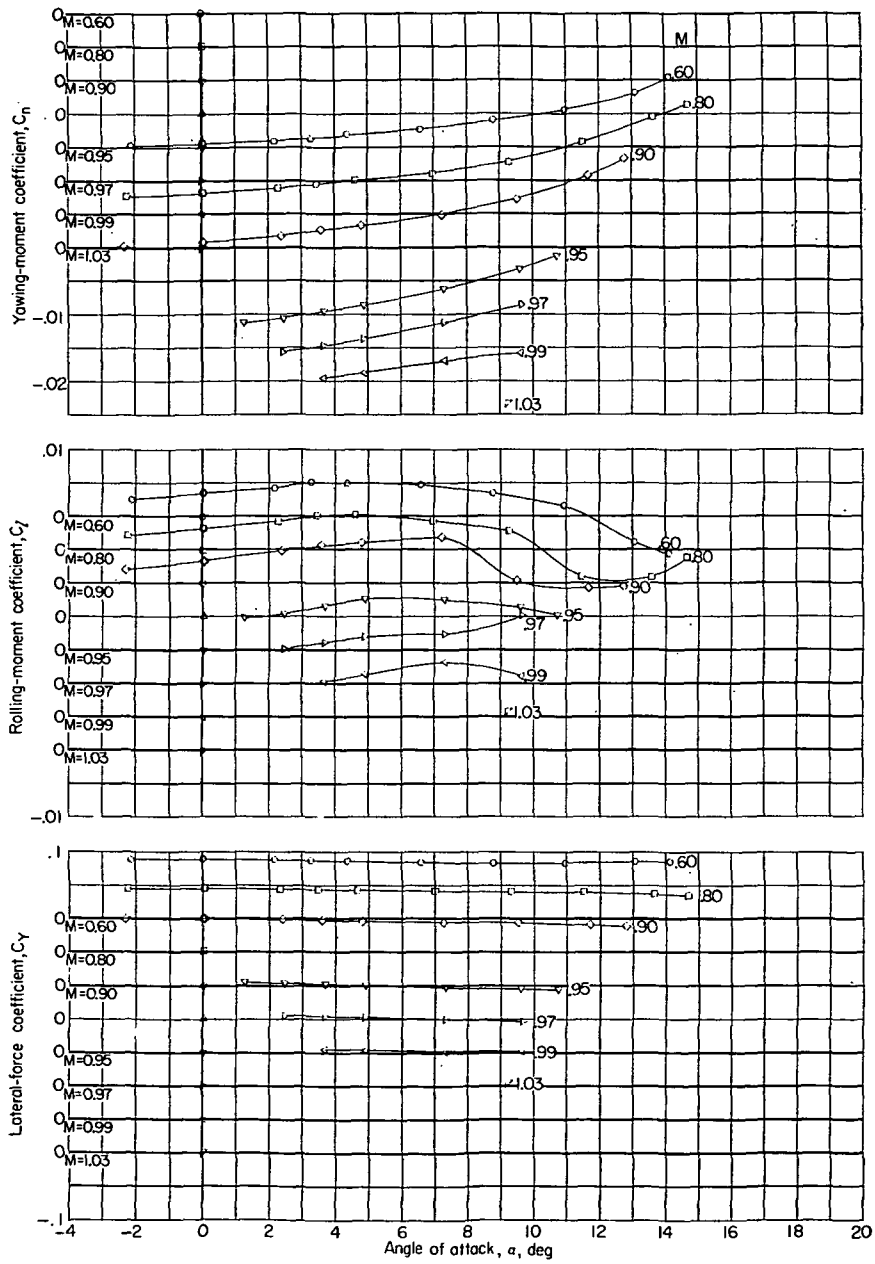

(c) Yawing-moment, rolling-moment, and lateral-force coefficients.

Figure 36.- Concluded.

[redacted]

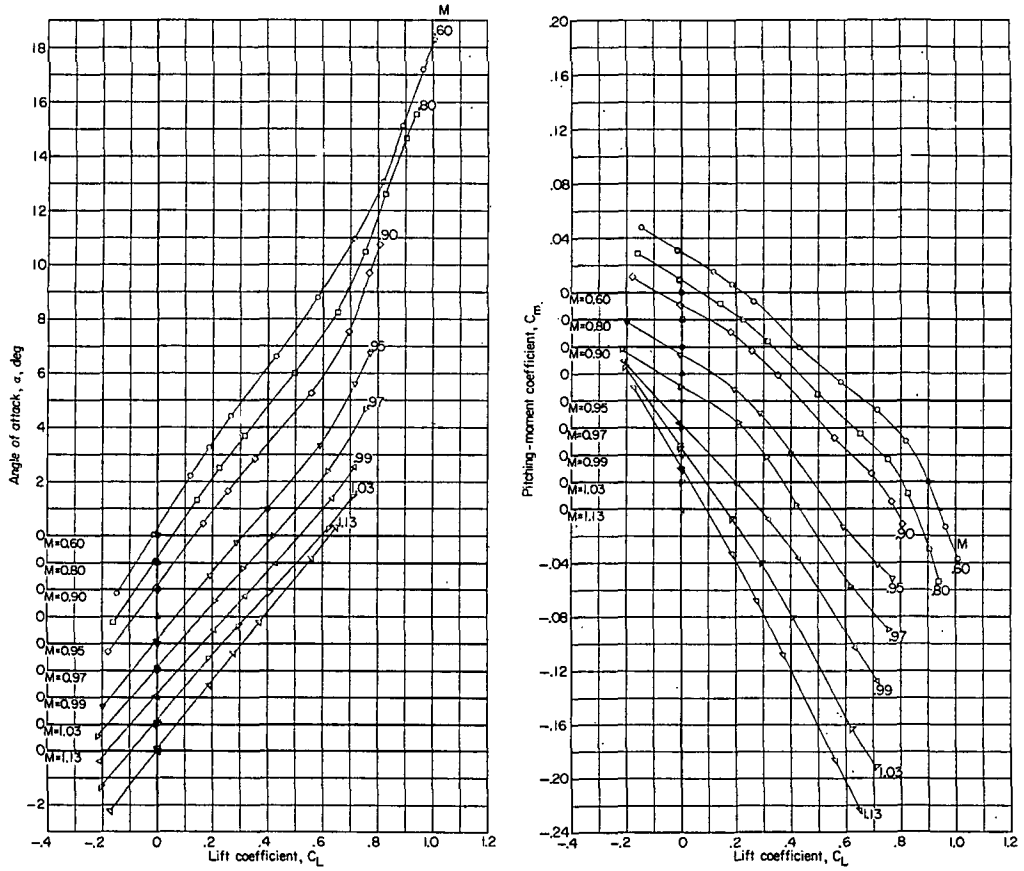

(a) Angle of attack and pitching-moment coefficient.

Figure 37.- Variation of aerodynamic characteristics with lift coefficient. Configuration 31; complete model with blocked inlet; i_t = -3°; body with afterbody bump; undrooped supersonic inlet (cruise condition).

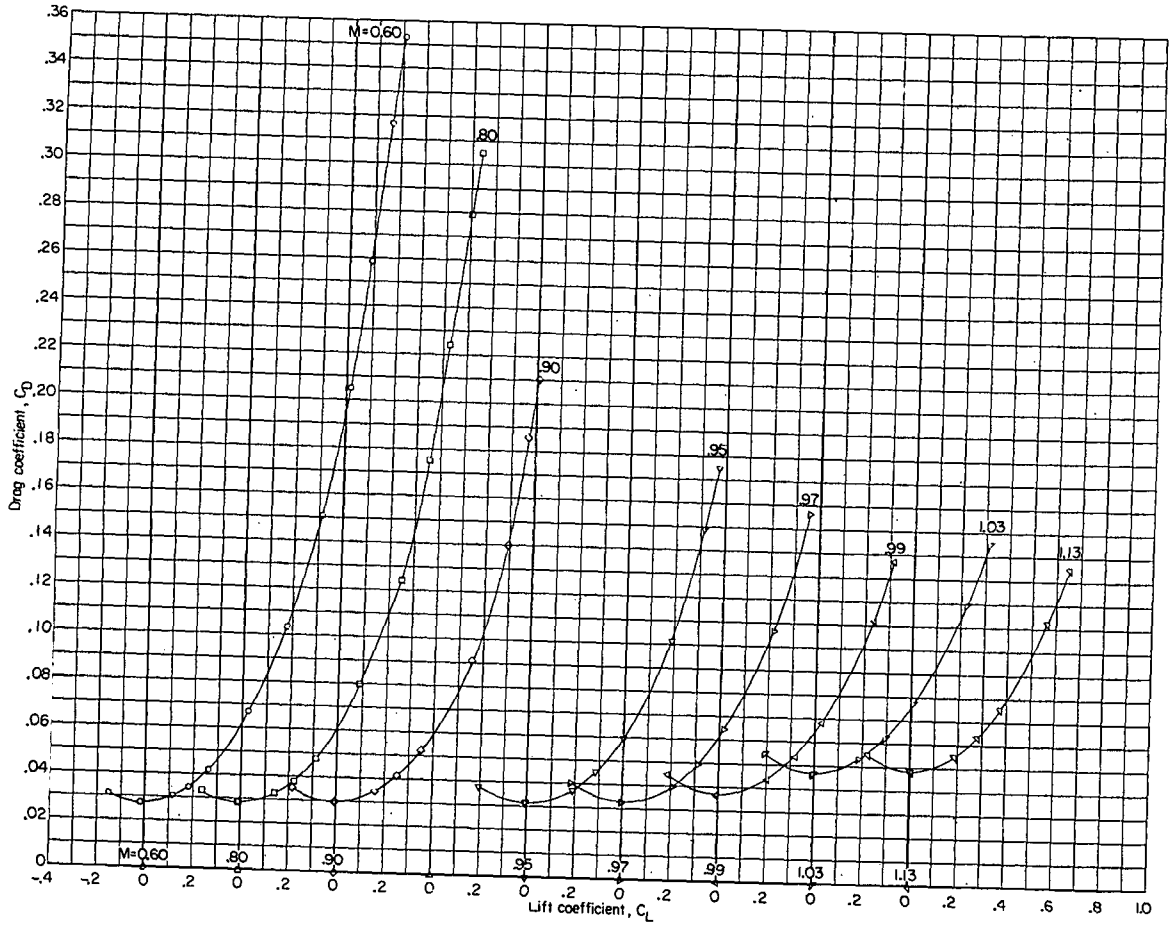

(b) Drag coefficient.

Figure 37.- Concluded.

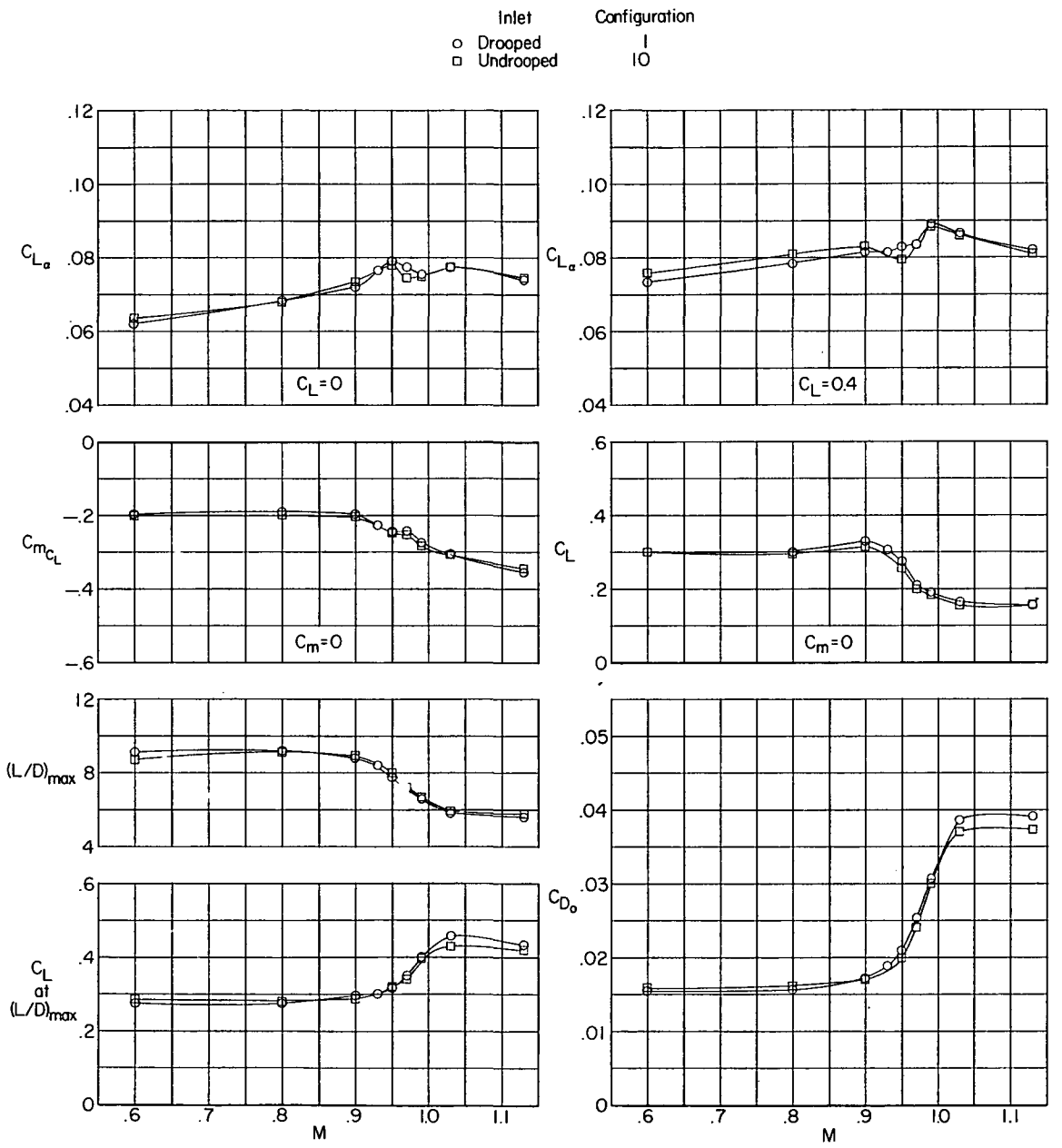

(a) $\delta_n = 0^o$.

Figure 38.- Effect of inlet droop on longitudinal aerodynamic characteristics. Complete model; $i_t = -3^o$; supersonic inlet (cruise condition).

[redacted]

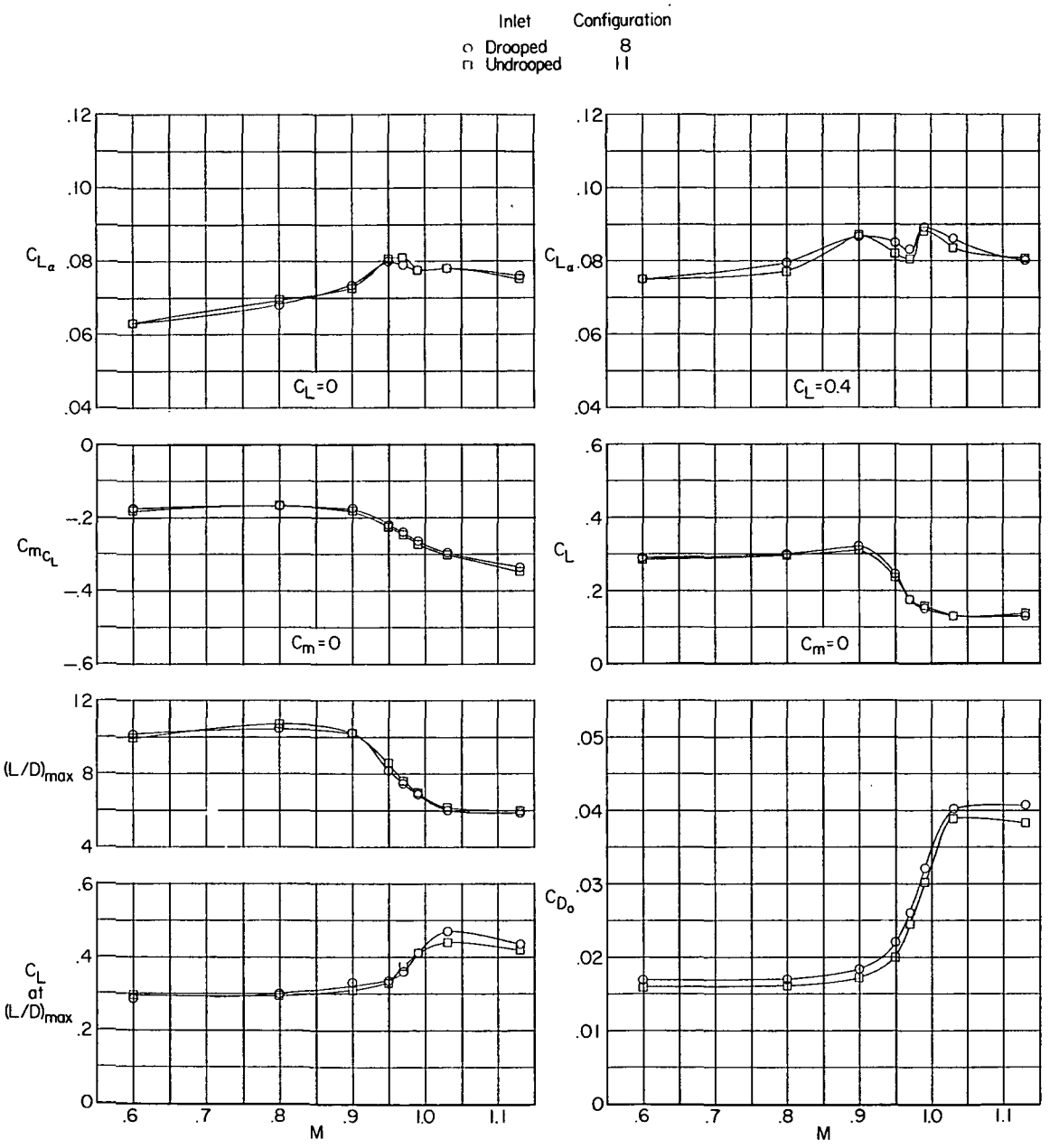

(b) $\delta_n = -7.5^\circ$.

Figure 38.- Concluded.

[redacted]

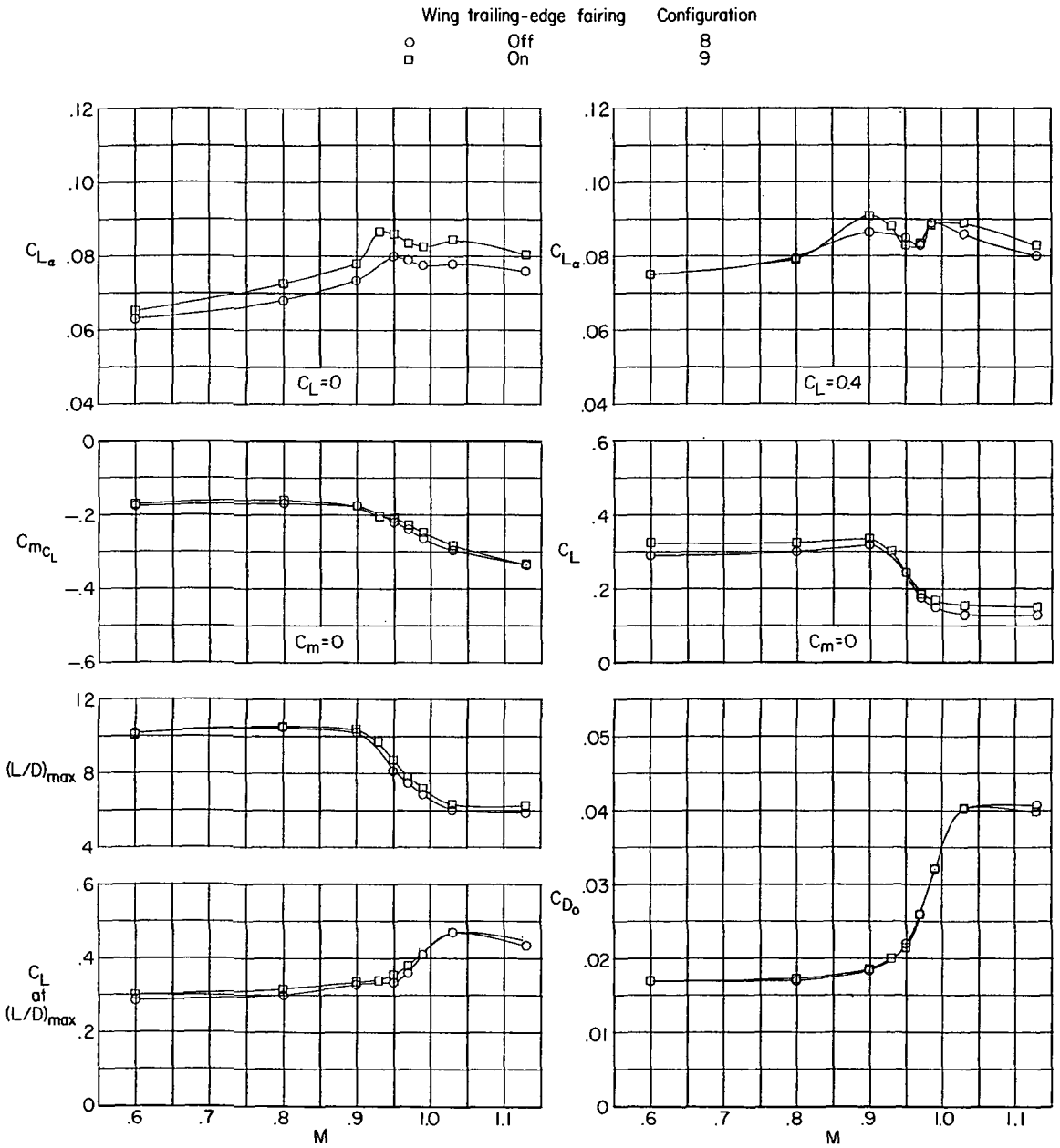

Figure 39.- Effect of wing trailing-edge fairing on longitudinal aerodynamic characteristics. Complete model; $i_t = -3^\circ$; $\delta_n = -7.5^\circ$; drooped supersonic inlet (cruise conditions).

[redacted]

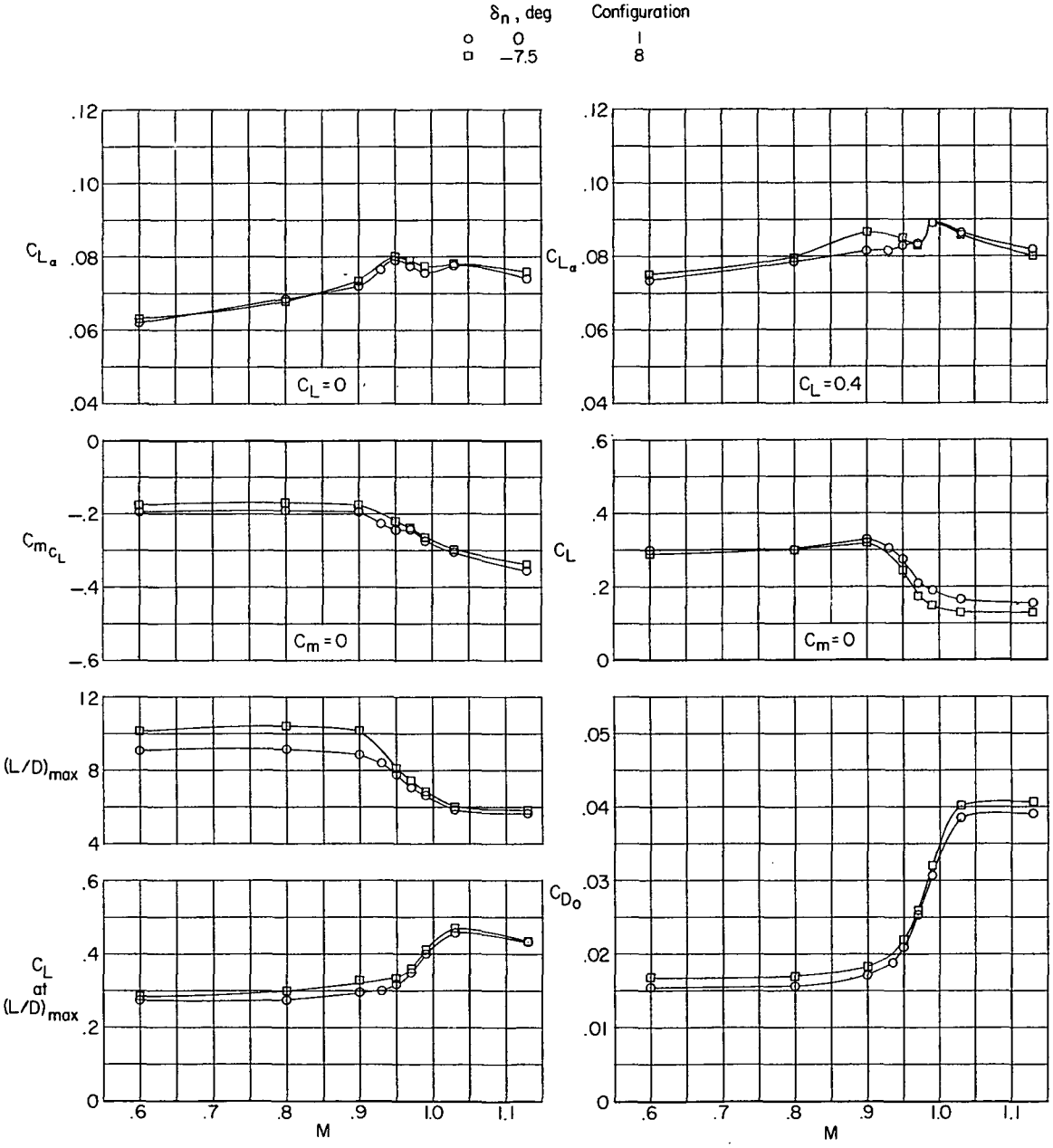

(a) Drooped inlet.

Figure 40.- Effect of deflection of wing leading-edge flap on longitudinal aerodynamic characteristics. Complete model; $i_t = -3^o$; supersonic inlet (cruise condition).

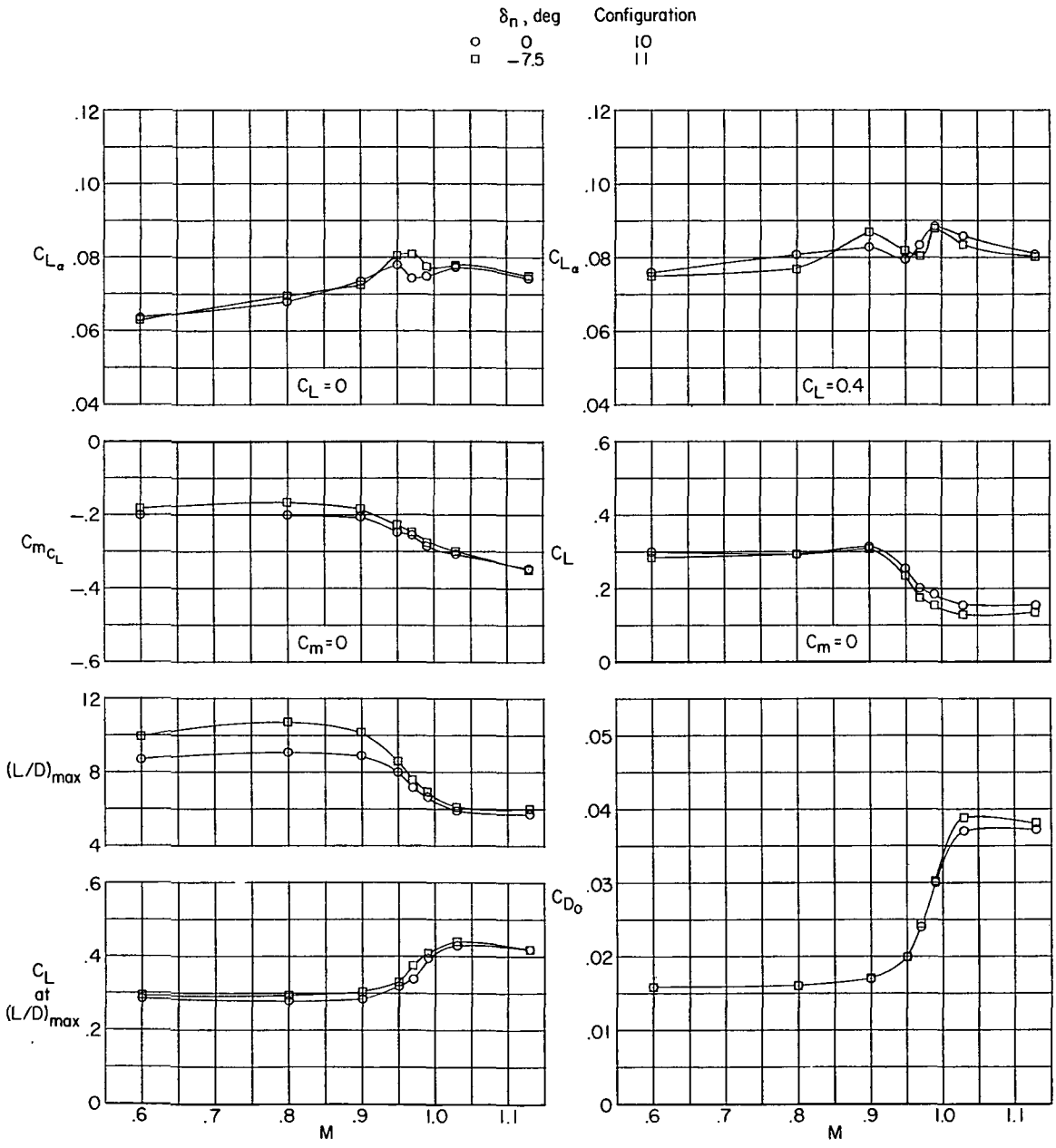

(b) Undrooped inlet.

Figure 40.- Continued.

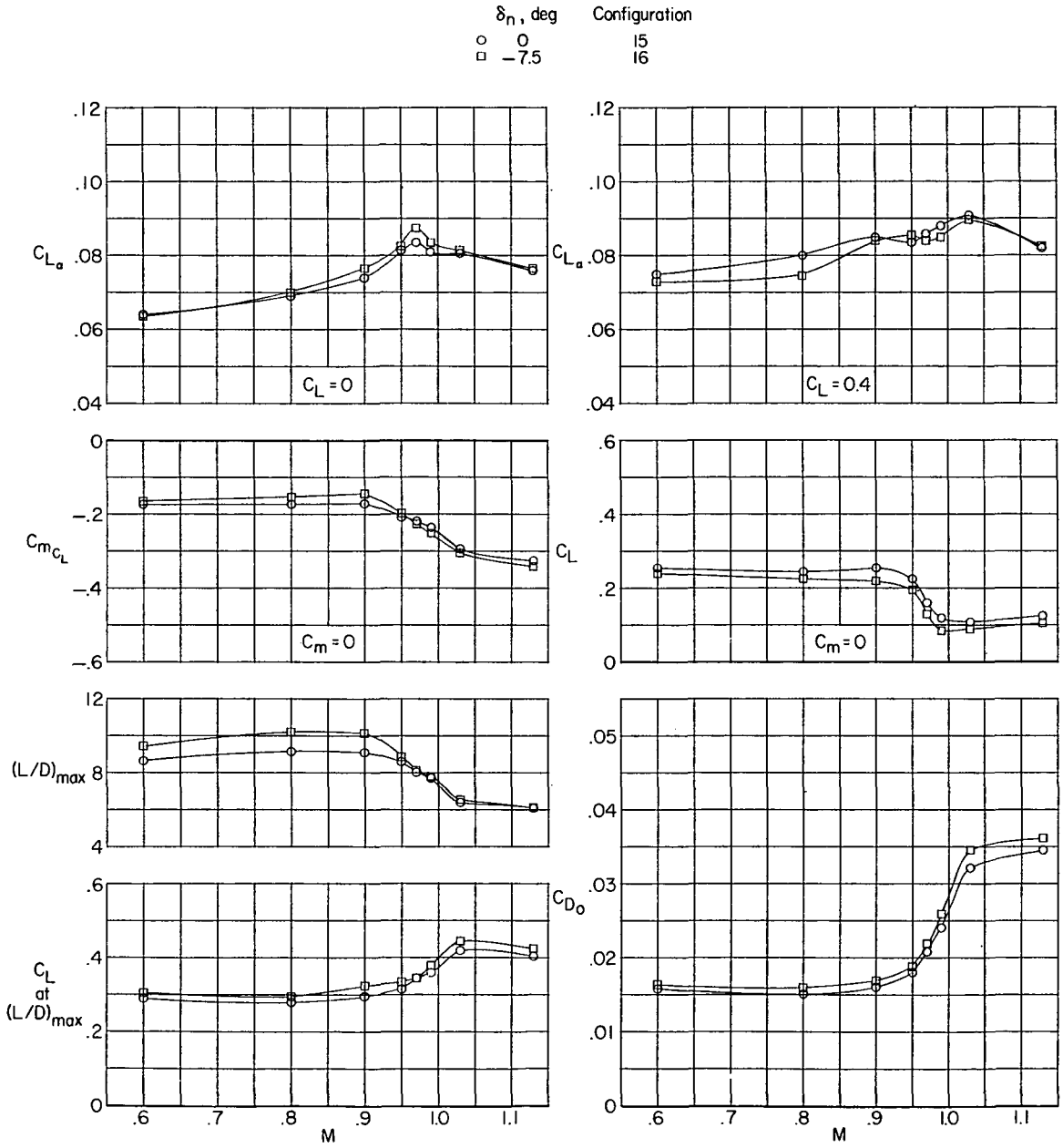

(c) Undrooped inlet; body with afterbody bump.

Figure 40.- Continued.

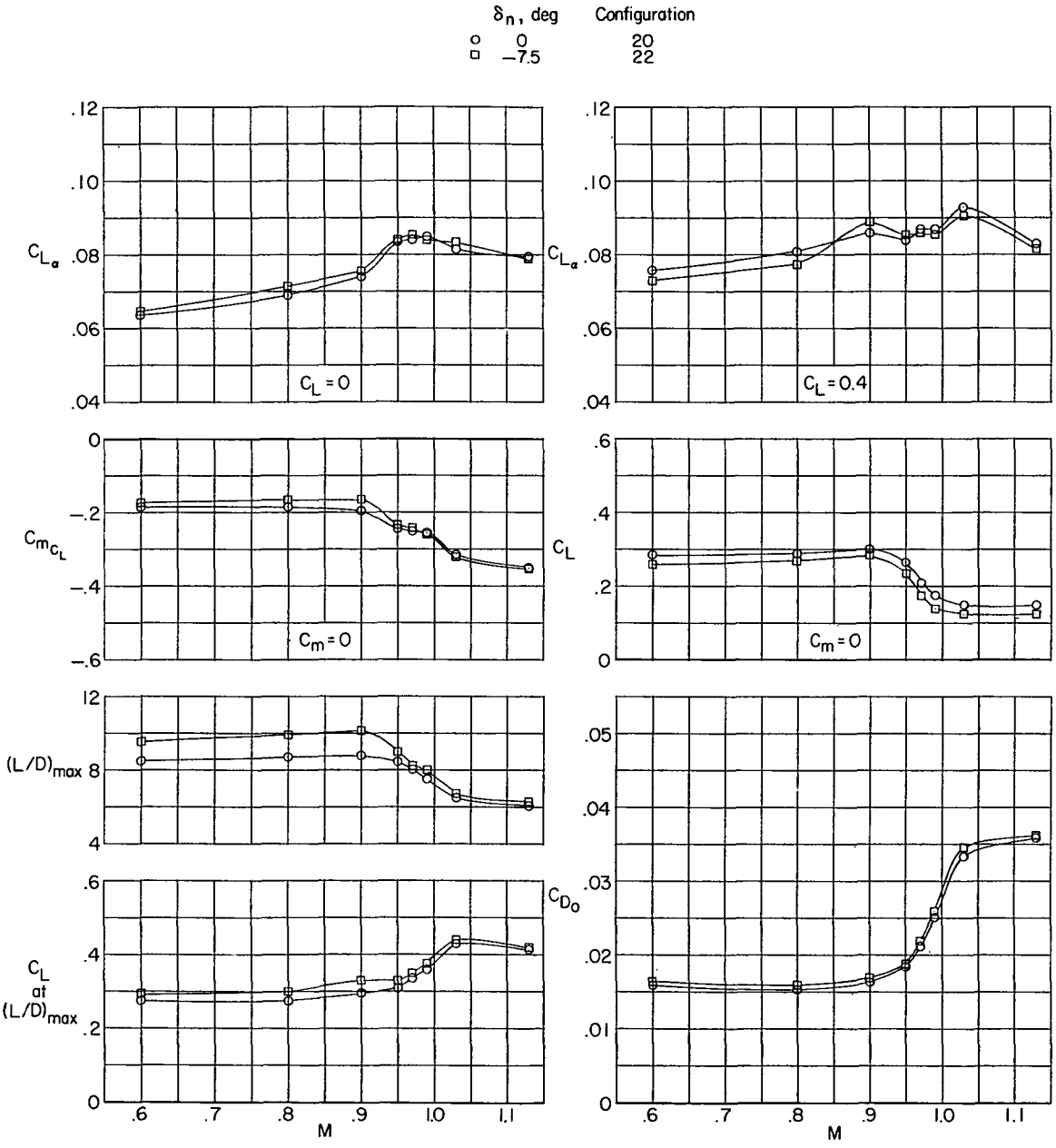

(d) Undrooped inlet; body with afterbody bump; $\delta_{tr} = -12.2^o$.

Figure 40.- Concluded.

[redacted]

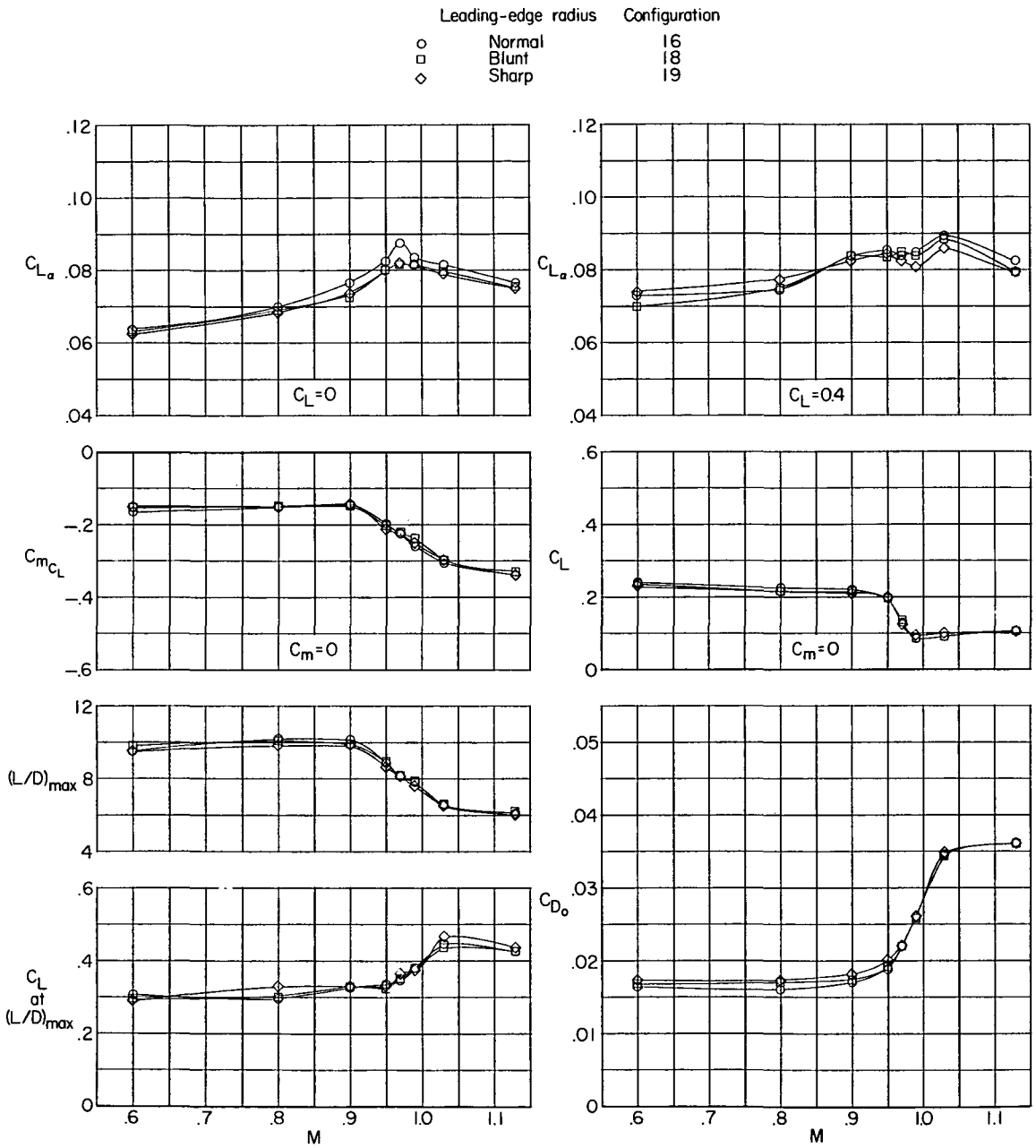

Figure 41.- Effect of leading-edge radius of leading-edge flap on longitudinal aerodynamic characteristics. Complete model; $i_t = -3^\circ$; $\delta_n = -7.5^\circ$; body with afterbody bump; undrooped supersonic inlet (cruise condition).

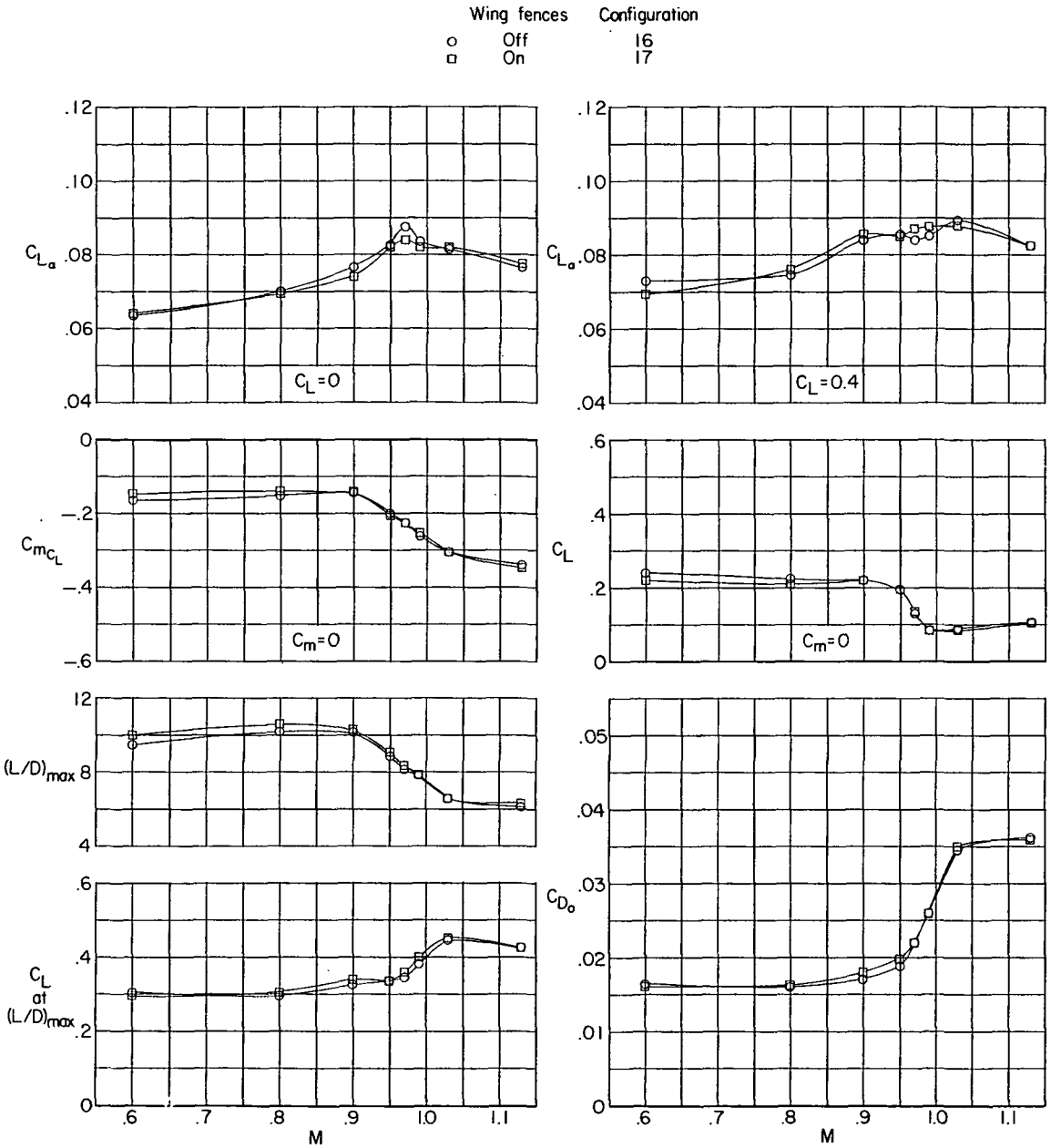

Figure 42.- Effect of wing fences on longitudinal aerodynamic characteristics. Complete model; $i_t = -3^\circ$; $\delta_n = -7.5^\circ$; body with afterbody bump; undrooped supersonic inlet (cruise condition).

[redacted]

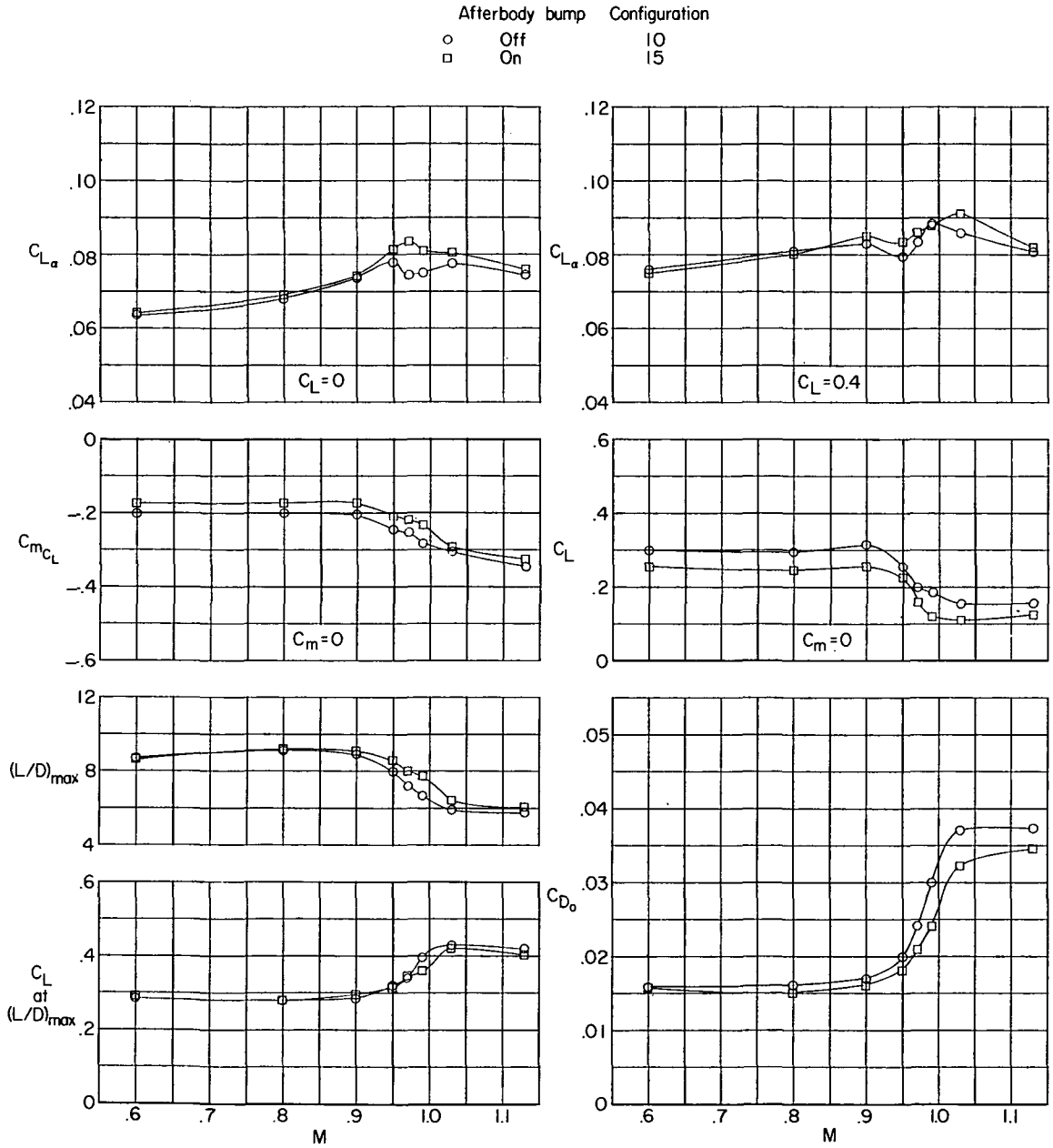

(a) $\delta_n = 0^o$.

Figure 43.- Effect of afterbody bump on longitudinal aerodynamic characteristics. Complete model; $i_t = -3^o$; undrooped supersonic inlet (cruise condition).

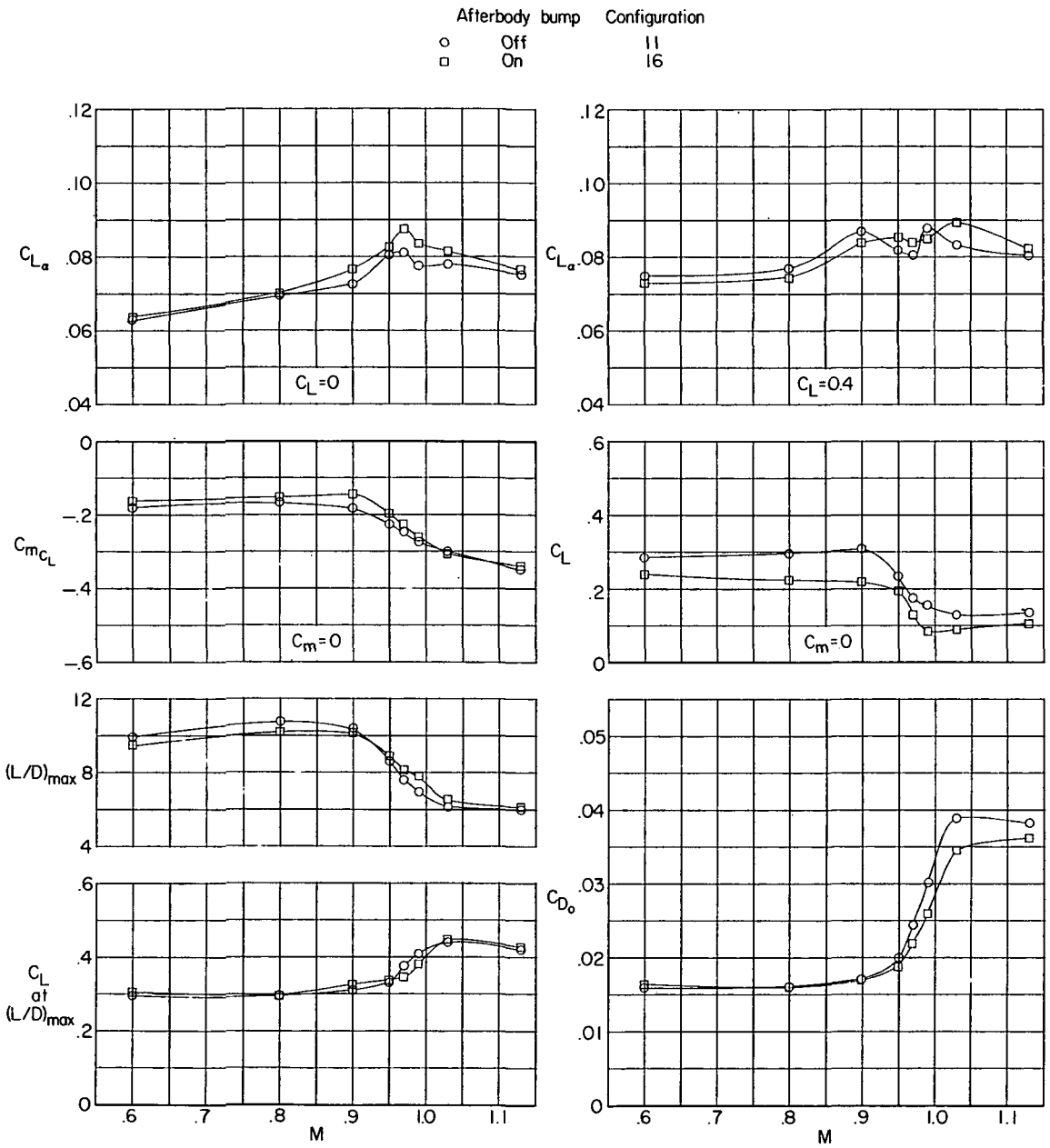

(b) $\delta_n = -7.5°$.

Figure 43.- Concluded.

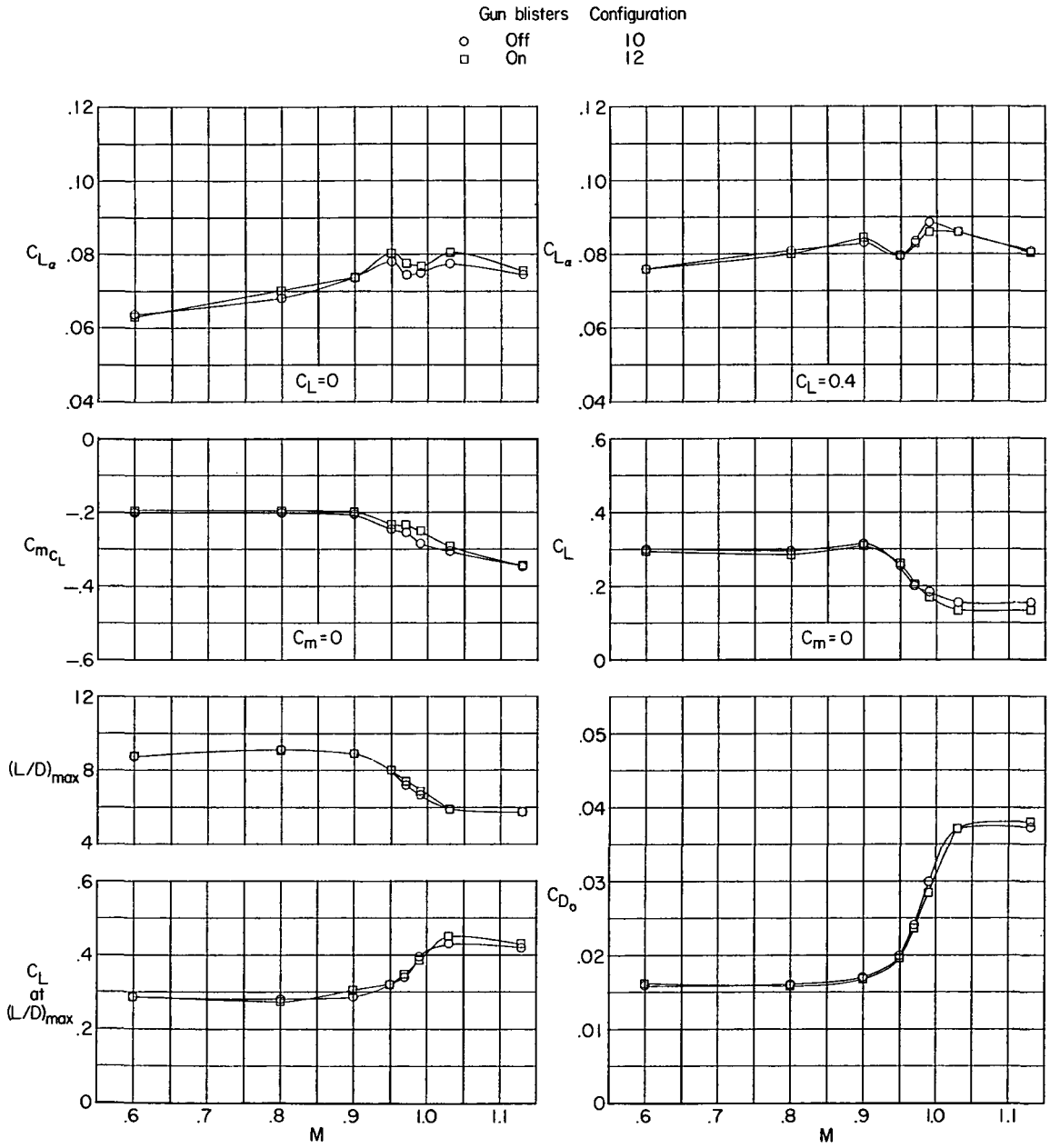

Figure 44.- Effect of gun blisters on longitudinal aerodynamic characteristics. Complete model; $i_t = -3^\circ$; undrooped supersonic inlet (cruise condition).

[redacted]

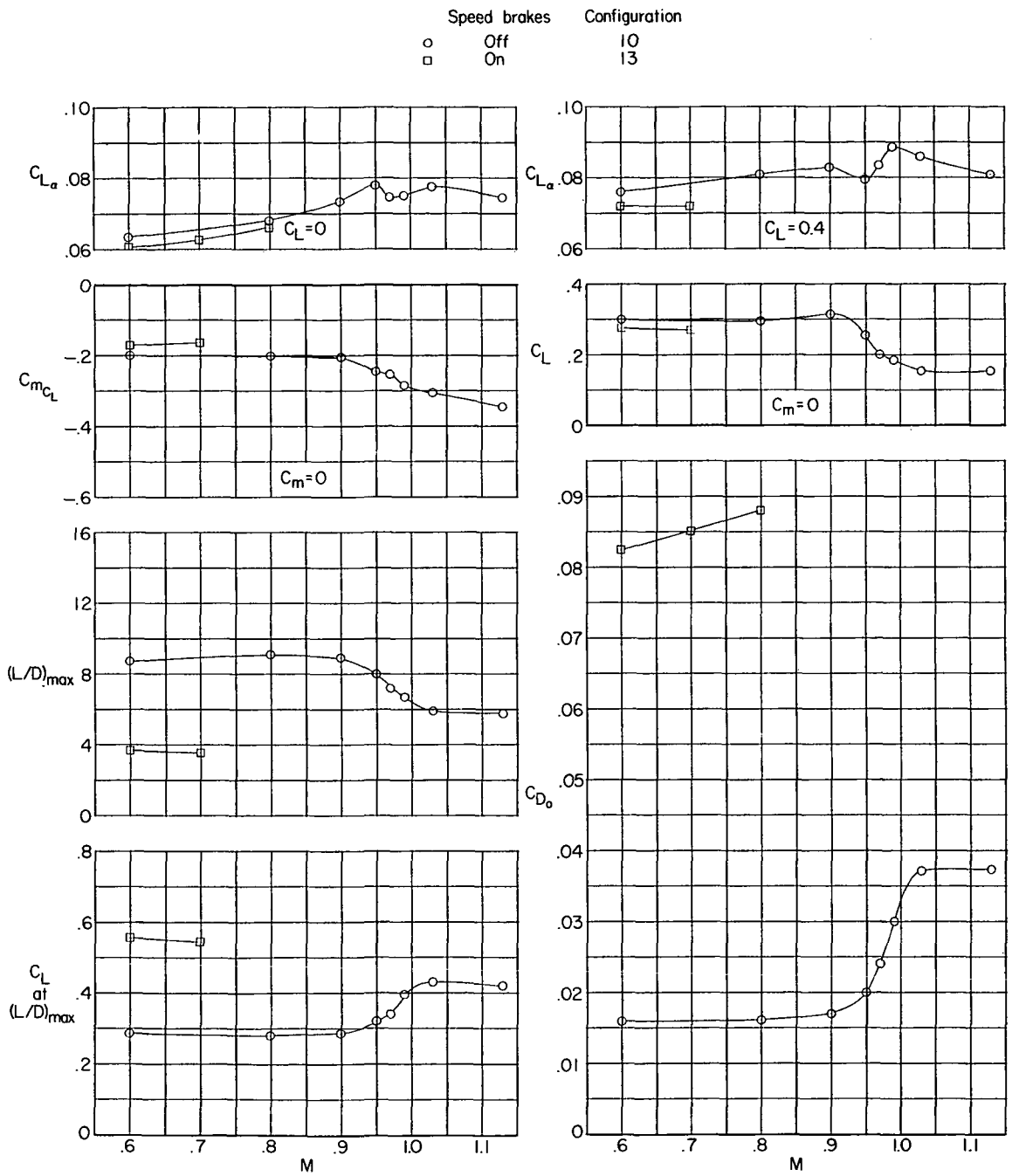

(a) C_{L_α}, $C_{m_{C_L}}$, $(L/D)_{max}$, and C_{D_o} characteristics; $i_t = -3^\circ$.

Figure 45.- Effect of 50°-deflected speed brakes on longitudinal aerodynamic characteristics. Complete model; undrooped supersonic inlet (cruise condition).

[redacted]

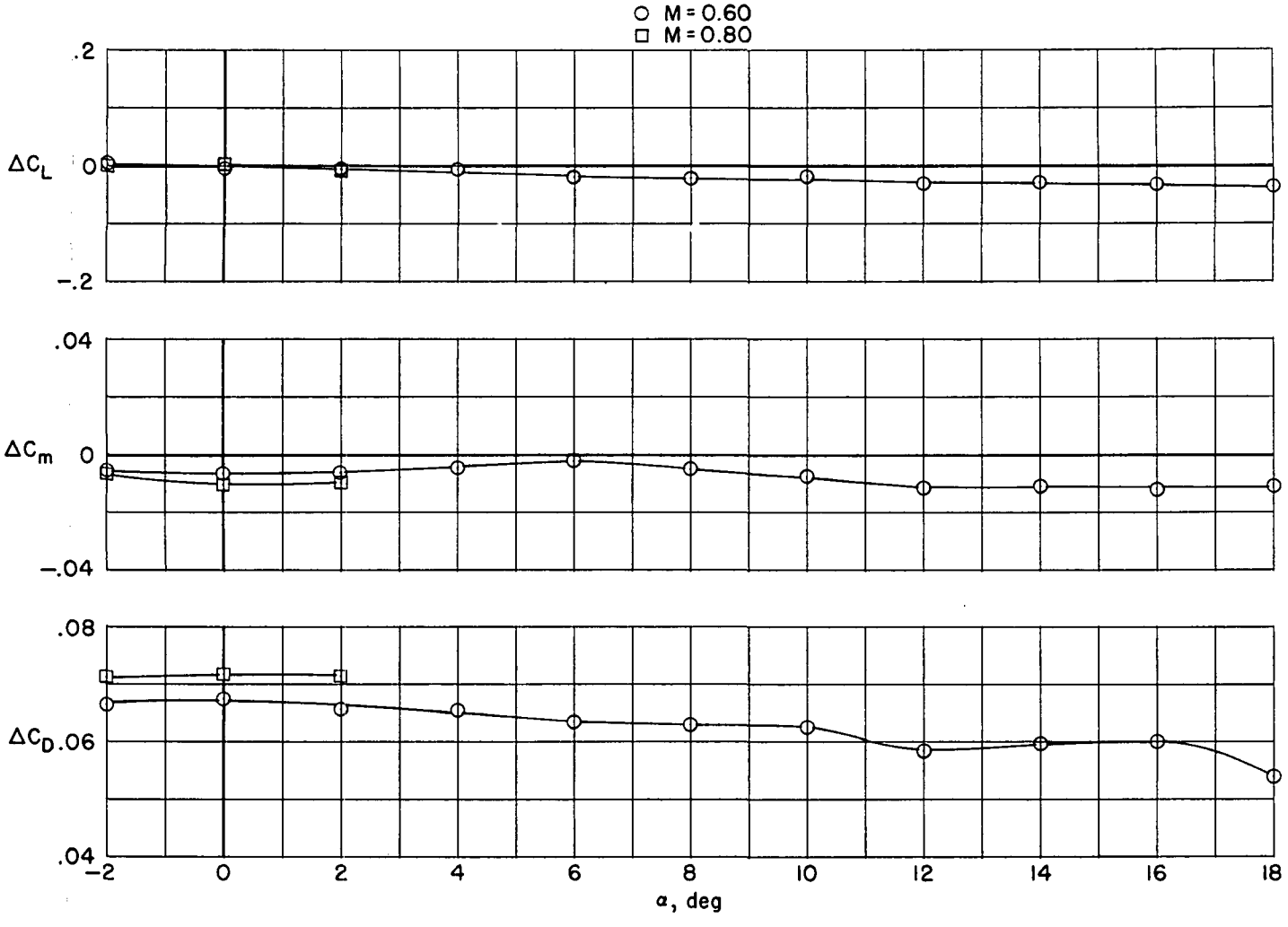

(b) ΔC_L, ΔC_m, and ΔC_D due to 50°-deflected speed brakes; i_t = -3°.

Figure 45.- Continued.

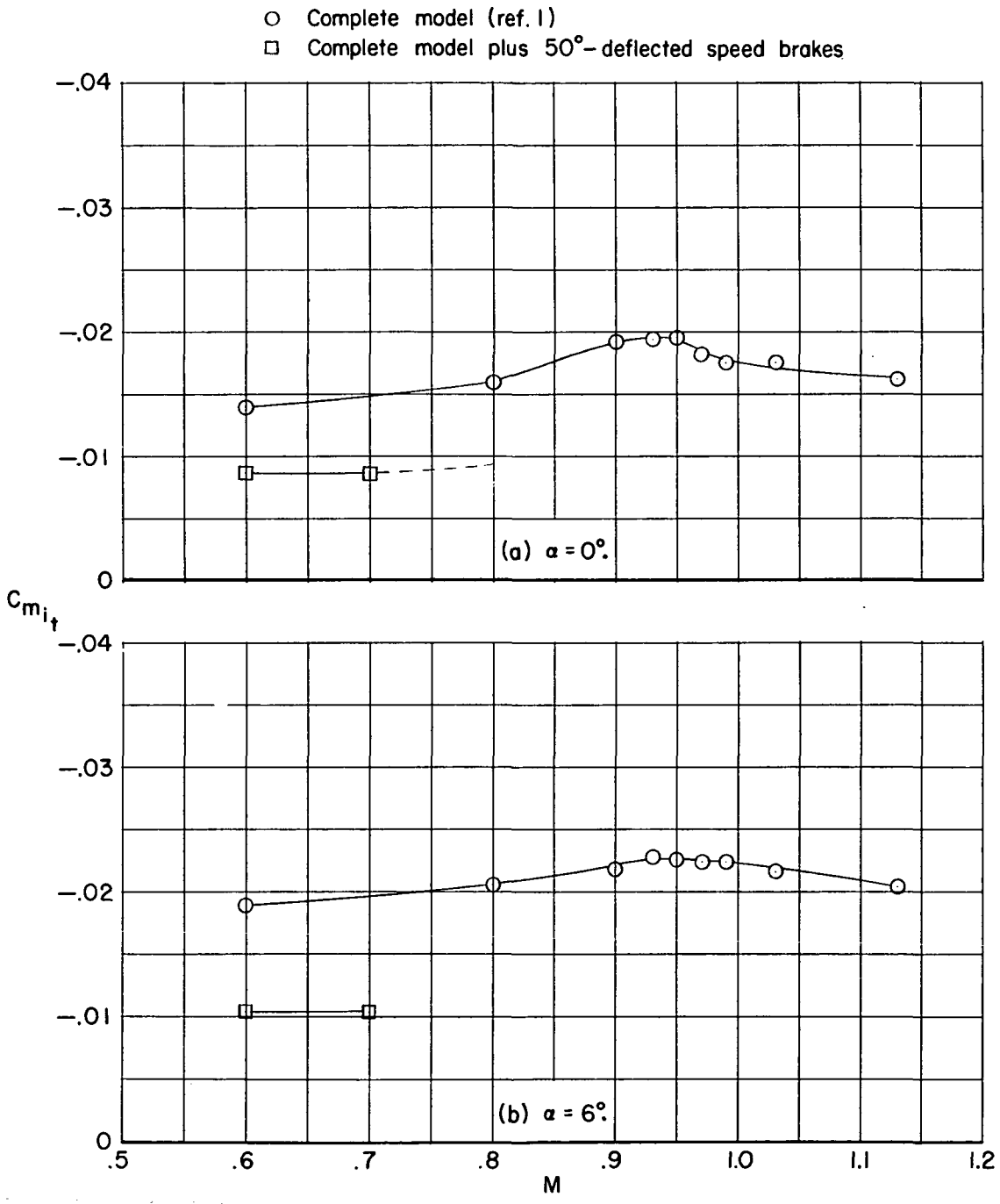

(c) Horizontal-tail effectiveness.

Figure 45.- Concluded.

[redacted]

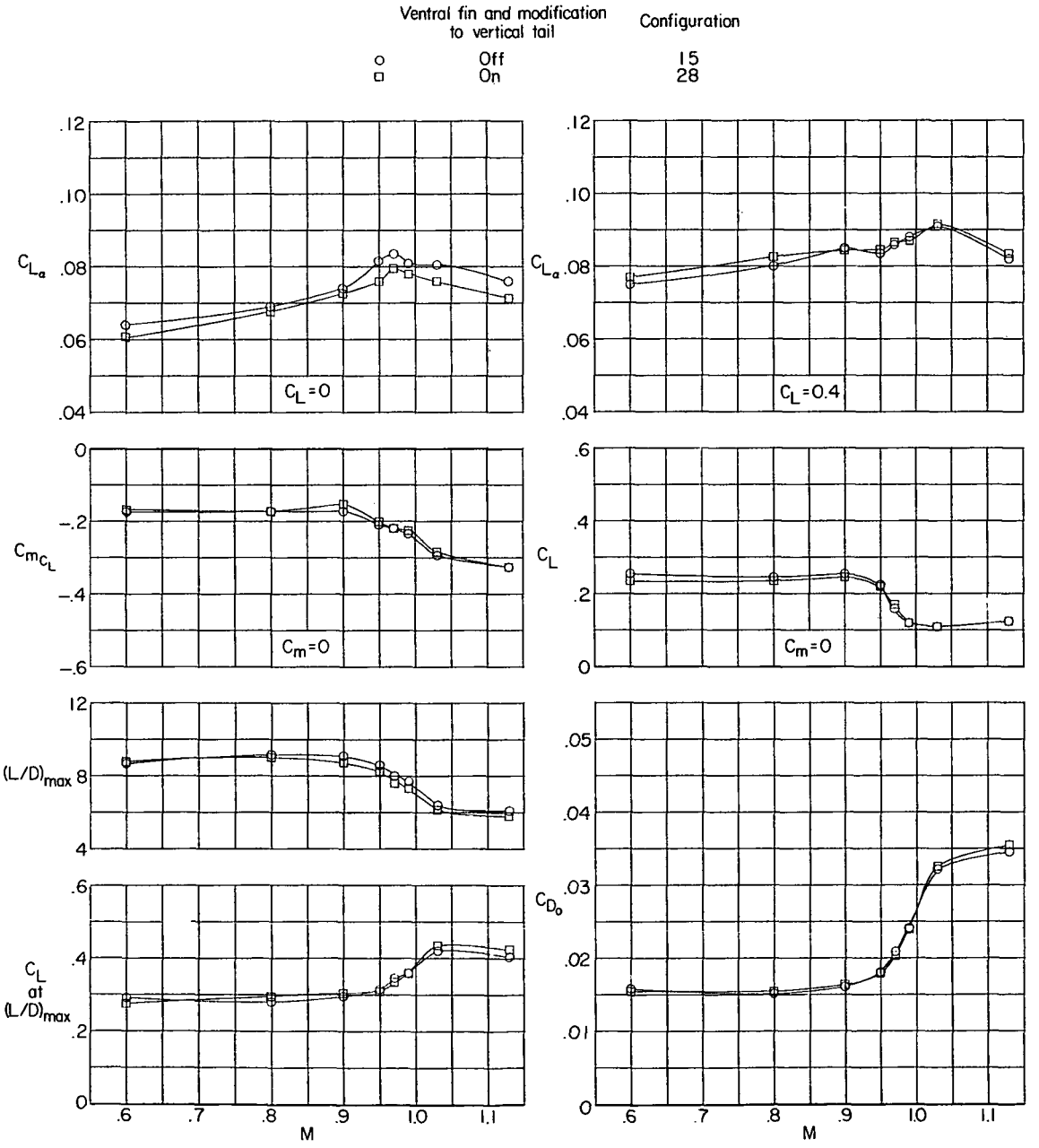

Figure 46.- Effect of ventral fin and modified vertical tail on longitudinal aerodynamic characteristics. Complete model; $i_t = -3^o$; body with afterbody bump; undrooped supersonic inlet (cruise condition).

[redacted]

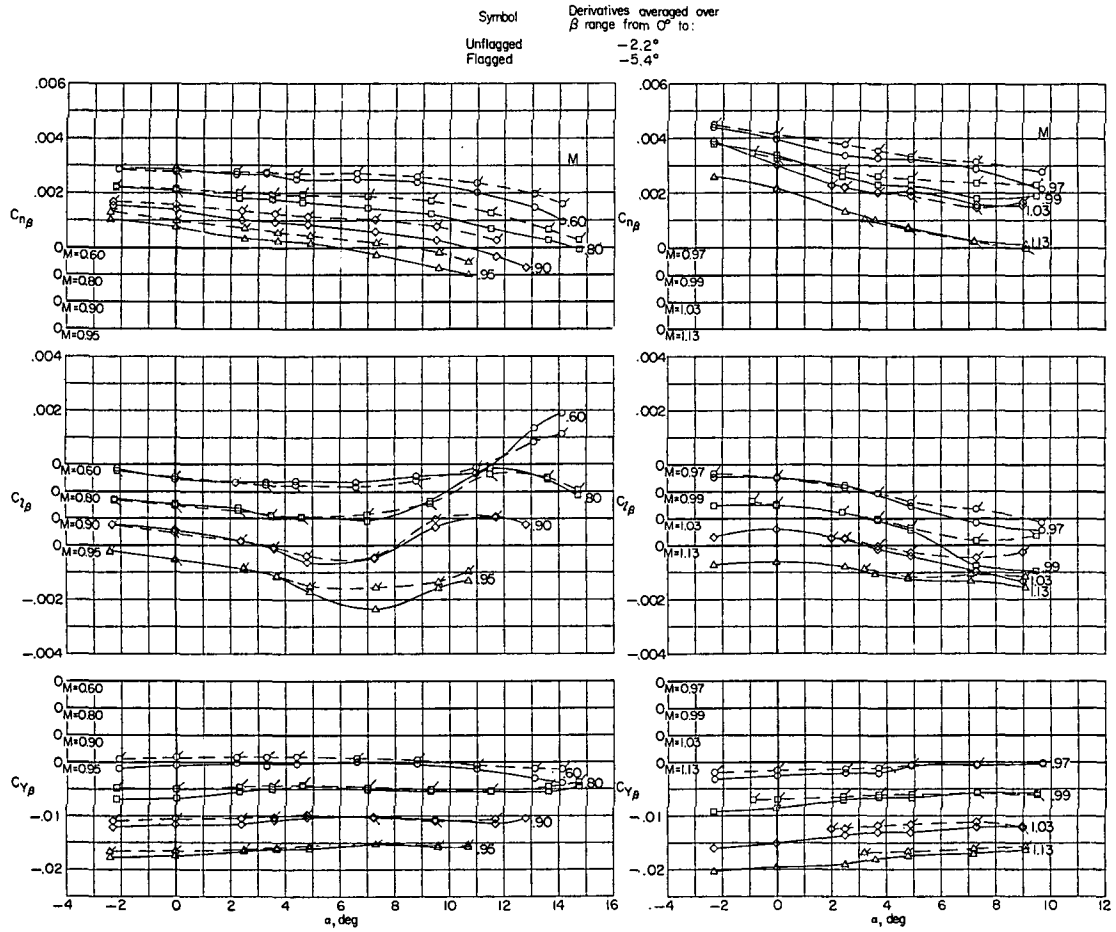

(a) Static lateral-stability derivatives against angle of attack.

Figure 47.- Variation of static lateral-stability derivatives with angle of attack and Mach number. Complete model; $i_t = -3°$; body with afterbody bump; undrooped supersonic inlet (cruise condition).

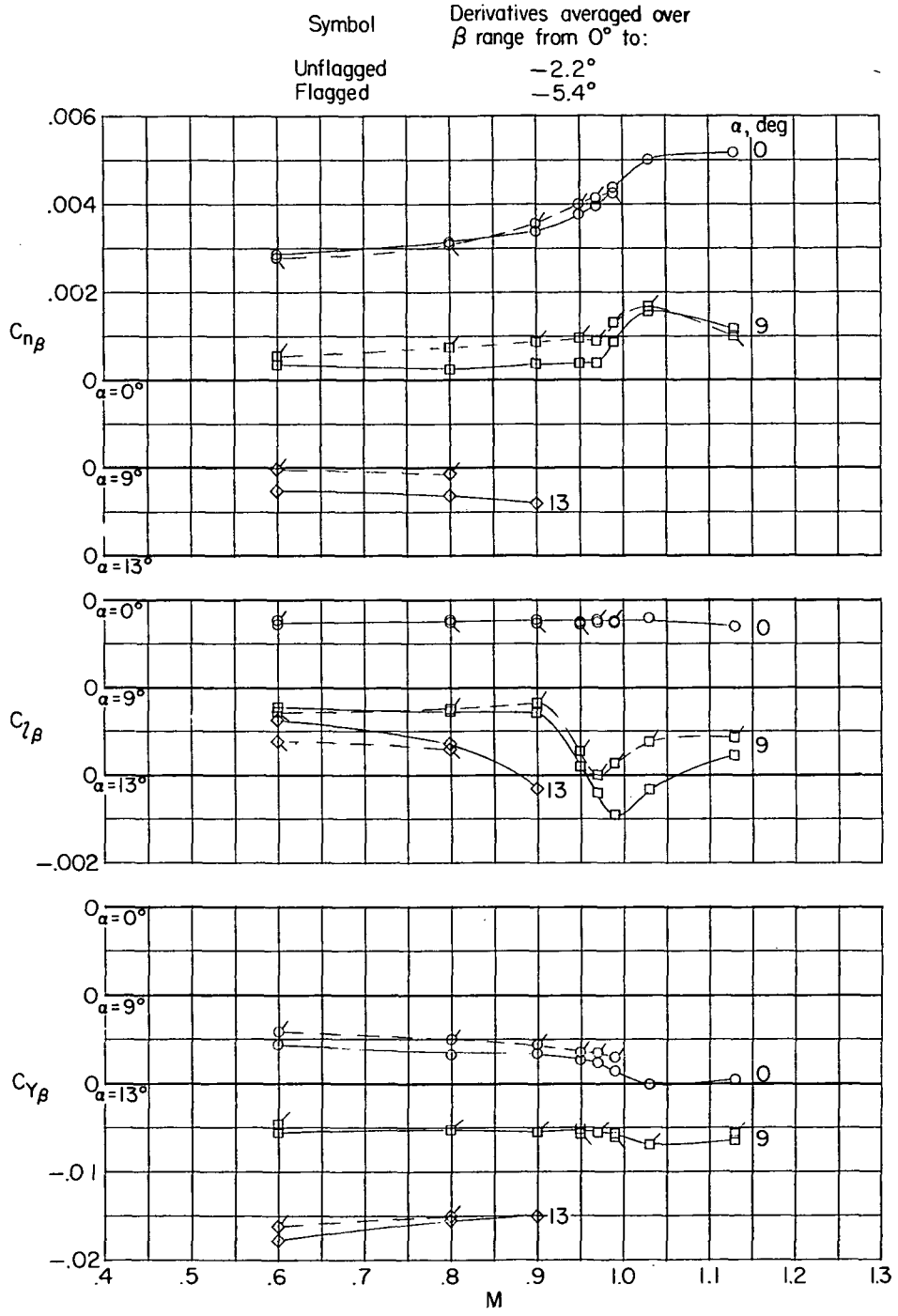

(b) Static lateral-stability derivatives against Mach number.

Figure 47.- Concluded.

[redacted]

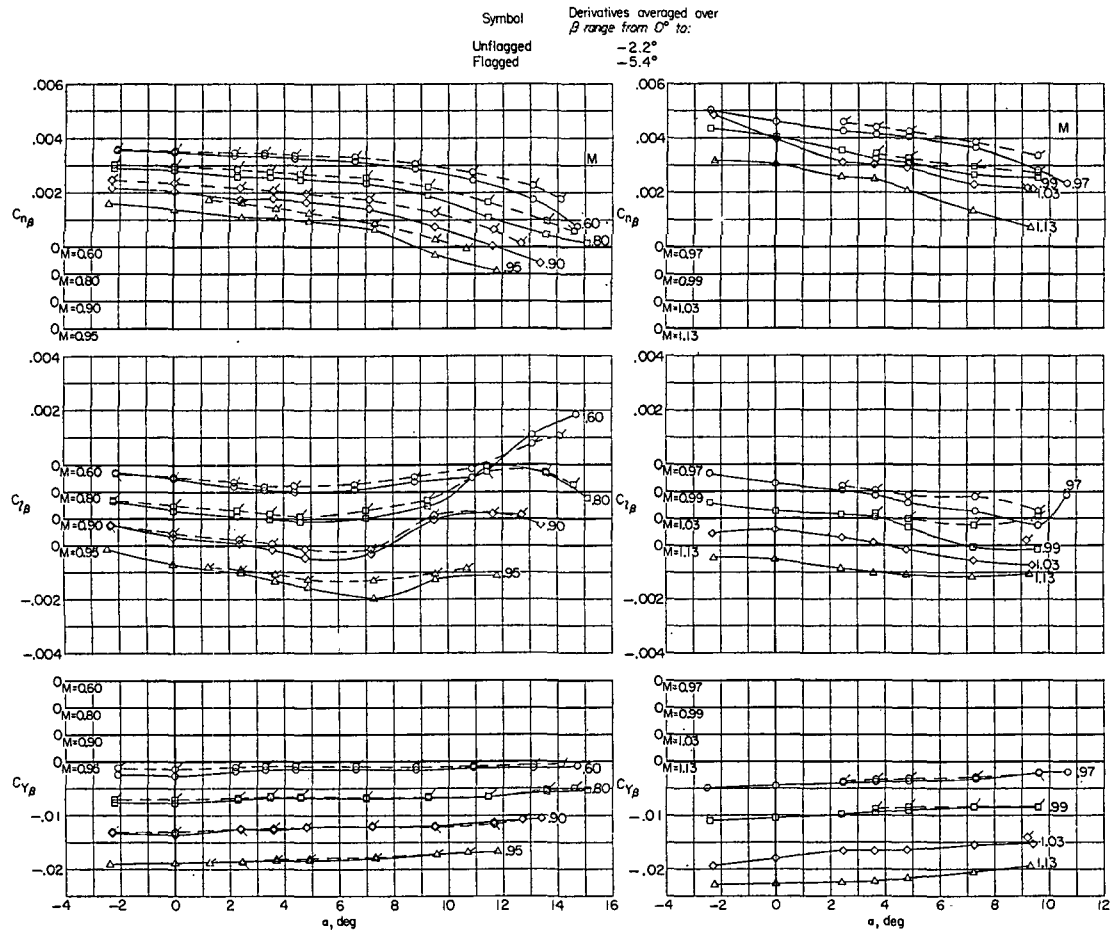

(a) Static lateral-stability derivatives against angle of attack.

Figure 48.- Variation of static lateral-stability derivatives with angle of attack and Mach number. Complete model with ventral fin and modified tail; $i_t = -3^\circ$; body with afterbody bump; undrooped supersonic inlet (cruise condition).

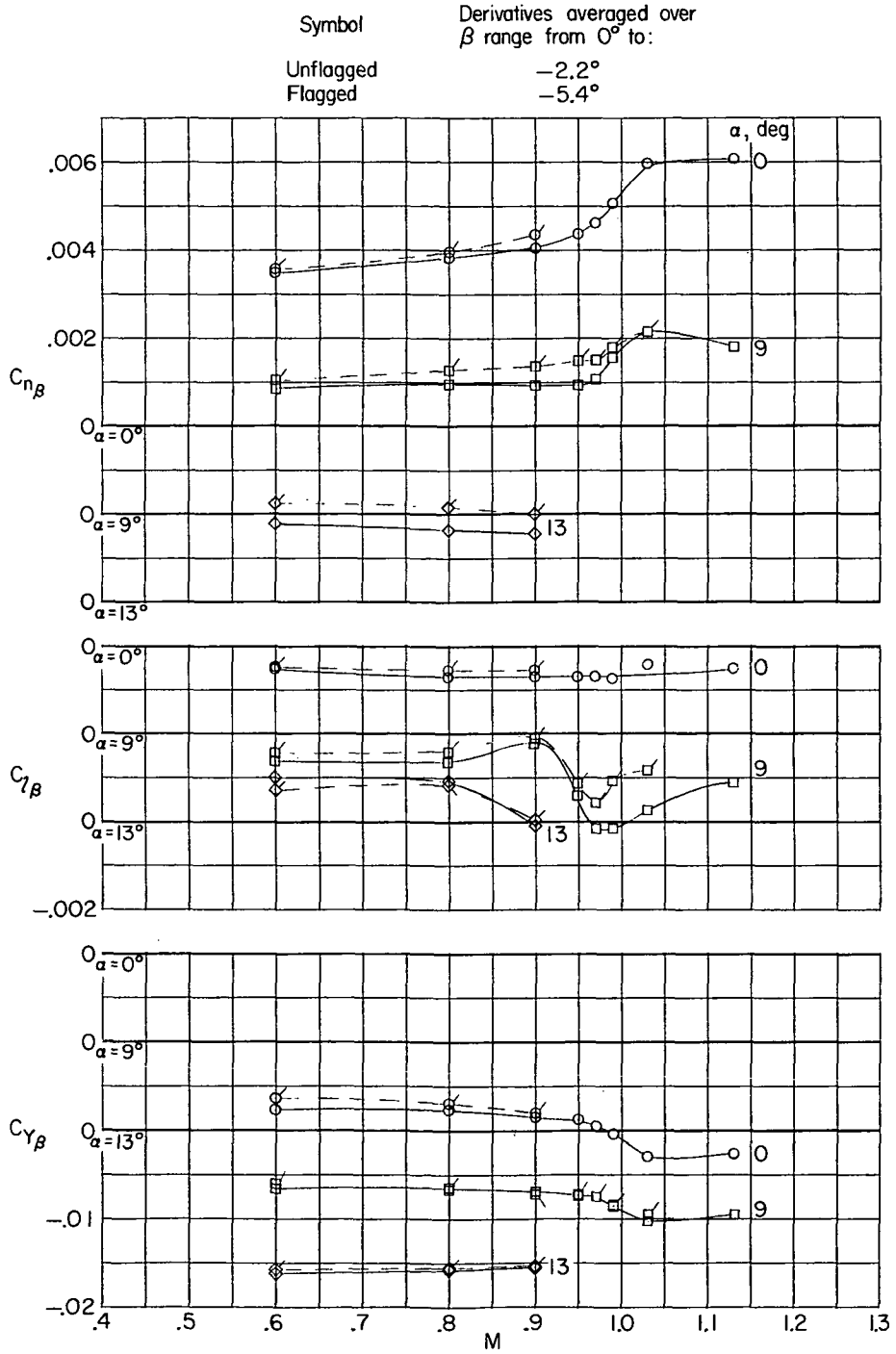

(b) Static lateral-stability derivatives against Mach number.

Figure 48.- Concluded.

[redacted]

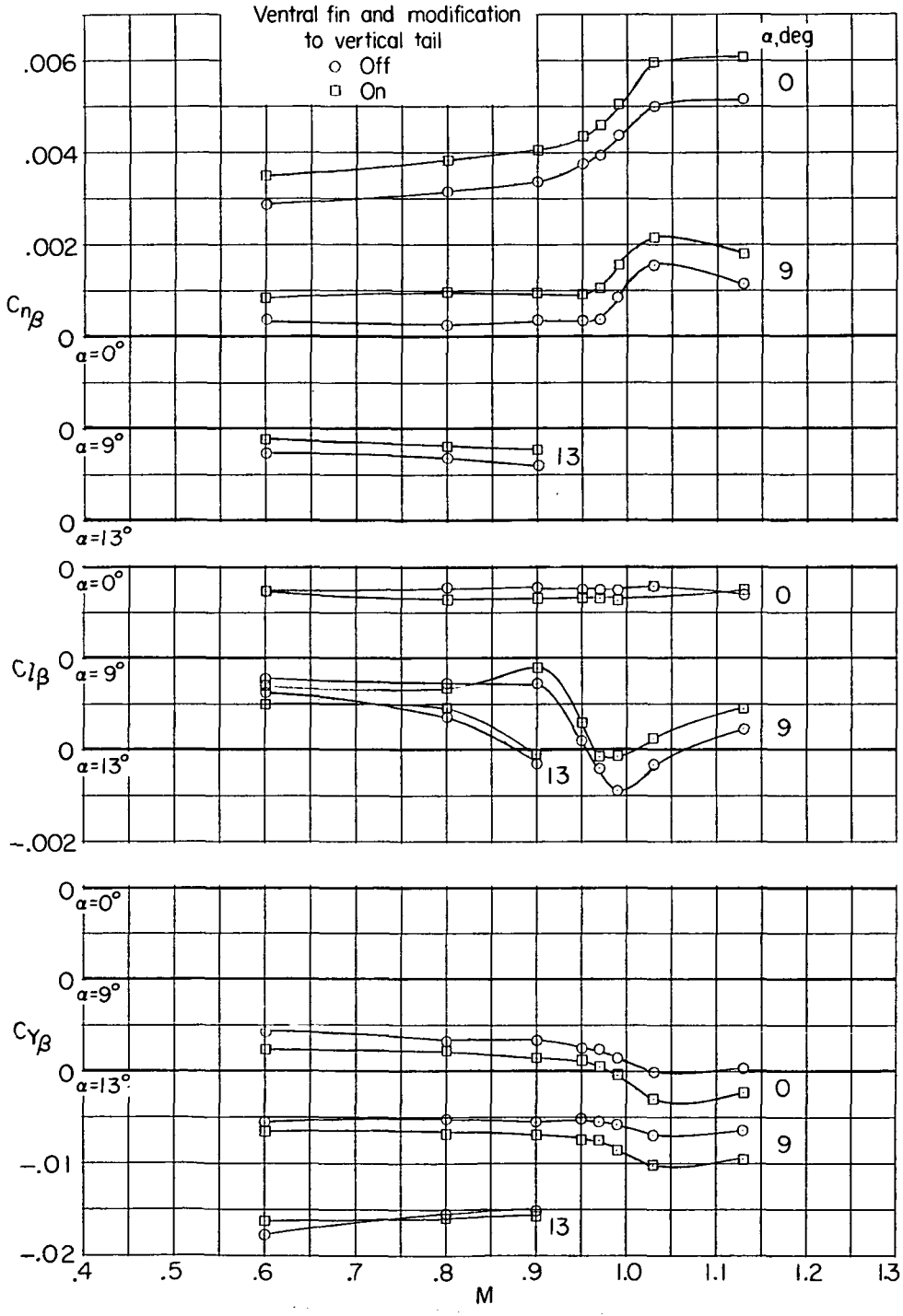

Figure 49.- Effect of ventral fin and modified vertical tail on static lateral-stability derivatives. Complete model; $i_t = -3°$; body with afterbody bump; undrooped supersonic inlet (cruise condition).

[redacted]

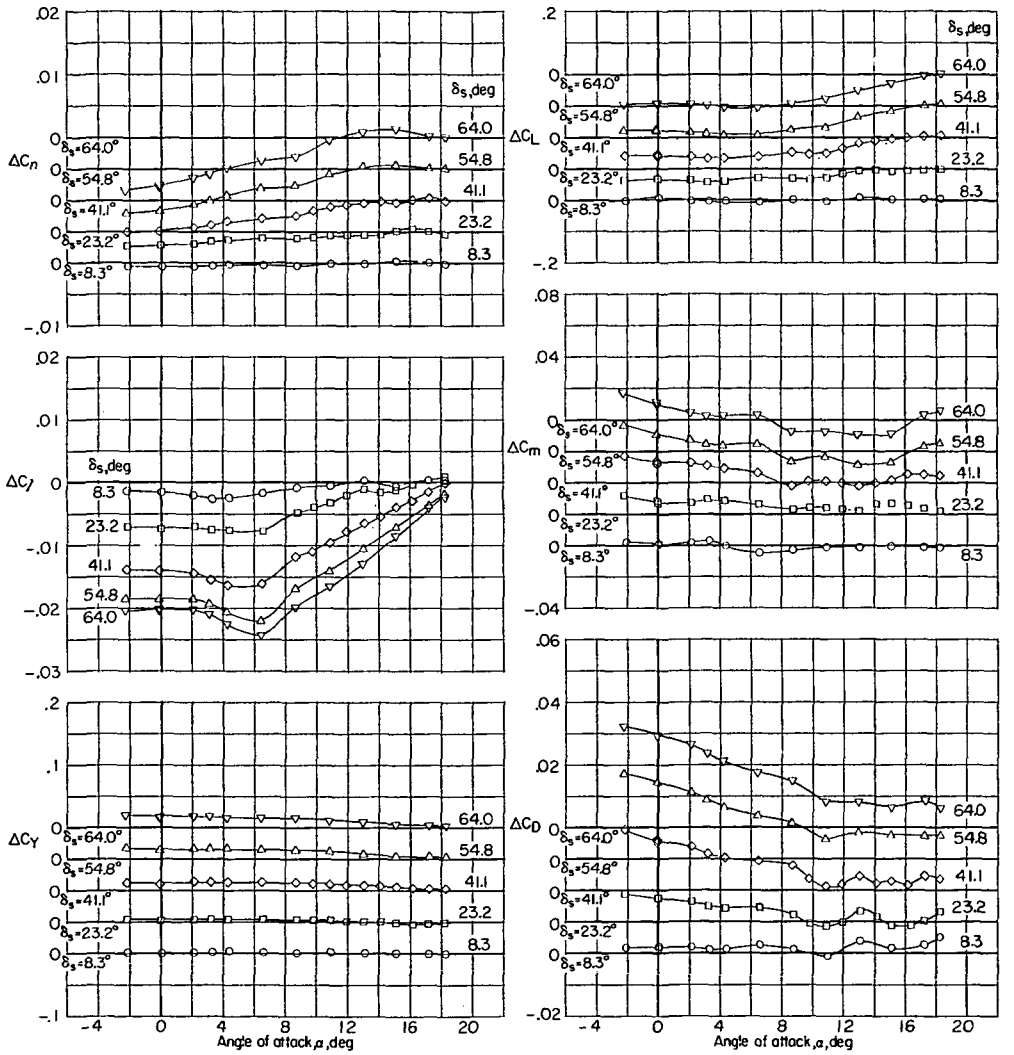

(a) M = 0.60.

Figure 50.- Variation of spoiler aerodynamic characteristics with angle of attack. Complete model; $i_t = -3^\circ$; drooped supersonic inlet (cruise condition).

[redacted]

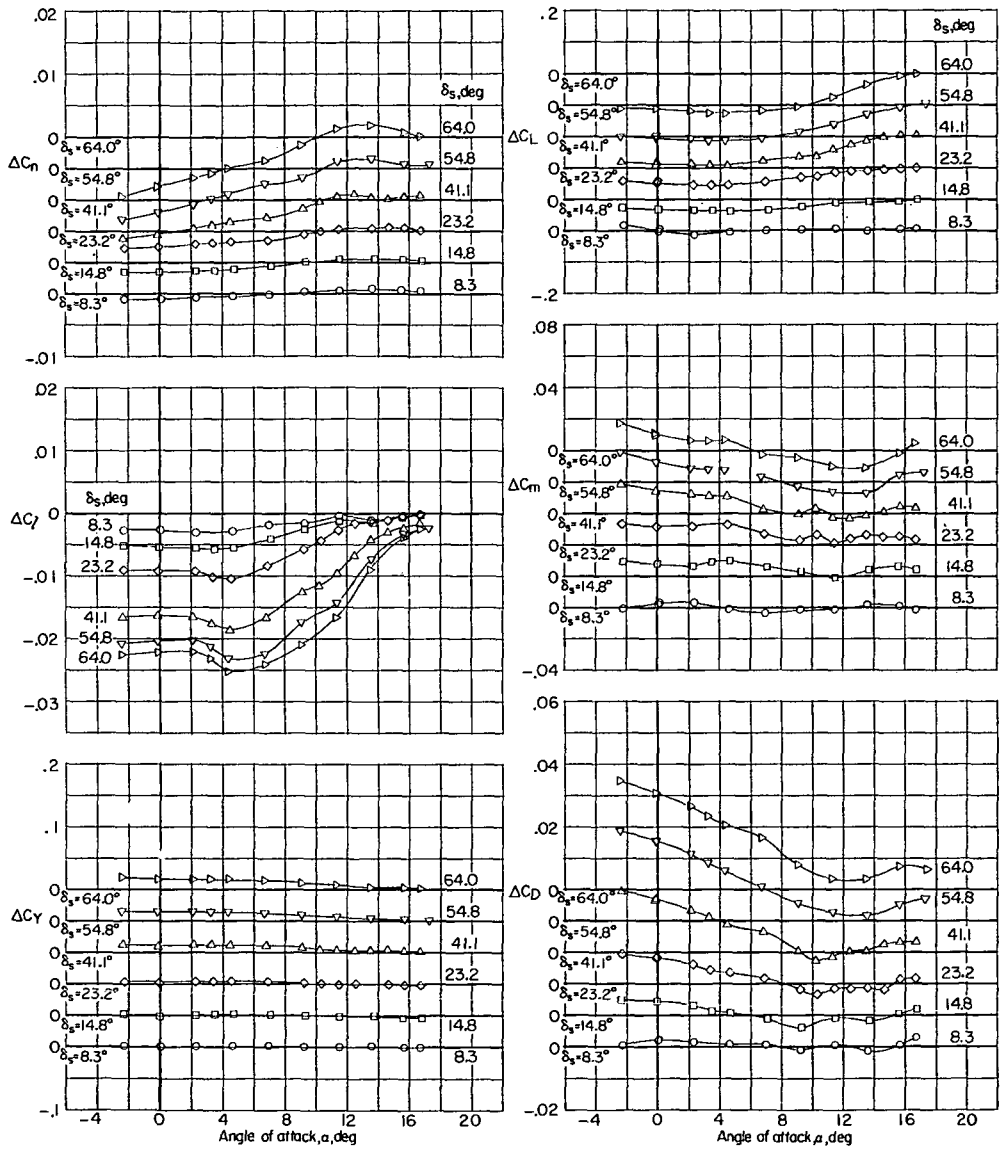

(b) M = 0.80.

Figure 50.- Continued.

[redacted]

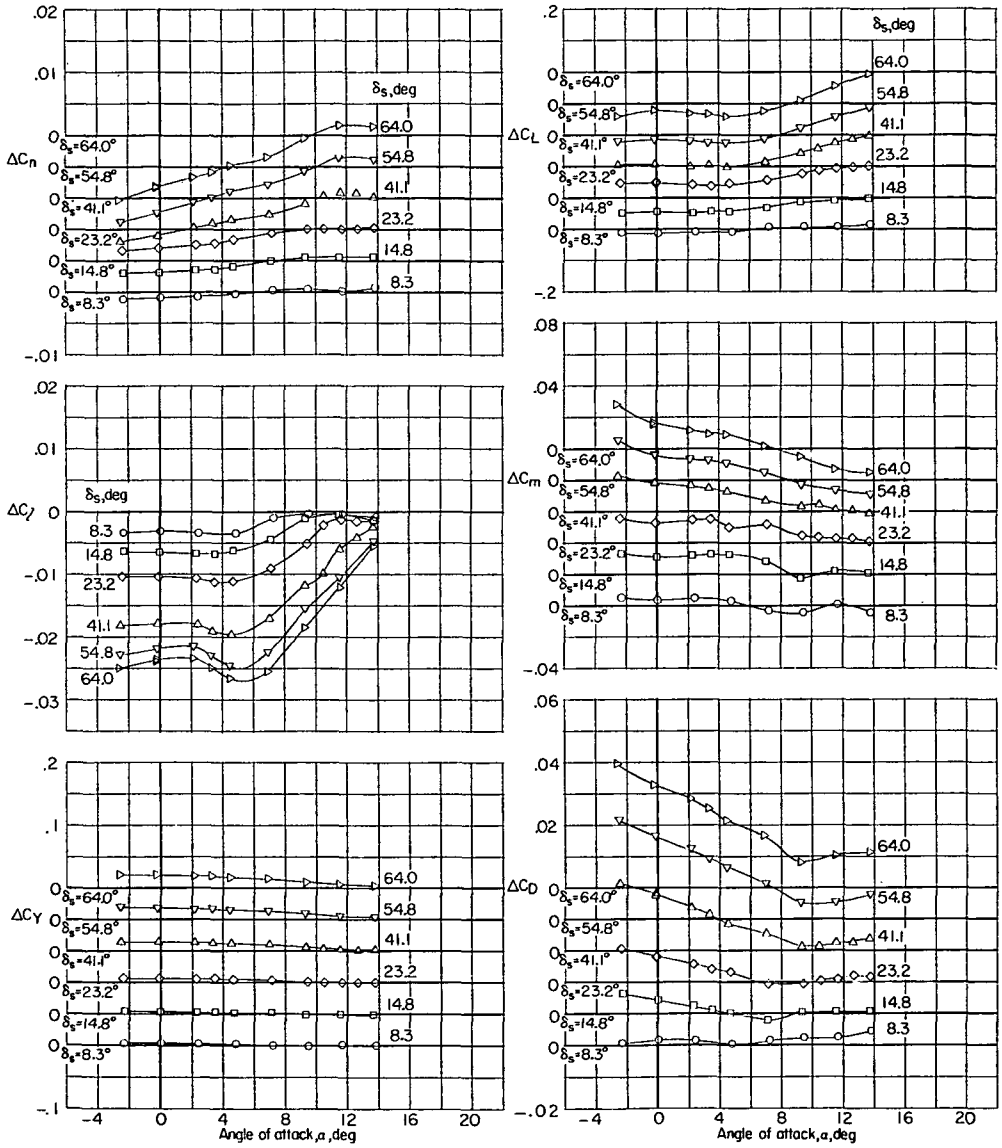

(c) M = 0.90.

Figure 50.- Continued.

[redacted]

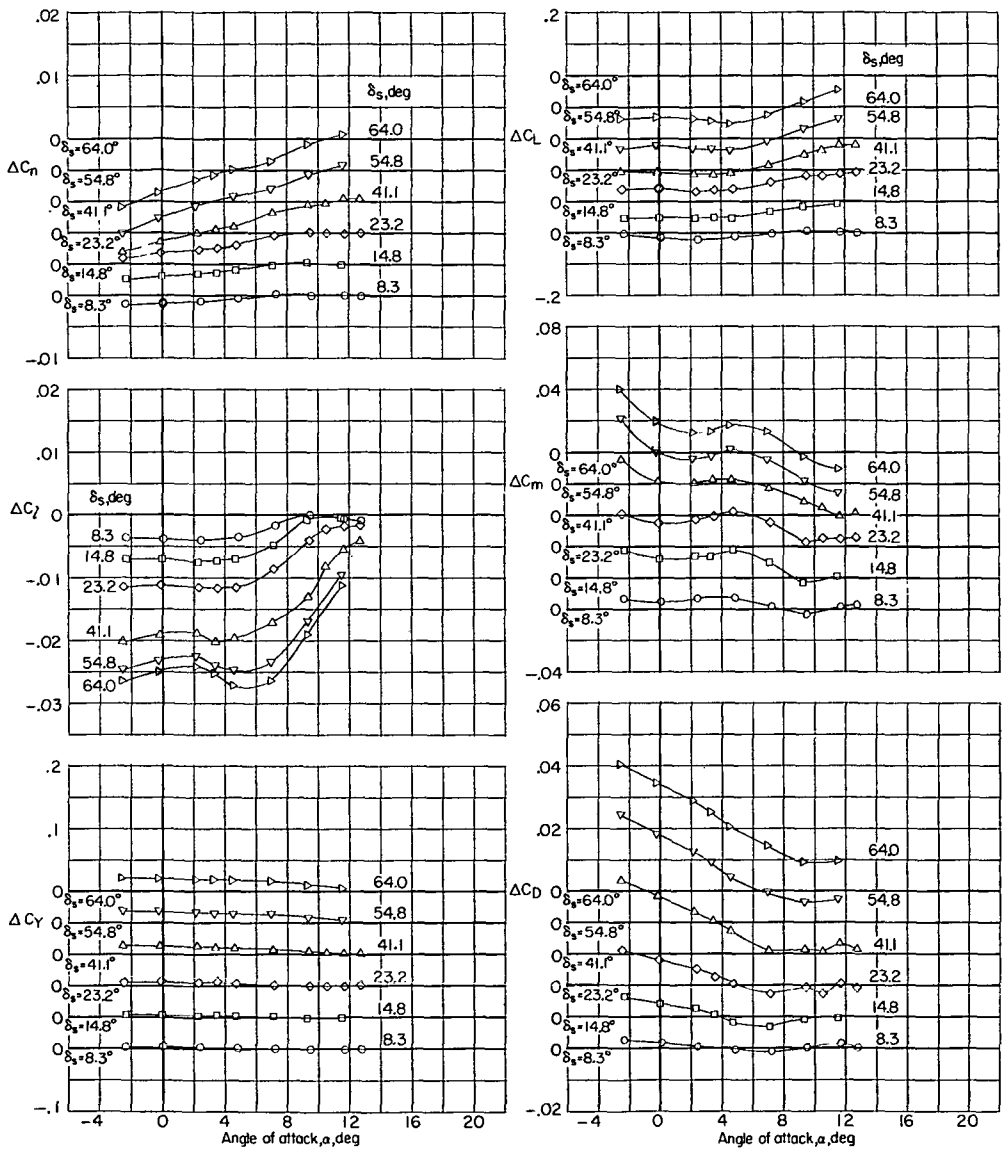

(d) M = 0.93.

Figure 50.- Continued.

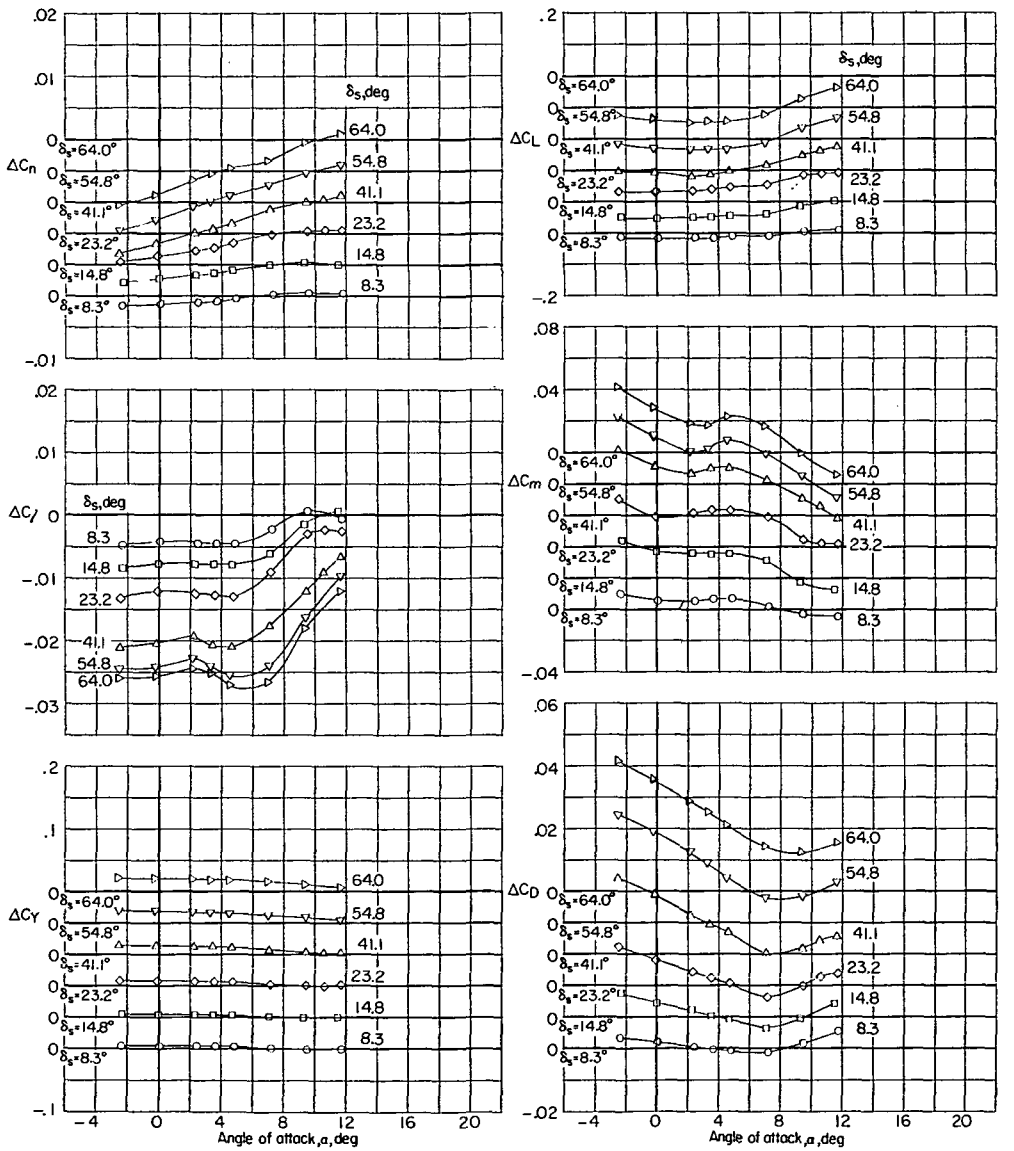

(e) M = 0.95.

Figure 50.- Continued.

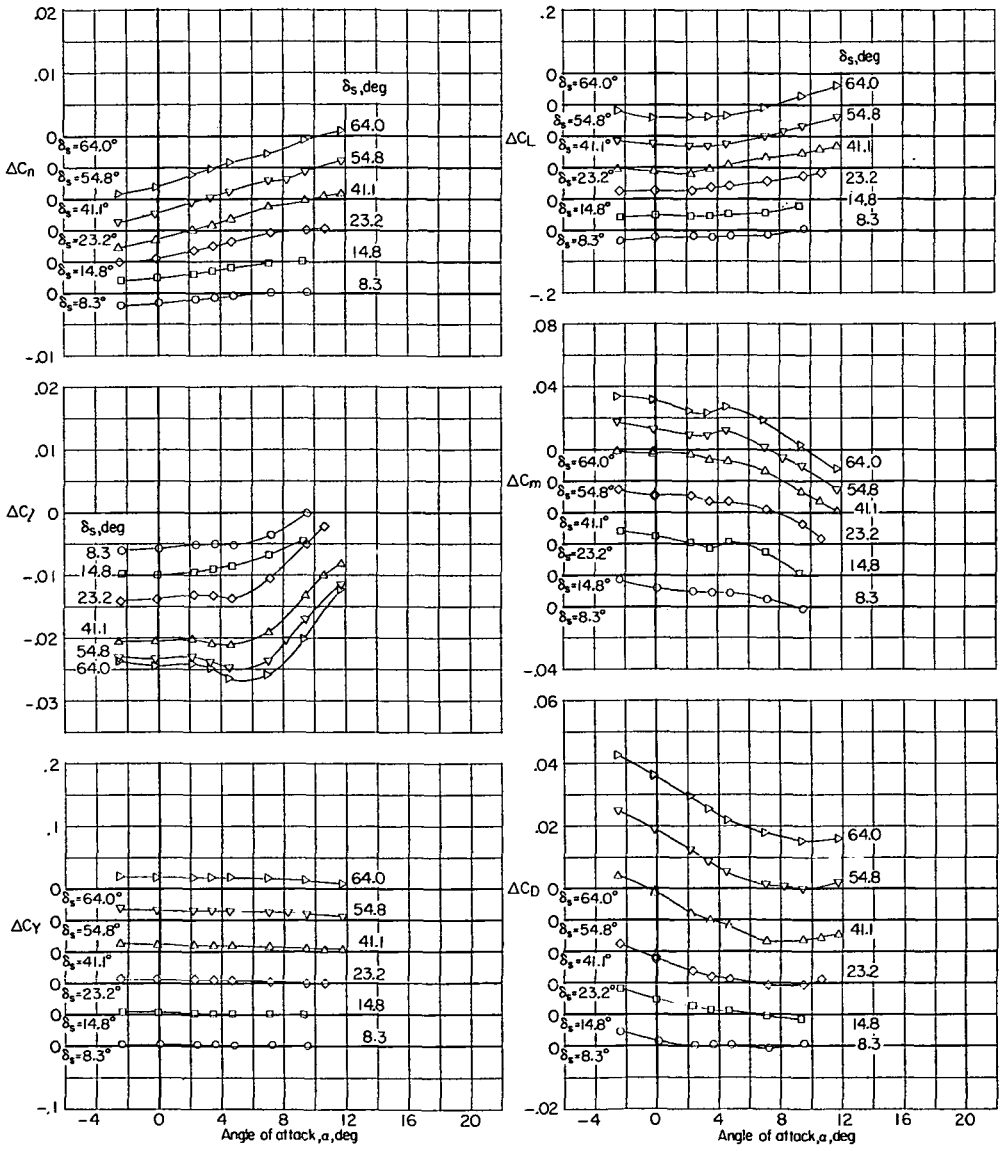

(f) M = 0.97.

Figure 50.- Continued.

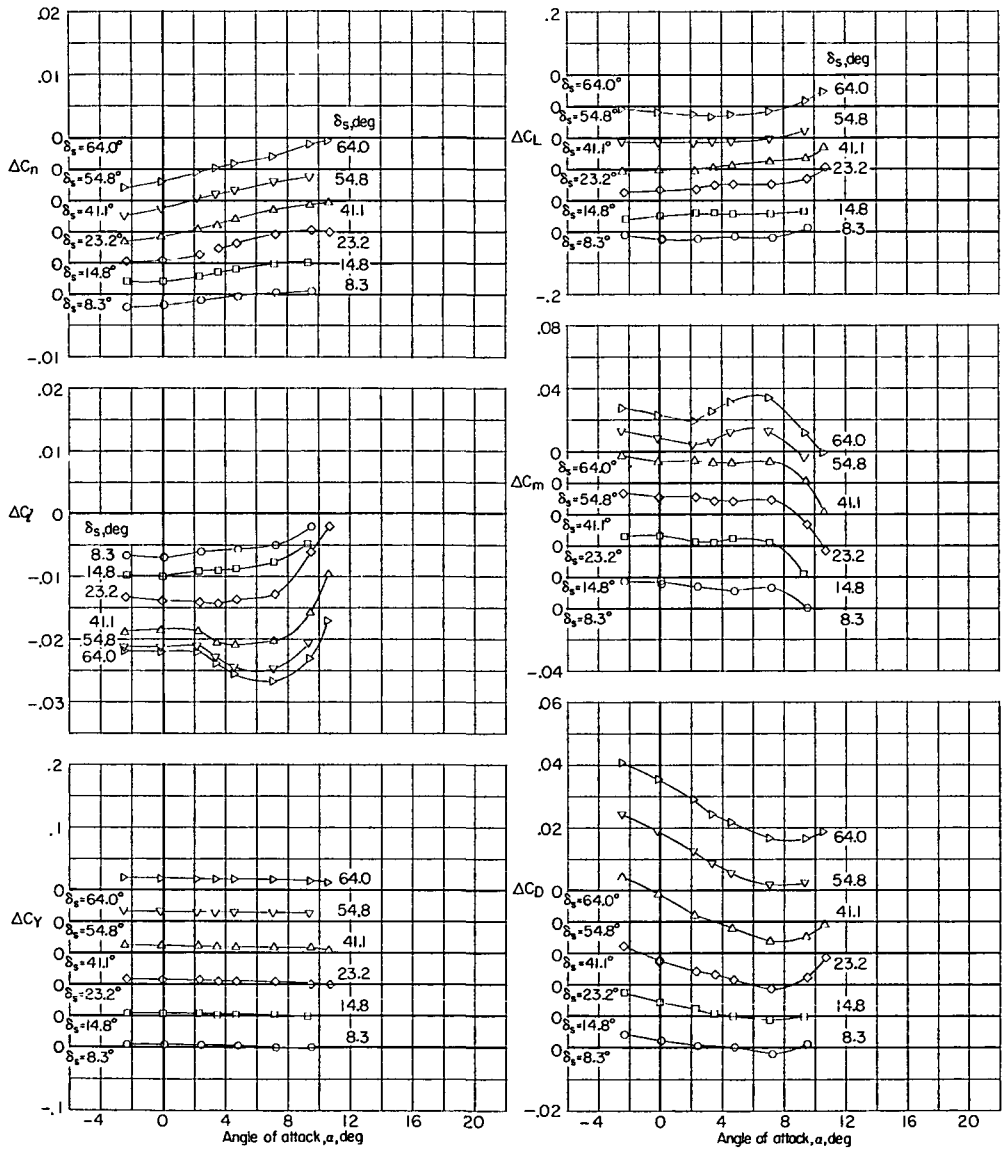

(g) M = 0.99.

Figure 50.- Continued.

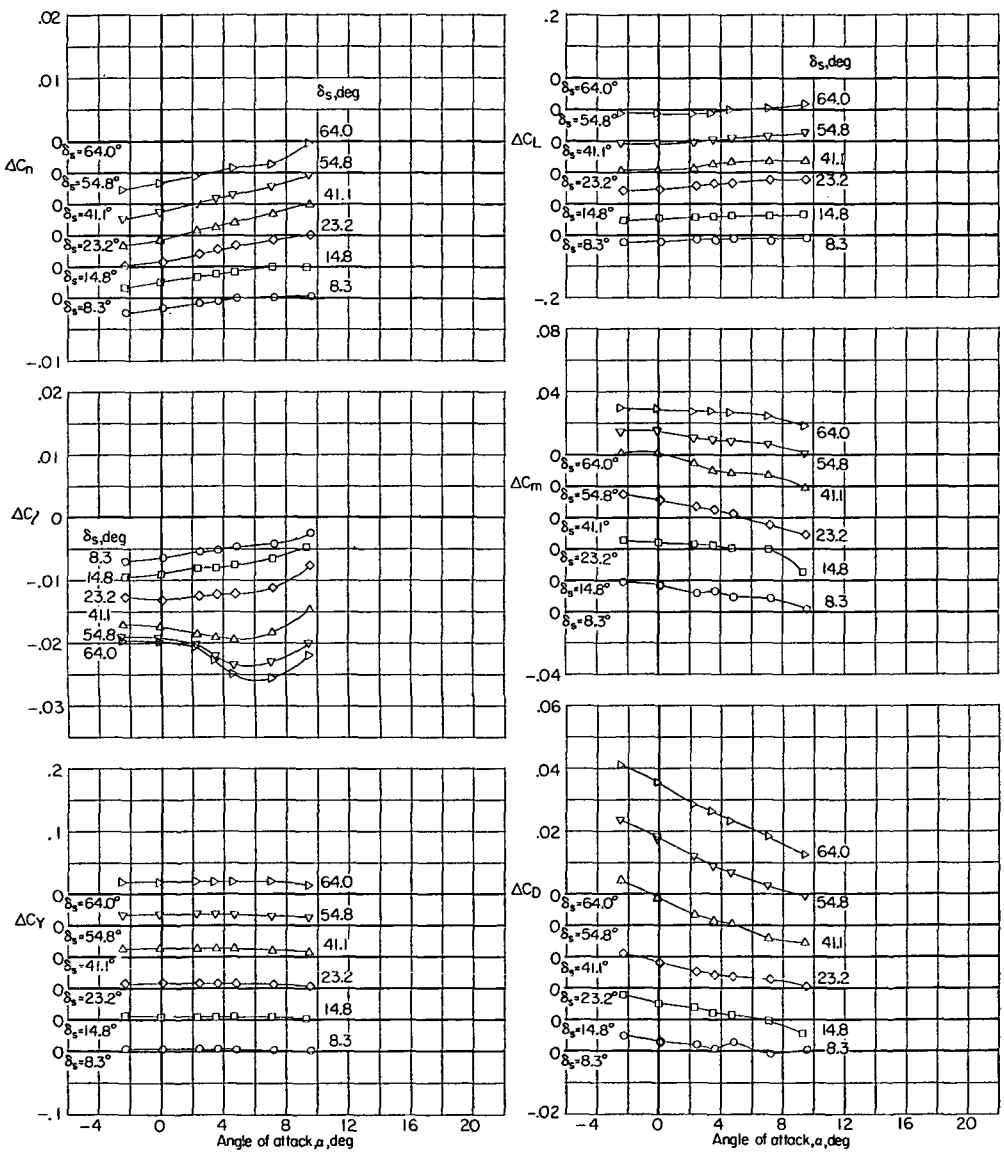

(h) M = 1.03.

Figure 50.- Continued.

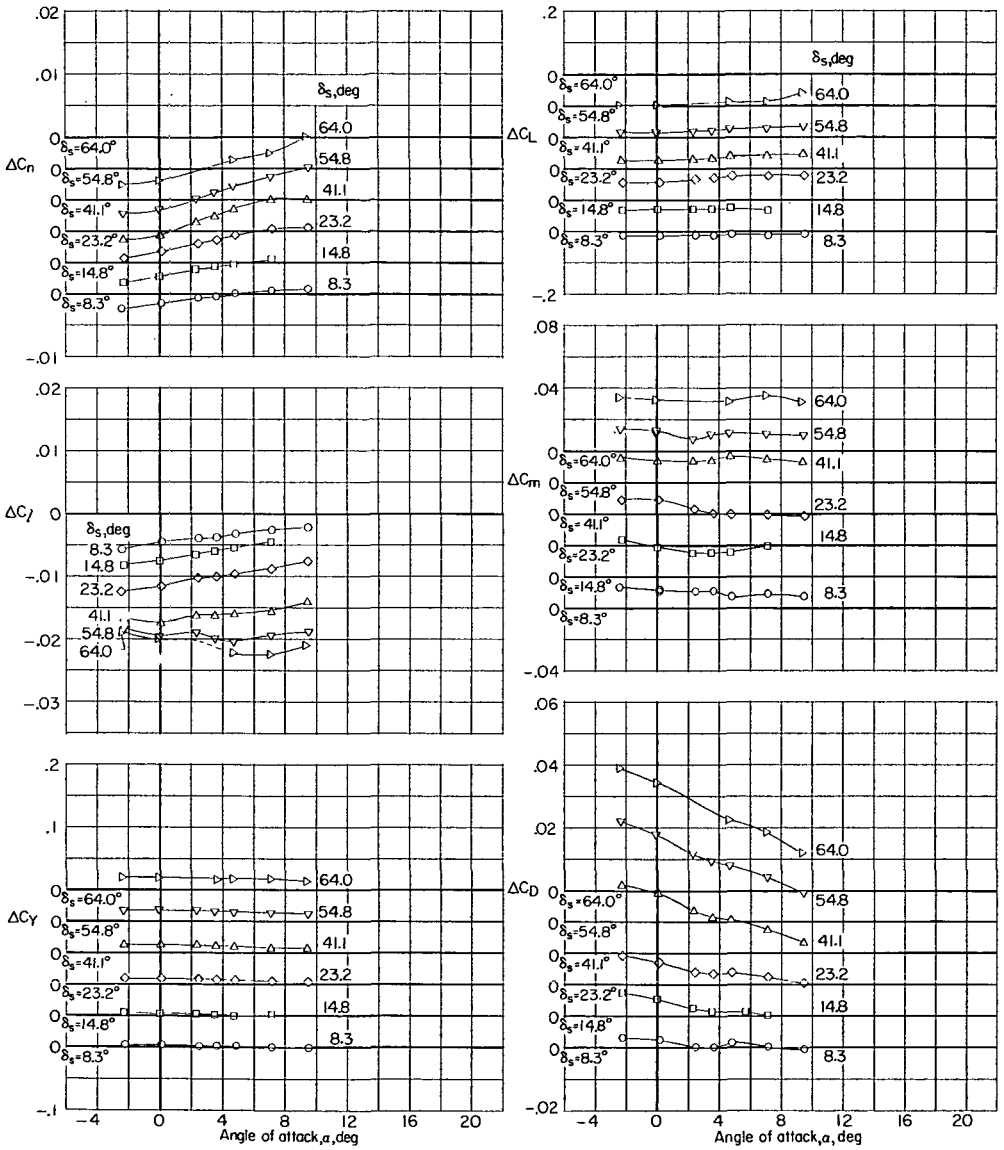

(i) M = 1.13.

Figure 50.- Concluded.

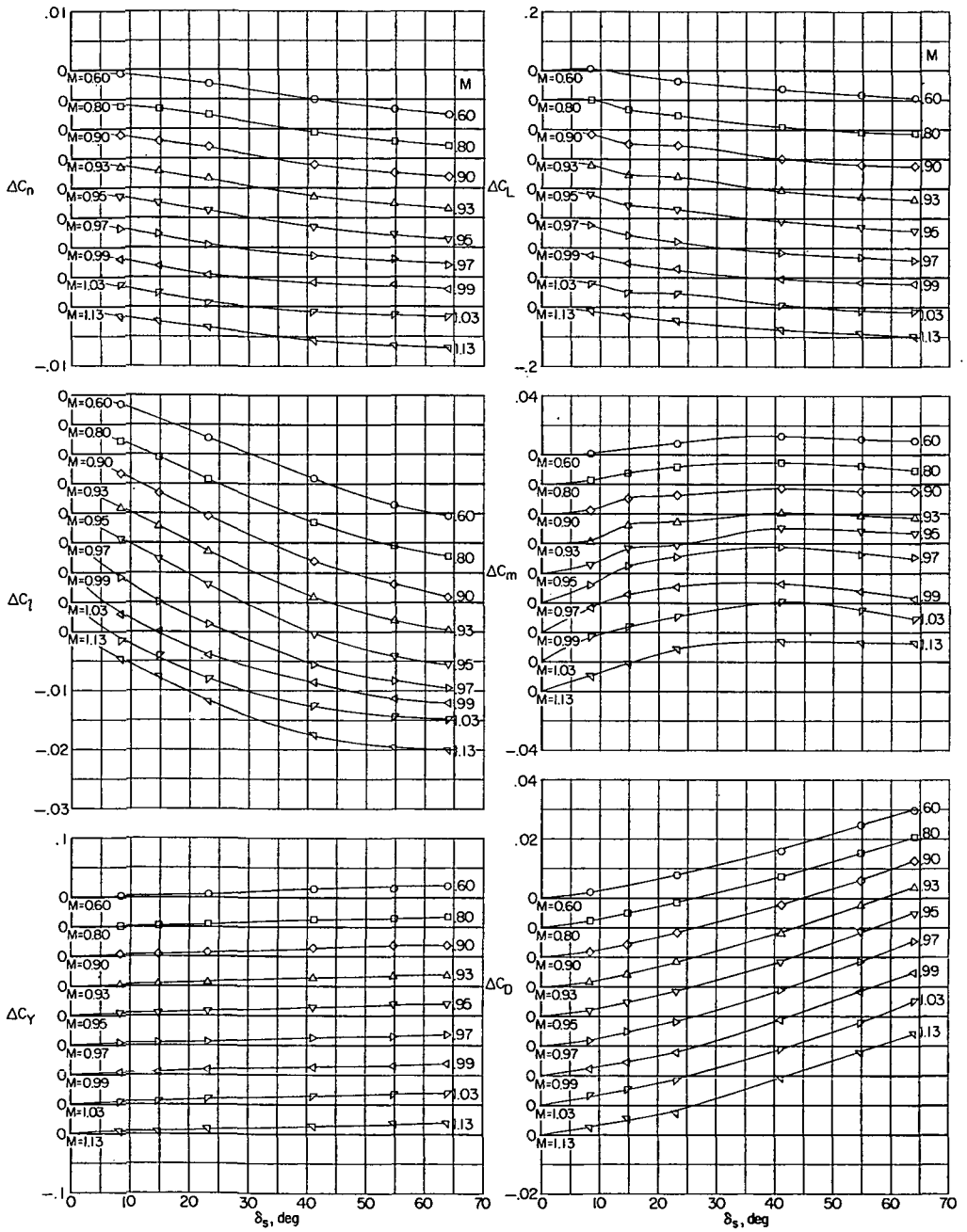

(a) $\alpha = 0^{\circ}$.

Figure 51.- Variation of spoiler aerodynamic characteristics with spoiler deflection. Complete model; $i_t = -3^{\circ}$; drooped supersonic inlet (cruise condition).

[redacted]

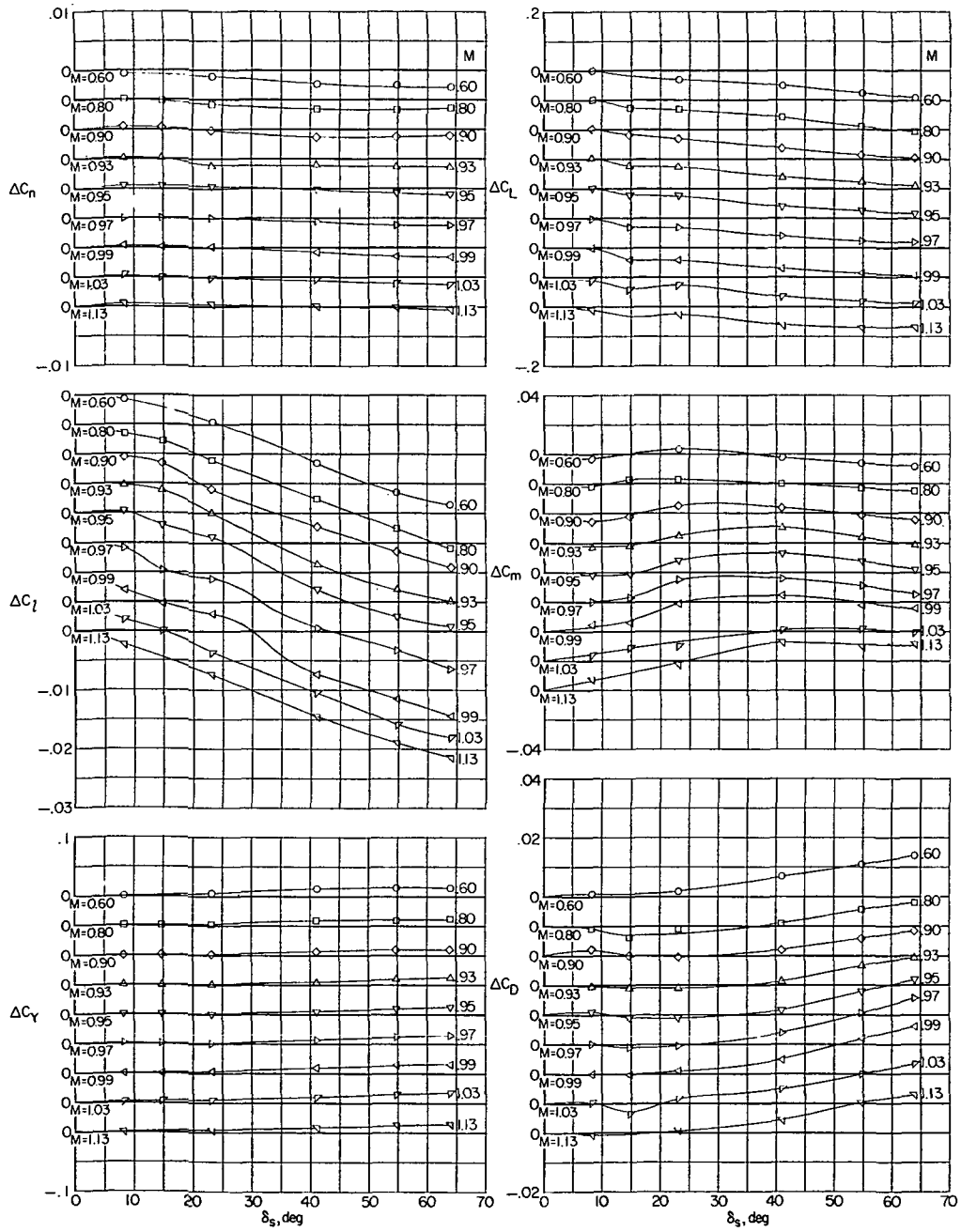

(b) $\alpha = 9^{\circ}$.

Figure 51.- Concluded.

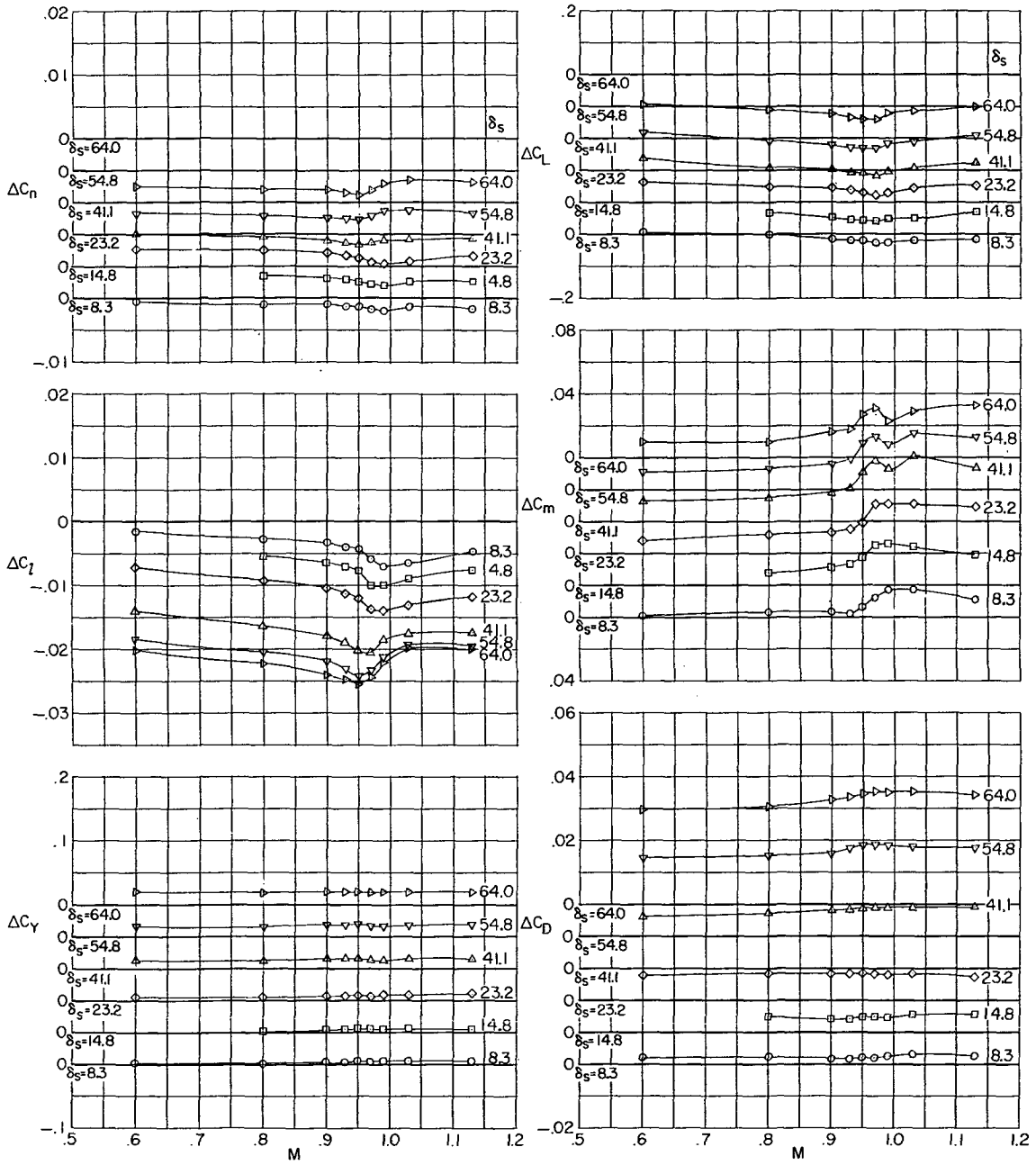

(a) $\alpha = 0^{\circ}$.

Figure 52.- Variation of spoiler aerodynamic characteristics with Mach number. Complete model; $i_t = -3^{\circ}$; drooped supersonic inlet (cruise condition).

[redacted]

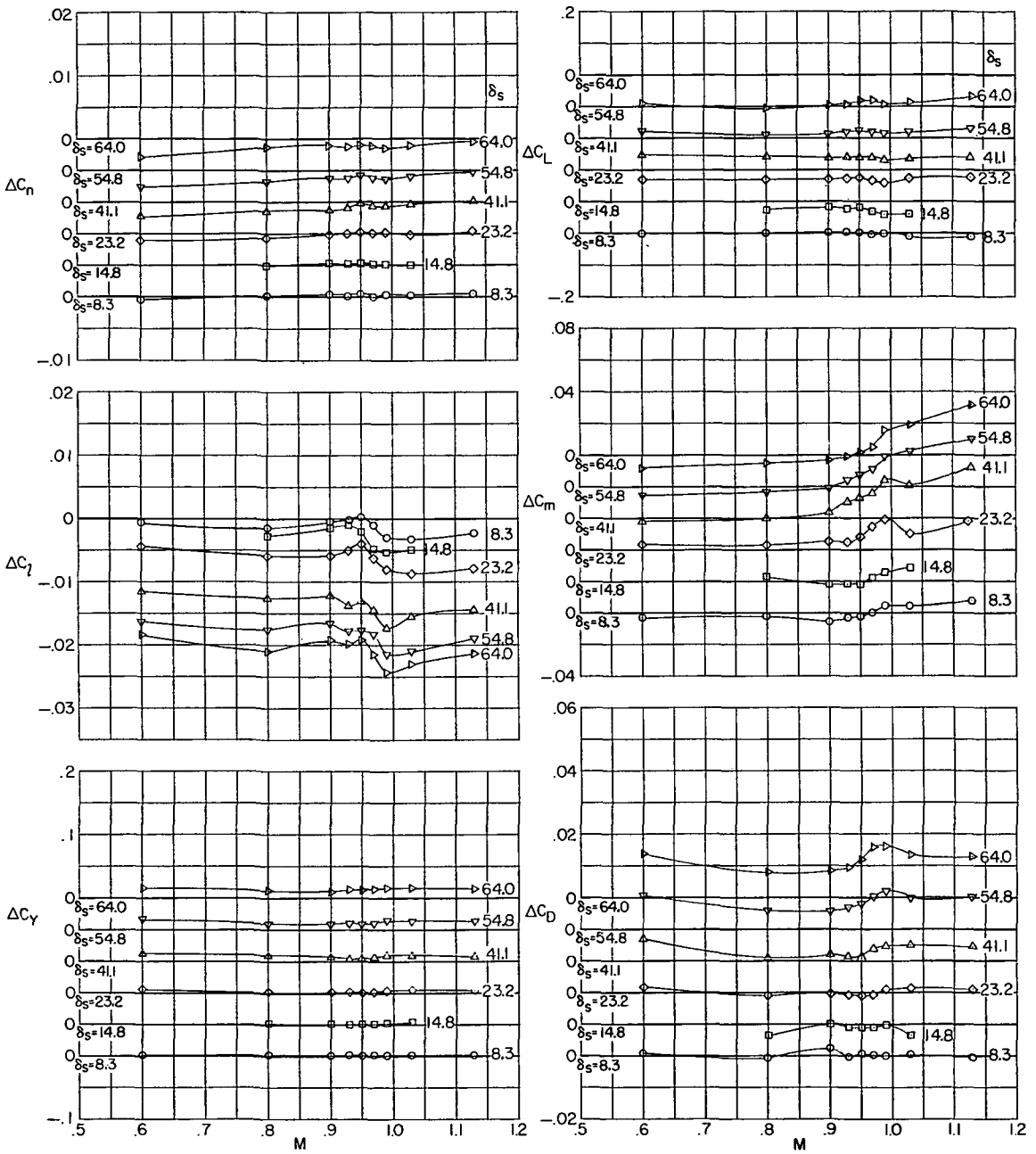

(b) $\alpha = 9^{\circ}$.

Figure 52.- Continued.

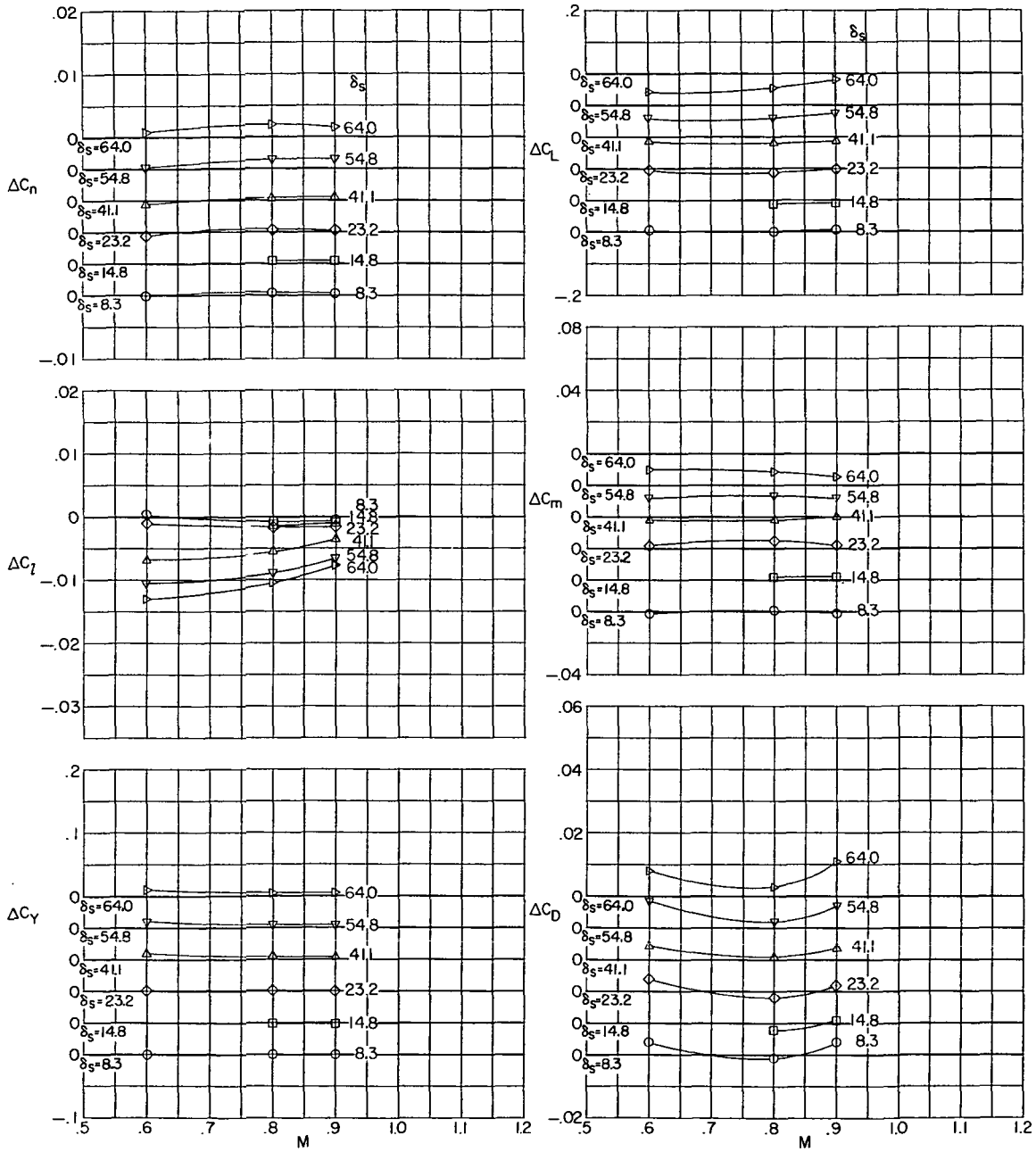

(c) $\alpha = 13^{\circ}$.

Figure 52.- Concluded.

[redacted]

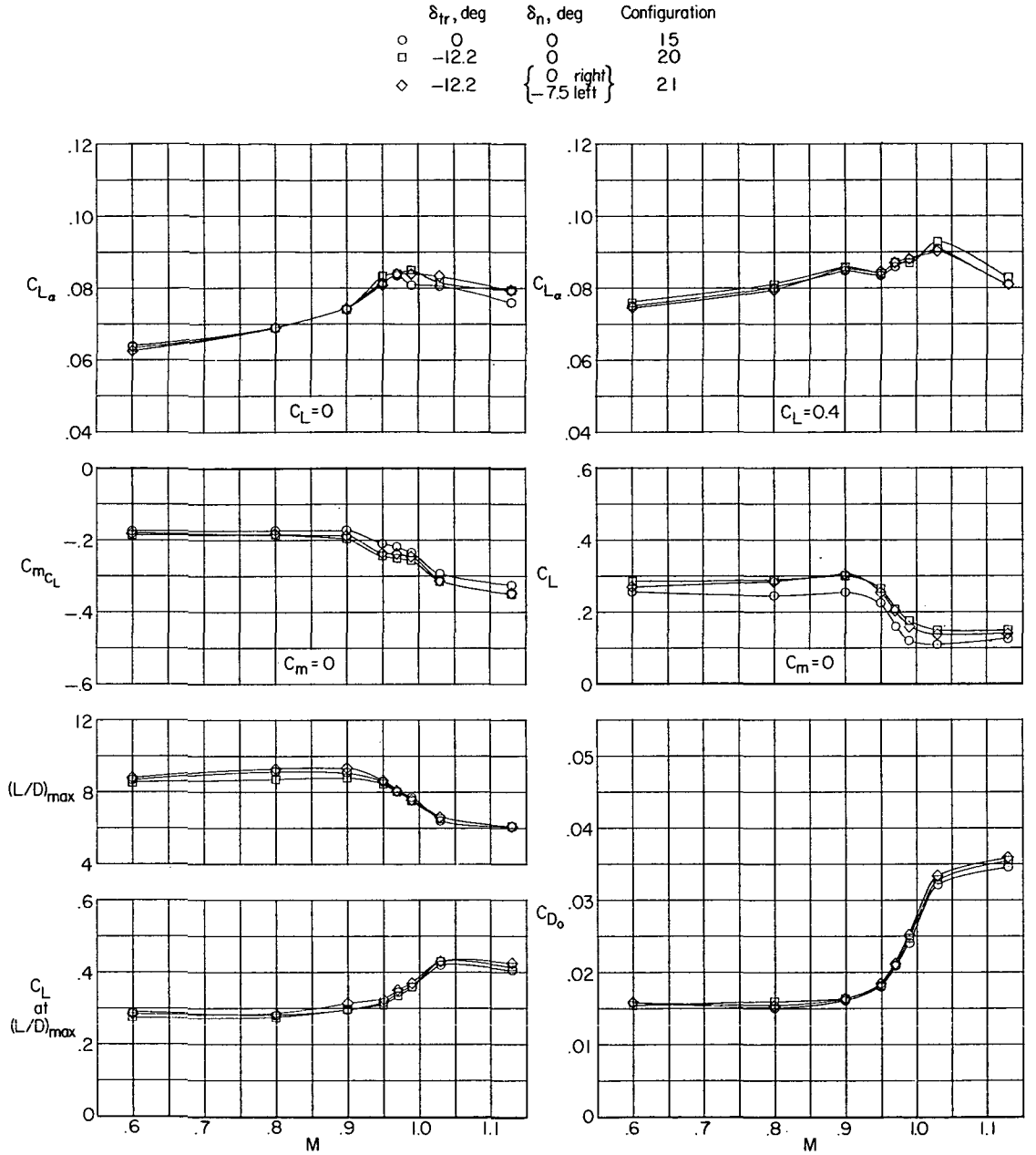

(a) $\delta_n = 0^o$.

Figure 53.- Effect of deflection of wing trim tab on longitudinal, lateral, and directional aerodynamic characteristics. Complete model; $i_t = -3^o$; body with afterbody bump; undrooped supersonic inlet (cruise condition).

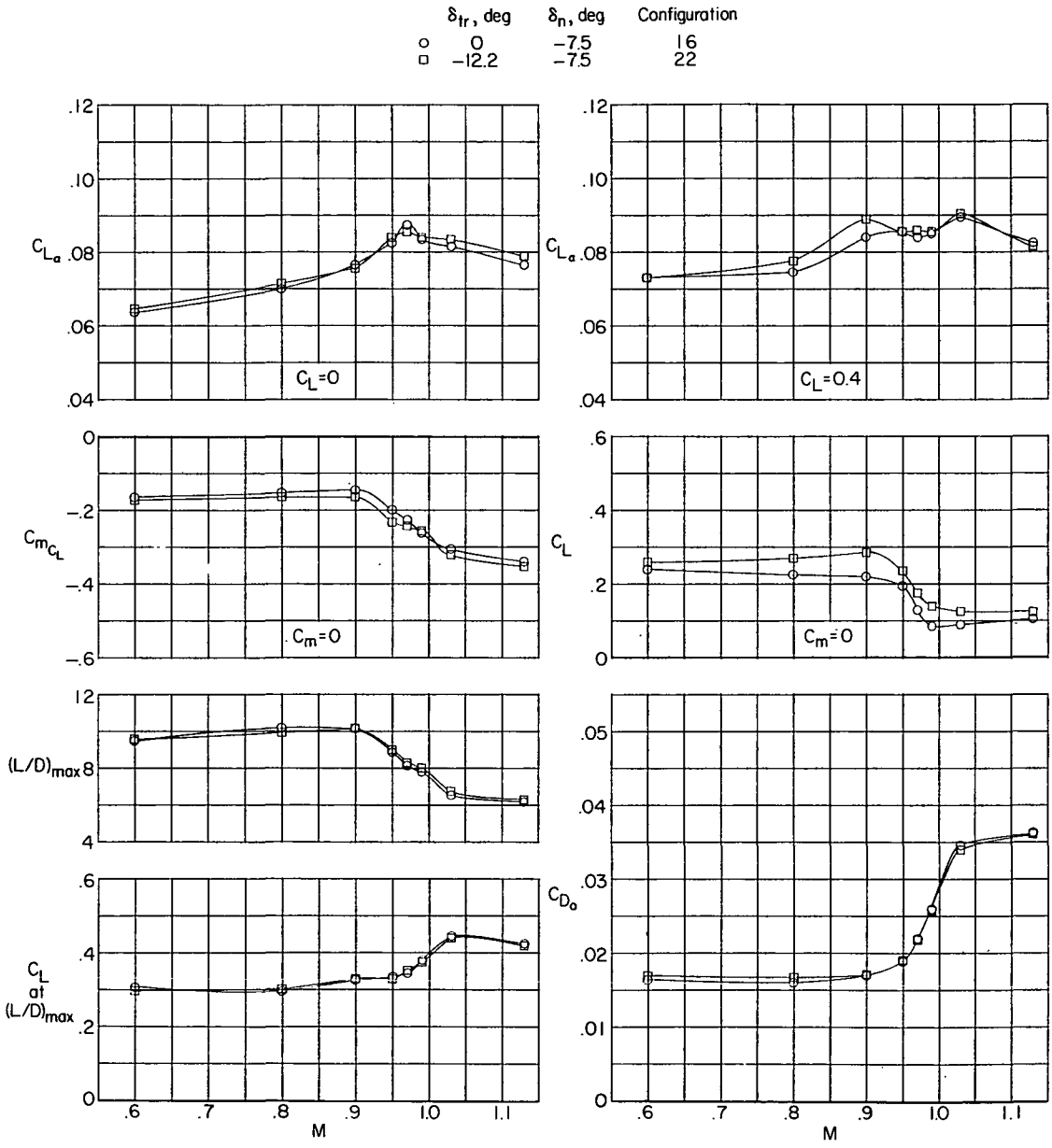

(b) $\delta_n = -7.5^\circ$.

Figure 53.- Continued.

[redacted]

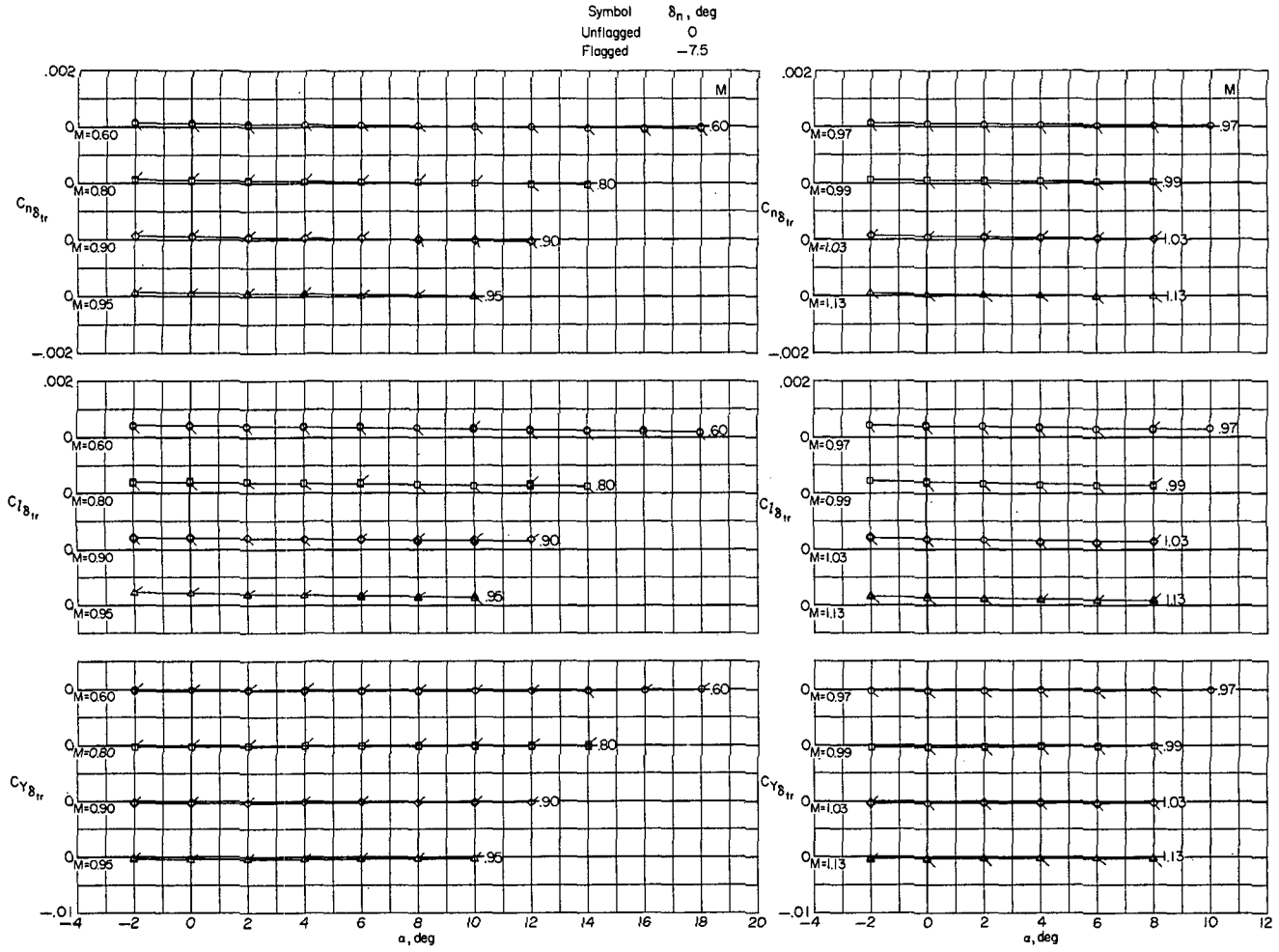

(c) $C_{n_{\delta_{tr}}}$, $C_{l_{\delta_{tr}}}$, and $C_{Y_{\delta_{tr}}}$.

Figure 53.- Concluded.

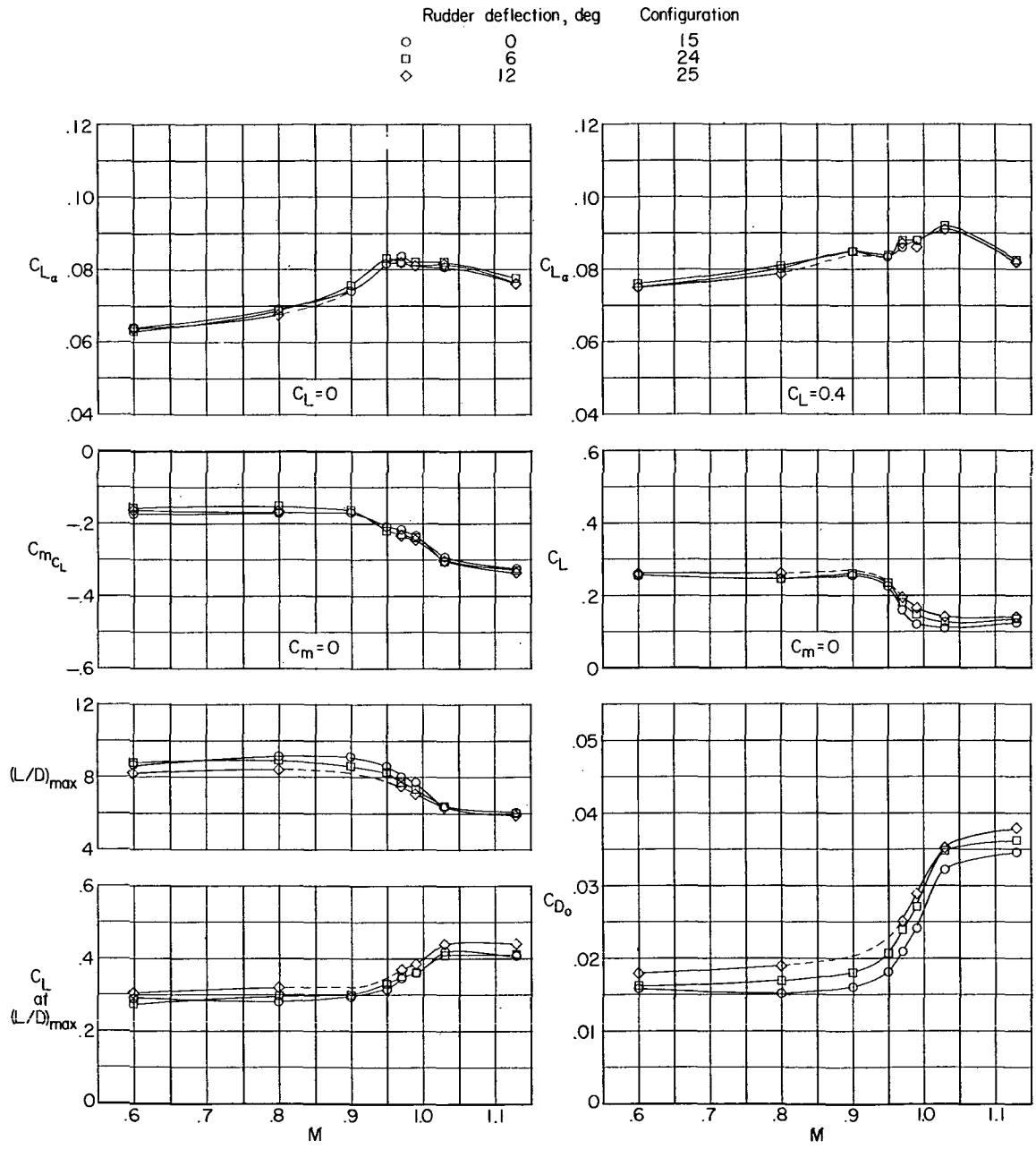

(a) C_{L_α}, $C_{m_{C_L}}$, $(L/D)_{max}$, and C_{D_o} characteristics.

Figure 54.- Effect of rudder deflection on longitudinal, lateral, and directional aerodynamic characteristics. Complete model; $i_t = -3^o$; body with afterbody bump; undrooped supersonic inlet (cruise condition).

[redacted]

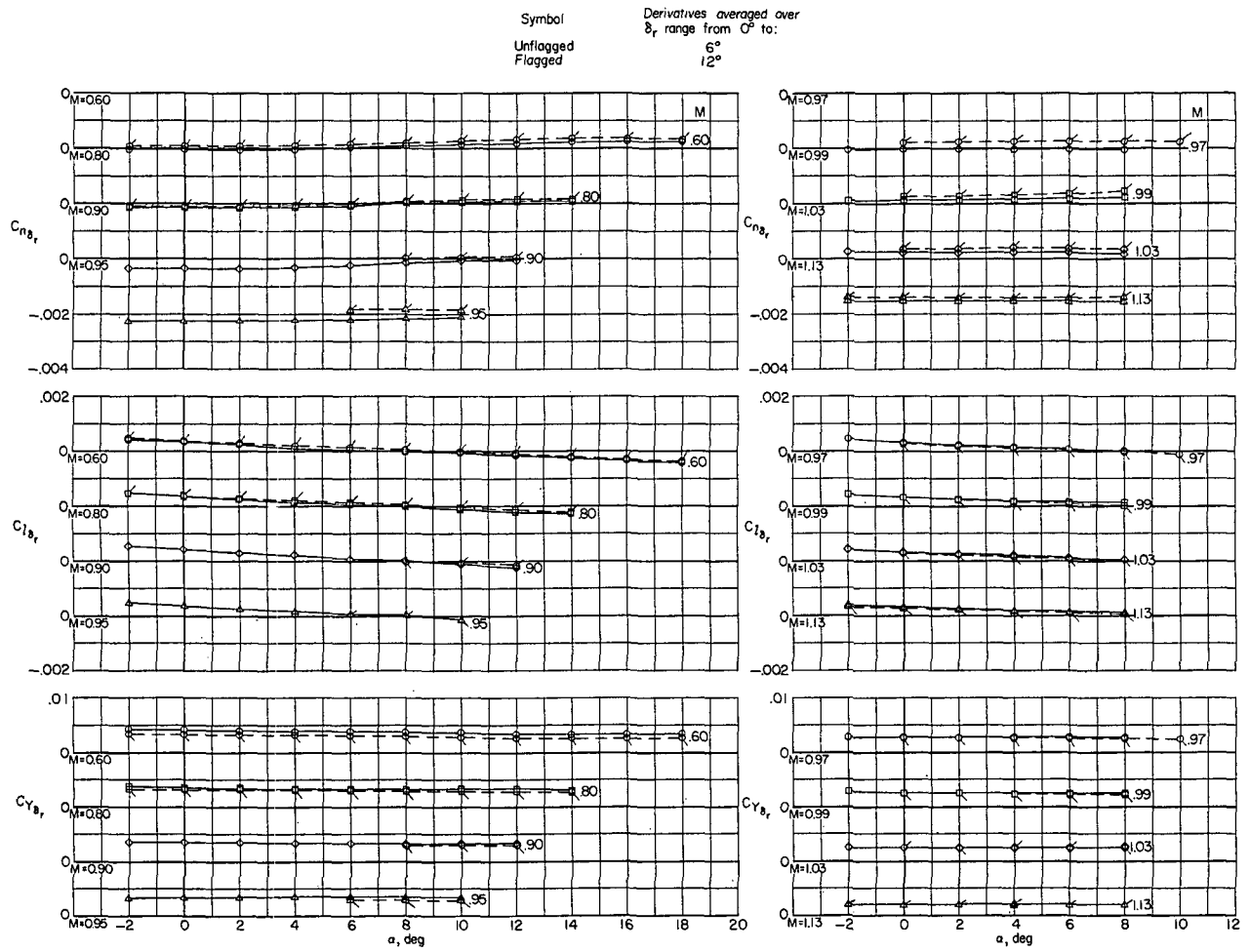

(b) $C_{n_{\delta_r}}$, $C_{l_{\delta_r}}$, and $C_{Y_{\delta_r}}$ against angle of attack.

Figure 54.- Continued.

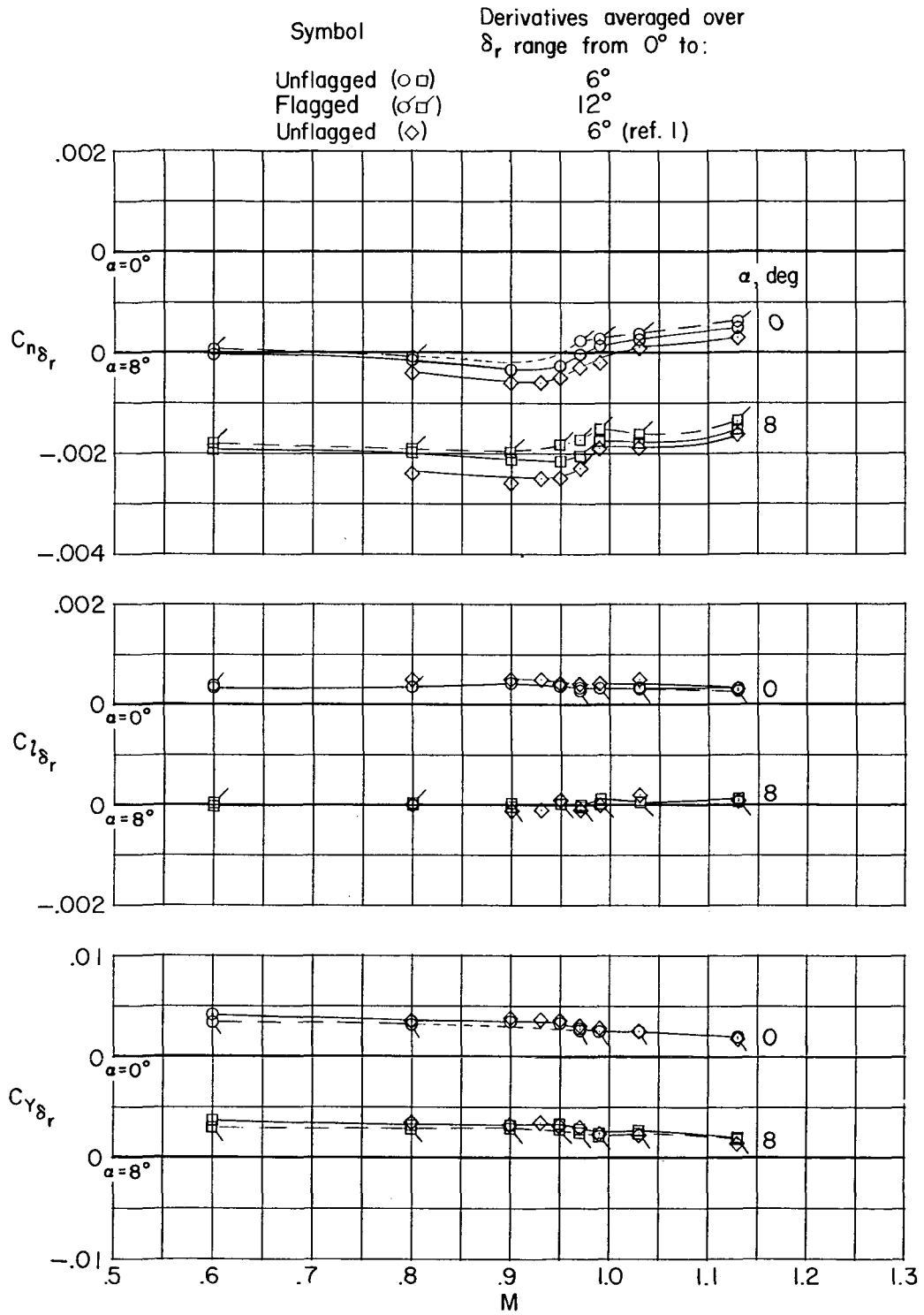

(c) $C_{n_{\delta_r}}$, $C_{l_{\delta_r}}$, and $C_{Y_{\delta_r}}$ against Mach number.

Figure 54.- Concluded.

[redacted]

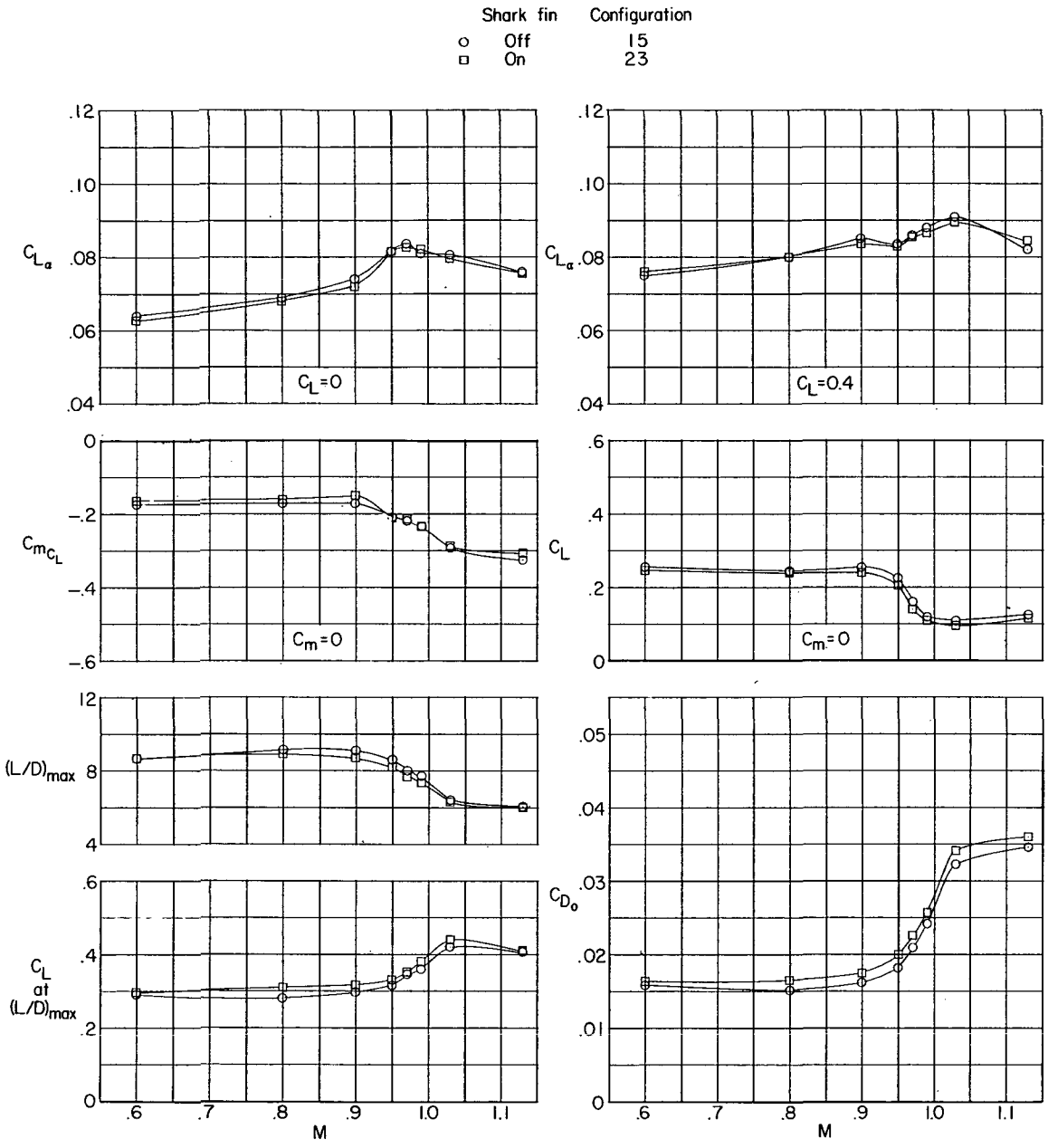

(a) C_{L_α}, $C_{m_{C_L}}$, $(L/D)_{max}$, and C_{D_o} characteristics.

Figure 55.- Effect of 10°-deflection shark fin on longitudinal, lateral, and directional aerodynamic characteristics. Complete model; $i_t = -3°$; body with afterbody bump; undrooped supersonic inlet (cruise condition).

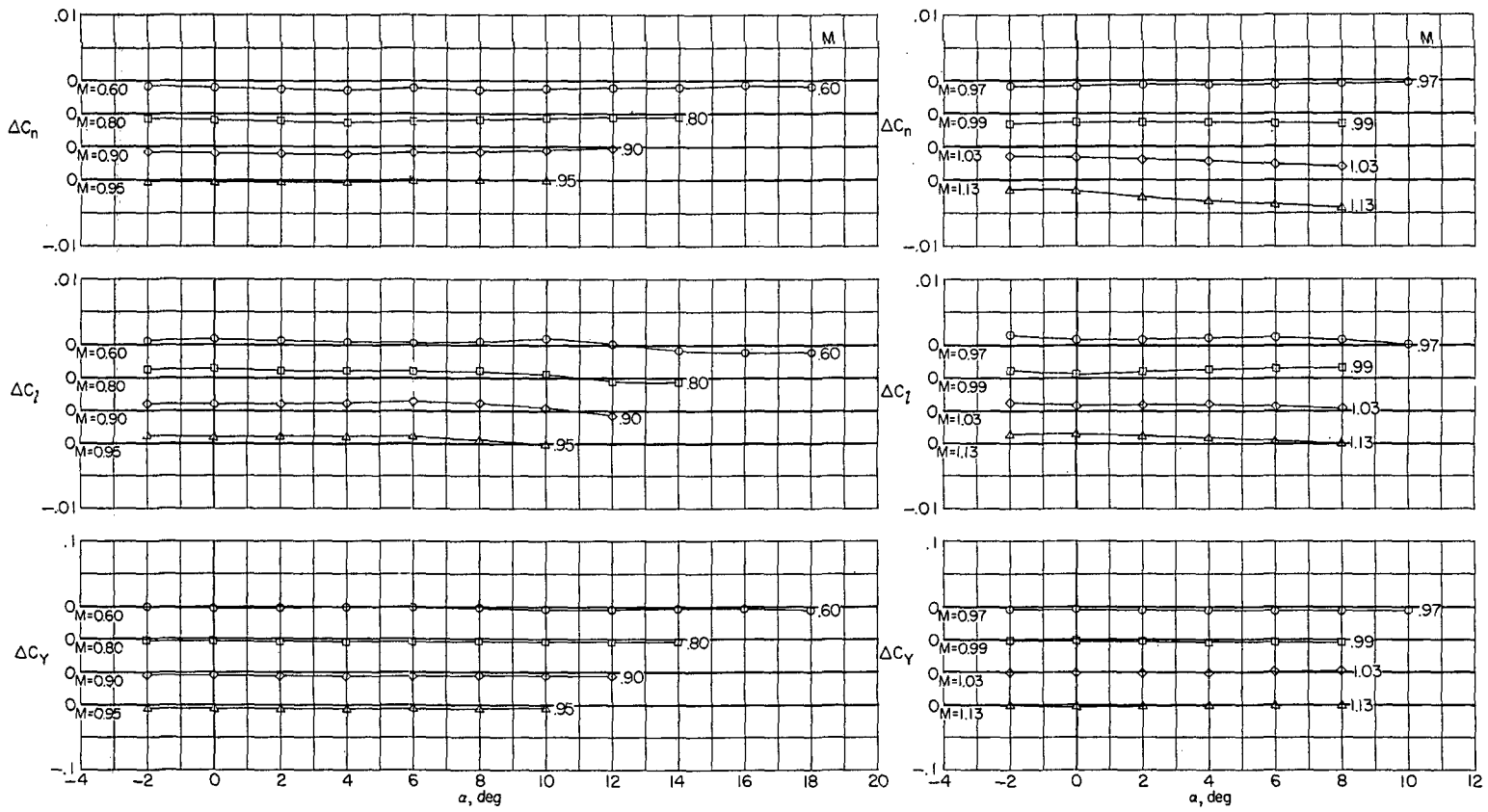

(b) ΔC_n, ΔC_l, and ΔC_Y due to shark fin.

Figure 55.- Concluded.

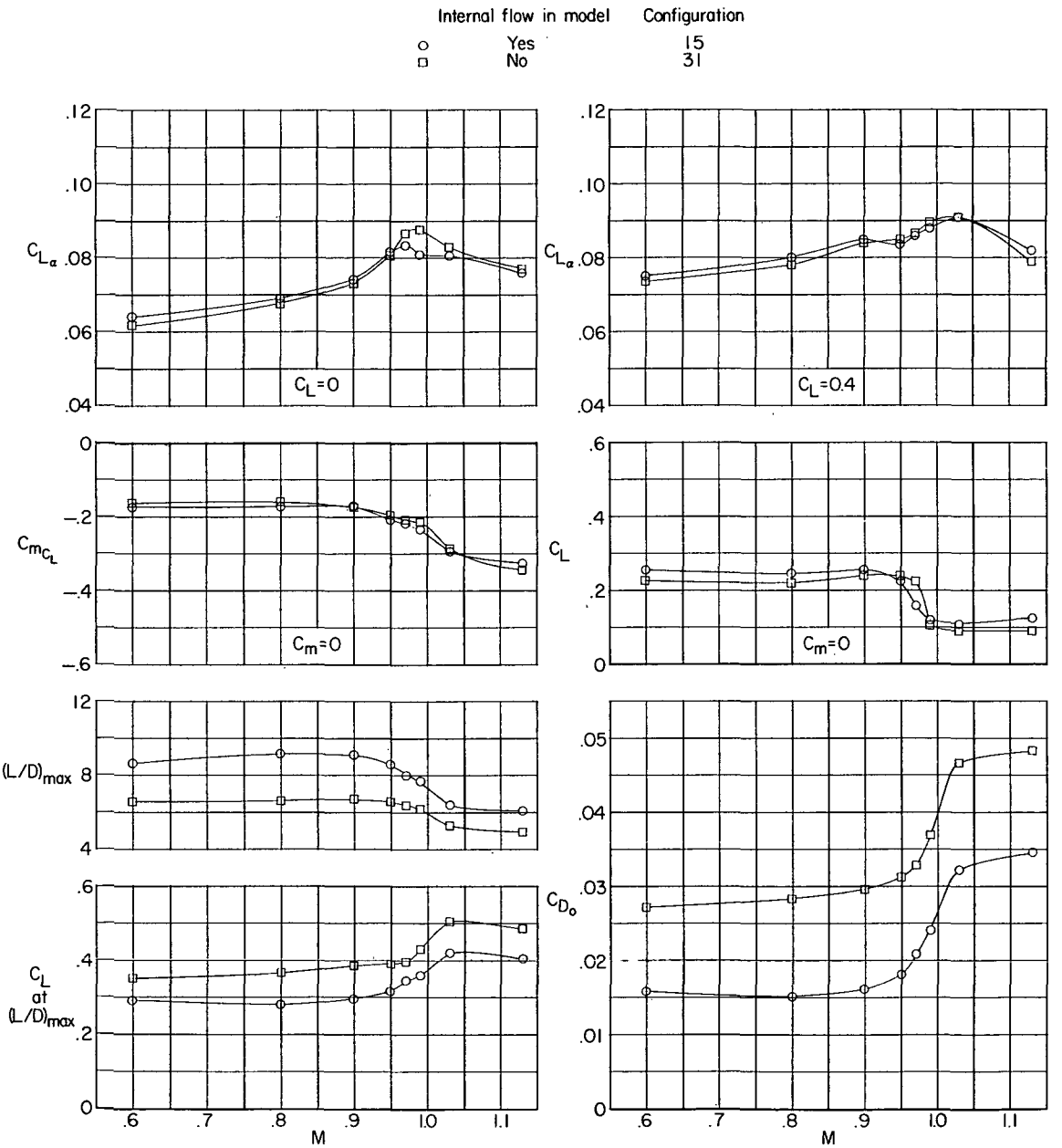

Figure 56.- Effect of blocked inlet on longitudinal aerodynamic characteristics. Complete model; $i_t = -3^o$; body with afterbody bump; undrooped supersonic inlet (cruise condition).

[redacted]

[redacted]

INVESTIGATION OF A 1/22-SCALE MODEL OF THE REPUBLIC F-105 AIRPLANE IN THE LANGLEY 8-FOOT TRANSONIC TUNNEL

LATERAL, DIRECTIONAL, AND ADDITIONAL LONGITUDINAL STATIC STABILITY AND CONTROL

By Arvo A. Luoma

ABSTRACT

An investigation was made of the lateral, directional, and additional longitudinal static stability and control characteristics of various configurations of a 1/22-scale model of the Republic F-105 airplane at Mach numbers from 0.60 to 1.13. The angle-of-attack range varied from approximately -2° to 16° at the lowest Mach number to -2° to 9° at the highest Mach number. Angles of sideslip of 0°, -2.2°, and -5.4° were tested.

INDEX HEADINGS

Airplanes - Specific Types	1.7.1.2
Stability, Longitudinal - Static	1.8.1.1.1
Stability, Lateral - Static	1.8.1.1.2
Stability, Directional - Static	1.8.1.1.3
Control, Lateral	1.8.2.2
Control, Directional	1.8.2.3

[redacted]